Metal Loss Defect Failure Analysis and Prognostics Considering Defect Interactions and Complex Service Conditions

by

Han Zhang

A thesis submitted in partial fulfillment of the requirements for the degree of

Doctor of Philosophy

Department of Mechanical Engineering
University of Alberta

Abstract

Clean energy has attracted intensive attention as the global energy transition is accelerated. Pipelines are significant for achieving large-scale clean energy transportation. Meanwhile, gears are vital components in wind turbines. Metal loss defects are dominant faults of pipelines and gears, impairing reliability and safety operations. Faulty equipment could result in enormous economic loss, catastrophic environmental pollution, and horrible casualties. Failure analysis and prognostics are critical for preventing equipment failures by investigating failure mechanisms and predicting operating conditions. Based on the obtained results, appropriate maintenance strategies can be enabled to improve equipment reliability and curtail operation costs. In engineering applications, pipelines and gears usually encounter complex service conditions. All these factors make deeply understanding the failure mechanisms of pipelines and gears subjected to metal loss defects and complex service conditions challenging. Thus, it is important to improve failure analysis and prognostics by considering complex service conditions.

This thesis aims to obtain insights into the mechanical and failure characteristics of some equipment subjected to metal loss defects and complex service conditions through more accurate failure analysis. The procured insights are further applied to improve prognostic methods. To this end, the overall objective of this research is to achieve more accurate failure analysis and develop advanced prognostic methods for equipment subjected to metal loss defects and complex service conditions. The research objective breaks down

into four sub-objectives.

First, novel interaction rules are developed to achieve more accurate limit spacing distance estimation by incorporating corrosion depth and material properties. An integrated prognostic method is proposed to accurately and efficiently predict the reliability of pipelines with multiple corrosion defects. The proposed method is more beneficial for the reliability prediction of corroded pipelines than conventional ones. How inner pressure fluctuations impact corroded pipelines' reliability is also discussed.

Second, a comprehensive study on how hydrogen damage affects failure behaviors and residual strength of corroded high-strength pipelines is conducted. To quantify the effect of hydrogen damage on residual strength and achieve accurate estimation, a new burst model and a GA-BP neural network are developed for hydrogen pipelines. The proposed methods are valuable for the safety and development of hydrogen transportation.

Third, insights into the mechanical behaviors of high-strength pipelines subjected to the coexistence of inner corrosion and spanning are procured through a systematic FE analysis, providing useful information to help face the challenge that the spanning is becoming more frequent. Parametric analysis is conducted to study the impact of essential factors, such as corrosion geometric features, spanning length, etc. The research results are valuable for improving pipeline integrity management.

Last, how pitting influences the contact status and surface wear of meshing gears is investigated by FEM and UMESHIMOTION. An improved integrated prognostic method is developed for gear surface wear. Uncertainty in the wear coefficient from a population

perspective and the effect of the variations in tooth profiles on wear propagation are incorporated. The proposed prognostic method is valuable in reducing parameter uncertainty and improving surface wear simulation.

The research in this thesis provides insightful investigations into the failure and mechanical behaviors of pipelines and gears subjected to metal loss defects and complex service conditions. Innovative models and prognostic methods are developed to improve prediction performance. The research results will contribute to preventing unexpected failures of equipment used in the clean energy industry, lowering operation costs, and ensuring stable energy supplies worldwide.

Preface

This thesis is an original work by Han Zhang. All the research work presented in this thesis was a collaboration with Dr. Zhigang (Will) Tian. The following works as parts of this thesis have been published or submitted for publication under Dr. Zhigang (Will) Tian's supervision. As for these research works, Han Zhang was responsible for concept formation, literature review, simulation, methods development, data collection, analysis, and manuscript composition. Meanwhile, as the supervisory author, Dr. Zhigang (Will) Tian was involved with concept formation, manuscript review, and edits.

Chapter 3 has been published as Han Zhang and Zhigang Tian. "An Integrated Reliability Method with a Newly Developed Interaction Rule for Steel Pipelines with Multiple Corrosion Defects". Journal of Pipeline Systems Engineering and Practice. Vol. 13, No. 4, pp. 04022045 (13 pages), 2022. Besides, a conference paper has been published and presented as Han Zhang, and Zhigang Tian [1]. "Reliability assessment of corroded pipeline considering multiple defects interaction based on an artificial neural network method". 2020, 2020 Asia-Pacific International Symposium on Advanced Reliability and Maintenance Modeling. IEEE. pp. 1-6, 2020 [2].

Chapter 4 has been published as Han Zhang and Zhigang Tian. "Failure analysis of corroded high-strength pipeline subject to hydrogen damage based on FEM and GA-BP neural network." International Journal of Hydrogen Energy. Vol. 47, No. 7, pp. 4741-4758, 2022 [3].

Chapter 5 brings up a submitted journal paper as Han Zhang and Zhigang Tian. “Numerical investigation of the mechanical behaviors of the high-strength spanning pipeline with internal corrosion,” manuscript completed and under review.

Chapter 6 is preliminary research and will be continued to be developed as a journal publication.

Acknowledgments

First and foremost, I would like to express my deep and sincere gratitude to my supervisor, Dr. Zhigang (Will) Tian, for his continuous support, encouragement, and patience throughout my entire Ph.D. study. I'm really grateful that I worked with Dr. Tian in the past years. His immense knowledge and professional guidance carried me through all the stages of my Ph.D. study with an enjoyable and rewarding experience. Meanwhile, I would also like to give my warmest thanks to the rest of my PhD examining committee members: Dr. Chongqing Ru, and Dr. Xiaodong Wang, Dr. Wenxing Zhou, Dr. Xinming Li, Dr. Ming Lu, and Dr. Jason Olfert for their precious time in reviewing this thesis and for valuable comments in improving this thesis and widening my research.

Secondly, I would like to give thanks to all the research fellows in the lab and office for their kind support and assistance. Moreover, a thank you to my lovely roomies, Da Wang and Hao Zheng. I do appreciate the days and nights we spent. Without all the joys experienced with them, this journey at the University of Alberta would be much less unforgettable.

Last but not least, words in this world cannot precisely express my love and gratitude to my beloved parents. I am so grateful to have such liberal and supportive parents. Their endless love and support bring my life journey here. Finally, I thank my dearest friends, Dr. Lin, Mrs. Zhong, Dr. Zhang, Jerry Wu, and Mr. Yuan, for every laugh and tear we shared. I wish them all the best and happiness in their whole life.

Table of Contents

List of Tables

List of Figures

List of Acronyms

ANN	Artificial neural networking
BP	Backpropagation
CSA	Canadian Standards Association
CW	Coulson and Worthingham
EHL	Elastohydrodynamic lubrication
FEM	Finite-element method
FOSM	First Order Second Moment
GA	Genetic algorithm
HE	Hydrogen embrittlement
ILI	In-line inspection
K&V	Kiefner and Vieth
LHS	Latin Hypercube Sampling
LSF	Limit state function
MCS	Monte Carlo simulation method
MFL	Magnetic flux leakage
MSE	Mean-square error
NRMSE	Relative root mean square error
PDE	Partial differential equations
PEEQ	Equivalent plastic strain
POF	Pipeline operator forum
PSWP	Poisson square wave process
UTS	Ultimate tensile strength
RUL	Remaining useful life
RV	Random variable
SCF	Stress concentration factor

UT	Ultrasonic tool
VIV	Vortex induced vibration

Chapter 1. Introduction

1.1 Background

Clean energy effectively reduces carbon emissions, serving as a supplement to meet the growing energy demands and eventually controlling climate change [4–6]. Based on renewability, clean energy can be classified into two types, i.e., renewable clean energy (like wind energy, solar energy, hydrogen energy, etc.) and non-renewable clean energy (like natural gas [7], nuclear energy, etc.). According to the report proposed by the International Energy Agency, the growth of renewable energy in 2022 is expected to be more than 10% [8]. The production and transportation of clean energy are essential for realizing the global energy transition process and stabilizing the global energy supply.

Engineering equipment used in the production and transportation process of clean energy is significant for achieving using energy in an environmentally benign and sustainable manner. However, various threats could significantly impact the reliable and safe operation of critical parts of the clean energy industry. Metal loss, defined as material losses on equipment's internal or external surface due to corrosive or/and erosive factors, is a dominating threat to engineering equipment, which could be easily affected by service conditions [9]. Corrosion, wear, and pitting, for example, are some typical metal loss defects that can lead to failures without proper handling [10]. Failures of engineering equipment due to metal loss defects could cause serious safety lapses and affect energy security. Thus, profoundly understanding failure mechanisms and effectively preventing potential failures due to metal loss defects are essential for operators and researchers in the clean energy industry to ensure a reliable energy supply, boost productivity, lower operating costs, etc.

Service conditions of clean energy equipment are complex because of many factors, such as operation conditions, defects, transmission media, inspection equipment operation,

extreme weather conditions, etc. Complex service conditions, such as hydrogen environment, interacting effect among multiple defects, and time-varying tooth profile, have significant effects on failure behaviors, reliability, and service life of clean energy equipment. Therefore, complex service conditions should be considered to improve the accuracy of failure analysis, reliability assessment, and prognostics. Besides, considering complex working conditions could provide a reference, which is more in accordance with the actual situation, for making follow-up maintenance strategies.

In this thesis, studies are conducted for failure analysis, reliability assessment, and prognostics of two typical engineering components of clean energy production and transportation, including pipelines transporting natural gas and hydrogen and wind turbine gears. Some typically complex service conditions, such as the interacting effect, hydrogen damage, and time-varying tooth profile, are taken into account to obtain more accurate and reliable results.

Pipelines are widely used in the clean energy industry as a powerful method to transport natural gas and hydrogen due to their remarkable advantages, such as excellent cost-effectiveness, simple structure, and high operating security [11,12]. Besides, pipelines could achieve large-scale and long-distance hydrogen transmission compared to other hydrogen transportation approaches. According to the report [13], the total length of the oil and gas pipeline has reached 2.12 million kilometers in 2022. As the third country ranked by pipeline length, Canada has more than 760 thousand kilometers of pipelines applied to transport energy-related products across the country [14]. Almost 100% of the natural gas is exported by pipelines in Canada. With the increase in energy consumption for diverse industries, the global pipeline market is forecasted to rise from $45.7 billion in 2022 to $73.1 billion by 2031 [15]. Pipelines' structural safety and operational reliability could impact the energy trade stability and the city's reliable operation. While operating, pipelines must face different failure modes. There are three major failure modes of pipelines: fatigue damage, corrosion damage, and mechanical damage. According to the report, in China,

offshore pipeline damage caused by corrosion defects is around 47% [16]. Besides, based on the statistics provided by PHMSA, corrosion is the most common cause of pipeline damage in the United States, which accounts for 23.3% of failure causes [17].

As a typical metal loss defect, corrosion could weaken the structural reliability of a pipeline. However, for pipelines transporting clean energy, corrosion, to some extent, is inevitable due to the reactions with the surrounding environment and transmission media [18]. Due to the serious consequence of pipeline failures, failure analysis and reliability assessment play an important role in managing risks, preventing incidents, and improving the safety of corroded pipelines. Figure 1-1 presents a pipeline with inner corrosion.

Figure 1-1 Pipeline corrosion [19].

Failure analysis is commonly performed to determine the cause of a machinery failure, help operators take corrective actions, and prevent future failures [20]. In the energy industry, three major categories of analysis methodologies are used to investigate the failure behaviors of corroded pipelines: experimental, theoretical, and numerical methods. Although it is costly, the experimental method is still widely used in the field because its results are worthy of reference for other analysis methods. Hydrotest is a typical experimental method used to study the burst behaviors of corroded pipelines [21]. Corrosion defects on pipeline specimens can be machined by spark erosion. However, conducting a full-scale pipeline burst test could be expensive. Besides, adjusting full-scale experiments to satisfy some requirements is time-consuming and complex. Based on experimental results and/or FE simulation results, several theoretical burst models considering material properties, pipeline geometry, and corrosion geometry have been

developed and utilized, such as the NG-18 model, ASME B31G model, ASME B31G Modified model, CSA Z662-07 model, DNV RP F-101 model, PCORRC model, SHELL92 model, RPA model and so on. Estimating burst pressure by a theoretical burst model is convenient, but no theoretical burst model could be suitable for any case. Each theoretical burst model has advantages and disadvantages, and the utilizing process should be based on specific conditions. The finite element method uses mathematical approximations to simulate real physical systems (geometry, loading, boundary condition, etc.). FEM has demonstrated good performance in analyzing the mechanical behaviors of pipelines subject to metal loss defects [22–25]. Besides, when problems become highly complex, such as multiple defects interaction, FEM makes solving complex problems feasible. Thus, FEM is selected as the major methodology in this research.

Reliability assessment is a significant process for evaluating the current operational state and predicting the future operational state of corroded pipelines. In pipeline integrity management, reliability assessment usually determines inspection and maintenance plans. Thus, the performance of a reliability assessment could significantly affect the pipe's safe operation and maintenance costs. An accurate reliability assessment could help prevent potential pipeline failures and lower operating and maintenance costs. Reliability assessment accuracy of corroded pipelines is usually rooted in the performance of the degradation prediction that depends on the failure analysis. Over the past years, several techniques have been applied to evaluate the reliability of corroded pipelines. Monte Carlo simulation method (MCS), First Order Second Moment (FOSM), Bayesian networks, and the artificial neural networking (ANN) method, for example, are commonly used. However, in most cases, corrosions on pipelines are treated as isolated when conducting the reliability analysis.

As the most important clean energy transportation approach, pipelines must snake through different areas and face different service conditions. Complex service conditions could significantly impact failure analysis, reliability assessment, and further operation safety of

pipelines. To improve the accuracy and credibility of the failure analysis and reliability assessment of corroded pipelines, complex service conditions should be considered instead of simply treating the service condition as an ideal experimental condition.

According to previous research and field records, corrosions on a pipeline wall usually occur in patches, and very few corrosions exist in isolation. Pipelines' failure behaviors with multiple corrosions are different from those with isolated ones, making the service condition more complex [26–28]. The interacting effect between adjacent corrosion defects could impair the bear capacity of corroded pipelines and introduce inaccuracy to maintenance decisions. The limit spacing distance is the threshold that determines whether the interacting effect should be considered in the residual strength estimation and the reliability assessment. Interaction rules, like the DNV interaction rule and 6WT interaction rule, are commonly used to estimate the limit spacing distance of successive corrosions.

As the energy transition from traditional fuel energy to clean energy is promoted worldwide, hydrogen has attracted more and more attention. Hydrogen has various advantages, like carbon zero, diverse supply resources, high in energy, non-toxic, and can be used as a clean energy carrier [29,30]. By far, pipelines are regarded as the most significant means to transport large-scale hydrogen over long distances. Due to the enormous costs of hydrogen pipeline construction, blending hydrogen into natural gas pipeline networks has become a promising alternative to hydrogen transportation. However, with the existence of hydrogen, a noticeable loss in ductility of the pipe steel could be observed [31], which could impair the bearing capacity as well as influence the failure behaviors of corroded pipelines. The phenomenon of the reduction in material strength caused by hydrogen absorption is defined as hydrogen embrittlement (HE). Figure 1-2 shows a pipeline subjected to hydrogen damage [32]. For constructed natural gas pipelines, inner corrosion defects are almost inevitable. Once the corrosion and hydrogen embrittlement simultaneously appear, the service condition of pipelines becomes tougher. Thus, failure behaviors are different, and failure probability could increase.

Figure 1-2 A pipeline subjected to hydrogen damage [32].

In regions where the geological condition is unstable, such as mountains, oceans, and rivers, pipeline spanning could occur due to geological hazards (soil erosion, ground subsidence, etc.), extreme weather (flood, hurricane, etc.), and artificial factors (submarine equipment connection, residual stress, etc.)[33,34]. Pipeline spanning is commonly defined as a part or several parts of a pipeline becoming supportless. Spanning parts of a pipeline could result in significant deformation, stress concentration, and vibration [35]. Figure 1-3 shows a spanning pipeline caused by flood [36]. For corroded pipelines, spanning would cause residual strength degradation and lead to different failure behaviors. Without proper maintenance strategies, pipeline spanning might eventually lead to unexpected pipeline failures, like fractures and buckling. The probability that a spanning pipeline has already corroded is high. The existence of both spanning and corrosion makes pipelines transporting clean energy more likely to be failed and lead to disastrous pipe accidents.

Figure 1-3 Spanning pipeline caused by flood [36].

Over the past decades, wind energy utilization has been growing rapidly worldwide. Wind turbines are usually installed onshore and offshore to capture wind energy. As the main component of a wind turbine, gears transmit torque in mechanical power transmission systems through meshing with another toothed part. In operation, heavy load on the cut teeth significantly impacts the health of gears [37]. There are four major failure modes of gears, i.e., surface wear, bending fatigue (fatigue cracking), contact fatigue, and scoring [38]. As a critical failure mode that significantly impacts the reliability and remaining useful life (RUL) of gears, surface wear is induced by mating faces' sliding motion. As a result, material loss happens to gears, which could change gear tooth profile geometry and ultimately accelerate gear failure.

Moreover, pitting is a typical metal loss defect of gears that frequently occurs due to friction between sliding surfaces and excessive contact load [39]. Pitting on the tooth surface will impair bearing capacity, change tooth profile and result in apparent changes in mesh stiffness and load distribution, which could influence the failure behaviors and RUL of gears [40]. Besides, due to the change in the contact status, the wear propagation process will also be affected. Unexpected failures of gears in transmission systems will eventually result in a severe failure of the wind turbine. Analytical methods and FEM are widely used to perform the contact analysis of gears with pitting. The experimental method is the most commonly used approach to study the wear behaviors of gears. In recent years, FEM has started to be applied to simulate the wear process. To prevent unexpected failures, prognostic methods are usually employed. As a core task of integrated system health management, prognostics are essential for improving system safety, reliability, and availability [41]. In engineering, prognostics is regarded as a RUL assessment for systems and equipment subject to degradation caused by operation conditions or third-party damage. Utilizing prognostics in gears subjected to surface wear has many benefits, including preventing possible failure by the knowledge beforehand about the time to failure, minimizing downtime, and optimizing maintenance strategy [42,43]. The existing

prognostic methods are generally categorized into three types, i.e., physics-based methods, data-driven methods, and integrated methods. To improve performance, integrated methods usually combine different methods, such as physics-based methods, monitoring data, etc.

Failures of clean energy equipment due to metal loss defects cause serious production impairment, unstable energy supply, enormous economic loss, and even catastrophic safety accidents. Since pipelines are one of the most significant methods of transporting clean energy and gears are the critical components of wind turbines, their safety and reliability are essential to the clean energy industry. In engineering practice, complex service conditions could worsen equipment performance, resulting in unexpected failures. Thus, there is an urgent need to conduct more accurate failure analysis, reliability assessment, and prognostics of pipelines and gears subjected to metal loss defects and complex service conditions to ensure a safe and stable operation. With the consideration of different complex service conditions, in this thesis, we could better investigate the failure behaviors and better evaluate the current and future state of pipelines and gears subjected to metal loss defects, thus getting a better understanding of how to prevent catastrophic failures from underestimation.

1.2 Research motivations

For the clean energy industry, the safety and reliability of engineering equipment are essential for a stable energy supply. Pipelines are widely regarded as the blood vessel used to achieve large-scale and long-distance energy transportation, while gears used in wind turbines are the key components ensuring wind energy production. Over the past decades, a great number of pipelines have been constructed and implemented. The total length of pipelines is still expanding worldwide. The Business Research Company's latest report states that the global pipeline safety market is forecasted to reach $12.64 billion in 2026 at a compound annual growth rate of 10.3% [44]. Meanwhile, global wind energy is growing

at a fast speed as well. The global wind turbine market is predicted to be worth $94.26 billion by 2026 [45]. The enormous demand for clean energy draws intense attention from academic and industrial communities. However, metal loss defects could significantly threaten pipelines' and gears' reliable and safe operation. The consequences of pipeline incidents and gearbox failures caused by metal loss defects could be disastrous to the environment and modern society. Hence, the safety of pipelines and gears is an issue of critical concern. In the meantime, complex service conditions of equipment subjected to metal loss defects should be systematically investigated to achieve a more accurate failure analysis, reliability assessment, and prognostic, thus ensuring safe operation and a stable clean energy supply.

Since corrosion defects usually appear in patches on a pipeline’s surface, the interacting effect between adjacent corrosion defects should be considered an important influencing factor when conducting failure analysis and reliability assessment. However, most previous relevant research just simply treated corrosion as isolated without considering the interacting effect.

Moreover, in specific cases, whether the interacting effect should be taken into account has a significant effect on the residual strength estimation, reliability assessment, and further integrity management strategies. Existing interaction rules, like the DNV interaction, are widely used to estimate the limited spacing distance that determines the existence of the interacting effect. Most existing interaction rules take the corrosion length or wall thickness as the criterion. However, corrosion depth and pipe steel grade have an evident impact on the corroded pipeline’s burst behaviors and could also influence adjacent corrosions' interactions. Previous research has not systematically discussed how corrosion features impact the interacting effect. Inaccurate estimation of the limit spacing distance will cause inaccuracy in burst pressure estimation and further reliability assessment of pipelines with multiple corrosion defects. Thus, it is essential to conduct a sensitivity analysis to determine the most influential factor of the interacting effect. There is also an urgent

demand to develop a more accurate interaction rule taking corrosion depth and pipe steel grade into account and reducing inaccuracies in pipeline integrity management.

Over the past years, several techniques have been employed to estimate the reliability of corroded pipelines. Although each technique has advantages, the Monte Carlo simulation (MCS) method is still the most widely used reliability analysis method for corroded pipelines. However, the efficiency of the MCS is relatively low. When the situation becomes complex, such as with multiple interacting corrosion defects, the MCS's applicability worsens. Therefore, a new reliability analysis approach is required to conduct a more accurate and efficient reliability assessment of pipelines with multiple corrosion defects. Due to unstable flow conditions or significant changes in demand for conveying media, pressure fluctuations inside a pipeline might occur, which could impact the corroded pipeline's operation state. Nevertheless, the effect of pressure fluctuation on the reliability of pipelines with multiple corrosion defects is barely discussed. Thus, it is necessary to investigate how internal pressure fluctuation affects the reliability assessment of corroded pipelines.

Safe hydrogen transportation is a critical issue for the global energy transition. At present, gaseous hydrogen transportation is popular in the field because it is more mature than other techniques. Hydrogen pipelines attracted tons of attention as a major way to transport gaseous hydrogen. Hydrogen pipeline construction, operation, and maintenance show great potential in the renewable energy industry. Nevertheless, the overall cost of a pure hydrogen pipeline is 1.5-3 times higher than that of using conventional natural gas pipeline systems with the same energy flow. Although blending hydrogen into existing natural gas pipelines could lower the overall cost, the accompanying increased failure risk cannot be underestimated. For steel pipelines, hydrogen embrittlement could increase the risk of leakage and explosion of existing pipelines. Since corrosion is, to some extent, inevitable in pipelines, the probability of corrosion and hydrogen embrittlement coinciding is high.

With the increase in strength, pipeline steel becomes more sensitive to hydrogen

embrittlement. However, previous research mainly focuses on the hydrogen-induced crack and degradation process of low and moderate pipe steels. Moreover, barely any of the existing burst models of corroded pipelines considers the effect of hydrogen damage despite several models, such as ASME B31G, PCORRC, SHELL 92, etc., are widely used in the pipeline industry. The scenario of using the conventional evaluation method to assess pipelines transporting hydrogen could introduce inaccuracy in the residual strength estimation and result in unexpected failures. According to the literature review, the impact of hydrogen damage on the interacting effect between adjacent corrosion defects has yet to be discussed. Thus, there is an urgent need to investigate the effects of hydrogen damage on the failure behaviors and interacting effect of high-strength corroded pipelines and develop burst pressure estimation methods considering the hydrogen damage.

As the earth has shown signs of entering a new geologically active epoch and extreme weather events have increased in frequency, pipelines transporting clean energy must face more complex service conditions, and the phenomenon of spanning is more likely to occur. Once spanning appears, pipelines will suffer from significant deformation, stress concentration, and additional vibration that could accelerate failure, increase maintenance costs, and lower transportation efficiency. Without appropriate risk handling measurements of spanning, horrible pipeline incidents might happen and result in great economic loss. The basis for avoiding pipeline failures caused by the spanning phenomenon is a deep understanding of the mechanical behaviors of spanning pipelines. Over the past years, FEM has been widely used in the field to investigate mechanical behaviors of spanning pipelines, such as the most dangerous location and the stress concentration factor (SCF). As mentioned above, corrosion is a major threat to almost every steel pipeline. When it comes to spanning pipelines, simply ignoring the effect of corrosion could result in inaccuracy in the failure analysis and further maintenance strategies. With the coexistence of corrosion and spanning, a pipeline's failure risk could be much higher, and the mechanical behaviors could differ. However, most previous research only takes defectless pipelines as research

objects. Thus, there is an urgent need to investigate the mechanical behaviors of spanning pipelines with inner corrosion systematically. The study results are valuable for future fatigue life analysis and reliability assessment of spanning pipelines.

The health of gears is vital to mechanical power transmission systems. Among a variety of threats, surface wear is a kind of critical metal loss defect threatening the performance of gears by causing metal loss, changing gear tooth profile, increasing vibration and noise, and ultimately shortening service life [37,46,47]. Thus, it is essential to investigate gears' wear behaviors and make accurate prognostics based on the actual situations to avoid unexpected failures and ensure designed transmission capacity. Pitting is a typical metal loss defect that could significantly impact the contact status of the mating gears. In most previous studies, the research focus is on contact analysis of pitting gears. Due to the changes caused by pitting on the contact status, surface wear propagation could be influenced. However, previous research barely involves the effect of pitting on the wear behaviors of gears. Thus, it is essential to investigate how the surface wear propagation of gears is impacted by pitting. The outcomes are valuable for further failure analysis. Over the past years, outstanding contributions have been made to the surface wear of gears. Experimental methods and physics-based models are two widely used approaches to investigate the wear behaviors of gears. Archard’s model is a physics-based model commonly used to describe wear propagation. However, it could be significantly impacted by the wear coefficient [46].

Due to different contact material properties or contact conditions, the wear coefficient could dramatically change in value. Simply ignoring the change in wear coefficient will result in inaccuracy in the investigation of wear behavior as well as the prognostics. However, the wear coefficient of a population of gears is usually set as fixed in most previous research when conducting the wear process simulation [48,49]. Besides, most research treated the contact pressure between mating surfaces as fixed when estimating the RUL of gears subjected to surface wear. However, as surface wear propagates, the tooth

profile changes correspondingly, resulting in variations in the contact status. Simply ignoring the variations in the contact status will induce inaccurate simulation results, wear propagation estimation, and RUL prediction. Thus, new prognostic approaches are badly needed to tackle these problems and improve surface wear prediction.

1.3 Research contributions

By and large, this thesis study aims to achieve more accurate failure analysis and develop advanced prognostic methods for equipment used in the clean energy industry, which is subjected to metal loss defects and complex service conditions. Based on the motivations and challenges mentioned above, the primary objectives of this Ph.D. research are summarized below:

(a) To investigate the effects of the corrosion geometric features on the interacting effect, develop new interaction rules considering corrosion depth and material properties, and propose an integrated method for the reliability assessment of pipelines with multiple corrosion defects, providing valuable aid in more accurate and efficient reliability estimation.

(b) To study the effects of hydrogen damage on failure behaviors and residual strength of the high-strength corroded pipeline and develop new burst pressure estimation methods considering the hydrogen damage effect.

(c) To investigate the effects of the coexistence of internal corrosion and spanning phenomenon on the mechanical behaviors of the high-strength pipeline, providing beneficial information for future fatigue life estimation.

(d) To study how pitting influences gears' contact status and surface wear propagation. Moreover, to develop an integrated prognostic scheme for gears with surface wear by considering uncertainty in the wear coefficient of a gear population and the effect of the variations in the tooth profile on the contact status, providing valuable aid in better prediction.

The main contributions of the four topics from this thesis are summarized as follows:

- In the first research topic, the influences of the corrosion geometric features on the interacting effect are quantitatively investigated, and the most influential feature is determined. The effects of corrosion depth and steel grade on the interacting effect and limit spacing distance of a pipeline with multiple corrosion defects are systematically discussed. Two new interaction rules considering both corrosion depth and steel grade are developed for the X65 and X80 pipelines and proved to have better performance than conventional interaction rules. An integrated reliability method is proposed for pipelines with multiple corrosion defects to realize a more accurate and more efficient reliability assessment of corroded pipelines by incorporating the interacting effect and new interaction rule for the first time. The effects of the interacting effect and different interaction rules on the pipeline's reliability estimation are systematically discussed instead of simply treating corrosion defects in isolation. The effect of pressure fluctuations on the reliability of the pipeline with multiple corrosion defects is investigated instead of simply treating the pressure as static.
- In the second research topic, the effects of the conjunction of corrosion and hydrogen damage on the failure behaviors and residual strength of the high-strength pipeline transporting hydrogen are investigated through a series of validated FE models with different features and different degrees of hydrogen damage. A new burst pressure model incorporating the hydrogen damage is developed for better estimation accuracy of hydrogen pipelines through regression analysis. A Genetic Algorithm-Back Propagation (GA-BP) neural network is established and trained to achieve accurate and rapid residual strength prediction of corroded hydrogen pipelines, which could help alleviate the computational burden of FEM. The effects of hydrogen damage on the interacting effect and the limit spacing distance between multiple corrosion defects are studied for the first time.

- In the third research topic, a series of numerical models of high-strength pipelines with the coexistence of corrosion and spanning phenomenon is established and simulated. Based on the simulation results, the mechanical behaviors of the corroded spanning pipeline are investigated. The differences in the mechanical behaviors between corroded and intact spanning pipelines are studied. A parametric analysis is conducted to study the impact of essential factors, such as corrosion geometric features, spanning length, internal pressure, etc. The plastic responses of the high-strength spanning pipeline with internal corrosion are discussed for the first time. The results of this research topic, like how corrosion affects SCF of spanning pipelines, are valuable for future fatigue life estimation and integrity management.
- The fourth research topic investigates the effects of pitting on the contact status and surface wear propagation of gears by combining FEM and UMESHMOTION. Moreover, considering the impacts of variations in tooth profile during wear propagation and the uncertainty of wear coefficient from a gear population, an integrated prognostic method is proposed for gears subjected to surface wear by integrating FEM, physics-based models, Bayesian inference and condition monitoring data. Examples are introduced to demonstrate and validate the proposed method. The proposed method could reduce the uncertainty in model parameters and improve the accuracy of surface wear prediction.

The innovative methods proposed and the results obtained in this research will help promote the clean energy industry by improving reliability and preventing unexpected failures of equipment.

1.4 Thesis organization

The thesis is prepared following the dissertation requirements from the Faculty of Graduate Studies and Research (FGSR) at the University of Alberta. This thesis, with seven chapters,

is organized as follows:

Chapter 2 provides a thorough literature review and extensive background knowledge on methods and techniques applied in the field of the safety of corroded pipelines focusing on complex service conditions. This chapter also presents the fundamentals of gears used in wind turbines, widely used prognostic methods, and some basics of the physical model for surface wear.

Chapter 3 investigates the effects of corrosion depth and steel grade on the interacting effect and the limit spacing distance of a pipeline with multiple corrosion defects. An orthogonal test is applied to quantitatively investigate the corrosion geometric features' influences on the interacting effect. Regression analysis is used to develop new interaction rules considering both corrosion depth and steel grade. This chapter also proposes an integrated reliability method for pipelines with multiple corrosion defects. The results of this chapter have been published in a journal paper [1].

Chapter 4 investigates the impact of the conjunction of corrosion and hydrogen damage on the failure behaviors and residual strength of the hydrogen pipeline made of high-strength steel. Regression analysis is employed to develop the new burst pressure model considering the hydrogen damage effect. GA-BP ANN is modeled and trained to accurately and rapidly estimate the residual strength of corroded hydrogen pipelines. This chapter also discusses the effects of hydrogen damage on the interacting effect. The results of this chapter have been published in a journal paper [3].

Chapter 5 investigates the effects of the coexistence of corrosion and spanning phenomenon on the mechanical behaviors of the high-strength pipeline. Parametric analysis is used to study the impacts of essential factors. The manuscript is completed and under review for possible publication.

Chapter 6 investigates the effects of pitting on contact status and surface wear propagation of gears. Besides, an integrated prognostic method is proposed for gears with surface wear by integrating FEM, physics-based models, and condition monitoring data. Examples are

introduced to demonstrate and validate the proposed method.

Chapter 7 summarizes the thesis and suggests several possible future research interests.

Chapter 2. Literature review and background knowledge

2.1 Literature review

As the negative impacts of climate change on the planet grow faster than expected, many countries are increasing investment in clean energy to accelerate progress on the global energy transition. As foundations of the clean energy industry, engineering equipment play a critical role in energy production and transportation. Since pipelines are the most crucial approach to achieving large-scale and long-distance transportation of natural gas and hydrogen, their safety and reliability have attracted intensive attention from both industrial and academic communities. According to previous studies, corrosion, as a typical metal loss defect, is a dominant threat to pipelines' safe operation. Over the past decades, many academic papers and technical reports have been published on the mechanical behaviors and reliability of corroded pipelines. Other than pipelines, gears applied in wind turbines are also our focus in this thesis. As a critical component of wind turbines, gears are the primary research objective for operators and scholars in the wind energy field. Surface wear and pitting are severe metal loss defects that could significantly impact the performance and RUL of gears. A great deal of contribution has been made to investigations of contact analysis, surface wear simulation, and prognostic methods of gears. In this chapter, the literature review is conducted for the research studies on failure and reliability analysis of corroded pipelines subjected to complex service conditions. Besides, the review of failure analysis and prognostic methods for gear surface wear and pitting are given. Some fundamental background knowledge is also presented.

2.1.1 Corroded pipeline

2.1.1.1 Corrosion mechanism

As a dominant threat to pipelines' integrity, corrosion is a typical metal loss defect that could be easily impacted by the service environment. Pipeline corrosion is an electrochemical process that relies on the operation time and local environment. Based on the location, corrosion defects are usually categorized into two types: inner corrosion and external corrosion. Factors that affect external corrosion include soil chemistry, soil moisture, pH, and water chemistry [50]. Oxygen content, reactions between pipeline steel and liquids carried by the transportation media, flow rate, operation pressure, and the usage of corrosion inhibitors are the main factors that impact internal corrosion [51]. Besides, the distance between the cathodic protection station influences inner and external corrosion growth. Without proper handling, pipeline corrosion could lead to several harmful consequences, such as substantial economic loss, environmental contamination, and personnel casualties. Thus, the integrity management of corroded pipelines is of great importance. For pipeline integrity management, corrosion inspection and monitoring provide essential information for follow-up studies. Magnetic flux leakage (MFL), circumferential MFL, Tri-axial MFL, and ultrasonic tool (UT) are popular inspection methods for pipeline corrosion [52]. Each inspection method has advantages and disadvantages. Thus, selecting an inspection method should depend on the particular requirements. Coatings and cathodic protection are pipelines' most important corrosion control techniques [53].

2.1.1.2 Failure analysis

Inner and external corrosion impair pipelines' structural reliability and capacity to withstand the designed operation conditions. Therefore, corroded pipelines are more prone to fail. Over the past years, the research topic of failure analysis for corroded pipelines has

drawn intensive attention from both industry and academia. A failure criterion usually determines the failure of corroded pipelines. Many failure criteria have been developed and applied, such as the corrosion depth reaching the threshold (e.g., 80% of the wall thickness), plastic failure criterion, yield failure criterion, and so on. In previous research, the Von Mises yield criterion and limit state function are the two most widely used failure criteria for corroded pipelines. The Von Mises yield criterion defines the failure of a corroded pipeline from a material perspective: a failure happens when the maximum Von Mises stress of the corroded pipeline is larger than the stress limit. Using limit state functions as the failure criterion is more prevalent in the industry because there is no need to conduct stress analysis, which defines failure as the burst pressure of a corroded pipeline being smaller than the operation pressure. Thus, accurately estimating the burst pressure of pipelines plays an important role. Based on experimental and numerical approaches, a number of theoretical models have been proposed to estimate the burst pressure of corroded pipelines, such as ASME B31G [54], RSTRENG [55], CSA Z662-15 [56], DNV-RP-F101 [57], PCORRC [58], SHELL93 [59], and so on. Material properties and geometric features of corrosion and pipeline are essential to theoretical models. The performances of different burst models in estimating burst pressure have been investigated by Bhardwaj et al.[60], Mondal et al. [61], and Ma et al.[62]. Since each theoretical model has its own merits and demerits, the selection of the model should be based on specific conditions.

In recent years, FEM has been regarded as a powerful tool for investigating failure behaviors and evaluating the burst pressure of corroded pipelines. According to ASME, FEM is treated as a level 3 evaluation approach for corroded pipelines [54]. Compared with theoretical burst models, FEM could provide a more accurate burst pressure estimation by considering more complex situations, such as complex loading conditions and corrosion geometry. Belachew et al. [63] established a series of FE models to investigate the effects of corrosion length, depth, and width on the burst pressure of corroded pipelines. Mondal and Dhar [64] compared the burst pressures estimated by FEM and that estimated by

typical theoretical models. Besides, FEM is also applied to determine the significant factors that influence the Folias factor. A large number of FE models of corroded pipelines with different corrosion geometric features, internal pressures, and longitudinal compressions are established by Zhang and Zhou [65] to develop a correction factor that can be used in the burst models to improve the estimation of pipelines under combined loads.

Although FEM could improve the accuracy of burst pressure estimation for corroded pipelines, it could be computationally expensive, especially when the situation becomes complex. Nowadays, artificial neural networks are applied to tackle such problems. Since the full-scale test of corroded pipelines could be expensive, FEM is usually used as the data source to integrate with artificial neural networks in previous studies. Kumar et al. [66] proposed a burst pressure model for corroded pipelines under internal pressure and compressive stress based on the weights and biases of the ANN trained by the burst pressures estimated by FEM simulations. Based on the burst pressures estimated by FEM, Lo at al. [67] trained an artificial neural network to efficiently predict the burst pressure for pipelines with single external corrosion. Based on the data collected from previous research, Phan and Dhar [68] used a random forest, support vector machine, and artificial neural network to predict the burst pressure of corroded pipelines. Besides, the performances of these approaches are compared, and it is found that the random forest has the worst performance.

2.1.1.3 Reliability analysis

The reliability of a corroded pipeline is defined as the probability of it performing its designed functions under specified operating conditions for a specified period. Reliability analysis is applied to evaluate the reliability of corroded pipelines by considering the current pipeline conditions [69]. Based on the estimated reliability of the corroded pipeline, the remaining useful life can be predicted, as well as inspection and maintenance strategies can be made. Thus, reliability analysis of corroded pipelines is important for preventing

unexpected failures and extreme economic losses.

Monte Carlo simulation, the first-order reliability method (FORM), and Bayesian networks are some typical approaches used for estimating the reliability of corroded pipelines. Based on MCS and a series of theoretical burst models, Gómez et al. [70] systematically investigated how theoretical burst models impact the reliability analysis of pipelines with single corrosion. Shuai et al. [71] also used MCS to estimate the reliability of pipelines with single corrosion. Besides, the effects of pipeline features and corrosion geometric features on the reliability of the corroded pipeline are studied. Abyani and Bahaari [72] compared the performances of MCS and Latin Hypercube Sampling (LHS) in estimating the reliability of a pipeline with internal corrosion. It is found that LHS is considerably less in computational cost without losing too much accuracy. Bhardwaj et al. [73] assessed the uncertainties in reliability through FORM for a high-strength pipeline with thick wall thickness and isolated multiple corrosion defects. It was found that the corrosion depth has a strong impact on the reliability estimation. Pourahmadi and Saybani [74] estimated its reliability by FORM, proposed limit state function and inspection data by taking corroded submarine pipelines as the research object. Wen et al. [75]proposed an integrated reliability analysis method for pipelines with isolated corrosion defects based on the optimized ANN. Seghier et al. [76] proposed a hybrid reliability analysis method by integrating the M5 tree and MCS to improve the reliability estimation efficiency for corroded pipelines.

Since the failure of a pipeline due to corrosion is a small probability event, field failure data for reliability assessment is commonly insufficient. Despite the fact that many reliability analysis methods have been developed and applied, MCS is still the most widely used method for corroded pipelines. The reason is that the reliability of corroded pipelines estimated by the Monte Carlo simulation is usually regarded as a benchmark in the pipeline industry.

2.1.1.4 Complex service conditions

Service conditions could significantly influence the safety and reliability of pipelines transporting natural gas and hydrogen. As pipelines usually must face challenging operation tasks or working conditions, the effects of complex service conditions should not be simply ignored.

2.1.1.4.1 Interacting effect between adjacent corrosion defects

Based on the DNV-RP-F101 standard [57], corrosion defects on pipelines are commonly categorized into three categories: single corrosion defects, interacting corrosion defects, and complex-shaped corrosion defects. According to previous research and field records, corrosion defects on pipeline walls usually occur in patches, and very few corrosions exist in isolation. Failure behaviors of pipelines with multiple corrosion defects are expected to differ from those with isolated corrosion defects. Chouchaoui and Pick [77,78] numerically investigated the failure behaviors of pipelines with longitudinally and circumferentially aligned corrosion defects. It was found that there was no apparent interaction between closely spaced defects in the circumferential direction. Through the experimental method, Benjamin et al. [79] investigated the effects of multiple corrosion defects on the burst pressure and the interaction between multiple corrosion defects. Besides, the performances of some typical theoretical burst models on estimating the burst pressure of pipelines with multiple corrosion defects were also discussed. Han et al. [80] used the finite element method to study how the spacing distance between adjacent corrosions affects the burst pressure. The results show that the interacting effect between corrosions decreases with the increase of the spacing distance. Sun and Cheng [81] used FEM to investigate the interaction between multiple corrosion defects with multiple layers. It is found that the corrosion depth and length have a more noticeable impact than corrosion width on the interaction between multiple corrosion defects. Considering the interacting effect between corrosions makes the burst pressure prediction and the reliability analysis of the corroded

pipeline much more complex.

According to previous studies, the interacting effect only exists if the spacing distance between adjacent corrosions is short enough. In engineering practice, the limit spacing distance is defined as the distance determining whether the interaction between adjacent corrosion defects should be considered. Once the spacing distance is smaller than the limited spacing distance, the interacting effect should be considered in the burst pressure assessment and further reliability analysis. Otherwise, multiple corrosion defects should be regarded as isolated. Namely, the interacting effect should be ignored. Over the past years, many interaction rules have been developed to evaluate the limit spacing distance of corroded pipelines. Several interaction rules, such as the DNV interaction rule, Kiefner & Vieth interaction rule, and the 6WT interaction rule, have been widely used in the field. Based on Project 3-805 and the RSTRENG burst model, Kiefner and Vieth [55] developed an interaction rule for the corroded pipe considering the corrosion length and the pipe's wall thickness. The limited spacing distance is defined as the minimum among the corrosion lengths and six times the wall thickness. Similar to the Kiefner & Vieth interaction rule, CSA Z662-15 [56] also defines the limited spacing distance in terms of the corrosion length. To avoid the possible underestimation of the corrosion length and incorporate the variance in the wall thickness, Lamontagne [82] proposed the 6WT rule, which defines the limited spacing distance as six times the wall thickness. Li et al. [83] proposed an interaction rule based on experimental and finite element simulation results to estimate the limited spacing distance for short and long corrosions. Besides the interaction rules mentioned above, other interaction rules, such as ASME, CW, etc., are also widely used in the pipeline industry. Based on the finite element analysis, Benjamin et al. [84] found that the DNV rule could realize the best performance, followed by the POF rule and the Kiefner & Vieth interaction rule. Xu et al. [85] conducted the failure analysis for pipelines with multiple corrosion defects based on the finite element and the neural network methods. The results show that the burst pressure of the corroded pipeline could be

significantly influenced by the corrosion depth and the spacing distance. Besides, it is also implied that the corrosion depth could impact the variance in the burst pressure with the increase of the spacing distance, while the corrosion length has a relatively low influence. According to widely used burst pressure models, the properties of pipeline steel in terms of controlling flow stress play an essential role in burst pressure estimation, which could eventually affect the performance of the interaction rule. Ref. [10,86,87] conducted reliability analyses of pipelines with multiple corrosion defects, which are all treated as isolated.

However, in previous studies, the effects of corrosion features on the limit spacing distance are barely investigated. More accurate interaction rules are also needed to improve burst pressure estimation and reliability analysis. Moreover, the interacting effect between adjacent corrosion defects is usually ignored in reliability analyses in previous research, which could introduce inaccuracies.

2.1.1.4.2 Hydrogen damage

Hydrogen is becoming increasingly significant as it is an important approach for achieving energy transition globally. As the most abundant element in the universe, hydrogen has multiple resources, such as steam methane reforming and water electrolysis. Eliaz et al.[88], LaChance et al.[89], and Schmetz and Miller [90] reviewed hydrogen sources and production approaches. Meanwhile, hydrogen, as a secondary energy carrier, could not only be used to store and transport other energies, like wind energy but is also carbon footprint-free when used. Besides, hydrogen has the highest energy content by weight. As hydrogen becomes increasingly popular as clean energy, its storage and transportation attract incentive attention.

Based on the application scenarios, hydrogen storage approaches can be divided into two types: stationary and mobile storage [91]. Stationary storage approaches are usually designed for on-site hydrogen storage in terms of production and usage and stationary power generation. Mobile approaches have much more application scenarios, such as

transportation, aerospace, and vehicle. Since hydrogen is low in energy density by volume, large-scale hydrogen storage is the key [92].

Transportation approaches play an essential role in the application of hydrogen because they have a significant impact on energy usage and cost. Based on the physical states of hydrogen, transportation approaches are mainly categorized into three types: gaseous hydrogen transportation, liquid hydrogen transportation, and material-based hydrogen transportation. Compared with other transportation approaches, gaseous hydrogen transportation is much more mature in its application in the fields. Tube trailers and pipelines are the two major gaseous hydrogen transportation methods [93,94]. At present, pipelines are the most important approach to realizing large-scale and long-distance hydrogen transportation. According to the report, about 2500 Km and 100 Km of hydrogen pipelines have been constructed in the United States and China, respectively [91].

Although hydrogen pipelines have many advantages, the construction cost is enormous. According to previous studies [95,96], the cost of adjusting a natural gas pipeline to be suitable for hydrogen transportation is only 21-33% of constructing a new hydrogen pipeline because of less labor cost, and so on. Therefore, blending hydrogen into constructed natural gas grids is treated as a promising way to lower the cost of hydrogen transportation. The possibility of blending gaseous hydrogen into existing natural gas grids has been systematically investigated by Melaina et al. [97], Dickinson et al. [98], Florisson [99], and Tzimas et al. [100]. Based on the experimental approach, NaturalHy [101] project investigated the effects of blending hydrogen on the operating safety of existing pipelines. Since the hydrogen-natural gas blend has different properties compared with pure natural gas, the combability between natural gas pipelines and hydrogen should be noticed. The addition of hydrogen could result in unexpected safety issues.

Over the past years, outstanding contribution has been made to the effects of hydrogen on material properties. For pipeline steels, hydrogen embrittlement is the most critical damage caused by the hydrogen environment, which deteriorates the material performance and

bearing capacity [102]. The process of hydrogen-induced damage can be found in Ref. [103]. Some experimental approaches, such as tensile tests, fracture toughness tests, and fatigue tests, can be used to quantitatively investigate the effects of hydrogen on the mechanical properties of pipeline steels [100]. Cathodic charging and a high-pressure gaseous hydrogen environment are two major ways to make pipeline steels damaged by hydrogen. The index of elongation failure, index of fracture toughness, and index of crack growth increment are commonly used to quantify the hydrogen damage [104]. Nanninga et al. [105] compared the tensile properties of three types of pipeline steel in high-pressure gaseous hydrogen and air environments. It was found that a hydrogen environment could result in an apparent reduction in elongation at failure and ductility. Based on the experimental method, Briotte et al. [106] investigated the mechanical behaviors of X80 steel in a hydrogen environment. They observed a noticeable decrease in material toughness and an acceleration in fatigue crack growth. Zhang et al. [107] found that the tensile strength of pipeline steel subjected to hydrogen could decline with increased hydrogen concentration. The severity of the hydrogen-induced damage usually depends on certain factors such as hydrogen concentration, partial pressure, temperature, exposure time, pipeline material, pipeline surface conditions, and so on [108]. It is well known that pipeline steels become more sensitive to hydrogen as strength grows [109].

Although great efforts have been made to figure out the HE mechanism, the exact mechanism that can be used to comprehensively explain HE is still controversial. Hydrogen-enhanced decohesion model, hydrogen-affected localized plasticity model, hydrogen-enhanced localized Plasticity, and adsorption-induced emission are some proposed HE mechanisms [110]. Without proper handling, hydrogen-induced damages in pipelines could result in hazards such as leakage, fire, and explosion.

In previous research, the effects of hydrogen damage on failure behaviors and residual strength of corroded pipelines are barely mentioned. Approaches suitable for estimating the residual strength of corroded pipelines in a hydrogen environment are urgently needed.

Besides, how is the interacting effect between multiple corrosion defects affected by hydrogen damage is barely discussed.

2.1.1.4.3 Pipeline spanning

Pipeline spanning occurs when one or several pipe segments are not supported by surrounding soil or seabed. For long-distance pipelines, their working conditions could be extremely tough because many of them are located in remote regions where the geological conditions are complex and volatile. In areas where geological conditions are unsteady, such as mountains, seabed, and riverbanks, pipeline spanning is more likely to occur because of geological hazards (soil erosion, ground subsidence, uneven seabed, underwater landslides, etc.), extreme weather (flood, hurricane, storms, etc.), and artificial factors (submarine equipment connection, residual stress, thermal stress, etc.). Once spanning occurs, pipelines must face excessive deformation, bending, and stress concentration. As for submarine pipelines, vortex-induced vibration (VIV) will happen that might lead to resonance which could significantly damage the structural reliability of the spanning pipeline [35]. Spanning might happen throughout pipelines' whole service life, leaving pipelines in dangerous situations. In the past years, serval pipeline accidents were directly caused by the spanning phenomenon. For example, the Ledong gas field pipeline accident in 2009, the Huizhou natural gas submarine pipeline accident in 2010, and the east China sea in 2012 were all caused by spanning. Pipeline accidents caused by the spanning phenomenon could be vital and result in not only enormous economic loss but also disastrous environmental pollution.

Since extreme weather occurs much more frequently worldwide, pipelines are now facing a higher probability of spanning. Therefore, more and more researchers continuously contribute to investigating spanning pipelines for risk reduction. In previous research, critical spanning length estimation and fatigue analysis were the major topics that attracted attention. Besides, overstress failure analysis under steady-state loading conditions is also of interest.

Methods used for the critical spanning length estimation usually can be categorized into three types: static strength analysis, dynamic response method and fatigue limit analysis. The first type of static strength analysis is conducted to estimate the bending stress of a spanning pipeline, comparing the bending stress with the allowable stress of pipeline steel. The critical spanning length should ensure that the bending stress is smaller than the allowable stress. The second type of static strength analysis is instructed by ASME B31.8, and a detailed process can be found in Ref.[111]. Xu [112] applied ASME B31.8 to evaluate the allowable spanning length of a submarine pipeline. Besides, the effects of the hurricane on the allowable spanning length were investigated. It is found that the allowable spanning length of pipelines under ordinary weather conditions is evidently shorter than that under a hurricane.

Dynamic response methods for determining the allowable spanning length depend on the vibration characteristics of the spanning pipelines. There are also two types of dynamic response methods. Type one is based on avoiding the resonance induced by VIV. Resonance occurs when the natural frequency of a spanning pipeline equals the vortex shedding frequency [113]. DNV [114] provided simplified theoretical models for estimating the natural frequency of spanning pipelines with or without considering the pipe-soil coupling effect. Through modal analysis, Xu et al. [115] estimated the natural frequency of a spanning pipeline laid on the seabed. Based on FEM, He et al. [116] investigated the effects of spanning length on the natural frequency of the spanning pipeline. The frequency of VIV can be analytically calculated [117,118]. Wang et al. [119] discussed the factors that impact the VIV of a spanning pipeline. The second dynamic response method is based on the reduced velocity. The reduced velocity is a dimensionless variable defined as a function of a spanning pipeline's natural frequency and diameter, as well as the flow velocity normal to the pipe axis. The reduced velocity is applied to determine the velocity ranges within which VIV might occur [120]. According to the DNV code, in-line vortex shedding might happen when the reduced velocity is within 1.0~3.5 [111].

Using fatigue limit analysis to evaluate the allowable spanning length is based on the comparison between the designed fatigue life and the predicted fatigue life provided by the fatigue analysis of spanning pipelines under different spanning lengths. Once VIV occurs, fatigue analysis must be performed [121]. The fatigue analysis scheme proposed in DNV-RP-F105 has been widely used in previous studies to estimate the fatigue life for spanning pipelines. Besides, it is also used as the baseline for fatigue life estimation. This scheme is anchored in physical models evaluating the responses of spanning pipelines to wave and current loads and estimating fatigue capacity. Fyrileiv et al. [122] applied the DNV-RP-F105 in free-span design and re-assessment. Based on the DNV-RP-F105 and FEM, Rezazadeh et al. [123] performed fatigue analysis on submarine pipelines with multiple spannings. It is found that the first natural frequency has the most significant impact on fatigue damage. He [116] took the factors of the typhoon, current, wave, and pipeline assembly into consideration to predict the allowable spanning length through FEM and fatigue cumulative damage theory proposed by the DNV code. However, the fatigue analysis scheme in DNV-RP-F105 is usually regarded as conservative [124], which could result in increments in maintenance and design costs. Based on the probabilistic analysis, Monte Carlo simulation, DNV-RP-F105, and S-N fatigue curve, Esplin and Stappenbelt [125] proposed a method to reduce the conservatism in the fatigue analysis of spanning pipelines.

As for spanning pipelines with defects or configuration changes, such as corrosion defects and welds, the stress concentration factor is highly important for fatigue analysis. Stress concentration is commonly defined as a point or location in a part where the stress is much greater than that of its surrounding area because of an interruption of the stress flow. It is a dimensionless index used to represent the severity of stress concentration. Moreover, combined with the fatigue analysis method proposed by DNV-RP-F105, SCFs of the defects on spanning pipelines can be used to quantify the effect of defects on the fatigue life [126]. A parametric analysis was performed by Wang et al. [36] to study the effects of

butt welds' features and the spanning length on the SCF of the spanning pipeline. The effects of SCF caused by dents on fatigue life reduction were discussed in Ref. [127].

Although valuable contribution has been made to spanning pipelines, the effects of the simultaneous presence of inner corrosion and spanning phenomenon on the mechanical behaviors of high-strength pipelines are hardly investigated.

2.1.2 Surface wear of gears

2.1.2.1 Physics of surface wear

Gear surface wear is a typical metal loss defect caused by sliding motion between mating surfaces, contact of asperities, debris, bad lubrication condition, etc. Generally, surface wear can be divided into three types, i.e., adhesion, abrasion, and polishing. In previous research, surface roughness is commonly ignored when conducting analytical and numerical analysis for gear surface wear. The surface wear propagation is usually estimated by Archard's model [128]. In Archard's model, the wear depth is expressed as proportional to the sliding distance, contact pressure, local surface temperature, lubrication condition, etc. Eq. (2-1) is the expression of Archard's model.

$$\frac{dh}{ds} = f(p, v, T, C_{lub}, \dots) \tag{2-1}$$

where h represents the wear depth, s stands for the sliding distance, p is the contact pressure, v is the sliding speed, T is the local surface temperature, and C_{lub} is the lubrication condition.

For a meshing point on the mating surface, the wear propagation described by Archard's model is usually expressed in terms of a differential equation, as follows [129]:

$$\frac{dh}{ds} = kp \tag{2-2}$$

where k is the wear coefficient that describes the wear rate. The wear coefficient incorporates the effects of material, speed, lubrication condition, and so on.

2.1.2.2 Prognostic methods

As an essential part of condition-based maintenance, prognostics are applied to predict damage degradation and future failures. To achieve such objectives, health condition models are usually required. The existing prognostic methods are usually classified into three types, i.e., physics-based, data-driven, and integrated prognostic methods [130]. Physics-based prognostic methods are developed based on the degradation process's physics, and physics models are commonly used. Data-driven prognostic methods are developed based on failure histories and/or condition monitoring data. The essential factors for a successful data-driven included appropriate inspection tool selection with minor measurement errors, sufficient data sources, good data process, reliable health indicators, excellent learning algorithm for the relationship between actual health conditions and measured data, and so on. Integrated prognostic methods are proposed to overcome the shortcomings of the other two types of methods by integrating condition monitoring data into the physics-based models.

2.1.2.2.1 Physics-based prognostic methods

In physics-based prognostic methods, physical models are typically the most critical part. Physical models are usually a set of equations developed by the knowledge of physical laws and engineering practice. When experiments and data are unavailable, physics-based prognostic methods are especially useful.

However, physics-based prognostic methods are particularly designed for specific failure modes. Fatigue crack is a common failure mode caused by cyclic loadings. Paris' law is a theoretical model widely used to predict crack propagation. The application of Paris' law in the physics-based methods can be found in Ref. [131–133]. Since pitting is also a failure mode introduced by cyclic loadings, its propagation can also be estimated by Paris' law [134]. Since fatigue pitting is caused by the maximum shear stress beneath the mating surface, the shear stress is used in Paris' law instead of the normal stress (mode I crack)

[135]. Unlike fatigue crack or pitting, surface wear is caused by the sliding contact between mating surfaces. Although lubrication is usually used to reduce friction, it is not enough to provide full protection from surface wear. Archard's model is commonly used to model the surface wear propagation of gears. Based on Archard's model, Flodin and Andersson [136] proposed a simplified wear model to predict the surface wear of helical gears. Bajpai et al. [38] employed Archard's model to predict the surface wear propagation of parallel-axis gear pairs. The results obtained by the physical model were validated against experimental results.

Lubrication conditions have a significant effect on the surface wear of gears. Thus, elastohydrodynamic lubrication (EHL) conditions have drawn intensive interest. Recently, the research involving EHL mainly focused on its impact on the wear rate (wear coefficient) so that physical wear propagation models can be modified. Wang et al. [137] proposed an adhesive wear model for helical gears by modifying Archard's model to be applicable to the mixed lubrication condition. The proposed physical model was applied to predict the wear propagation in mixed EHL and found that surface wear is less severe than that in dry contact. By incorporating the Mixed-EHL model and Archard's model, Zhu et al. [138] developed a prediction model for gears subjected to surface wear in mixed EHL conditions. Since the changes in geometry and EHL conditions were both considered, the predicted surface wear propagation complies with the experimental observations. Besides static models, researchers also made a great contribution to dynamic models. Wu and Cheng [139] improved the physical model for gear wear under partial-EHL conditions in Ref. [140] by considering gear dynamics, such as dynamic loadings. Ding and Kahraman [141] investigated the interactions between surface wear and gear dynamics. Besides, a dynamic wear prediction model is proposed considering the dynamic tooth forces and transmission error.

Although physics-based methods seem convenient to be applied, they have limited application scenarios that are simple and specific. Besides, extra efforts are often needed

to modify physical laws.

2.1.2.2.2 Data-driven prognostic methods

Data-driven prognostic methods principally depend on data, including condition monitoring data and failure histories. There are several essential steps for data-driven fault prognostics, including data acquisition, data processing, health indicator selection, prognostic model selection, and RUL prediction.

In order to conduct condition monitoring data acquisition, sensors should be installed at different locations on a gearbox. Wear debris sensors, acoustic emission sensors, and vibration sensors are three commonly used sensors for gears. Wear debris sensors are applied to measure the metal loss from gear teeth. Besides these three sensors, other sensors, such as torque sensors, are also used to collect other data. Measurement accuracy, cost, working condition, sensitivity, etc., should be considered when selecting appropriate sensors. Appropriate data acquisition systems are applied to acquire useful information from sensors as discrete digital data.

Once the data acquisition process is finished, the collected data should be processed for further analysis because these data may be contaminated by disturbances. Many signal-processing approaches have been developed to eliminate the effects of these contaminations. The time synchronous averaging method (TSA), for example, can be used to generate harmonics TSA signals which is useful for diagnosing surface wear and pitting of gears [142,143].

Health indicators are quantitative measurements describing or reflecting the performance and health status of a component or a population. Health indicators used in gears are generally extracted from previously processed or raw data. Over the past decades, a number of health indicators have been constructed for gear failures, such as reliability, RMS, crest factor, GMF harmonics amplitude, M6A, FM4, and so on [144–147]. Kurtosis, Matched filtered RMS, FM0 and ALR can be used for gear wear [148]. For data-driven prognostic methods, the selection of health indicators is very significant because the performance and

sensitivity of the selected health indicator significantly impact the accuracy of fault classification and prognosis.

Artificial neural networks, particle filters, and deep learning are some typical prognostic models for gears suffering different degradation. Due to the limitation on the run-to-failure data, the number of publications on this topic is relatively small. The application of ANN to remaining useful life prognostics of rotating components can be found in [149–151]. The outcomes of different types of ANN are different. The outcomes, for example, could be vibration magnitude and life percentage. To overcome the disadvantages of traditional data-driven prognostic methods, such as the need for explicit model equations and much prior information, Deutsch et al. [152] proposed a new prognostic method for the remaining useful life prediction of rotating components based on deep learning techniques and big data. When big data is available, the proposed method could realize fully automatic feature extraction and prognosis without any manual operation.

Data-driven prognostic methods show the ease of application because they can directly use the sensor data with few or no human interventions. However, data-driven prognostic methods couldn't perform well when data is insufficient due to measurement errors and inspection costs. Moreover, they might lead to meaningless extrapolation.

2.1.2.2.3 Integrated prognostic methods

As mentioned above, physics-based and data-driven prognostic methods have non-negligible disadvantages, such as a difficult parameter estimation process or being heavily dependent on sufficient data. Several integrated prognostic methods have been developed to overcome the weaknesses and exploit the strengths of physics-based and data-driven methods. By integrating valuable information provided by condition monitoring data with physical models that have real physical meanings, integrated prognostic methods are expected to show better performance.

In the past years, Tian et al. [46,153–155] made a great contribution to developing integrated prognostic methods for gears subjected to cracks and surface wear. In Tian’s

papers, the framework of the integrated prognostic methods is commonly divided into three major parts: physical models, updating process, and data. For crack propagation and RUL prediction, Paris' law is employed. Meanwhile, Archard's model is applied to gears with surface wear. Bayesian inference is used to realize the updating process of essential parameters, such as wear coefficient and crack initiation time, at every inspection point by the information about the current physical condition provided by the real-time condition monitoring data. In Ref. [154], the integrated prognostic method is modified to be able to estimate the crack propagation of gears under time-varying conditions. Besides, in Ref. [155], the integrated prognostic method is extended to consider the sudden jump in the degradation path caused by random shock. Error and uncertainty in prognosis reduce with the updating process going. Therefore, a more accurate prediction of remaining useful life can be obtained.

Other than Tian, other researchers also developed different integrated prognostic methods. Particle filter is a kind of data-driven method which is particularly useful for the degradation considering dynamic characteristics. He et al. [156] proposed a modified particle filter-based prognostic method by integrating a data mining approach and whitening transform to tackle the problem related to degradation state transition in conventional particle filters. Choi et al. [157] proposed an integrated prognostic method for spur gears under crack failure mode. Based on the gear vibration data, the crack size is predicted by a feed-forward neural network.

2.1.3 Pitting gears

As a common type of surface fatigue, pitting on gear teeth is a dominant cause of gear failures, which results in almost 60% of failures [158]. Based on the size, pitting is usually categorized into two types: micro pitting and micro pitting. Micro pitting is defined as the pitting that the naked eye can't observe. Pitting initiates as fatigue cracks occur at or beneath the mating surface under cyclic loadings. With the propagation of cracks, metal

fragments detach from the surface, shaping a pitting with sharpened edges [159]. Under the working condition, pitting on gear teeth could be progressive and gradually forms craters that are large in area. A bad lubrication condition and lubricant contamination could also be the causes of pitting failures [160]. Pitting on gear teeth could lead to a reduction in bearing capacity, alteration in tooth profile, and evident changes in mesh stiffness. Thus, the failure behaviors and remaining useful life could be impacted [40].

Experimental, analytical, and FE methods are three commonly used approaches for investigating pitting gears. An experimental study is conducted by Yang et al. [161] to investigate the spalling mechanism of meshing gears and to predict possible initial positions of spalls. A series of experiments are carried out by Aslantaş and Taşgetiren [162] to determine the pitting formation life of meshing gears. It is also found that pits mainly appear around the pitch line. Chaari et al. [163] analytically investigated the impact of a single pitting on the gear mesh stiffness. It was found that a reduction in mesh stiffness is caused by tooth pitting. Liang et al. [164] proposed an analytical method for the mesh stiffness estimation of spur gears with pitting on the mating surface. The pitting severity level was mimicked by the number of pits. Besides, the relationship between the pitting severity level and mesh stiffness was established. Based on the probability distribution of the pits' locations, Lei et al. [165] developed an analytical model to investigate the effects of a group of pits on the time-varying mesh stiffness of spur gears. To investigate the effects of multiple pits around the pitch line on the mesh stiffness and vibration of the spur gear, Liu et al. [39] established several FE models. It was found that gear mesh stiffness decreases with the increase in pitting severity. Based on FEM, Chen et al. [166] established a series of 3D models of helical gears with different spalling defects to study the effects of spalling on contact stress and mesh stiffness. Zhang et al. [167] proposed a FEM-based elastic-plastic contact fatigue model considering the root of mean square values of surface roughness to investigate the competing mechanism between pitting failure and micro pitting failure of gears.

In previous research, the effects of pitting on the surface wear propagation of gears are barely investigated. Existing prognostic methods for gear wear are mainly based on the contact pressure and sliding distance evaluated by theoretical models, which are developed from many simplifications. Moreover, the impact of variations in tooth profile during wear processes is commonly ignored.

2.2 Background knowledge

2.2.1 Burst pressure models

As mentioned in the literature review, many theoretical burst models have been developed and applied to estimate the burst pressure of corroded pipelines. Some widely used burst models are presented in the followings [54,57,168–171].

2.2.1.1 NG-18

$$P_b = P\frac{1-\frac{A}{A_0}}{1-\frac{A}{A_0 M}} = \frac{2t\sigma_f}{D}\frac{1-\frac{A}{A_0}}{1-\frac{A}{A_0 M}} \tag{2-3}$$

where P_b is the burst pressure, P is the burst pressure of the intact pipe, A is the area of the river-bottom profile, $A_0 = lt$ is the reference area, M is the Folias factor, t is the wall thickness, l is the corrosion length, σ_f is the material flow stress, D is the diameter of the pipeline [172]. Folias factor is a term used to describe the bulge effect that occurs in the shell surface where it is thinner in the wall thickness than the surrounding areas. In 1964, Folias analytically developed this factor by considering the surface crack along the axis of a shell with cylindrical shape. It is usually used to measure the stress concentration level for expanding crack's tip under internal pressure [173].

2.2.1.2 ASME B31G

$$P_b = \begin{cases} \frac{2t}{D}\left(1.1\sigma_y\right)\left[\frac{1-\frac{2}{3}\left(\frac{d}{t}\right)}{1-\frac{2}{3}\left(\frac{d}{t}\right)M^{-1}}\right], & \frac{l^2}{Dt} \le 20 \\ \frac{2t}{D}\left(1.1\sigma_y\right)\left[1-\frac{d}{t}\right], & \frac{l^2}{Dt} > 20 \end{cases} \quad (2\text{-}4)$$

$$M = \sqrt{1+0.8\left(\frac{l^2}{Dt}\right)} \quad (2\text{-}5)$$

where σ_y is the yield stress of the pipe steel, d is the corrosion depth.

2.2.1.3 ASME B31G modified

$$P_b = \frac{2t}{D}\left(\sigma_y + 69\right)\left[\frac{1-0.85\left(\frac{d}{t}\right)}{1-0.85\left(\frac{d}{t}\right)M^{-1}}\right] \quad (2\text{-}6)$$

$$M = \begin{cases} \sqrt{1+0.6275\left(\frac{l^2}{Dt}\right)-0.003375\left(\frac{l^2}{Dt}\right)^2}, & \frac{l^2}{Dt} \le 50 \\ 3.3+0.032\left(\frac{l^2}{Dt}\right), & \frac{l^2}{Dt} > 50 \end{cases} \quad (2\text{-}7)$$

2.2.1.4 CSA Z662-07

It is applied for describing the plastic collapse at a surface corrosion defect.

$$P_b = \begin{cases} e_1 P_{bi} + (1-e_1)P - e_2\sigma_u, & \sigma_y > 241\text{MPa} \\ e_3 P_{bi} + (1-e_3)P - e_4\sigma_y, & \sigma_y \le 241\text{MPa} \end{cases} \quad (2\text{-}8)$$

$$P_{bi} = P\left[\frac{1-\left(\frac{d_a}{t}\right)}{1-\left(\frac{d_a}{t}\right)M^{-1}}\right] \quad (2\text{-}9)$$

$$P = \begin{cases} \frac{2t(0.9\sigma_u)}{D}, & \sigma_y > 241\text{MPa} \\ \frac{2t(1.15\sigma_y)}{D}, & \sigma_y \le 241\text{MPa} \end{cases} \quad (2\text{-}10)$$

$$M = \begin{cases} \sqrt{1+0.6275\left(\frac{l^2}{Dt}\right)-0.003375\left(\frac{l^2}{Dt}\right)^2}, & \frac{l^2}{Dt} \le 50 \\ 3.3+0.032\left(\frac{l^2}{Dt}\right), & \frac{l^2}{Dt} > 50 \end{cases} \quad (2\text{-}11)$$

where is the e_1 is the deterministic model error, $e_1 = 1.04$, e_2 is an additive model error, $e_2 \sim N(-0.00056, 0.001469^2)$, e_3 is a deterministic multiplicative model error, $e_3 = 1.17$, e_4 is an additive model error, $e_2 \sim N(-0.007655, 0.006506^2)$, σ_u is the ultimate

tensile strength of the pipe steel, P_{bi} is the calculated pressure strength.

2.2.1.5 DNV RP F-101

$$P_b = 1.05\frac{2t\sigma_u(1-\frac{d}{t})}{(D-t)(1-\frac{d}{t}M^{-1})} \tag{2-12}$$

$$M = \sqrt{1+0.31(\frac{l^2}{Dt})} \tag{2-13}$$

2.2.1.6 PCORRC

$$P_b = \frac{2t\sigma_u}{D}\left\{1-\frac{d}{t}[1-\exp(-0.157\frac{l}{\sqrt{r(t-d)}})]\right\} \tag{2-14}$$

2.2.1.7 SHELL92

$$P_b = \frac{2t(0.9\sigma_u)}{D}[\frac{1-(\frac{d}{t})}{1-(\frac{d}{t})M^{-1}}] \tag{2-15}$$

$$M = \sqrt{1+0.8(\frac{l^2}{Dt})} \tag{2-16}$$

2.2.1.8 RPA

$$P_b = \frac{2t}{D}(\sigma_y+69)\left[\frac{1-a(\frac{d}{t})}{1-a(\frac{d}{t})M^{-1}}\right] \tag{2-17}$$

$$M = \begin{cases}\sqrt{1+0.6275\left(\frac{l^2}{Dt}\right)-0.003375(\frac{l^2}{Dt})^2}, & \frac{l^2}{Dt}\le 20\\ 2.1+0.7\left(\frac{l^2}{Dt}\right), & \frac{l^2}{Dt}>20\end{cases} \tag{2-18}$$

$$a = \begin{cases}0.85, & \frac{l^2}{Dt}\le 20\\ 1-0.15(64\times10^6)\left(\frac{l^2}{Dt}\right)^6, & \frac{l^2}{Dt}>20\end{cases} \tag{2-19}$$

2.2.2 Monte Carlo simulation

Monte Carlo simulation, also called the Monte Carlo method, is a computational

mathematical technique used to assess possible outcomes and their probabilities and figure out the influence of uncertainty through repeated random sampling. The usage of randomness is the key to the Monte Carlo simulation. Monte Carlo simulations are widely used for problems that other methods cannot solve. Numerical integration, optimization, and generating graph images from probability distributions are the major problems to which Monte Carlo simulations are applied [174]. In the reliability assessment, the Monte Carlo simulation has been verified as feasible and reliable. It is the most common method for uncertainty propagation.

The following basic steps are usually required for general Monte Carlo simulations used in the reliability assessment. First, determine the deterministic predictive computation, identifying both the output variable (to be predicted) and the input variables. Second, ascertain the probability distributions of the input variables with uncertainty. Third, generate a set of random values of the input variables over a specific domain and then apply them to the deterministic predictive computation to obtain the predicted output. Last, repeat the third step to aggregate enough data sets and predicted outputs to obtain the final estimation of the output variable. During the process of using the Monte Carlo simulation to assess the reliability of a corroded pipeline, for instance, the first step is to determine the burst pressure model and the limit state function used to determine a pipeline's failure. Then, determine the probability distributions of the random input variables, such as corrosion depth and length, through inspection or historical data. After each simulation, we can determine the index that tells whether the corroded pipeline is failed or not. Finally, the predicted reliability can be calculated after a certain number of simulations.

The number of simulations is a critical factor that significantly impacts the accuracy and efficiency of the Monte Carlo simulation [75]. A small number of simulations could improve the computational efficiency but reduce the estimation accuracy. On the contrary, a large number of simulations could improve the estimation accuracy but lower the computational efficiency. Therefore, it is important to determine an appropriate number of

simulations. Efficiency and stability analysis is recommended. The most optimal number of simulations can be obtained by analyzing the boxplots, skewness, and elapsed time under different numbers of simulations. However, Monte Carlo simulation could be undesirable for a large and complex system because of the computing time required to achieve acceptable simulation accuracy.

2.2.3 Finite element method

The finite element method is a numerical technique used to solve partial differential equations (PDE) appearing in engineering and mathematical problems. In given physical phenomena, PDEs are widely used to depict laws of physics for time- and space-relevant problems. However, for most of these complicated PDEs, conventional analytical methods are longer valid for getting solutions. FEM is aimed at computing approximations instead of exact analytical solutions for these PDEs based on different types of discretization. In FEM, a huge domain or large system is subdivided into a finite number of smaller and simpler parts, namely finite elements. In practice, the discretization process is achieved through meshing. Direct or iteration methods can be applied to solve the numerical model equations in discretized elements that approximate the PDEs. To solve the whole problem over the entire domain, equations in finite elements should be assembled into a large group of equations. The FEM then gets the final approximation as the accurate solution for the PDEs once the error is minimized to meet the convergence criteria.

For general FEM, there are three major steps. The details of each step are presented in the following.

Step 1: Pre-processing

Numerical models are defined based on the practical problem. A lot of features need to be appropriately defined before computing, including but not limited to element type, material property, geometric structure, boundary condition, loading, etc.

Step 2: Computing and solving

Finite elements are assembled into equation groups which will be solved through the direct method or iteration method. The simulation results are approximating values on the element nodes.

Step 3: Post-Processing

The obtained solutions are analyzed and evaluated according to relevant criteria.

Since the early forties last century, FEM has been developed, improved, and applied to address problems in many fields, such as solid mechanics, heat transfer, fluid flow, electromagnetic potential, etc. After years of improvement, FEM also shows some exciting potential applications, such as fluid-structure interaction, thermo-chemo-mechanical problems, etc. Over the past decades of application, FEM has demonstrated distinct advantages. First, it is more suitable and efficient for solving problems with complex shapes and irregularities. Second, FEM has a relatively lower cost than conventional full-scale experiments. Third, FEM has great flexibility that allows users to build different models based on specific requirements. Last but not least, FEM could provide satisfactory simulation accuracy. Nevertheless, the disadvantages of FEM cannot be simply ignored. First, a large amount of data, in which uncertainties may exist, is needed for modeling and meshing. FEM may always incorporate these uncertainties. Second, the idealization of the actual problem could significantly affect the simulation results. Third, the problem or geometry becomes highly complex, and the computational time required for FEM could dramatically increase. Moreover, the performance of FEM heavily relies on boundary conditions, assumptions, idealizations, solver selection, etc.

FEM simulation results inevitably show differences in the behaviors of the real object. Therefore, FE model validation is usually required, which is employed to validate the idealization and simulation results. In practice, the feasibility and reliability of a FE model are typically validated by comparing the simulation results with the results of physical testing. Once the differences between FE and experimental results are acceptable, the FE model is validated. The acceptance criteria usually differ from one problem to another.

2.2.4 Orthogonal test

The orthogonal test is an efficient statistical approach for testing problems with multiple parameters and levels [175]. For such issues, conducting exhaustive tests of every possible input and its combinations could be time-consuming and expensive [176]. Thus, the orthogonal test method is usually used to cover the entire functionality in the testing scope without losing efficiency. For example, conducting an exhaustive test for a problem with three parameters and three levels needs at least 27 tests. However, only nine tests are required for the orthogonal test. Although the orthogonal test has some distinct advantages, it is usually focused on problems with a relatively small number of inputs. In the orthogonal test, representative levels of inputs are selected and permutated to collect unique pieces of information and then be gathered to obtain the complete information that could be provided by exhaustive testing. The representative levels of inputs should be uniformly distributed. The design of an orthogonal test is based on the orthogonal array, also known as the orthogonal table. There are two essential requirements for an orthogonal array. Specifically, different symbols (or numbers) appear equally in each column of the array. Second, in each row, every random selection of two array columns could form a type of number pair, and different pairs should appear equally.

There are four major steps for the orthogonal test, namely: (1) based on research and requirements, determine the objective of the test; (2) analyze possible factors to determine majors factors and their levels as the inputs; (3) design the orthogonal array and conduct tests accordingly; (4) analyze the test results.

Once the results are obtained from the orthogonal test, they can be analyzed through range analysis to determine the contribution of each parameter to the output [177]. The range value is defined as the difference between the average maximum and minimum and is used to represent the measures of variations in output caused by the variations in the inputs. The bigger the range value of a parameter is, the more significantly the variation in this parameter could impact the output. The following equation can calculate the range value

of a parameter j in the orthogonal test:

$$R_j = \max\left(\overline{k_{J1}}, \overline{k_{J2}}, \dots, \overline{k_{Jm}}\right) - \min\left(\overline{k_{J1}}, \overline{k_{J2}}, \dots, \overline{k_{Jm}}\right) \quad (2\text{-}20)$$

where R_j is the range value of the parameter j, $\overline{k_{Jm}}$ is the average of the sum of the values of j parameter at m level.

2.2.5 Bayesian inference

Bayesian analysis can naturally be applied to conduct uncertainty quantification for model parameters. As a classical statistical inference method, Bayesian inference allows the update process to perform on the probability of an assumption once more information can be obtained. Thus, Bayesian inference is widely used to integrate physics-based models with condition monitoring data. The general expression for Bayesian inference is presented by Eq. (2-21). H is the parameter of our concern, and it has a prior distribution $f_{prior}(H)$. Through some techniques, such as in-line inspection, a set of observed data $\boldsymbol{d} = \{d_1, d_n, \dots, d_n\}$ can be collected, and the marginal density function of $\boldsymbol{d}$ is $f(\boldsymbol{d})$. Through the inference process, the posterior distribution for the parameter, $f_{post}(H|\boldsymbol{d})$, can be obtained.

$$f_{post}(H|\boldsymbol{d}) = \frac{l(\boldsymbol{d}|H) f_{prior}(H)}{f(\boldsymbol{d})} \quad (2\text{-}21)$$

where $l(\boldsymbol{d}|H)$ is the likelihood of obtaining these observed values given parameter H.

As described above, the major task of Bayesian inference is to evaluate the posterior distribution of the parameter by absorbing the new information provided by the observed data. Therefore, the uncertainty in the parameter can be reduced, and the parameter can be updated to be more accurate. In this way, a more accurate prognosis will be realized. The posterior distribution of the parameter can be obtained through the Monte Carlo simulation.

Chapter 3. An integrated reliability method with a newly developed interaction rule for steel pipelines with two corrosion defects

3.1 Overview

Pipelines have been proven to be a significant method of transporting natural gas and other petroleum products [178,179]. While operating, steel pipelines will inevitably be corroded by reactions with the surrounding environment and transmission media. According to a report, around 47% of the damage to offshore steel pipelines in China is caused by corrosion defects, as shown in Figure 3-1 [16]. As one of the most dominant damages, corrosion defects could impair pipelines' strength and threaten their structural reliability, resulting in serious pipeline incidents [180,181]. Previous research and field records show that corrosion defects on a pipeline wall usually occur in patches. Considering the interacting effect between corrosion defects makes the reliability analysis process of the corroded pipeline much more complex. Therefore, it is critical to have an accurate reliability estimation for a pipeline with multiple corrosion defects to improve its safety performance and reduce the pipeline system's accident rate.

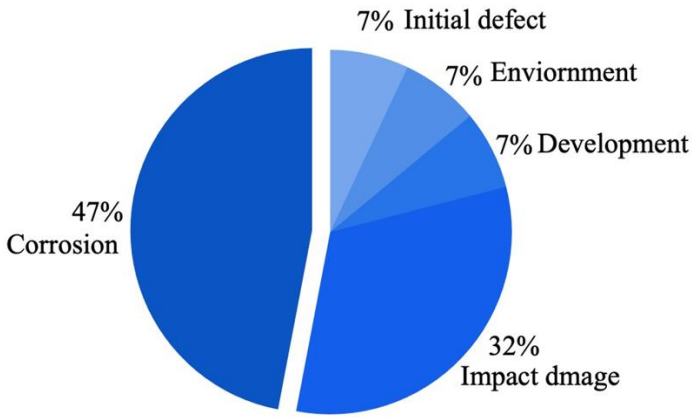

Figure 3-1 Causes of pipeline damage in China.

Over the past decades, a great deal of research has been conducted to estimate the reliability

of corroded pipelines. Monte Carlo simulation (MCS), the first-order reliability method (FORM), and Bayesian networks, for example, are commonly used techniques for the reliability estimation of corroded pipelines. Based on MCS, Shuai et al. [71] investigated the effect of burst models on the reliability of a pipeline with single corrosion. The results show that burst pressure models have a significant effect on the reliability estimation for corroded pipelines. Taking corroded, thick, high-strength pipelines with isolated corrosion defects as the research object, Bhardwaj et al. [73] assessed the uncertainties in reliability through FORM. It was found that the corrosion depth has a strong impact on the reliability estimation. Using dynamic Bayesian networks, Palencia et al. [182] investigated the degradation processes of corroded pipelines. Seghier et al. [76] developed a hybrid reliability analysis method based on the M5 model tree and Monte Carlo simulation for a corroded pipeline with isolated corrosion. The results show that the corrosion length has a relatively low influence on the reliability estimation. Based on FORM, Abdelmoety et al. [183] conducted reliability analyses to estimate the failure probabilities associated with design and safety factors. A weighted Monte Carlo method was used to validate the results obtained by FORM.

Because of its ease of application and high accuracy, MCS is widely used for the reliability analysis of corroded pipelines. The reliability of a corroded pipeline obtained by MCS is usually regarded as a benchmark for estimating other methods' performances, and thus MCS was employed in this chapter.

For corroded pipelines, MCS usually involves a limit state function (LSF) that is used to determine failures by comparing burst pressure with operation pressure. There are three major types of burst pressure prediction methods: finite-element method (FEM), theoretical burst models, and intelligent methods [184].

In recent years, FEM has been frequently applied to determine the burst pressure and investigate the failure behaviors of pipelines with multiple corrosion defects [185]. Based on FEM, Han et al. [80] found that the interacting effect between corrosion defects

decreases with the increase of the spacing distance. Sun and Cheng [81] used FEM to investigate the effects of longitudinal and circumferential spacing distances on the interacting effect and burst pressure. The results show that circumferential spacing distance has a lesser impact. In this chapter, FEM is applied to investigate the burst pressure and interacting effect of the pipeline with multiple corrosion defects.

Over the past years, various burst pressure models considering geometric features and material properties have been developed, such as ASME B31G [54], RSTRENG [55], CSA Z662-15 [56], DNV-RP-F101 [57], and PCORRC [58,186]. Each burst model has its advantages and limitations. Thus, choosing a burst pressure model for the burst pressure assessment should be based on specific conditions. Because of assumptions about corrosion geometric features and yield criteria, some burst pressure models might result in prediction errors that can be calibrated by the model's uncertainty factors [60]. For a pipeline with multiple corrosion defects, the volumetric method is usually combined with burst models to quantify the interacting effect. However, not every adjacent corrosion will interact with others. Therefore, the limit spacing distance is commonly used as the threshold to determine whether the interacting effect should be considered.

Interaction rules have been developed to estimate the limit spacing distance of corroded pipelines. Based on Project PR 3-805, Kiefner and Vieth [55] developed an interaction rule for a corroded pipe considering the corrosion length and wall thickness. CSA Z662-15 [56] defines the limit spacing distance in terms of the corrosion length. Li et al. [83] proposed an interaction rule based on both the experimental and finite-element results to estimate the limit spacing distance for short and long corrosion defects. Based on FEM, Benjamin et al. [84] found that the DNV rule could realize the best performance in the burst pressure estimation, followed by the pipeline operator forum (POF) rule and the Kiefner and Vieth (K&V) interaction rule. Based on 14 corroded pipeline specimens, the effects of five classical interaction rules on burst pressure were studied by Bao and Zhou [187]. The results show that the Canadian Standards Association (CSA) interaction rule is the most

effective. Zhang et al. [186] found that the limit spacing distance of pipelines with external corrosion defects is larger than that of pipelines with both external and internal corrosion defects. Through failure analysis, Xu et al. [85] found that corrosion depth has a more serious impact than corrosion length does on the variation in the burst pressure with an increase in the spacing distance.

Although several interaction rules have been developed for limit spacing distance estimation, very few consider the effects of both corrosion depth and steel grade, which significantly impact the burst behaviors and interacting effect of corroded pipelines. Moreover, very little previous research estimates the reliability of corroded pipelines considering the interacting effect between adjacent corrosion defects or mentions how the interaction rule affects the reliability analysis.

Therefore, this chapter proposes a new reliability method for pipelines with multiple corrosion defects by integrating FEM, regression analysis, burst pressure model, sensitivity analysis, MCS, and the artificial neural network (ANN) method. A series of finite-element models of the corroded pipeline were established and validated to investigate how the effects of corrosion depth and steel grade affect the interaction and the limit spacing distance between adjacent corrosion defects. Based on the simulation results, new interaction rules that consider corrosion depth and steel grade for X65 and X80 pipelines were developed through regression analysis. The MCS considering the interacting effect and interaction rule was developed to improve reliability estimation accuracy and generate reliability data sets for ANN training. An efficiency and stability analysis were performed to determine the sampling number of MCS. Moreover, the effects of interaction rules on the reliability estimation of the pipeline with multiple corrosion defects are discussed. A sensitivity analysis was conducted using the Sobel method to filter raw data and simplify the ANN structure. In addition, feature scaling was applied to input data. An ANN was established and trained to estimate the reliability of pipelines with multiple corrosion defects accurately and effectively. An example of an X65 corroded pipeline was employed

to illustrate the proposed method and its advantages.

Because of the complexity of a corroded pipeline's degradation process, which could be impacted by external factors, it is almost impossible to establish a numerical model or develop a reliability method based strictly on the actual situation. Therefore, in previous studies, some reasonable assumptions were made. In this chapter, the following assumptions are made to ensure the feasibility of the research:

(1) only corrosion defects are considered; (2) only internal pressure is considered (other loadings, such as traffic loadings, are not considered); (3) the influence of the surrounding environment, such as the overburdened soil and temperature, is ignored; and (4) the corrosion profile of FE models is simplified to a rectangle shape combined with smooth rounding, which refers to artificially machined defects in previous experiments.

The following is a summary of the main innovative contributions of this chapter:

- The influences of the corrosion geometric features on the interaction effect between adjacent corrosion defects are quantitatively investigated. The most significant corrosion geometric feature is determined.
- The effects of corrosion depth and steel grade on the interacting effect and limit spacing distance of the pipeline with multiple corrosion defects are systematically discussed.
- Through the finite-element results and regression analysis, two new interaction rules considering both corrosion depth and steel grade are developed for the X65 and X80 pipelines. The performance of the new interaction rules predicting the limit spacing distance is better than conventional interaction rules.
- The reliability method proposed in this chapter integrates FEM, regression analysis, calibrated burst model, sensitivity analysis, feature scaling, and ANN to realize accurate and efficient reliability estimation of corroded pipelines by incorporating the interacting effect and new interaction rule for the first time. The effects of the interacting effect and different interaction rules on the pipeline's reliability estimation

are systematically discussed instead of simply treating corrosion defects in isolation. The performance of the proposed method is tested by an example and found to be excellent. The computational efficiency is high.

• The effect of pressure fluctuations on the reliability of the pipeline with multiple corrosion defects is investigated instead of simply treating the pressure as static.

In the remainder of this chapter, the procedure for the proposed reliability method is presented in Section 3.2. Next, the detailed process of the interaction rule development and a discussion of the effects of corrosion depth and steel grade on the interacting effect and limit spacing distance are presented in Section 3.2.1. Section 3.3 describes the detailed reliability analysis process. A case study of the X65 pipeline is given to demonstrate the proposed method in Section 3.4. Finally, the last section concludes by summarizing major conclusions and outlining areas for future research.

3.2 Proposed integrated reliability analysis method

In most previous relevant studies, the reliability analysis of corroded pipelines was based on isolated corrosion defects. A new reliability method is proposed to fill the gap in the reliability analysis that ignores the interacting effect between adjacent corrosion defects. It integrates a series of numerical approaches, including the FEM, MCS, sensitivity analysis, and artificial neural network method. The flowchart of the proposed reliability method estimating the reliability of the corroded pipeline considering the interacting effect is shown in Figure 3-2. This framework has six steps, which can be divided into two major procedures: interaction rule development (Steps 1–2) and reliability analysis (Steps 3–6).

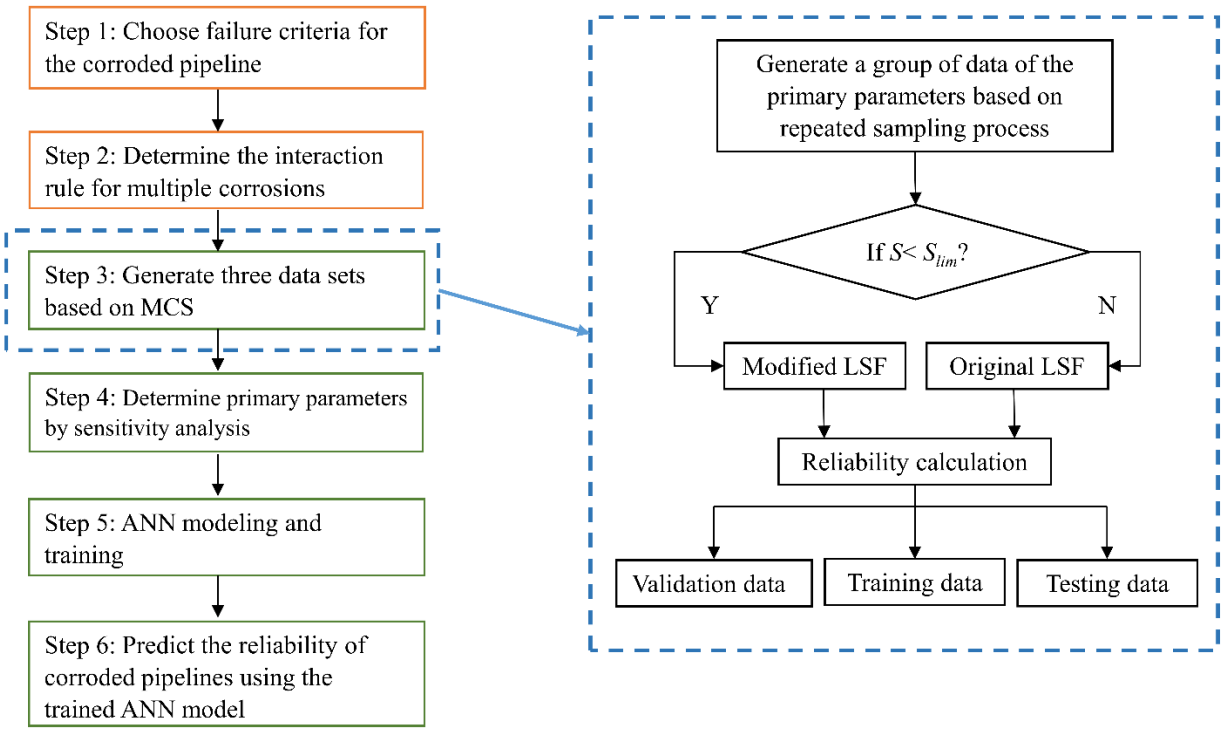

Figure 3-2 Proposed method for reliability assessment of pipelines with multiple corrosion defects.

3.2.1 Interaction rule development

The application of the limit spacing distance estimated by the interaction rule is described by Eq. (3-1). Thus, choosing an appropriate interaction rule is essential for ensuring the burst pressure estimation accuracy and the further reliability analysis of corroded pipelines.

$$z = S_{lim} - l_s \tag{3-1}$$

where z is the status indicator, S_{lim} is the limit spacing distance, l_s is the real spacing distance. If $z \geq 0$, the interacting effect should be considered; otherwise, corrosion defects are isolated, and the burst pressure of the corroded pipeline is the minimum estimated by each corrosion defect.

3.2.1.1 Failure criteria for corroded pipeline

Many failure criteria are available for determining the failure of a corroded pipeline, such

as the 80% of the wall thickness failure criterion, the plastic failure criterion, the yield failure criterion, and so on. Among the existing failure criteria, the Von Mises yield criterion and limit state function are the most widely used.

The Von Mises yield criterion determines if a corroded pipeline will suffer from plastic collapse. Once the Von Mises stress (σ_v) exceeds the stress limit, and a failure occurs. According to previous research, setting the ultimate tensile strength (UTS) as the stress limit could improve prediction accuracy. The Von Mises yield criterion, expressed by Eq. (3-2), is employed in the finite-element analysis.

$$\sigma_v \leq \text{UTS} \tag{3-2}$$

However, the Von Mises yield criterion is no longer useful in the reliability analysis. According to the structure reliability theory, the LSF, expressed as Eq. (3-3), is used to determine a failure.

$$g = P_{corr}^{CB} - P \tag{3-3}$$

where P_{corr}^{CB} is the calibrated burst pressure, P is the internal pressure. If the operating pressure is within the calibrated burst pressure, i.e., $g > 0$, the corroded pipeline is in a safe operating state; otherwise, the corroded pipeline has failed.

The value of burst pressure in the LSF is estimated by a theoretical burst model. The PCORRC model was developed by Leis and Stephens [58]. To make the estimating process feasible, the PCORRC model uses simplified geometric features of the corrosion. Although the corrosion profile is simplified, the PCORRC model is a comprehensive or synthetic approach to accurately assess the corroded pipeline's residual strength because it simultaneously incorporates material properties, geometric features, and the remaining wall thickness. The PCORRC model is recommended for pipelines with moderate- or high-toughness steel. Moreover, the PCORRC model was established based on finite-element simulations, making it better at predicting the burst pressure obtained. Therefore, the PCORRC model was employed in this chapter to conduct the burst pressure estimation. The PCORRC model can be expressed as Eq. (3-4).

$$P_b = \frac{2t\text{UTS}}{D}\left(1 - \frac{d}{t}M\right) \tag{3-4}$$

$$M = 1 - \exp\left(-0.157\frac{l}{\sqrt{r(t-d)}}\right) \tag{3-5}$$

where P_b = burst pressure obtained by burst models; t = wall thickness; D = outer diameter; d = corrosion depth; M = Folias factor; and r = radius of the pipe. The parameter -0.157 is a constant obtained through regression analysis.

Because of assumptions of the yield criteria and the corrosion geometric features, the PCORRC model might introduce some level of conservatism. The calibration process expressed in Eq. (3-6) should be considered to improve prediction accuracy. Detailed information about Eq. (3-6) can be found in the study conducted by Bhardwaj et al. [60].

$$P_{corr}^{CB} = X_{corr}^{G} \times P_b \tag{3-6}$$

where X_{corr}^{G} is the global uncertainty factor.

3.2.1.2 New interaction rule

Over the past decades, different companies and researchers have developed several interaction rules. Some typical interaction rules are listed in Table 3-1. However, almost no existing interaction rules consider the effects of the corrosion depth and pipe steel grade. Such ignorance might induce inaccuracy in the burst pressure assessment or further reliability analysis.

Table 3-1. Interaction rules.

Interaction rule	Longitudinal limit (mm)
DNV-RP-F101	$S_{lim} = 2\sqrt{Dt}$
Coulson and Worthingham	$S_{lim} = \min(l_1, l_2)$
ASME B31G	$S_{lim} = 3t$
Kiefner and Vieth	$S_{lim} = \min(6t, l_m, l_n)$

In Step 2, FEM is applied to investigate how the corrosion depth and steel grade influence the limit spacing distance. Performing full-scale experiments could be expensive and

challenging to keep the experiment results satisfactory. Meanwhile, FEM has many remarkable merits, such as relatively low cost and high efficiency. Using FEM to address nonlinear problems about corroded pipelines has been proven to be cost-effective and could obtain satisfactory results. Based on the simulation results and regression analysis, new interaction rules considering the effects of the corrosion depth and pipe steel grade can be developed.

3.2.1.3 Numerical simulation model

The 3D FE model of the pipeline with axially distributed corrosion defects shown in Figure 3-3 was established in Abaqus 6.14. According to previous research [188], in a situation where only internal pressure is considered, the interacting effect of circumferentially aligned corrosion defects is ignorable compared with that of axially distributed corrosion defects. Because of the symmetries of the geometrical features and the load, only a quarter of the whole numerical simulation model was needed to improve the computing efficiency without losing simulation accuracy. The geometrical features of the corroded pipeline were obtained from the previous study [189]. The outer diameter of the pipeline was 458.8 mm, the wall thickness was 10 mm, and the length was 1500 mm. The corrosion defects were all located on the outer wall of the pipeline. The corrosion length and width were 52 and 32 mm, respectively. According to previous research, the corrosion width has an insignificant effect on interacting behaviors. Eight-node and hexahedron elements were applied to mesh the pipeline model with multiple corrosion defects. Meshes of the areas around the corrosion defects were refined to improve simulation accuracy and computing efficiency. The mesh size of the refined area was 1 mm, while that of other areas was 3 mm, which has been proven to be reliable. In this chapter, two widely used pipeline steels at different grades, i.e., X65 and X80, were selected. The fundamental parameters of the X65 and X80 pipe steel are listed in Table 3-2. Because of the effect of the hardening of the pipe steel on the mechanical behaviors of the corroded pipeline, plastic properties and hardening

behaviors should be considered. The true stress-strain curves of X65 [190] and X80 [191] pipe steels are shown in Figure 3-4.

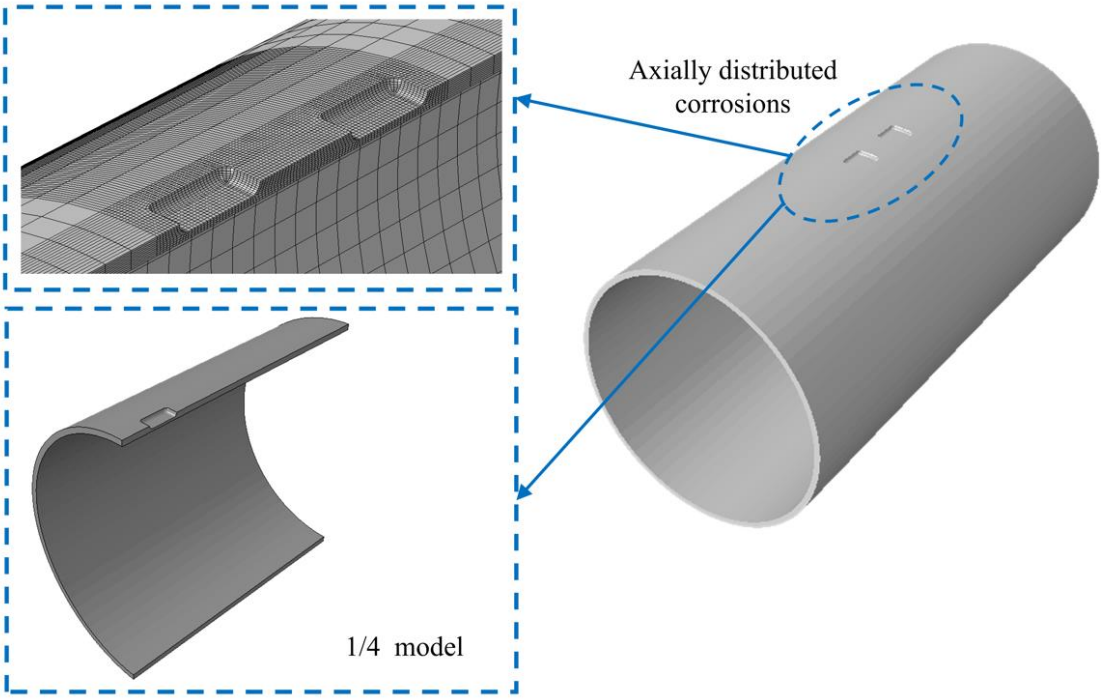

Figure 3-3 Three-dimensional finite-element model of the pipeline with axially distributed corrosion defects.

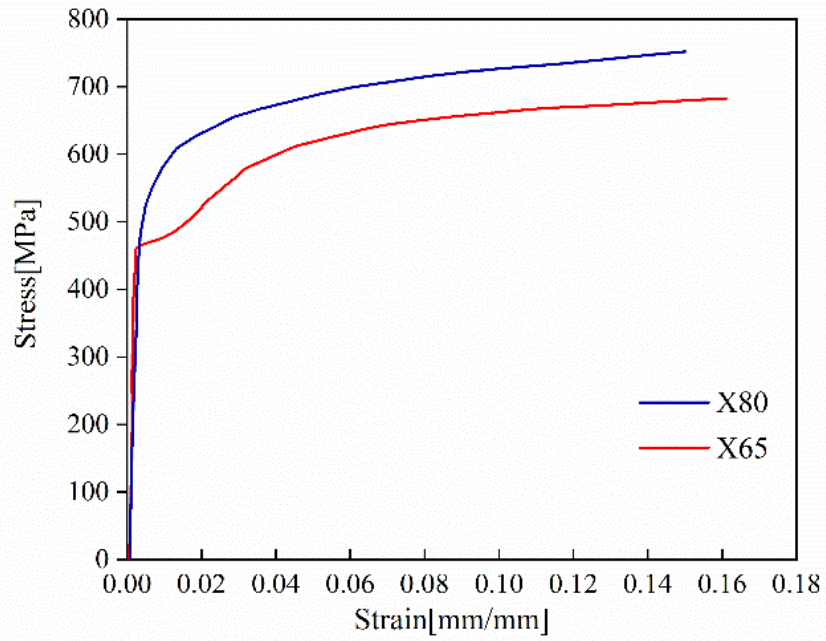

Figure 3-4 True stress–strain curves of pipeline steels.

Table 3-2. Material properties of X65 and X80 steel.

Property	X65 steel [190]	X80 steel [27]
Young's modulus (GPa)	206	200
Yield strength (MPa)	456	534.1
UTS (MPa)	565	718.2

3.2.1.4 Numerical model validation

The feasibility and reliability of using the finite-element method to solve failure problems of corroded pipelines can be validated by comparing the simulation results with other reliable data, such as the experimental results. Validation of numerical models was established based on a series of experiments [190,191]. The key parameters, geometric features, and corrosion defect distributions of the selected experimental specimens are listed in Table 3-3. Such validation method for finite element models has been widely used in previous studies, such as Ref. [188,192,193].

Table 3-3. Parameters of experimental pipe specimens.

Specimen	Steel	D (mm)	t (mm)	d (mm)	l (mm)	w (mm)	l_c (mm)	l_c (mm)	Distribution
IDTS-2	X80	458.8	8.1	5.39	39.6	21.9	-	-	Isolated
IDTS-3	X80	458.8	8.1	5.32	39.6	31.9	20.5	-	Axial
IDTS-4	X80	458.8	8.1	5.62	39.6	32	-	9.9	Circumferential
X65-DB	X65	762	17.5	8.8	200	50	-	-	Isolated

Figure 3-5 shows the burst pressure calculated by FEM and the experimental burst pressure of each testing specimen mentioned previously. The four cases' average relative error is only 3.7%, which is acceptable when conducting FEM. Therefore, the numerical simulation models were validated to be feasible and reliable in assessing the corroded

pipeline's burst pressure.

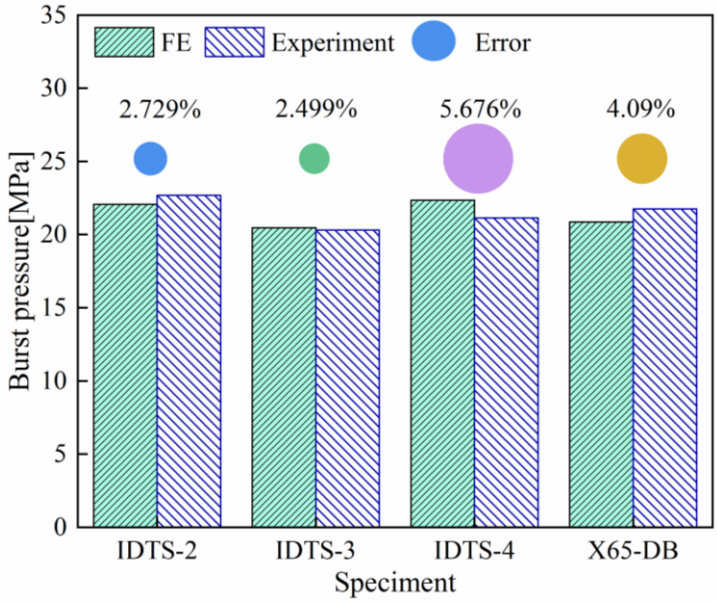

Figure 3-5 Comparison of burst pressures obtained by experiments and FE simulations.

3.2.1.5 Simulation results and discussion

The corrosion geometric features were our major concern for a specific pipeline, while other parameters, like pipeline wall thickness, were already determined. To investigate the effects of corrosion geometric features, including depth-to-thickness ratio (DTR), corrosion length (l), and corrosion width (w), on the burst pressure and interacting effect, an $L_4(2^3)$ orthogonal test was designed and performed. The testing results, which were analyzed by the range analysis, are listed in Table 3-4. Range value can quantify the test index's variation caused by the variation in input. Figure 3-6 shows the range values of d, l, and w. It is apparent that DTR has the most significant contribution to burst pressure and interacting effect.

About 120 numerical simulation models with different geometric features were built and simulated according to the aforementioned parameters. Eq. (3-7) is a rule widely used in the research of pipelines with interacting corrosion defects to determine if the longitudinally aligned corrosion defects should be regarded as interacting defects [81].

$$\frac{P_{mul}}{P_{iso}} < 0.99 \tag{3-7}$$

where P_{mul} and P_{iso} = burst pressures of a pipeline with multiple and isolated corrosion defects, respectively.

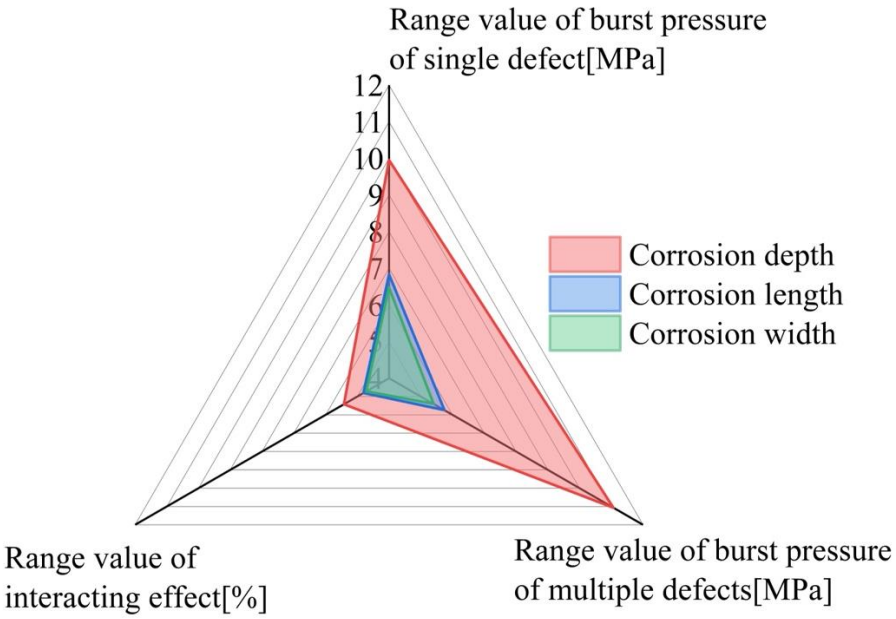

Figure 3-6 Results of the orthogonal test.

Table 3-4. $L_4(2^3)$ orthogonal test.

Specimen	DTR	l (mm)	w (mm)	P_{iso} (MPa)	P_{mul} (MPa)	P_{mul}/P_{iso} (%)
1	0.1	40	20	25.05	25.02	99.86
2	0.1	160	40	24.69	24.68	99.95
3	0.8	40	20	21.57	19.6	89.72
4	0.8	160	40	8.26	8.2	99.25

If the ratio between the burst pressure of the pipeline with multiple corrosion defects and that of the pipeline with single corrosion is smaller than 0.99, the interacting effect between corrosion defects is supposed to be considered.

The effects of the corrosion depth and spacing distance on P_{mul}/P_{iso} of the X65 and X80 pipelines are shown in Figure 3-7. The value of P_{mul}/P_{iso} becomes much lower when the

corrosion depth grows, which indicates that the extent of the interacting effect between adjacent corrosion defects increases to a higher level once the depth of the corrosion defect grows. The limit spacing distance is defined as the spacing distance that makes $P_{mul}/P_{iso} = 0.99$. As pipeline steel grade grows, the steel has a higher yield strength and tensile strength, which allows a corroded pipeline to withstand greater deformation before experiencing failure. The surrounding area of corrosion could be impacted more evidently and area impacted by the bulging effect between defects can be expanded. Thus, the limit spacing distance expands. Based on the simulation results, the limit spacing distances under different corrosion depths can be inferred.

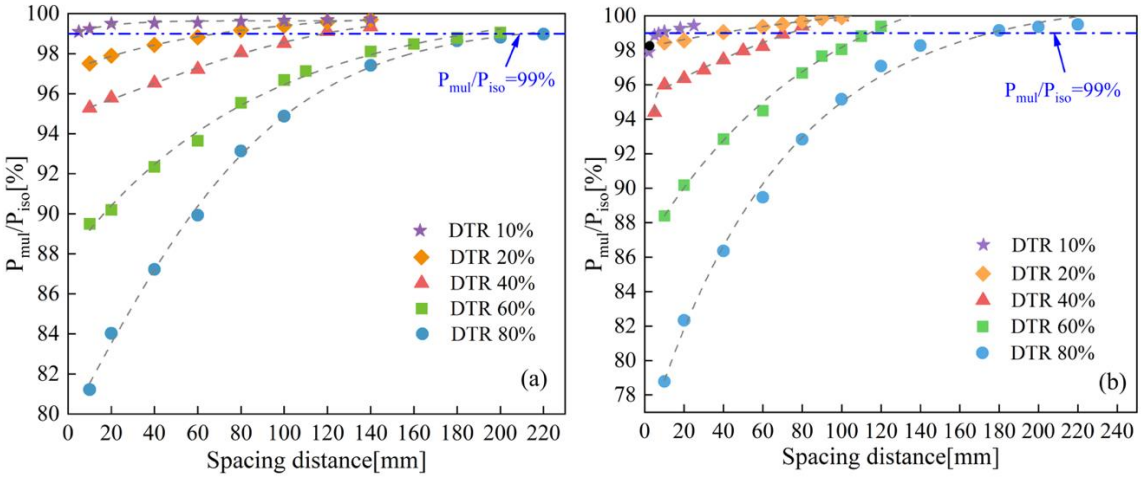

Figure 3-7 Effects of corrosion depth and spacing distance on P_{mul}/P_{iso} of the corroded pipeline: (a) X65; and (b) X80.

Based on the simulation results, the limit spacing distances of the X65 and X80 pipelines with different DTRs are shown in Figure 3-8. The limit spacing distances of both the X65 pipeline and the X80 pipeline are sensitive to DTR variations. With DTR increases, the limit spacing distance shows an upward trend for both the X65 and X80 pipes. The limit spacing distance of the X80 pipe with 80% DTR is about 124 times larger than that with 10% DTR. For the X65 corroded pipeline, when DTR increases from 10% to 80%, there is a 22-fold growth in the limit spacing distance. Thus, the increase in the steel grade could enhance the corrosion depth's effect on the limit spacing distance. When the DTR is larger

than 10%, there exists a significant difference between the limit spacing distance of the X65 pipe and that of the X80 pipe at the given DTR.

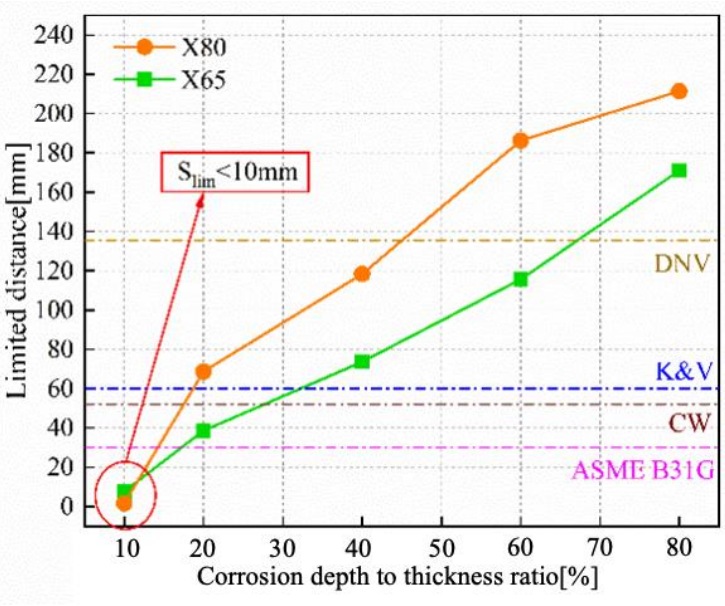

Figure 3-8 Effect of DTR on the limit spacing distance between adjacent corrosion defects.

Despite the existence of several interaction rules, none quantifies the effects of the corrosion depth and the steel grade. When the DTR is 10%, for the X65 and X80 pipes, the limit spacing distances obtained by FEM are smaller than 10 mm, while the limit spacing distances estimated by the four interaction rules are all greater than 30 mm. The limit spacing distance assessed by the DNV interaction rule is 80 times larger than that evaluated by the simulation results of the X80 pipeline. In other words, the DNV interaction rule will induce unnecessary conservatism in further assessment. When the DTR is larger than 40%, K&V, Coulson and Worthingham (CW), and ASME B31G will underestimate the limit spacing distance. Therefore, developing new interaction rules that consider the effects of the corrosion depth and pipeline steel grade is of great value for improving the accuracy of the burst pressure estimation and the reliability analysis.

Figure 3-9 shows the nonlinear relationships between the normalized limit spacing distances and the normalized corrosion depths of the X65 and X80 pipelines. According to

the scatter points' regularities, the asymptotic function was employed to fit the limit spacing distances under different normalized corrosion depths. The solid lines in Figure 3-9 are the fitted lines for the X65 and X80 pipes. The average R^2 value of these two fittings is larger than 0.99, which manifests the goodness of the fit. Through regression analysis, the new interaction rules incorporating the corrosion depth are expressed as Eqs. (3-8~3-9) for the X65 pipe and the X80 pipe, respectively.

X65: $$S_{lim} = \left(3954.875 - 3956.144 \times 0.994^{\frac{d}{t}}\right) \times t \quad (3\text{-}8)$$

X80: $$S_{lim} = \left(27.831 - 33.22 \times 0.132^{\frac{d}{t}}\right) \times t \quad (3\text{-}9)$$

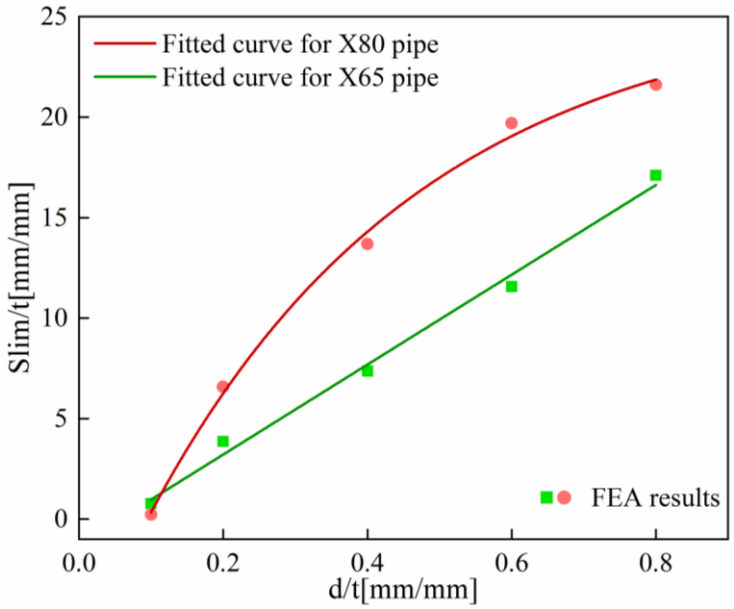

Figure 3-9 Fitted curves for normalized limit spacing distance with different normalized corrosion depths.

3.3 Reliability analysis for corroded pipelines considering interacting effect

Once failure criteria are determined and the new interaction rule is developed, they can be used in burst pressure estimation and reliability analysis.

3.3.1 Data sets generation–based on MCS

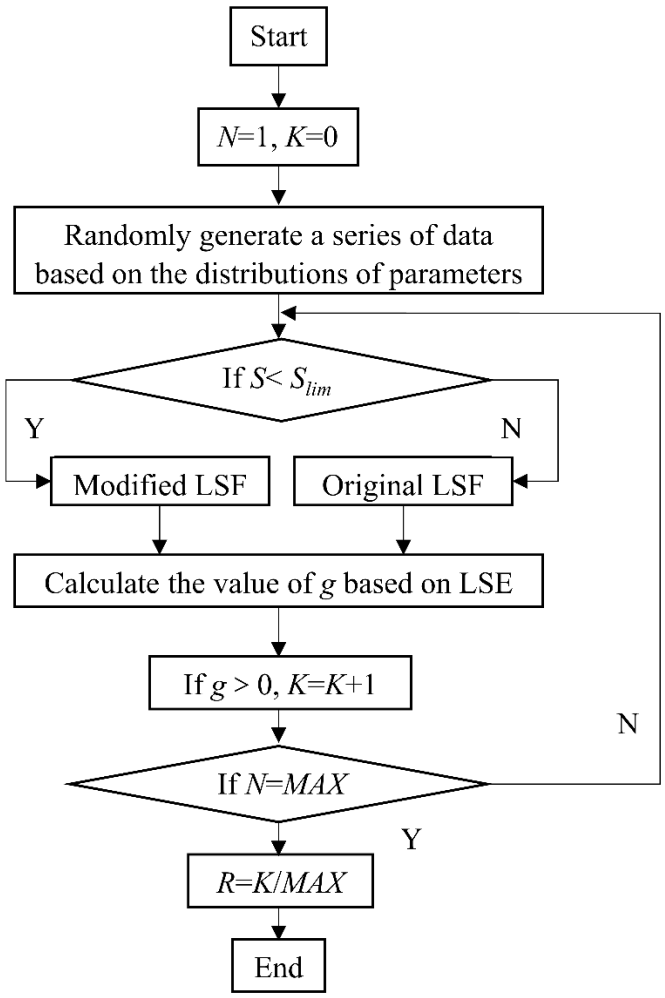

Figure 3-10 Reliability prediction by MCS.

As a small probability event, pipeline failure owing to corrosion defects usually lacks sufficient in-line inspection (ILI) data for reliability prediction. Thus, appropriate statistical methods are needed to gather enough data for reliability analysis. MCS is a computerized mathematical algorithm that has been verified as reliable and feasible in the reliability analysis. The MCS procedure calculating the corroded pipeline's reliability while considering the interacting effect is shown in Figure 3-10. Based on the probability distributions of the parameters, the data set needed for the burst pressure estimation can be

generated through random sampling. The generated data set will then be put into the burst pressure model to calculate the burst pressure. Next, the estimated burst pressure will be put into the LSF to determine if the corroded pipeline fails.

The database generated for the reliability analysis should be separated into two groups according to the limit spacing distance estimated by the interaction rule. If the generated spacing distance l_s is within the limit distance S_{lim}, the data set will be classified into the group in which the modified LSF is applied to consider the interacting effect. Otherwise, the data set will be classified into the group in which the original LSF is applied. In the modified LSF, the burst pressure is estimated by the burst model that incorporates the impairment of residual strength caused by the interacting effect. Spacing distance is usually defined as the distance between the edges of adjacent corrosion defects. The equivalent corrosion length and depth expressed by Eqs. (3-10~3-11), respectively. They are employed to substitute for the original ones in the burst model to quantify the interacting effect, as shown in Figure 3-11. The corrosion depth used is the maximum depth of the corrosion defect [194].

$$l_e = l_1 + l_2 + l_s \tag{3-10}$$

$$d_e = \frac{l_1 d_1 + l_2 d_2}{l_e} \tag{3-11}$$

where l_e is the equivalent corrosion, l_1 and l_2 is the length of corrosion 1 and 2, respectively, d_1 and d_2 is the depth of corrosion 1 and 2, respectively.

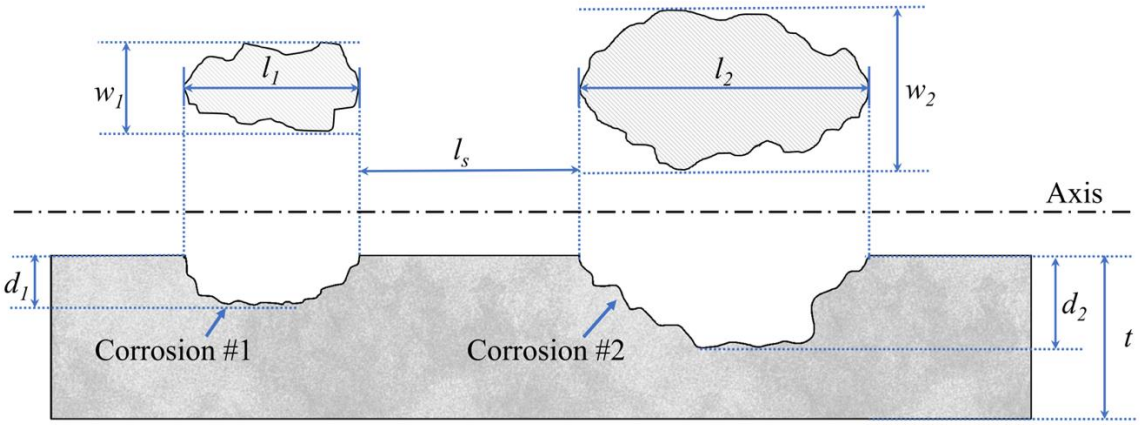

Figure 3-11 A pipeline with interacting corrosion defects.

In actual use, because of the corrosive environment and other factors, the corrosion defects on the pipe wall will expand in the axial and radial directions. Thus, corrosion growth should also be considered in the reliability analysis. According to previous research, the corrosion growth in both the axial and radial directions can be evaluated by Eqs. (3-12~3-13), respectively [194].

$$l(t) = l_0 + V_l(T_c - T_0) \tag{3-12}$$

$$d(t) = d_0 + V_d(T_c - T_0) \tag{3-13}$$

where $l(t)$ is the current corrosion length; l_0 is the initial corrosion length, V_l is the corrosion growth rate along the length, T_c is the current time, T_0 is the initial time, $d(t)$ is the current corrosion depth, d_0 is the initial corrosion depth, and V_d is the corrosion growth rate along the depth.

Finally, the entire database generated through MCS will be separated into three groups for ANN training, validation, and testing. The percentage of the entire database for each group should be determined based on specific requirements. The ANN inputs are the sampled parameters, while the outputs of the ANN are the reliabilities estimated by the MCS.

3.3.2 Determine the primary parameters through sensitivity analysis

The input parameters significantly influence the complexity and the computing time of an ANN. The number of ANN input neurons is usually determined by the parameters of the burst pressure model and operation parameters. Burst models are functions of geometric parameters and material parameters. Although an increase in the parameters, to some extent, could improve the accuracy of the ANN prediction, it would make the ANN structure more complex and lower the computing efficiency. Thus, the number of parameters must be limited to guarantee computing efficiency and avoid overfitting. Even so, the number of input neurons cannot be arbitrarily reduced because the reduction could impact the ANN performance. Sensitivity analysis is applied to determine the primary parameters kept in

the ANN modeling to avoid an arbitrary reduction.

As a variance-based statistical method, the Sobol method is widely used in reliability analysis to estimate each parameter's contribution to the predicted reliability [195]. The Sobol method is a global method that could assess the sensitivity based on the inputs' whole scale and effectively deal with the nonlinearities. Through the Sobol method, two Sobol indexes, S_i and S_{Ti}, can be obtained to evaluate the estimated reliability's sensitivity to the parameters. The functions of these two indexes are expressed by Eqs. (3-14~3-15), respectively. The total-effect index is generally used in sensitivity analysis to represent sensitivity.

$$S_i = \frac{\mathrm{var}_{Xi}\left(E_{X_{\sim i}}(Y|X_i)\right)}{\mathrm{var}(Y)} \tag{3-14}$$

$$S_{Ti} = \frac{E_{X_{\sim i}}\left(\mathrm{var}_{Xi}(Y|X_{\sim i})\right)}{\mathrm{var}(Y)} \tag{3-15}$$

where S_i is the first-order sensitivity index, X are input parameters, Y is the output, and S_{Ti} is the total-effect index.

3.3.3 ANN modeling and training

Because the reliability analysis of pipelines with multiple corrosion defects involves several primary parameters and their nonlinear relationships, traditional approaches, such as linear regression, are no longer suitable. The artificial neural network approach has been shown to have effective and flexible performance for estimating pipeline reliability because of its powerful capacity to deal with complex and nonlinear relationships between multiple parameters. The input neurons of the ANN are the selected primary parameters, and the output is the reliability of the corroded pipeline. The differences in the orders of magnitude of inputs could be significant, making the trained ANN not sensitive to parameters with a small order of magnitude. The corrosion depth is of the order of magnitude of 10, for example, while the pipe steel's ultimate tensile strength is of the order of magnitude of 10^8. Therefore, a feature scaling approach is required to ensure parameters or features are on a similar scale. The function of the feature scaling is expressed by Eq. (3-16). Through the

feature scaling process, each parameter's range will be adjusted from -1 to 1.

$$y = (y_{max} - y_{min}) \times \frac{(x - x_{min})}{(x_{max} - x_{min})} + y_{min} \quad (3\text{-}16)$$

where y is the value of x after feature scaling, x_{min} and x_{max} is the minimum and maximum value of x vector, respectively.

3.3.4 Using the trained ANN to conduct reliability prediction

The ANN, which is established, trained, and validated in the last step, is a powerful tool for quickly and effectively estimating the reliability of pipelines with multiple corrosion defects.

3.4 Case study for the integrated reliability analysis

This section presents an example of an X65 pipeline with two axially aligned corrosion defects to demonstrate the proposed integrated reliability method. The proposed methodology aims to estimate the corroded pipeline's reliability considering the interacting effect over the operating lifetime. The probability distributions of the major parameters in an initial state are listed in Table 3-5 [71]. Each parameter will be used in the limit spacing distance estimation, burst pressure assessment, MCS, and ANN training. It is assumed that two corrosion defects are on the same pipe segment and in the same corrosive environment, i.e., the corrosion growth rates are the same for the defects. The spacing distance between the longitudinally aligned corrosion defects is 100 mm in the initial state, and it will be shortened because of the corrosion growth. Additionally, some geometric and material parameters remain stable during the operating period, such as the ultimate tensile strength and the outer diameter.

In Step 1, the LSF expressed by Eq. (3-3) is selected as the failure criterion of the X65 corroded pipeline. The calibrated burst pressure used in the function can be estimated by Eq. (3-6). Because X65 is medium-grade steel, X_{corr} is 1.21 [60].

In Step 2, FEM is employed to develop the interaction rule. Detailed information is

presented in Section 3.2.1.2. The new interaction rule described in Eq. (3-8), which considers the effects of the corrosion depth and X65 pipe steel, is applied to determine the limit spacing distance between corrosion defects in the following step.

In Step 3, MCS is used to generate the reliability data sets. The process of MCS is shown in Figure 3-10. The number of sampling times influences the accuracy and efficiency of MCS. Therefore, choosing an appropriate number of sampling times is significant. Based on the probability distributions listed in Table 3-5, the efficiency and stability analysis is carried out to investigate the effects of the number of sampling times on the MCS results and computing efficiency. Figure 3-12 shows comparisons of boxplots, skewness, and elapsed time needed for simulation under different numbers of sampling times. When the number of sampling times is less than 10^6, although the elapsed time is relatively short, the skewness, median value, and range within 1.5 times the interquartile range fluctuate with the variation of the number of sampling times. If the number of sampling times is greater than or equal to 10^6, the elapsed time of MCS shows a significant rise with the increase in the sampling times. However, the skewness and boxplot are stable. Therefore, 10^6 was set as the number of sampling times in this chapter. A data set was generated through MCS, including input data and target data for ANN training.

Table 3-5. Probability distributions of parameters.

Parameters	Mean value	COV (%)	Distribution
UTS (MPa)	565	7	Normal
D (mm)	458.8	3	Normal
DTR	0.3	10	Normal
t (mm)	10	5	Normal
P (MPa)	8	8	Gumbel max
L (mm)	52	50	Normal
V_d (mm/year)	0.097	75	Normal
V_l (mm/year)	3	13	Normal

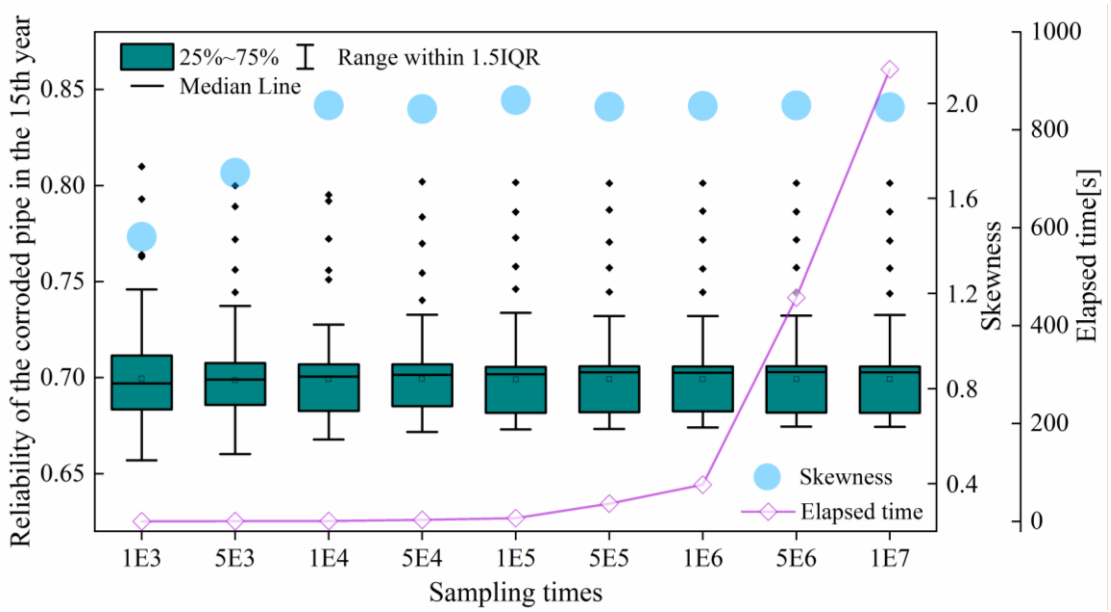

Figure 3-12 Decision on the sampling times of the Monte Carlo simulation.

Based on MCS, the reliabilities of the X65 pipeline with multiple corrosion defects under different interaction rules are shown in Figure 3-13. During a 30-year operating time, the reliability shows a descending trend, but the rate of descent is different. For this case study, the reliability stays relatively steady before 15 years, regardless of the type of interaction rule. After 15 years, reliabilities estimated by the CW and new interaction rules are the first to decrease. For single corrosion and ASME, the descent starts about 4 years later. Before 22 years, the ASME interaction rule treats corrosion defects as isolated. It is evident that both the interacting effect and the interaction rule significantly impact the reliability analysis of the pipeline with multiple corrosion defects. Pipeline reliability is usually used by operators to determine if maintenance is needed. An underestimation of the interacting effect might delay the maintenance action and result in unexpected accidents. When the reliability is 0.9, which is typically set as the threshold for maintenance, the time lag between the single corrosion and the interacting corrosion defects is more than 7.5 years. Thus, a corroded pipeline's reliability analysis must consider the interacting effect between adjacent corrosion defects to ensure reliable predictions. The time lag between the ASME

rule and the new rule is about 1 year. Because the new interaction rule was developed for this specific case and proved to be highly accurate in the limit spacing distance estimation, it can provide a more reliable reliability prediction for the corroded X65 pipeline. When plotting failure probability, a log scale is often used because it can help to better visualize small probabilities on the same plot as larger probabilities. This makes it easier to see patterns and trends in the data, especially when the variations in the failure probabilities are large. The failure probability on log scale of the corroded pipeline estimated based on different interaction rules is shown in Figure 3-14. The plot of the failure probability on the log scale could help operators better understand the change rule and determine maintenance actions more accurately.

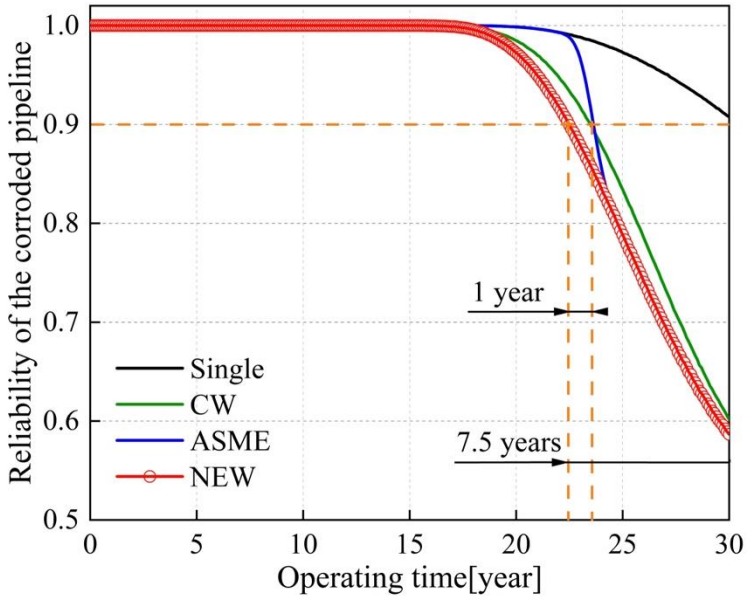

Figure 3-13 Reliability predictions with different interaction rules versus operating time.

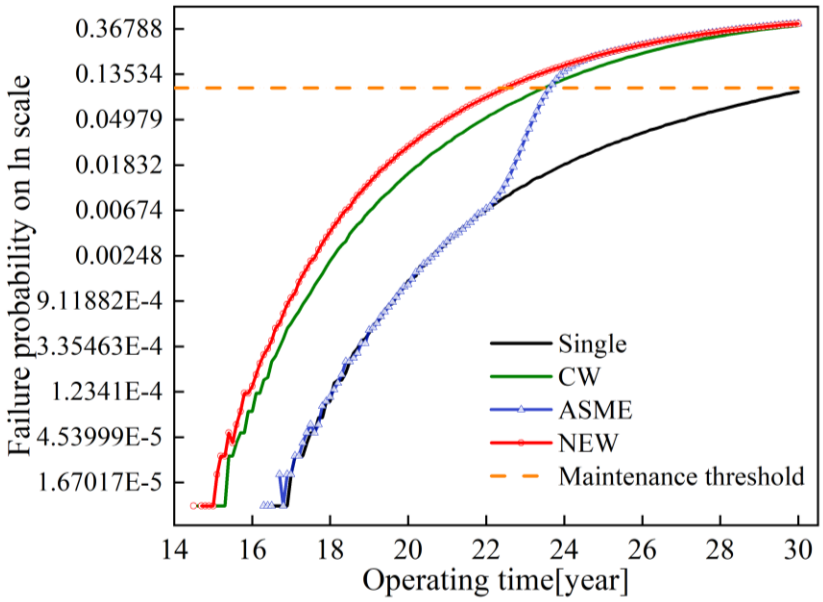

Figure 3-14 Reliability predictions with different interaction rules versus operating time.

Because of unstable flow conditions or significant changes in demand of the conveying media, pressure fluctuations might occur that could impact the corroded pipeline's reliability. The Poisson square wave process (PSWP) can be applied to simulate the internal pressure considering pressure fluctuations. Detailed information about the simulation process can be found in Tee and Pesinis [196]. Because of the inadequacy of time history for the internal pressure, the generation rate (λ) in the PSWP model is assumed as 0.75, 1.0, and 1.5. Figure 3-15(a) shows the simulated pressures under different λ values. The reliability predictions with different internal pressures, including pressures simulated by the PSWP and random variable (RV), are shown in Figure 3-15(b). In this case study, it is evident that the pressure fluctuations have little impact on the reliability prediction of the corroded pipeline around the maintenance threshold. Thus, pressure fluctuations are not considered in the proposed method. However, in future work, once a real λ is obtained, the effect of pressure fluctuations could be considered.

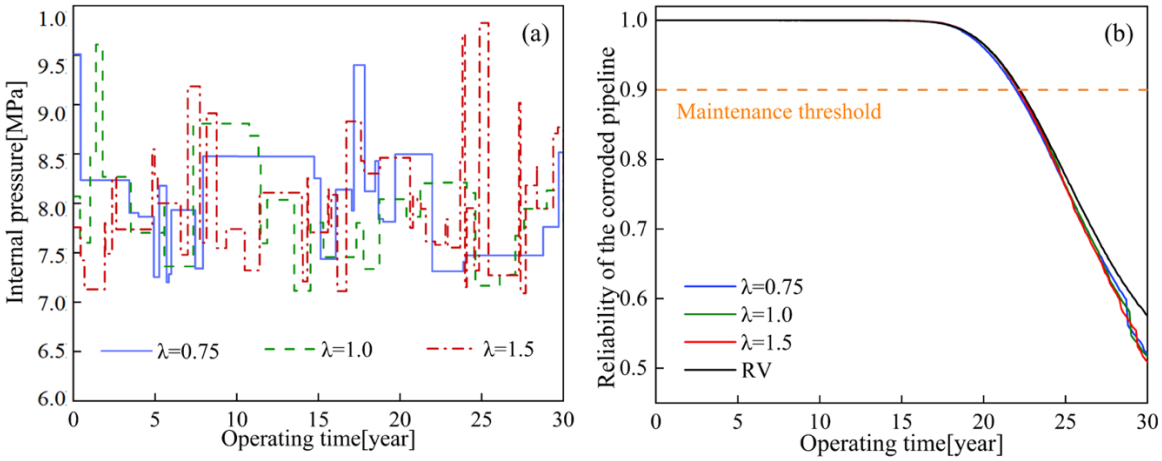

Figure 3-15 Effects of pressure fluctuations on reliability of the corroded pipeline: (a) simulated internal pressure based on PSWP; and (b) reliability predictions with different internal pressures.

In Step 4, the Sobol method is implemented to determine primary inputs for further ANN construction. Based on previous simulation examples, ranges of parameters are as follows: P = 6~14 MPa, t = 9.5~10.5 mm, DTR = 0.3~0.6, l = 50~150 mm, UTS = 525~605 MPa, D = 445~473 mm, V_d=0.05~0.2 mm/year, and V_l=2~6 mm/year. The time is from 0 to 30 years. The total-effect index expressed by Eq. (3-15) is employed to represent the contribution of each parameter. The Sobol analysis results of this corroded X65 pipeline segment are shown in Figure 3-16. The maximum contribution to the reliability is conducted by the operating time, and the pipeline's outer diameter causes the minimum contribution. The total effect of D and UTS only accounts for 0.83% of the global contribution. Usually, at least 99% of the global contribution is kept ensuring prediction accuracy. Thus, the variation of pipeline outer diameter can be ignored in the further reliability analysis for this case. The selected primary parameters for the reliability analysis are the time, P, t, DTR, l, V_d, and V_l.

In Step 5, a feed-forward neural network with back-propagation learning (BP ANN) is established and trained. The data set generated in the previous steps contains 9,000 data points, which is enough for the ANN training in this case. The generated data set is

separated into three parts for ANN training (70%), validation (15%), and testing (15%). The built-up ANN with a three-layer structure is shown in Figure 3-17. The input-layer neurons are the primary parameters selected through the sensitivity analysis in Step 4. There is only one output, i.e., the reliability of the corroded pipeline. Before putting all the parameter variables into the ANN training process, the feature scaling approach described by Eq. (3-16) is applied to inputs. The best validation performance of the trained ANN is 8.37×10^{-6}. Moreover, the mean-square error (MSE) of the testing data set (15%) is around 8.51×10^{-6}, which is very small. Thus, the performance of the trained ANN is excellent.

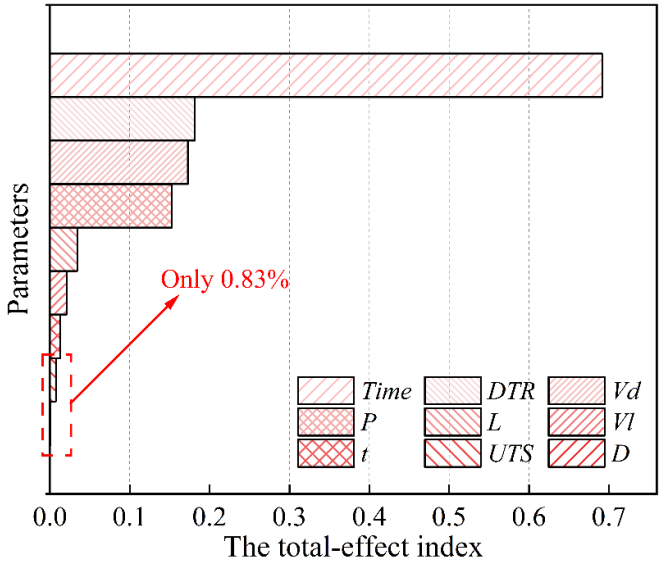

Figure 3-16 Sobol analysis results of the parameters.

The trained ANN could predict the pipeline's reliability with multiple corrosion defects. Reliabilities of the corroded pipeline over 30 years are estimated by the trained ANN and MCS to compare their prediction performances. The simulation results are plotted in Figure 3-18. Each reliability curve contains 60 estimating points, which are evenly spaced. The corroded pipeline's reliability estimated by the trained ANN is noticeably similar to that estimated by MCS. The mean-square error is only 2.4×10^{-6}, which is acceptable. The reliability estimated by MCS has been commonly used as a validating reference in previous studies. Therefore, the trained ANN has an excellent prediction performance. To obtain the

reliability evaluation results shown in Figure 3-17, 52.28 seconds of elapsed time is needed in MATLAB for MCS, while only 1.08 seconds is needed for the ANN prediction. Thus, the proposed ANN-based method is much more efficient than MCS for pipeline reliability evaluation.

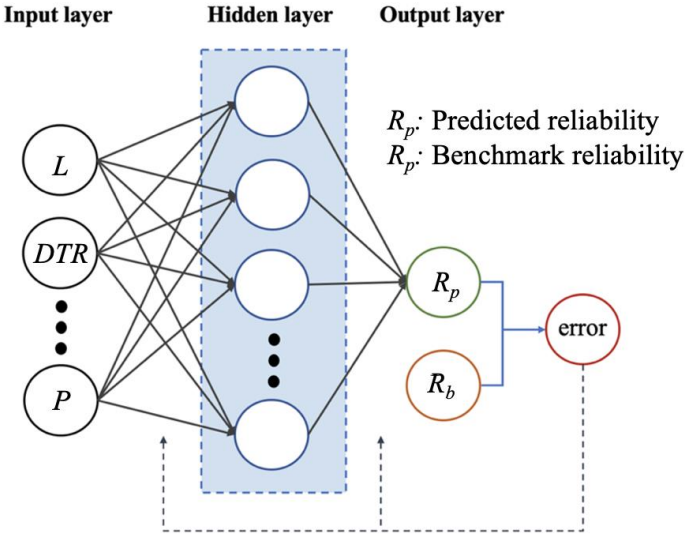

Figure 3-17 ANN model architecture.

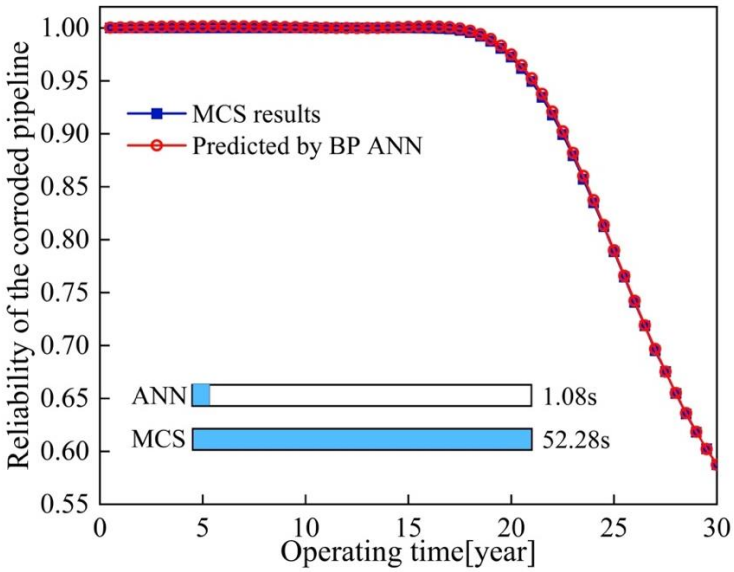

Figure 3-18 Comparison of the reliabilities assessed by MCS and the trained ANN.

Thus, assessing the pipeline's reliability with multiple adjacent corrosion defects through the trained ANN has remarkable merits. For example, the simulation results' accuracy is satisfactory, and the computing efficiency is reasonably high, addressing nonlinear

relationships among parameters becomes much easier. Moreover, the trained ANN could be updated once new data are obtained, making the ANN more flexible. These remarkable advantages make the trained ANN a powerful tool for conducting reliability analysis and subsequent maintenance management. Especially in situations where the corrosion condition of the pipeline is more complex, the artificial neural network method could greatly boost the performance of the reliability analysis.

3.5 Conclusions

This chapter proposes an integrated method for the reliability analysis of pipelines with multiple corrosion defects, considering the interacting effect and the interaction rule. The framework of the proposed method can be divided into two major procedures: interaction development and reliability analysis. A series of numerical simulation models of corroded pipelines were first established and validated to investigate the effects of corrosion depth and steel grade on the interacting effect and limit spacing distance. An orthogonal test was designed and performed to investigate the contributions of corrosion geometric features to the interacting effect and burst pressure. Performances of the existing interacting rules when estimating the limit spacing distance were discussed. Two new interaction rules considering corrosion depth and steel grade were developed based on the simulation results and regression analysis. Furthermore, burst pressure models, MCS, sensitivity analysis, feature scaling, and ANN were integrated to realize a more accurate and effective reliability analysis of pipelines with multiple corrosion defects. MCS was used to generate raw data for the ANN training. Besides, interaction rules' effects on the pipeline's reliability estimation with multiple corrosion defects were discussed. The sensitivity analysis was applied to simplify ANN's structure. Finally, a BP ANN is established and trained to improve computing efficiency. The conclusions are summarized as follows:

- Corrosion depth significantly impacts the interacting effect and burst pressure compared with corrosion length and width. With the increase of the corrosion depth,

the interacting effect between adjacent corrosion defects is enhanced.

- As the corrosion depth grows, the limit spacing distance shows an upward trend for the X65 and X80 pipelines. As DTR increases from 10% to 80%, the limit spacing distance growth of the X80 pipeline is more significant than that of the X65 pipeline.
- Existing interaction rules introduce conservatism or underestimation to the estimation of the limit spacing distance because they ignore the effects of the corrosion depth and steel grade. When the DTR exceeds 40%, K&V, CW, and ASME interaction rules underestimate the limit spacing distance. Based on simulation results and regression analysis, two new interaction rules considering the corrosion depth and steel grade were developed for better prediction accuracy.
- The interacting effect plays a vital role in the reliability analysis of corroded pipelines. For the case study in this chapter, the time lag between the maintenance time of the pipeline with isolated corrosion defects and that of the pipeline considering the interacting effect is more than 7.5 years. In addition, different interaction rules result in different reliability descending paths. Because the new interaction rule was developed for this case, it could provide a more accurate reliability analysis.
- Compared to other parameters, the pipeline's outer diameter causes the minimum total-effect index. Thus, it is screened out from the input variables of the ANN. The trained ANN shows excellent prediction accuracy and high computing efficiency. For the case study, the MSE of the predicted reliability estimated by the trained ANN is only 2.4×10^{-6}. The elapsed time needed for the ANN prediction in MATLAB is 1.08 s, while 52.28 s is required for the traditional MCS.

The proposed method and results of this chapter are beneficial for improving the integrity management of corroded pipelines. Future work should consider the effects of the surrounding environment, like temperature, traffic loading, and geological movement, to develop a more accurate reliability method for corroded pipelines.

Chapter 4. Failure analysis of corroded high-strength pipeline subject to hydrogen damage based on FEM and GA-BP neural network

4.1 Overview

At a time of increasing climate change, 195 countries and regions signed the Paris Agreement to pursue efforts to limit greenhouse gas (GHG) emissions and fight global warming [197]. According to the review proposed by the BP public limited company, in 2019, around 84% of the world's energy consumption was still fossil fuels, whose utilization leads to massive GHG emissions [198,199]. Thus, a transition to different energy sources is an urgent task for the world. As the most abundant element in the universe, hydrogen plays a vital role in the global energy transition process due to various advantages. During the hydrogen-burning process and electrochemical reaction, there is no carbon emission or any contaminant. As secondary energy, hydrogen is high in energy, and its calorific value is around 140.4MJ/Kg, which is 3~4 times larger than that of other common fuels. Hydrogen has rich application scenarios. It is also non-toxic and a clean energy carrier to transport and store energy. It can also be used as a medium to transform electric power, heating power, liquid fuel, and other energies to realize the collaborative optimization between different energy networks [200].

At present, gaseous hydrogen transportation is an effective approach used in the field because its technologies are more mature than other approaches. The use of pipelines and tube trailers are the two major ways to transport gaseous hydrogen. Since pipelines is an important means to achieve long-distance and large-scale hydrogen transportation, many countries started investigating and building hydrogen pipelines. According to the report, around 2500 Km of pipelines transporting hydrogen were constructed in the United States, while only 100 km were constructed in China. Hydrogen pipeline construction and

operation show great potential in the renewable energy industry. However, the one-time investment in a hydrogen pipeline is enormous. To be more specific, the overall operation cost hydrogen pipeline is 1.5-3 times larger than that of a pipeline transporting natural gas with the same energy flow [201]. Thus, using existing natural gas pipelines to transport hydrogen or a mixture gas of hydrogen and natural gas is a promising way to lower the cost of the early development stage [202,203]. Blending hydrogen into natural gas pipeline networks has been systematically investigated by Melaina et al. [204] and in the NaturalHy project [97]. With the existence of hydrogen, the combability between pipelines and hydrogen should be noticed. For polyethylene pipelines, hydrogen has a limited effect on material performance. Simultaneously, it will cause hydrogen embrittlement (HE) in pipeline steel, deteriorate material performance, and impair the bearing capacity [205]. However, natural gas pipelines made of steel are the most common. As shown in Figure 4-1, around 99.5% of transmission lines and 89.2% of gathering lines are made of steel in the United States. Thus, investigating the deteriorating effect of hydrogen on pipeline steels and ensuring pipelines' structural safety and operational reliability under a hydrogen environment are significant for developing the renewable energy industry.

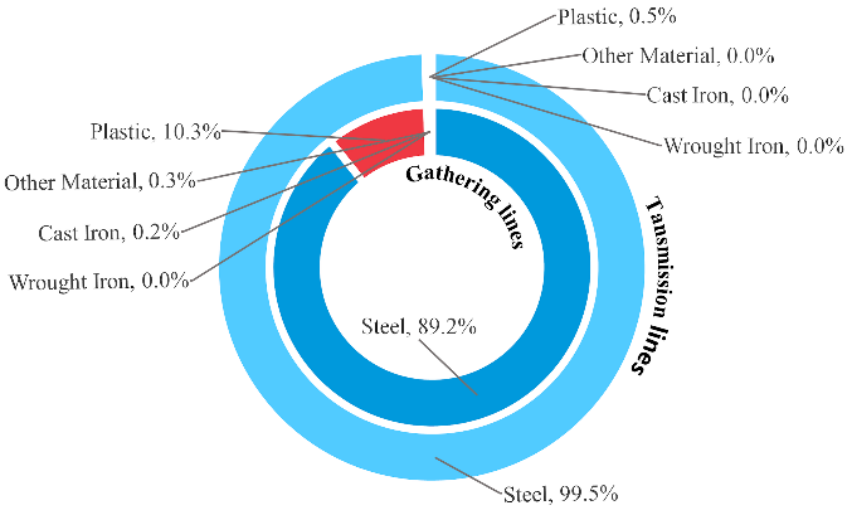

Figure 4-1 Proportions of pipe materials in gathering and transmission lines in the United States.

As a material loss defect caused by the surrounding environment, corrosion is regarded as

one of the most dominating pipeline damages. According to the statistics, corrosion accounts for 23% of pipeline failure causes, as shown in Figure 4-2. Due to the corrosion mechanism for steel pipelines, corrosions on the inner wall are almost inevitable. Corrosion defects could weaken a pipeline's bearing capacity and ultimately result in unexpected incidents like pipeline leakage and explosion. Although using existing natural gas pipeline networks to transport hydrogen has many benefits, corroded pipelines' mechanical behaviors in a hydrogen environment should be noted. With hydrogen damage, a noticeable loss in the pipe steel ductility could be observed [105], which could impair the bearing capacity and significantly impact the failure behaviors of corroded pipelines. Besides, blending hydrogen into the transmission medium could increase the risk of leakage and explosion because hydrogen could lower the ignition energy, accelerate the leak rate and increase the flammability range. In the scenario of using the evaluation system of a pipeline operating in normal conditions to assess pipelines in a hydrogen environment, unexpected failures might occur, resulting in disastrous environmental contamination, enormous economic losses, and horrible casualties. Hence, investigating failure behaviors and residual strength of the corroded pipeline suffering hydrogen damage is of great value for achieving a reliable and safe large-scale hydrogen supply.

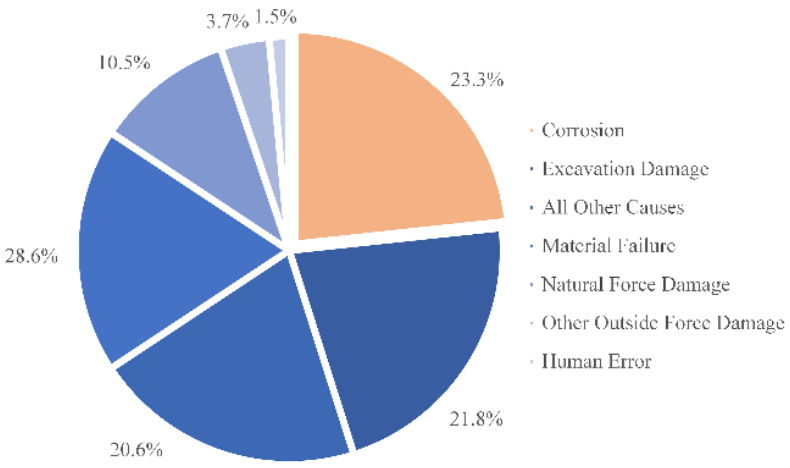

Figure 4-2 Pie chart of the causes of pipeline damage in the United States.

After years of research, scholars developed various theoretical models to estimate the burst

pressure of corroded pipelines based on experimental or finite element (FE) results, such as ASME B31G, modified B31G, PCORRC, RSTRENG, CPS, CSA Z662-07, DNV RP F-101, SHELL 92, etc. [70]. Burst pressure is usually used to define the residual strength of a corroded pipeline. The combined utilization of burst models and degradation models can be employed to conduct prognostic and health management for corroded pipelines [206]. Stochastic approaches, such as gamma, inverse Gaussian and Poisson square wave process, are commonly used to model the degradation process of pipeline corrosion defects [207,208]. The degradation model established by stochastic approaches could incorporate the effect of uncertainties [209]. Besides stochastic approaches, time series analysis techniques, like ARMA and ARIMA, are also widely used to analyze and predict the corrosion evolution of a pipeline based on the monitoring data [210]. Geometric features of the corrosion obtained by the degradation model or the time series analysis technique can then be applied in theoretical burst pressure models to estimate the residual strength. However, when the monitoring data of the corrosion growth is insufficient, the degradation process can't be precisely modeled. Since the controlling flow stress and the profile idealization of a corrosion defect are different, each theoretical burst pressure model's conservative level is different. Therefore, there is no single burst pressure model available for every situation. Choosing a proper burst pressure model to estimate a corroded pipeline's residual strength should take specific conditions into consideration. Although there are several valuable theoretical models for burst pressure estimation, barely any of them considers the effect of hydrogen damage. Hence, when it comes to using constructed pipelines to transport hydrogen, it is important to investigate a pipeline's failure behaviors after hydrogen damage. Nanninga et al. [211] compared the tensile properties of three pipeline steels in high-pressure gaseous hydrogen environments and air environments. It was found that a hydrogen environment could result in an obvious reduction in elongation at failure and ductility. Based on the experimental method, Briotte et al. [212] investigated the mechanical behaviors of X80 steel in a hydrogen environment. They observed an

obvious decrease in material toughness and an acceleration in fatigue crack growth. Ohaeri et al. [213] systematically studied the sources of hydrogen attack and the hydrogen-induced failure mechanism of pipelines and provided a detailed illustration of the electrochemical reaction process of pipeline corrosion. Based on the Tresca criterion and elastic theory, Chen et al. [214] proposed a novel burst pressure model that could store hydrogen under extremely low temperatures. Although many efforts have been put into the hydrogen pipeline field and many noteworthy research results have been obtained, very little research has been done to investigating failure behaviors and residual strength of full-scale high-strength corroded pipelines after hydrogen damage. The effect of hydrogen should be incorporated into the theoretical burst pressure model.

In this chapter, based on the experimental results from the tensile test of the X100 pipeline steel after hydrogen damage, a series of FE simulation models of the pipeline with isolated internal corrosion is established to investigate failure behaviors and the residual strength of the high-strength pipeline after hydrogen damage. Parametric analysis is employed to study how primary parameters affect the corroded pipeline's residual strength under different hydrogen damage levels. Several classical burst pressure models, including the ASME B31G model, ASME B31G Modified model, CSA Z662-07 model, DNV RP F-101 model, PCORRC model, Shell92 model, and RPA model, are applied to estimate the burst pressure of the corroded pipeline with the hydrogen effect and compared with the FE simulation results. Through the comparison, the Shell92 and CSA models have the best estimation performance for the X100 pipeline after hydrogen damage. A new burst pressure model considering hydrogen damage is proposed based on the simulation results through regression analysis. An orthogonal test is designed and performed to quantify the effect of the hydrogen. The results show that the contribution of the hydrogen damage is close to that of corrosion length.

Although the finite element method (FEM) has demonstrated excellent performance in solving problems with corroded pipelines, it is time-consuming. The artificial neural

network (ANN) method is a technology imitating how human brains analyze and process information. ANN has a powerful capacity to deal with complex and nonlinear relationships between multiple parameters while it has been applied in many pipe-related problems. Xu et al. [85] built a three-layer backpropagation (BP) ANN to predict the burst pressure of pipelines with single corrosion defects, and the prediction accuracy was satisfactory. Kumar et al. [66] trained an ANN based on FE results and used it to predict the burst pressure of the pipeline with single corrosion considering internal pressure and axial compressive stress. The combination of FEM and ANN could improve computing efficiency and lower the cost of calculation. However, previous research has not made significant investigations of simulation-driven ANN considering hydrogen damage. Genetic algorithm (GA) is a technology inspired by the process of natural selection that could be used to optimize the initial weights and threshold values of neural networks. To fill the gap, in this chapter, a GA-BP neural network considering corrosion features and hydrogen damage is established and trained based on the FE results to predict the burst pressure of the high-strength pipeline with internal corrosion. The trained GA-BP ANN can be applied to effectively and accurately estimate the residual strength of corroded pipelines after hydrogen damage.

In engineering practice, corrosion on pipeline walls often exists as corrosion colonies instead of occurring in isolation. The interacting effect between adjacent corrosion defects could influence the mechanical behaviors of the corroded pipeline. Han et al. [80] investigated the difference in mechanical behaviors between a pipeline with isolated corrosion and a pipeline with interacting corrosion defects based on the finite element analysis. The results show that the corroded pipeline's burst pressure decreases with the number of interacting corrosions. Sun et al. [81] also used the finite element analysis to study how the interaction effect between adjacent corrosions impacted the pipeline's burst pressure. It was found that the interaction effect decreases as the longitudinal spacing grows, and the circumferential spacing has a more negligible effect on the burst pressure. A

theoretical burst pressure model was developed by Benjamin and Cunha [191] to estimate the residual strength of the corroded pipeline considering the interaction effect. The limited spacing distance is the critical value determining if the interaction effect between corrosions should be taken into account when estimating the corroded pipeline's residual strength. Once the spacing distance is larger than the limited spacing distance, the interacting effect can be ignored. Like the DNV interaction rule, the Kiefner & Vieth interaction rule and the ASME interaction rule, various interaction rules have been developed and applied to assess successive corrosions' limited spacing distance [215]. Although there is much previous literature concerning the influence of the interacting effect on the corroded pipeline's residual strength, the impact of hydrogen damage on the interaction effect and limited spacing distance between adjacent corrosions has not been thoroughly addressed. Moreover, the interacting effect between a separated corrosion defect and a corrosion colony under hydrogen damage is hardly discussed. Thus, how hydrogen damage impacts the interaction effect, failure behaviors, and limited spacing distance of pipelines with multiple corrosions is of great value to be studied. A number of FE models of an X100 pipeline with multiple corrosions subject to different hydrogen damage levels are established and simulated to fill the gap. It is found that hydrogen damage could reduce the limited spacing distance between adjacent corrosions. The interacting effect and limited spacing distance between a separated defect and a corrosion colony are significantly affected by hydrogen damage.

In this chapter, several approaches, including the finite element method, regression analysis, orthogonal test, and artificial neural network method, are applied to investigate the effect of hydrogen damage on the failure behaviors, residual strength, and interacting effect between adjacent corrosions of the X100 pipeline with internal corrosions. First, a series of FE models are established and validated to investigate how the impact of the conjunction of hydrogen damage and corrosion affects the failure behaviors and residual strength of the high-strength pipeline transporting hydrogen. Second, a new burst pressure model

incorporating hydrogen damage is developed for the X100 pipeline based on the FE results and regression analysis. Third, a GA-BP neural network considering hydrogen damage is built and trained to accurately predict the corroded pipeline's residual strength and alleviate the burden of FEM calculation. Moreover, how the hydrogen damage influences the interacting effect and the limited spacing distance between multiple corrosions is also studied.

Section 4.2 introduces the failure criterion, typical idealization approaches for complex corrosion profiles, and several widely used burst models. Section 4.3 presents the material properties of the X100 after hydrogen damage, the built-up FE models, and the model validation. The results and discussion are presented in Section 4.4. The last section of this chapter gives conclusions.

4.2 Failure criterion and burst models

Corrosions on the internal pipeline wall will impair a pipeline's bearing capacity and result in local stress concentration. Burst models are usually used to estimate residual strength in terms of burst pressure. Some widely used burst models and the failure criterion selected in this chapter to determine the corroded pipeline's failure are introduced. In addition, commonly used idealization approaches are discussed.

4.2.1 Idealization approaches for complex corrosion profile

The complex shape of an actual corrosion defect on a pipeline wall could bring difficulties or even infeasibility to residual strength assessment. To make the theoretical estimation of the corroded pipeline's residual strength easy to perform, idealization approaches, as shown in Figure 4-3, are usually applied to simplify the corrosion defect profile [216]. Different idealization approaches would result in varying levels of conservatism to subsequent residual strength assessment.

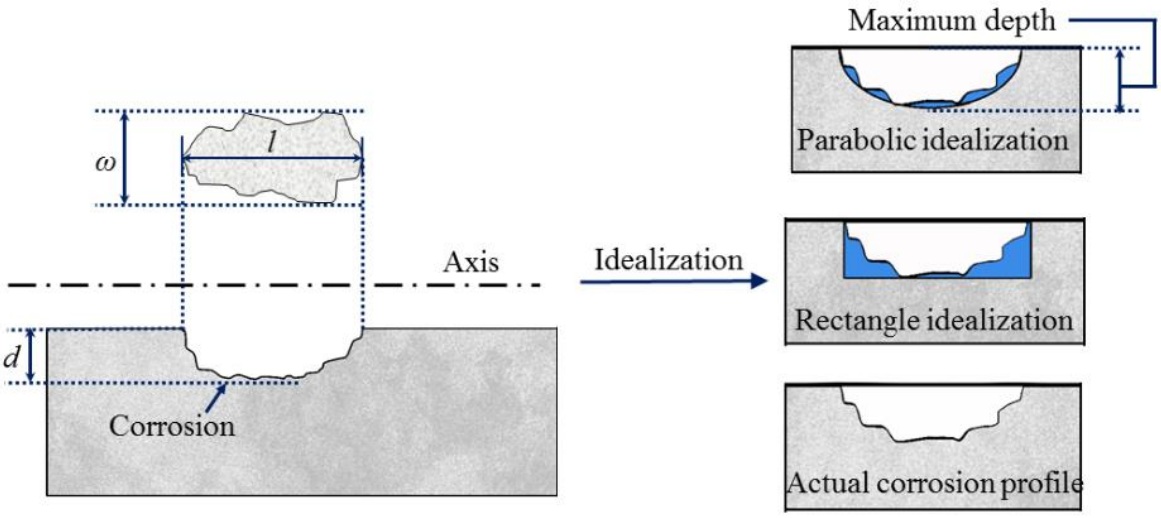

Figure 4-3 Idealization approaches for complex corrosion profile.

4.2.2 Failure criterion

Commonly, the failure of a corroded pipeline is defined as the tubular structure's bearing capacity that cannot reliably withstand the operating pressure. According to structural reliability theory, the limited state function (LSF) is applied to determine if a corroded pipeline is failed. The LSF used in this chapter is defined as follows [71]:

$$g = P_b - P_o \tag{4-1}$$

where P_o is the operating pressure, P_b is the burst pressure. Once the operating pressure exceeds the burst pressure, i.e., when $g < 0$, the corroded pipeline is failed and immediate maintenance action is needed; otherwise, the corroded pipeline is still safe.

4.2.3 Burst models

Developed from the NG-18 model, ASME B31G is one of the most widely used burst models in the energy industry. It incorporates simplified geometric features, which makes it more convenient to use. The ASME B31G burst model is defined as follows [217]:

$$P_b = \begin{cases} \frac{2t}{D}\left(1.1\sigma_y\right)\left[\frac{1-\frac{2}{3}\left(\frac{d}{t}\right)}{1-\frac{2}{3}\left(\frac{d}{t}\right)M^{-1}}\right], & \frac{l^2}{Dt} \leq 20 \\ \frac{2t}{D}\left(1.1\sigma_y\right)\left[1-\frac{d}{t}\right], & \frac{l^2}{Dt} > 20 \end{cases} \quad (4\text{-}2)$$

$$M = \sqrt{1 + 0.8\left(\frac{l^2}{Dt}\right)} \quad (4\text{-}3)$$

where t and D is the wall thickness and the diameter of the pipeline respectively, σ_y is the yield stress of the pipe steel, d is the corrosion's depth, M is the Folias Factor and l is the length of the corrosion.

To pursue a more accurate estimation of the burst pressure, the ASME B31G burst model was improved by two modifications, i.e., the controlling flow stress and shape-related factors. The expression of the ASME B31G Modified burst model is defined as follows [168]:

$$P_b = \frac{2t}{D}\left(\sigma_y + 69\right)\left[\frac{1-0.85\left(\frac{d}{t}\right)}{1-0.85\left(\frac{d}{t}\right)M^{-1}}\right] \quad (4\text{-}4)$$

$$M = \begin{cases} \sqrt{1 + 0.6275\left(\frac{l^2}{Dt}\right) - 0.003375\left(\frac{l^2}{Dt}\right)^2}, & \frac{l^2}{Dt} \leq 50 \\ 3.3 + 0.032\left(\frac{l^2}{Dt}\right), & \frac{l^2}{Dt} > 50 \end{cases} \quad (4\text{-}5)$$

The CSA Z662-07 burst model divides the pipelines into different types based on the yield stress of the pipe steel, i.e., high-grade steel ($\sigma_y > 241\text{MPa}$) and low-grade steel ($\sigma_y \leq 241\text{MPa}$). It is used to describe the plastic collapse at a surface corrosion defect. The CSA Z662-07 model is defined as follows [169]:

$$P_b = \begin{cases} e_1 P_{bi} + (1 - e_1)P - e_2\sigma_u, & \sigma_y > 241\text{MPa} \\ e_3 P_{bi} + (1 - e_3)P - e_4\sigma_y, & \sigma_y \leq 241\text{MPa} \end{cases} \quad (4\text{-}6)$$

$$P_{bi} = P\left[\frac{1-\left(\frac{d_a}{t}\right)}{1-\left(\frac{d_a}{t}\right)M^{-1}}\right] \quad (4\text{-}7)$$

$$P = \begin{cases} \frac{2t(0.9\sigma_u)}{D}, & \sigma_y > 241\text{MPa} \\ \frac{2t(1.15\sigma_y)}{D}, & \sigma_y \leq 241\text{MPa} \end{cases} \quad (4\text{-}8)$$

$$M = \begin{cases} \sqrt{1 + 0.6275\left(\frac{l^2}{Dt}\right) - 0.003375\left(\frac{l^2}{Dt}\right)^2}, & \frac{l^2}{Dt} \leq 50 \\ 3.3 + 0.032\left(\frac{l^2}{Dt}\right), & \frac{l^2}{Dt} > 50 \end{cases} \quad (4\text{-}9)$$

where e_1 is the deterministic model error, $e_1 = 1.04$, e_2 is an additive model error, $e_2 \sim N(-0.00056, 0.001469^2)$, e_3 is a deterministic multiplicative model error, $e_3 = 1.17$, e_4 is an additive model error, $e_4 \sim N(-0.007655, 0.006506^2)$, σ_u is the ultimate tensile strength of the pipe steel, P_{bi} is the calculated pressure strength, P is the pressure strength of the intact pipeline.

Based on the experimental and finite element simulation data, DET NORSKE VERITAS collaborated with BP Technology proposed the DNV RP F-101 burst model [57]. In this model, plastic collapse failure determines the corroded pipeline's defeat. The expression of the DNV RP F-101 can be defined as Eq. (4-10), and the 1.05 in the equation is generated by laboratory test comparison.

$$P_b = 1.05\frac{2t\sigma_u(1-\frac{d}{t})}{(D-t)(1-\frac{d}{t}M^{-1})} \quad (4\text{-}10)$$

$$M = \sqrt{1 + 0.31\left(\frac{l^2}{Dt}\right)} \quad (4\text{-}11)$$

The PCORRC burst model was proposed by Leis [58] by analyzing the simulation results from a set of finite element analyses. This model aims to estimate the pipeline's ultimate bearing capacity with blunt corrosion defects. The equation of the PCORRC model can be expressed as Eq. (4-12). The function in the bracket of Eq. (4-12) is defined as a Folias Factor. r is the radius of the pipeline.

$$P_b = \frac{2t\sigma_u}{D}\left\{1 - \frac{d}{t}\left[1 - \exp\left(-0.157\frac{l}{\sqrt{r(t-d)}}\right)\right]\right\} \quad (4\text{-}12)$$

The SHELL92 burst model was developed based on the ASME B31G model, and modifications were implemented to introduce a certain degree of conservativeness to burst pressure assessment. The SHELL92 burst model is defined as follows [170]:

$$P_b = \frac{2t(0.9\sigma_u)}{D}\left[\frac{1-(\frac{d}{t})}{1-(\frac{d}{t})M^{-1}}\right] \quad (4\text{-}13)$$

$$M = \sqrt{1 + 0.8(\frac{l^2}{Dt})} \tag{4-14}$$

The RPA burst model was also developed from the ASME B31G model by introducing a higher level of conservativeness to estimate the pipeline's residual strength with long corrosion defects. This model classifies corrosion defects into two different types, i.e., long corrosion ($\frac{l^2}{Dt} > 20$) and short corrosion ($\frac{l^2}{Dt} \leq 20$). The expression of the RPA burst model is defined as Eqs. (4-15~4-17) [171].

$$P_b = \frac{2t}{D}(\sigma_y + 69)\left[\frac{1-a(\frac{d}{t})}{1-a(\frac{d}{t})M^{-1}}\right] \tag{4-15}$$

$$M = \begin{cases} \sqrt{1 + 0.6275\left(\frac{l^2}{Dt}\right) - 0.003375(\frac{l^2}{Dt})^2}, & \frac{l^2}{Dt} \leq 20 \\ 2.1 + 0.7\left(\frac{l^2}{Dt}\right), & \frac{l^2}{Dt} > 20 \end{cases} \tag{4-16}$$

$$a = \begin{cases} 0.85, & \frac{l^2}{Dt} \leq 20 \\ 1 - 0.15(64 \times 10^6)\left(\frac{l^2}{Dt}\right)^6, & \frac{l^2}{Dt} > 20 \end{cases} \tag{4-17}$$

4.3 Numerical simulation model and materials

4.3.1 Process of hydrogen-induced damage

Figure 4-4 shows a schematic representation of the deterioration process in a steel pipeline caused by hydrogen. For steel pipelines transporting hydrogen or the mixture of natural gas and hydrogen, hydrogen molecules are absorbed on the pipeline wall's surface [103]. Then, atomic hydrogen will ingress into the pipeline steel from the hydrogen or hydrogen-producing species, like hydrogen sulfide [218]. Once atomic hydrogen is absorbed into the steel, it diffuses by the interstitial mechanism. Some of the absorbed atomic hydrogens typically gather in the void structure. Once the hydrogen increases to a certain amount, molecularization happens, and the local pressure in the void dramatically increases, which could cause void expansion [219]. Trap sites such as dislocations, grain boundaries, defects,

and alloying elements in the steel strongly impact the degradation in the pipeline induced by hydrogen. The formation of coalescences with defects occurs due to reduced mobility and cohesive energy caused by hydride, carbide, and hydride segregations forming in dislocations or along the grain boundaries [220].

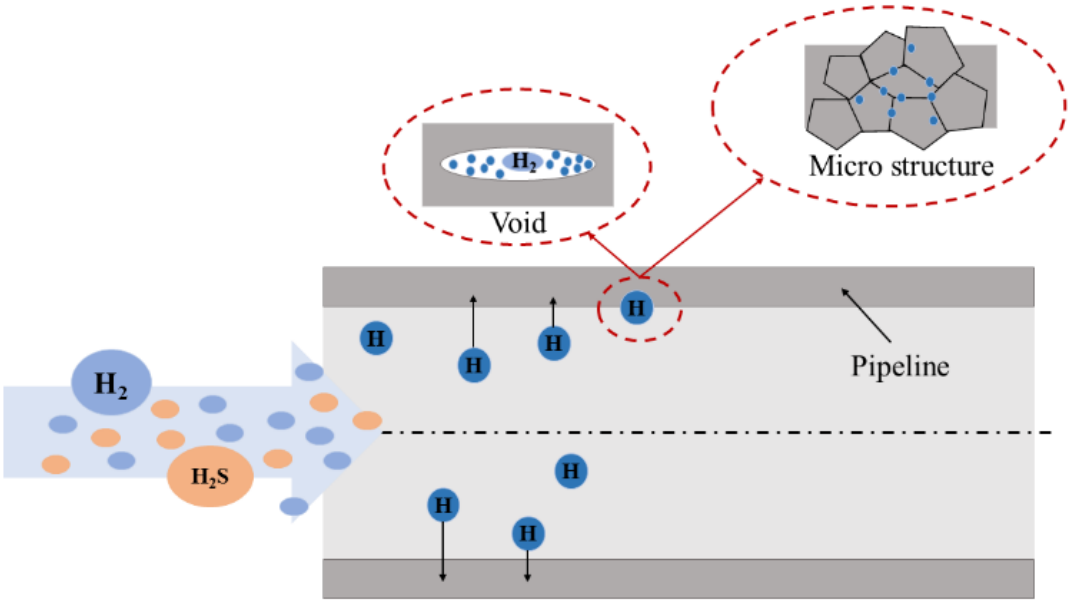

Figure 4-4 The deterioration process in a steel pipeline caused by hydrogen.

4.3.2 Material properties of X100 steel after hydrogen damage

X100-grade steel is a kind of high-strength steel that has been applied to make pipelines for large-scale and long-distance transmission. Because of its high strength, X100 steel can limit wall thickness under high pressure, which is beneficial for cost reduction. According to previous research, the cost of making hydrogen pipelines from high-strength steel only accounts for 60%-90% of the cost of making hydrogen pipelines from low-strength steel. In this chapter, the X100 pipeline is selected as an example to explore the hydrogen damage effect on the corroded high-strength pipeline's failure behaviors and residual strength. However, pipe steel becomes more sensitive to hydrogen embrittlement once the steel strength grows. Therefore, it is necessary to investigate the material properties of the X100 steel under a hydrogen environment and how these properties affect the pipeline's failure

behaviors with internal corrosion defects.

Through tensile test and electrochemical hydrogen charging, Wang [221] studied the effect of hydrogen on the mechanical properties of X100 steel. The stress-strain curves of the X100 steel under different hydrogen charging times are shown in Figure 4-5. With the increase of the hydrogen charging time, the hydrogen concentration in the steel increases, which decreases the elongation at failure and the strength of the pipe steel. With detailed information about the impairment in X100 steel's plasticity and strength provided by the electrochemical hydrogen charging and tensile test, the constitutive model of the X100 steel after hydrogen damage can be obtained, which can be used to describe the material properties in Abaqus.

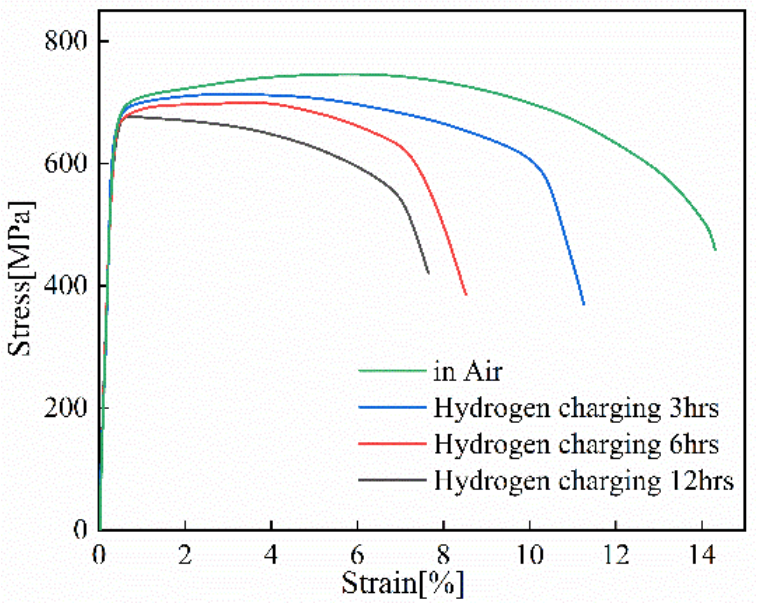

Figure 4-5 Stress-strain curves of pipeline steel under different hydrogen charging times.

4.3.3 Numerical simulation model

The FEM has demonstrated good performance in analyzing the mechanical behaviors of the pipeline with corrosion defects, which involves geometrical nonlinearity and material nonlinearity. Compared to full-scale experiments on corroded pipelines, FEM is more efficient, the cost is relatively low, and the simulation accuracy is satisfactory. Thus, in this

chapter, FEM is applied to investigate the corroded pipeline's failure behaviors considering hydrogen damage. The 3D numerical simulation model of the X100 pipeline with a single internal corrosion defect is shown in Figure 4-6. The model is established in Abaqus 14.

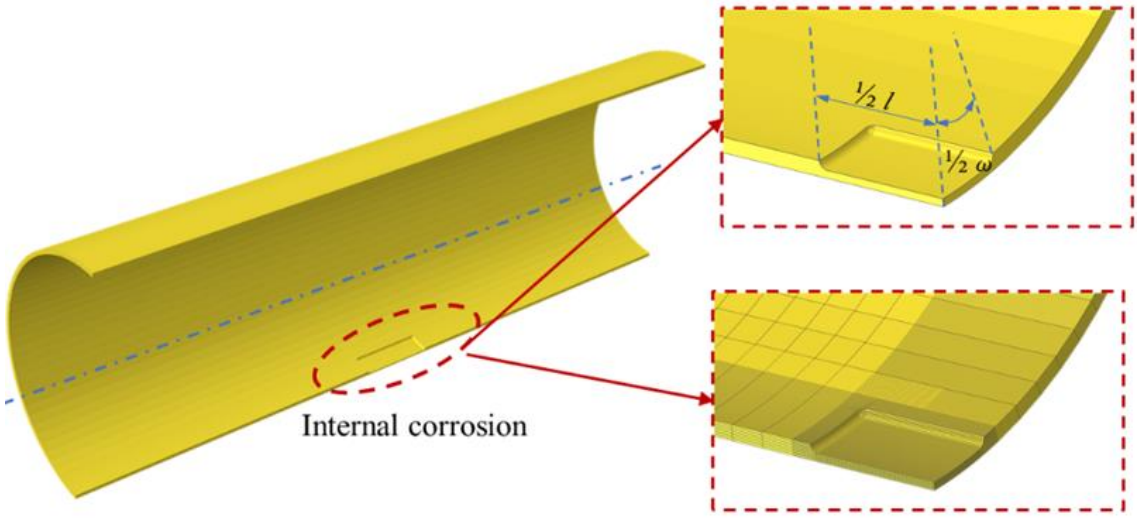

Figure 4-6 Numerical simulation model of the pipeline with single internal corrosion.

Since the geometric features and the applied load of the corroded pipeline is symmetric, a quarter model of the corroded pipeline is established to improve the computing efficiency and lower the simulation cost. In doing so, the accuracy of the simulation results will not be impaired. Table 4-1 lists the geometrical features of the X100 pipeline and the corrosion defect. The corrosion defect is located on the pipe's internal wall. To make the research more feasible, some reasonable assumptions are made:

(1) The corrosion structure is simplified as a rectangular shape combined with smooth rounding.

(2) Only internal pressure is taken into consideration.

The simulation model of the corroded pipeline is meshed by eight-node and hexahedron elements. The quality of meshes is a significant factor impacting the accuracy of simulation results. Thus, the meshes near the corrosion area are refined, while other pipeline areas are relatively coarsely meshed to improve simulation accuracy and computing efficiency. A mesh stability analysis is conducted to determine the reliable and efficient mesh size, as shown in Figure 4-7. When the number of elements is larger than 40448, the maximum

Von Mises stress of the corrosion defect becomes stable, which indicates simulation results become independent of the number of meshes. Thus, the mesh size for the defect area is 3 mm while the mesh size for other regions is 50 mm, i.e., the total number of meshes is 40448.

Table 4-1. Geometrical features of the X100 pipeline and the corrosion defects.

X100 pipeline			Corrosion defect		
Diameter (mm)	Length (mm)	Wall thickness (mm)	Length (mm)	Width (°)	Depth (mm)
1320	4000	22.9	400	20	11.45

The feasibility and reliability of utilizing FEM in residual strength estimation of the corroded pipeline are typically verified against relevant experimental results. In this chapter, the four pipeline burst experiments performed in [23] and [222] are chosen to make a comparison with FE simulation results, including single corrosion and multiple corrosion defects. Based on the experiments, four numerical simulation models are established, whose establishment procedure is the same as that of the FE model of the hydrogen pipeline. The relative error between the results obtained by finite element simulation and the experimental results is defined as Eq. (4-18). Figure 4-8 shows the comparison of the burst pressure estimated by our FE models with the experimental burst pressure. The average relative error of these four cases is only 3.736%, which indicates the excellent performance of FEM.

$$Error\_r(\%) = \left(\left|P_{FEM} - P_{b,t}\right|/P_{b,t}\right) \times 100\% \tag{4-18}$$

where P_{FEM} is the burst pressure calculated by the FEM, $P_{b,t}$ is the actual burst pressure obtained by the experiment.

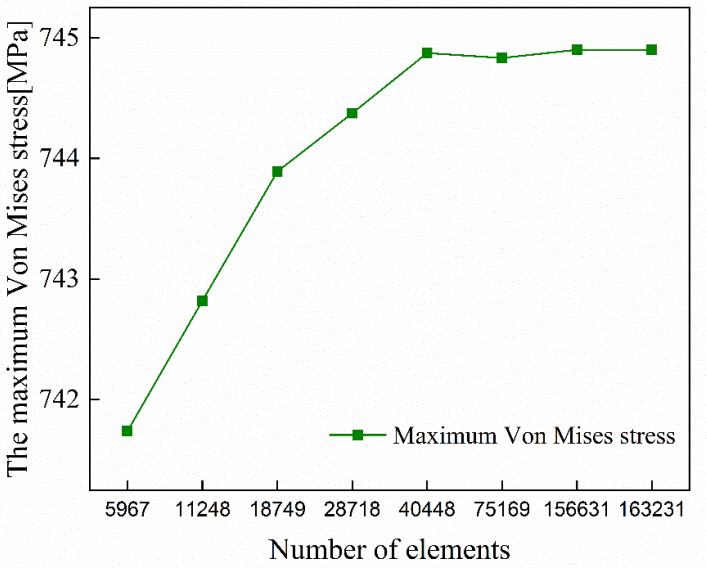

Figure 4-7 Results of mesh stability analysis.

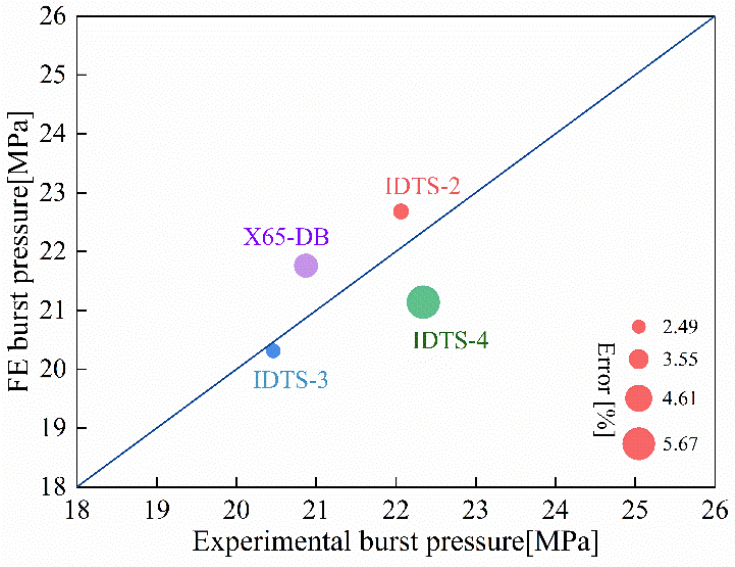

Figure 4-8 Comparison of FE burst pressure with experimental burst pressure.

4.4 Simulation results and discussion

The material properties of X100 steel are changed after hydrogen damage, resulting in different failure behaviors and residual strength of the corroded X100 pipeline. Figure 4-9 (a) shows the variation of the maximum Von Mises stress of the intact X100 pipeline under different hydrogen charging times. Before the operation pressure reaches 24 MPa, the

maximum Von Mises stress of the intact X100 pipeline linearly increases as the operating pressure grows with or without hydrogen damage. The ultimate bearing capacity before the intact pipeline's structural instability decreases with the increase of the hydrogen charging time. The difference between the ultimate bearing capacity before the X100 pipeline's structural instability operating in air and that of the X100 pipeline after 12 hours of hydrogen charging is around 3.5MPa. Thus, simply ignoring hydrogen damage in pipe steel could lead to unexpected failures. The Von Mises stress change curves of the X100 pipeline with internal corrosion, whose geometric features are described in Table 4-1 under different hydrogen charging times are shown in Figure 4-9(b). With the increase of the operation pressure, the maximum Von Mises stress grows. In the linear growth phase, the maximum Von Mises stress of the defected pipeline increases much faster than that of the intact pipeline. After the linear growth phase, the maximum Von Mises stress growth rate decreases as hydrogen charging time grows. With hydrogen damage, the ultimate bearing capacity of the defected pipeline before the structural instability is weakened. Compared to the intact pipeline, the difference between the ultimate bearing capacity before the structural instability of the defected pipeline operating in the air and that of the X100 pipeline after 12 hours of hydrogen charging is expanded to 4.8MPa.

Von Mises distributions of the X100 pipeline with single internal corrosion subject to hydrogen damage under different operating pressures are shown in Figure 4-10. With the increase of the operation pressure, the high-stress area first appears on the edges of the defect, then grows to the defect center, and ultimately expands to the areas around the defect. Before 14.4 MPa, the Von Mises distributions' change rules under different hydrogen damages are very similar. When the hydrogen charging time is 12 hours and the operating pressure is 16.8 MPa, the defect center's high-stress area disappears due to structural instability. Figure 4-11 shows variations of equivalent plastic strain (PEEQ) and the plastic strain distribution of the corroded pipeline subject to different hydrogen charging times. Before the operation pressure reaches 10 MPa, no plastic deformation

occurs to the corroded pipeline, no matter the hydrogen charging condition. After that, the growth rate of PEEQ grows with the increase in hydrogen charging time. For the X100 corroded pipelines under an air environment, with 3-hour hydrogen charging and 6-hour hydrogen charging, the plastic strain expands from the defect edges to the defect center. When the hydrogen charging time is 12 hours, no apparent plastic strain occurs on the defect center. With the increase of the hydrogen charging time, the maximum PEEQ decreases, which indicates the loss in the plasticity of the corroded pipeline due to the hydrogen damage.

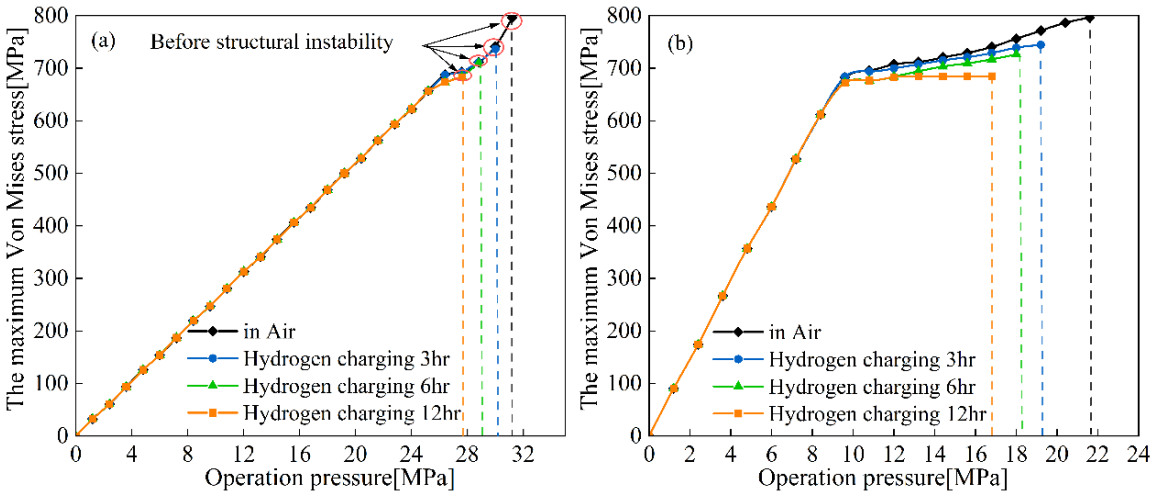

Figure 4-9 Variation of the maximum Von Mises stress with operation pressure under different hydrogen charging times for an (a) intact X100 pipeline, and (b) X100 pipeline with internal corrosion.

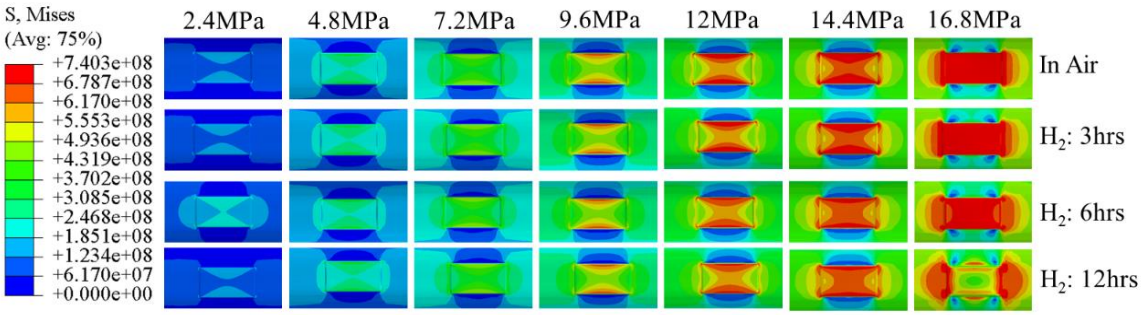

Figure 4-10 Von Mises stress distributions of an X100 pipeline with single internal corrosion subject to different hydrogen damage.

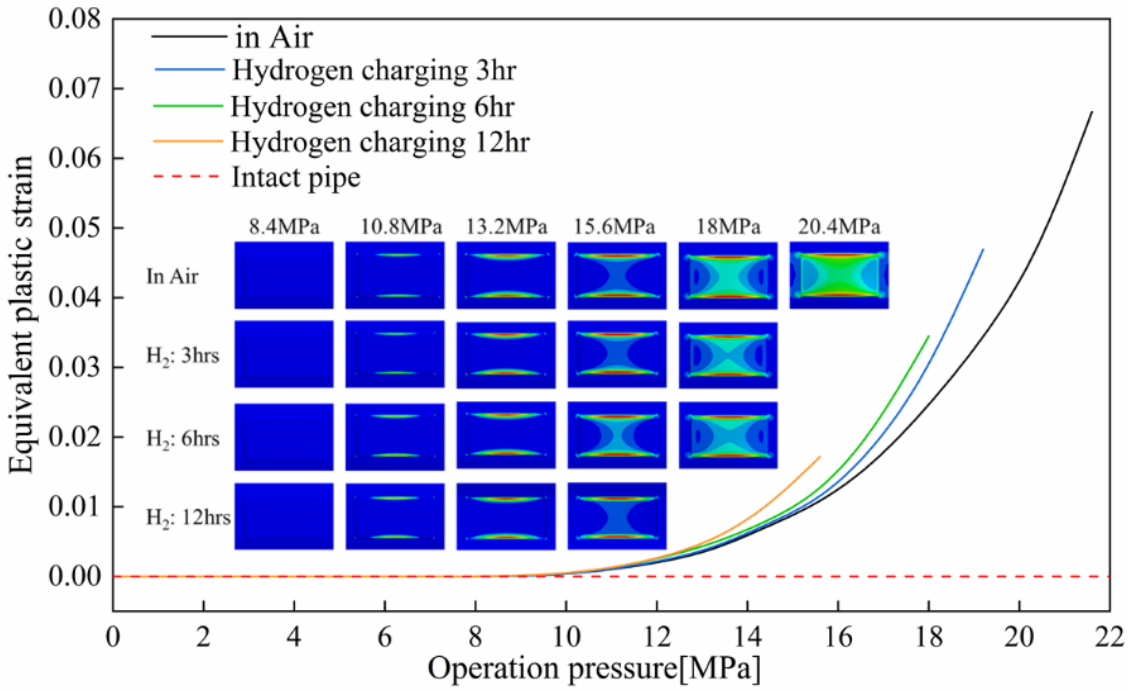

Figure 4-11 Variation of the PEEQ with operation pressure under different hydrogen charging times.

4.4.1 Parametric analysis

4.4.1.1 Effect of corrosion length

The geometric features of the X100 corroded pipeline listed in Table 4-1 are set as the default values that are used to establish numerical simulation models. Failure pressure and discrepancy of the X100 corroded pipeline subject to hydrogen damage under different corrosion lengths are shown in Figure 4-12. Hydrogen damage does not impact the change rule of the failure pressure versus the corrosion length. When the corrosion length is smaller than 300mm, the residual strength of the corroded pipeline decreases rapidly with the growth of the corrosion length. Meanwhile, the failure pressure's growth rate significantly reduces when the corrosion length is larger than 300mm. Hydrogen damage can impair the residual strength of the high-strength pipeline with corrosion. When hydrogen charging time is 3 hours and 6 hours, hydrogen damage has a similar influence on the failure pressure.

The discrepancy, which is defined as Eq. (4-19), is applied to represent the difference between the failure pressure of the corroded pipeline considering hydrogen damage and that of the corroded pipeline in the air. The maximum discrepancy always appears when the hydrogen charging time is 12 hours, which indicates an apparent loss in the residual strength of the corroded pipeline. For the 12-hour hydrogen charging situation, the discrepancy is large, close to 40%, when the corrosion length is smaller than 400 mm. After 400 mm, the discrepancy becomes more stable.

$$D_e = \frac{P_{air} - P_{H2}}{P_{air}} \times 100\% \tag{4-19}$$

where D_e is the discrepancy, P_{air} is the burst pressure of the corroded pipeline in air, P_{H2} is the burst pressure of the corroded pipeline considering hydrogen damage.

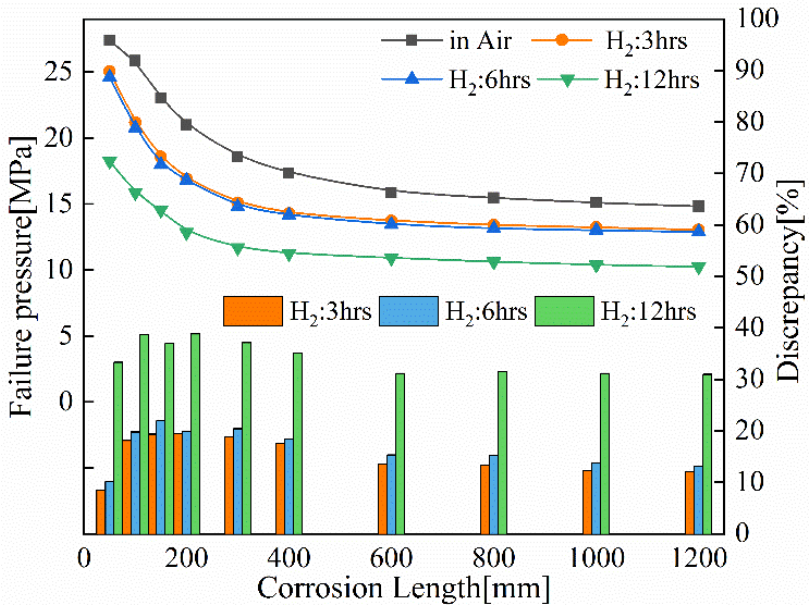

Figure 4-12 Failure pressure and discrepancy of the X100 corroded pipeline subject to hydrogen damage under different corrosion lengths.

4.4.1.2 Effect of corrosion width

As a parameter used to describe a defect's geometric features, corrosion width needs to be investigated to determine its impact on the residual strength of the pipeline. Figure 4-13 shows the failure pressure and relevant discrepancy of the X100 corroded pipeline subject

to hydrogen damage under different corrosion widths. With the increase of the corrosion width, the failure pressure of the corroded pipeline slightly decreases with or without hydrogen damage. When the hydrogen charging time is 3 hours or 6 hours, the discrepancy is around 20%, almost half of the discrepancy when the hydrogen charging time is 12 hours. The discrepancy is almost unchanged with the variation in the corrosion width no matter how long the hydrogen charging time is, indicating that the effect of the corrosion width on the failure pressure is relatively insignificant, which conforms to previous research [223]. Therefore, the ignorance of the corrosion width in previous burst models can be validated as reasonable.

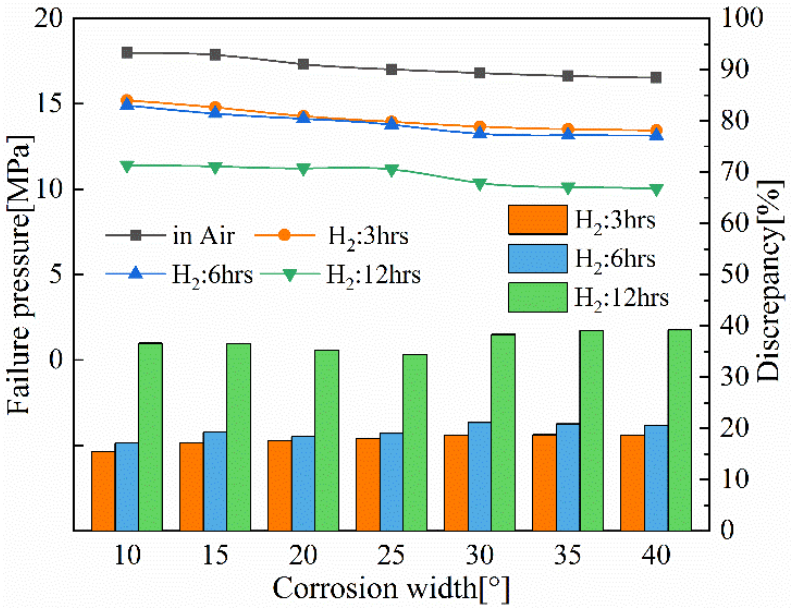

Figure 4-13 Failure pressure and discrepancy of the X100 corroded pipeline subject to hydrogen damage under different corrosion widths.

4.4.1.3 Effect of wall thickness

Failure pressure and the relevant discrepancy of the corroded pipeline after hydrogen damage under different pipeline wall thicknesses are shown in Figure 4-14. The corroded pipeline's failure pressure grows linearly with the increase of the wall thickness with or without hydrogen damage, which indicates that the rise in the wall thickness enhances the

corroded pipeline's structural reliability. When the wall thickness is 10mm, the corroded pipeline's failure pressures under these four hydrogen damage situations are close. The discrepancy between the failure pressure of the corroded pipeline in air and that of the corroded pipeline considering hydrogen damage becomes larger with the increase of the wall thickness. Thus, especially for thick-walled tubular structures, the effect of hydrogen damage on the residual strength cannot be ignored. The growth rate of the failure pressure versus the wall thickness decreases with the hydrogen charging time.

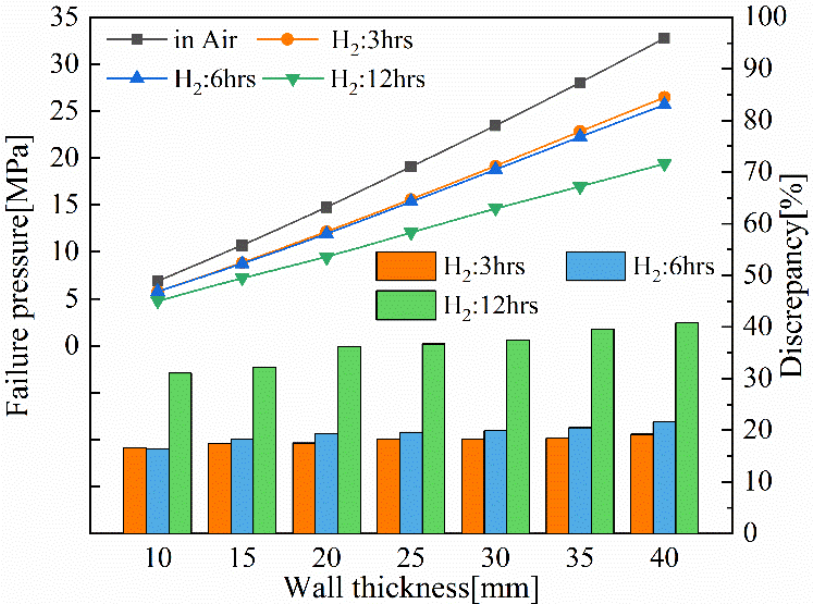

Figure 4-14 Failure pressure and discrepancy of the X100 corroded pipeline subject to hydrogen damage under different wall thicknesses.

4.4.1.4 Effect of corrosion depth to wall thickness ratio

The corrosion depth to wall thickness ratio is defined by Eq. (4-20). Once the depth to thickness ratio (DTR) equals 1, the pipeline will be penetrated by the corrosion defect, and leakage will occur. To avoid unexpected leakage, the allowable DTR is usually set as 0.8 [224]. The effects of DTR and hydrogen charging time on the corroded pipeline's failure pressure are investigated. Figure 4-15 shows the failure pressure and the relevant discrepancy of the corroded pipeline after hydrogen damage under different DTRs. A

significant loss in the corroded pipeline's residual strength can be observed as DTR grows with or without hydrogen damage. When the hydrogen charging time is 12 hours, about 80% of the residual strength loses due to the wall thinning (DTR from 0.1 to 0.8). When the pipeline works in the air or under the 3-hour\6-hour hydrogen charging conditions, the failure pressure's growth rates are close. With the increase of the DTR, the discrepancy between the failure pressure of the pipeline in the air and that of the pipeline after hydrogen damage gradually grows. When the DTR is 0.8, the burst pressures of the corroded pipeline with 3 or 6 hours of hydrogen charging are close to those of the pipeline with 12 hours of hydrogen charging.

$$\mathrm{DTR} = \frac{d}{t} \tag{4-20}$$

where DTR is the corrosion depth to wall thickness ratio.

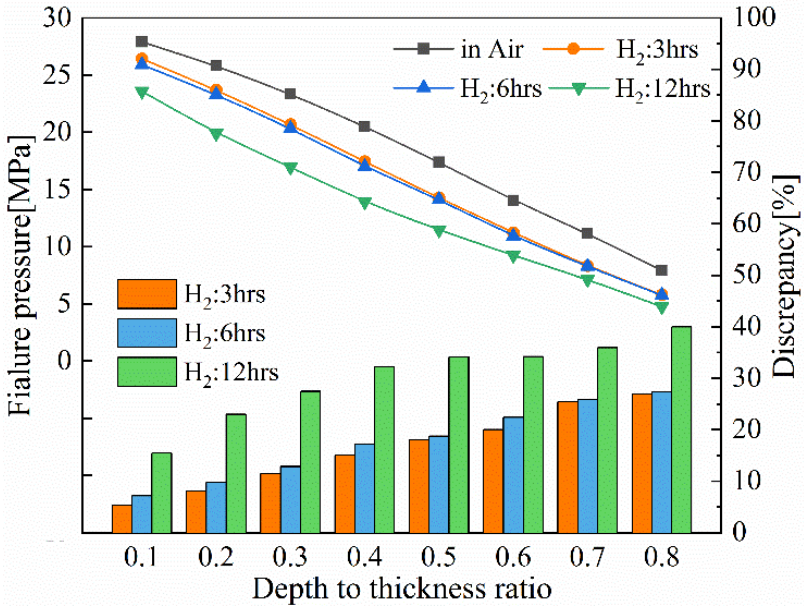

Figure 4-15 Failure pressure and discrepancy of the X100 corroded pipeline subject to hydrogen damage under different DTRs.

4.4.2 Estimation performance of burst models considering hydrogen damage

Based on experimental methods or the finite element method, many burst models, such as

the NG18 model, ASME B31G model, DNV model, etc., have been developed to assess the corroded pipeline's residual strength. It is convenient to use a theoretical burst model to predict the burst pressure. However, no theoretical burst model could be suitable for every case. Hydrogen damage could impact the failure behaviors and residual strength of the corroded pipeline. However, for most of the widely used burst models, the effect of hydrogen damage is not considered. Six typical theoretical burst models, including the ASME B31G Modified model, CSA Z662-07 model, DNV RP F-101 model, PCORRC model, SHELL92 model, and RPA model, are selected to investigate the estimation performance when hydrogen damage in the pipe steel is considered. Finite element analysis results are applied as references because the FE results' accuracy has been validated above. In Ref. [225], the error in the burst pressure estimated by theoretical models is much higher than that estimated by FEM. Thus, FEM results are more reliable and accurate. One hundred FE models of the X100 pipeline with single internal corrosion are established and simulated. Four hydrogen conditions are considered, i.e., hydrogen charging of 0 hours, 3 hours, 6 hours, and 12 hours. The relative error is employed to represent the deviation between the burst pressure estimated by the burst model and that estimated by FEM. The relative error is expressed by Eq. (4-21). The relative errors of the burst pressures estimated by these burst models under different hydrogen conditions are listed in Appendix A-D. The estimation performance of a burst model in each hydrogen condition is quantified by the normalized root mean square error (NRMSE), which is defined as Eq. (4-22). Figure 4-16 shows the NRMSE of burst pressures estimated by different burst models under different hydrogen conditions. For the ASME B31G model, ASME B31G Modified model, DNV model, PCORRC model, and RPA model, NRMSE grows with increased hydrogen charging time. Compared with the other four models, the Shell92 model and CSA model have better estimation performance when hydrogen damage is considered. However, the Shell92 model has the worst estimation performance when there is no hydrogen damage in the steel. When the hydrogen charging time is 12 hours, the ASME B31G Modified model

shows the worst performance, and the NRMSE exceeds 0.6, which is almost three times larger than the NRMSE caused by the Shell92 model. The following sequence by the estimation performance: the shell92 model, CSA model, PCORRC model, DNV model, RPA model, and ASME B31G Modified model.

$$RE = \frac{P_{FEM} - P_{model}}{P_{FEM}} \times 100\% \tag{4-21}$$

where RE is the relative error, P_{FEM} is the burst pressure obtained through FEM, P_{model} is the burst pressure estimated by burst models.

$$NRMSE = \frac{RMSE}{\overline{P_{FEM}}} = \frac{1}{\overline{P_{FEM}}} \times \sqrt{\frac{\sum_{i=1}^{i=n}(P_{FEM,i} - P_{model,i})^2}{n}} \tag{4-22}$$

where *NRMSE* is the relative root mean square error, $RMSE$ is the root mean square error, $\overline{P_{FEM}}$ is the mean value of the burst pressures obtained through FEM, n is the number of simulation cases in specific hydrogen conditions.

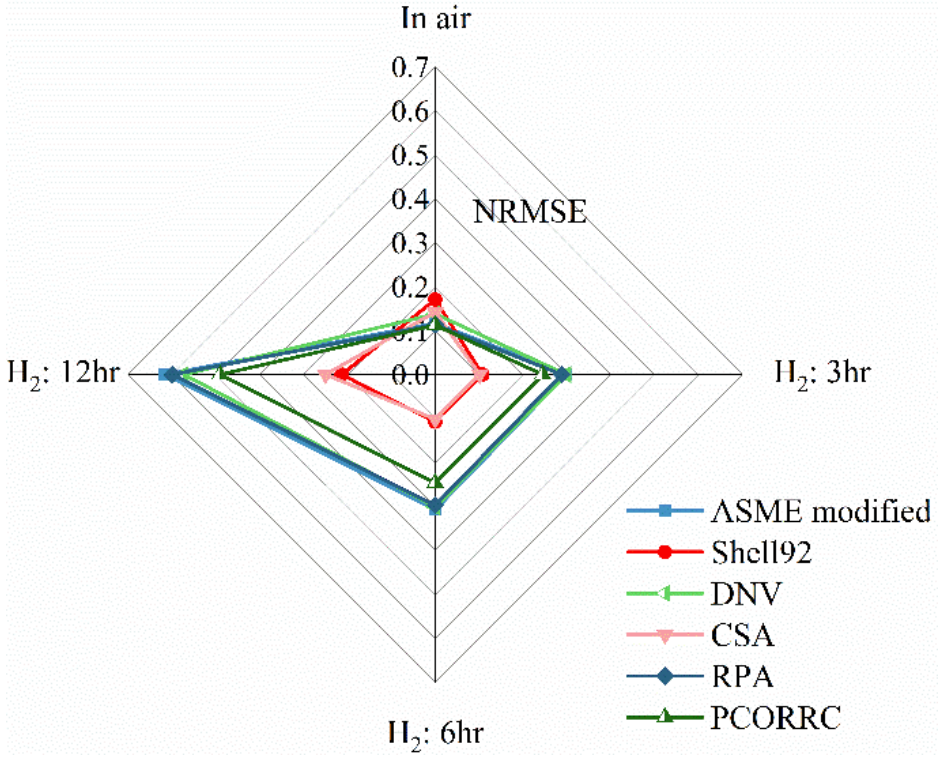

Figure 4-16 NRMSE of burst pressures estimated by burst models under different hydrogen conditions.

4.4.3 New burst model considering hydrogen damage

Although the Shell92 model has the best performance of estimating the burst pressure of the high-strength corroded pipeline subject to hydrogen damage, it does not incorporate a factor that quantifies hydrogen damage. Thus, a new burst model is developed through regression analysis and FE simulation results to include the hydrogen damage in high-strength pipeline steel. The new burst model is expressed by Eqs. (4-23~4-25). The regression analysis results show that the R-squared value is close to 1, indicating good goodness of fit.

$$P_b = \frac{2t(0.9\sigma_u)\times f_{H2}}{D}\left[\frac{1-\left(\frac{d}{t}\right)}{1-\left(\frac{d}{t}\right)M^{-1}}\right] \tag{4-23}$$

$$M = \sqrt{1 + 0.8\left(\frac{l^2}{Dt}\right)} \tag{4-24}$$

$$\mathrm{f}_{H2} = 1.18736 - 0.08311 \times \mathrm{T}_{\mathrm{H2}} + 0.01541 \times {\mathrm{T}_{\mathrm{H2}}}^2 - 0.0008927 \times {\mathrm{T}_{\mathrm{H2}}}^3 \tag{4-25}$$

where f_{H2} is the hydrogen damage factor used to quantify the hydrogen damage effect, T_{H2} is the hydrogen charging time. Due to the assumptions of failure criteria and corrosion geometry, there could be some level of conservatism. Thus, the constant in Eq. (4-25) can be used to calibrate the burst model when the hydrogen charging time is zero.

4.4.4 GA-BP neural network

It has been demonstrated that the artificial neural network approach has a powerful ability to solve problems with complex and nonlinear relationships between multiple parameters. For BP ANN, the initial weights and threshold values in the connections between neurons usually are determined randomly and then adjusted from a local angle, which could easily lead to local optimum. Therefore, such a demerit should be overcome to improve the performance of a BP ANN. GA is usually employed to optimize the initial weights and threshold values of the BP ANN. Genetic algorithm has many features, such as the objective function's values are used as searching information, the searching process is at a

global level, probabilistic search technology is applied, and so on [226]. In this chapter, a GA-BP neural network with a three-layer structure is established to predict the high-strength corroded pipeline's burst pressure considering hydrogen damage. Figure 4-17 shows the build-up GA-BP neural network. Four neurons are in the input layer, including corrosion length, DTR, wall thickness, and hydrogen charging time. The output of the GA-BP neural network is the burst pressure. Since the magnitude of these parameters is different, the normalization process is commonly used to ensure parameters are on a similar scale, improving the accuracy and efficiency of the ANN training. The FE simulation results of the X100 corroded pipeline with hydrogen damage are used to train and test the build-up GA-BP neural network. The data set contains 100 data points, in which 80% of the data are used as training data, and 20% of the data are used as testing data. Three burst tests in the orthogonal test, including test no.9, no.14, and no.15, are selected to validate the GA-BP ANN. The results show that the average error of GA-BP ANN is 5.78%, while that of BP ANN is 9.34%, which indicates the excellent performance of the GA-BP ANN. Once the training data becomes more plentiful, predicting accuracy could be further improved.

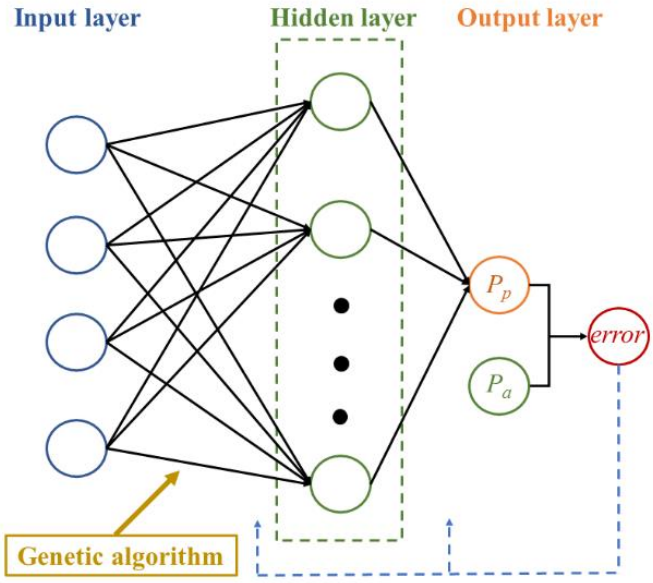

Figure 4-17 The build-up GA-BP neural network.

4.4.5 Orthogonal test

For multiple-parameter and multiple-level problems, exhaustive testing of every possible input to the systems is time-consuming and expensive. To solve such a problem, the orthogonal test has been developed and proven efficient and cost-effective. In the orthogonal test, representative factor levels are selected and permutated to obtain unique pieces of information that can be gathered to get the information provided by exhaustive testing.

An orthogonal test is designed and performed to investigate the effects of critical parameters on the burst pressure of the corroded high-strength pipeline. Based on the conclusion that the corrosion width has an insignificant impact on a corroded pipeline's residual strength, the critical parameters applied in the orthogonal test are wall thickness, DTR, corrosion length, and hydrogen charging time. The relevant burst pressure is the test index. A $L_{16}(4^4)$ orthogonal test is designed, and the testing results are listed in Table 4-2.

Range analysis is applied to the orthogonal test results to estimate the contribution of each key parameter on the residual strength of the X100 corroded pipeline. Range value can reflect the test index's variation caused by the variation in input (parameter). The bigger the range value is, the more critical the relevant input is. Figure 4-18 shows the range values of wall thickness, DTR, corrosion length, and hydrogen charging time. It is evident that wall thickness has the most significant contribution to the corroded pipeline's residual strength. Meanwhile, hydrogen charging time has the most minor contribution. However, the range value of hydrogen charging time is close to that of corrosion length, which is a critical parameter affecting a corroded pipeline's failure behaviors and residual strength in previous research. Therefore, when researching burst behaviors and residual strength of corroded pipelines, the effect of hydrogen damage cannot be simply ignored. Otherwise,

inaccuracies will be introduced into the residual strength estimation and further reliability analysis, resulting in unexpected failures and accidents.

Table 4-2. $L_{16}(4^4)$ orthogonal test.

Test Number	Wall Thickness(mm)	DTR	Corrosion length(mm)	H_2 charging time(hr)	Burst pressure (MPa)
1	10	0.1	70	0	12.543
2	10	0.4	200	3	7.571
3	10	0.6	400	6	4.578
4	10	0.8	600	12	2.37
5	20	0.1	200	6	22.851
6	20	0.4	70	12	14.778
7	20	0.6	600	0	11.175
8	20	0.8	400	3	4.674
9	30	0.1	400	12	28.884
10	30	0.4	600	6	21.375
11	30	0.6	70	3	29.078
12	30	0.8	200	0	12.643
13	40	0.1	600	3	45.367
14	40	0.4	400	0	37.806
15	40	0.6	200	12	19.958
16	40	0.8	70	6	36.37

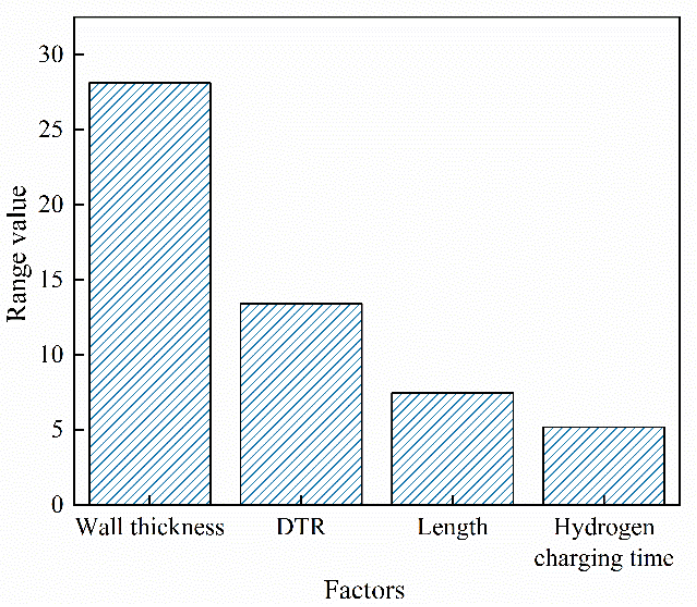

Figure 4-18 Range values of key parameters.

4.4.6 Effect of hydrogen damage on multiple corrosion defects

The 3D model of the X100 pipeline with two corrosion defects built in Abaqus is shown in Figure 4-19. The adjacent corrosion defects are longitudinally aligned on the internal wall of the pipeline. l_s is the spacing distance between adjacent corrosions. l_1 and l_2 are the corrosion length for corrosion 1 and corrosion 2, respectively. In this chapter, the adjacent corrosions are assumed as identical. The geometric features of the corrosion defects and the pipeline are listed in Table 4-1. According to previous research, the limited function defined by Eq. (4-26) is used to determine if the interacting effect between adjacent corrosion should be taken into consideration. Once P_{mul}/P_{iso} is larger than 99%, the interacting effect can be ignored. Thus, when the P_{mul}/P_{iso} equals 99%, the spacing distance between adjacent corrosions is the threshold, or called the limited spacing distance.

$$\frac{P_{mul}}{P_{iso}} < 99\% \tag{4-26}$$

where P_{mul} is the burst pressure of the pipeline with multiple corrosions, P_{iso} is the burst pressure of the pipeline with isolated corrosion.

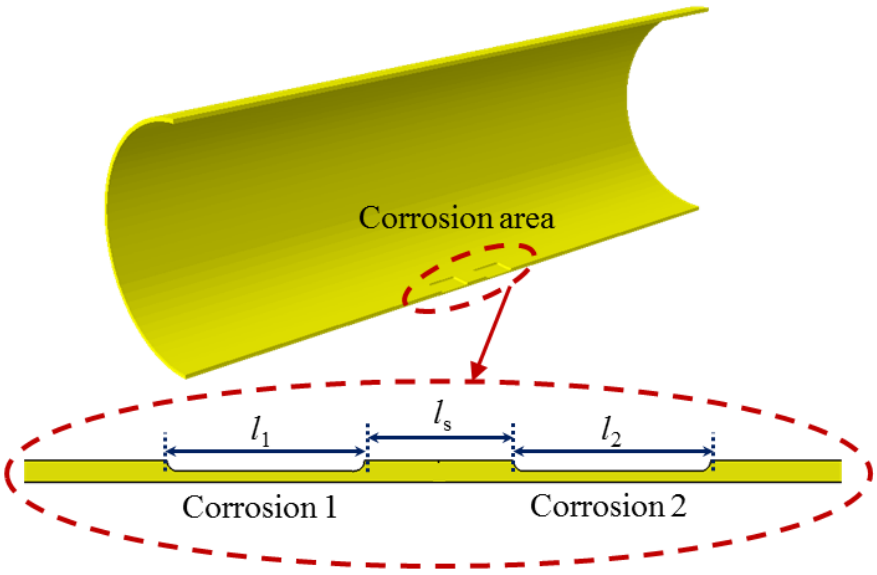

Figure 4-19 3D model of X100 pipeline with two internal corrosions.

Figure 4-20 shows the effect of the longitudinal spacing distance on the ratio of P_{mul}/P_{iso} of the X100 pipeline with two internal corrosions subject to different hydrogen charging time. P_{mul}/P_{iso} grows as the longitudinal spacing distance increases, indicating that the interacting effect between adjacent corrosions becomes weakened as the spacing distance grows. Once hydrogen damage occurs in the pipeline steel, losses in ductility and plasticity will be observed. It is seen that the limited spacing distance of the X100 pipeline suffering from hydrogen damage is smaller than that of the X100 pipeline without hydrogen damage. Several interaction rules are developed and widely used in the field to estimate the limited spacing distance, such as the Kiefner & Vieth (K&V) interaction rule, the ASME interaction rule, the CW interaction rule, and the DNV interaction rule. The limited spacing distance estimated by ASME and CW interaction rules is close to the corroded pipeline's actual limited spacing distance without hydrogen damage. For the corroded pipeline suffering from hydrogen damage, the K&V interaction rule could provide a more accurate prediction for the limited spacing distance. Thus, selecting a proper interaction rule for the corroded pipeline suffering from hydrogen damage should be based on specific situations. Conservatism will be introduced to burst pressure estimation and further reliability analysis

if the effect of the hydrogen damage on adjacent corrosions' interacting effect is ignored. An improper maintenance plan based on the reliability analysis without considering hydrogen damage will also cause a higher operation cost. Nevertheless, no matter whether the hydrogen charging time is 3 hours, 6 hours, or 12 hours, the limited spacing distances between adjacent corrosions are all around 100 mm, which indicates that the length of hydrogen charging time has a more negligible effect on the limited spacing distance.

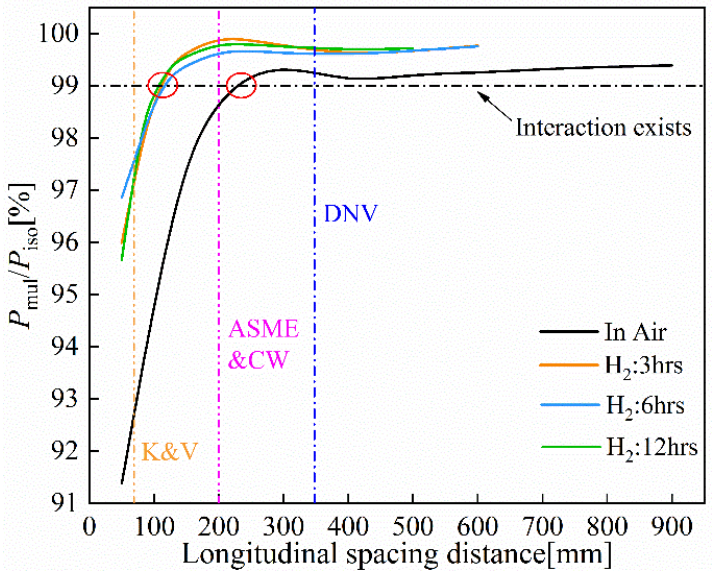

Figure 4-20 P_{mul}/P_{iso} of the X100 pipeline with two adjacent corrosions with different hydrogen charging times under different longitudinal spacing distances.

The 3D model shown in Figure 4-21 is established to investigate the interacting effect between a separated corrosion defect and a corrosion colony consisting of two longitudinal aligned defects and how the interacting effect is affected by the hydrogen damage. It is assumed that three corrosion defects on the internal pipeline wall are identical. The geometric features of the corrosion and the pipeline are listed in Table 4-1. The spacing distance between the corrosions in the corrosion colony is set as fixed in this research. l_s is the spacing distance between the corrosion colony and corrosion 2. The variation in l_s could impact the mechanical behaviors of the X100 corroded pipeline. Once the ratio of the burst pressure of the pipeline with triple corrosions (P_{mul_triple}) to that of the pipeline with a corrosion colony (P_{mul_double}) is larger than 99%, the interacting effect is regarded

as nonexistent.

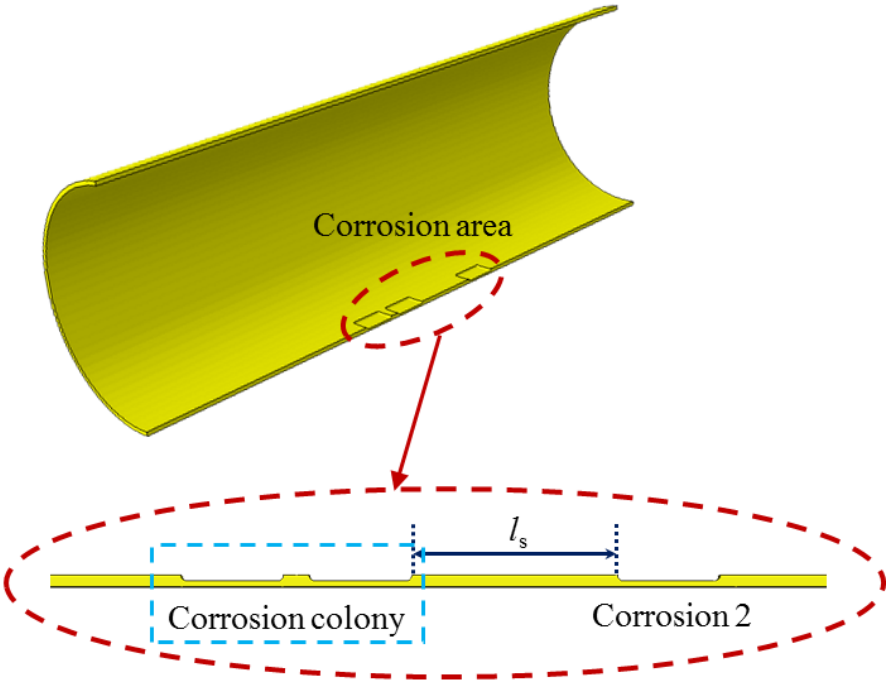

Figure 4-21 3D model of X100 pipeline with triple corrosion defects.

Figure 4-22 shows the effect of longitudinal spacing distance between the corrosion colony and corrosion on the ratio of $P_{mul\_triple}/P_{mul\_double}$ of the X100 pipeline subject to different hydrogen charging times. With the increase of the spacing distance, the ratio of $P_{mul\_triple}/P_{mul\_double}$ increases, indicating the interacting effect between the corrosion colony and the separated corrosion reduces. When hydrogen charging time is 12 hours, the limited spacing distance between the corrosion colony and the separated corrosion defect is the maximum. The minimum limited spacing distance appears when the hydrogen charging time is 3 hours. It can be seen that the change rule of the ratio of $P_{mul\_triple}/P_{mul\_double}$ is different from that of P_{mul}/P_{iso}, which indicates different interacting behaviors of the pipeline with triple corrosions. Besides, hydrogen damage in the pipeline steel has a significant impact on the interacting effect. The limited spacing distance between the corrosion colony and the separated corrosion is critically affected by the hydrogen charging time. The limited spacing distance estimated by ASME and CW interaction rules is close to the limited spacing distance of the X100 pipeline subject to 6-

hour hydrogen charging.

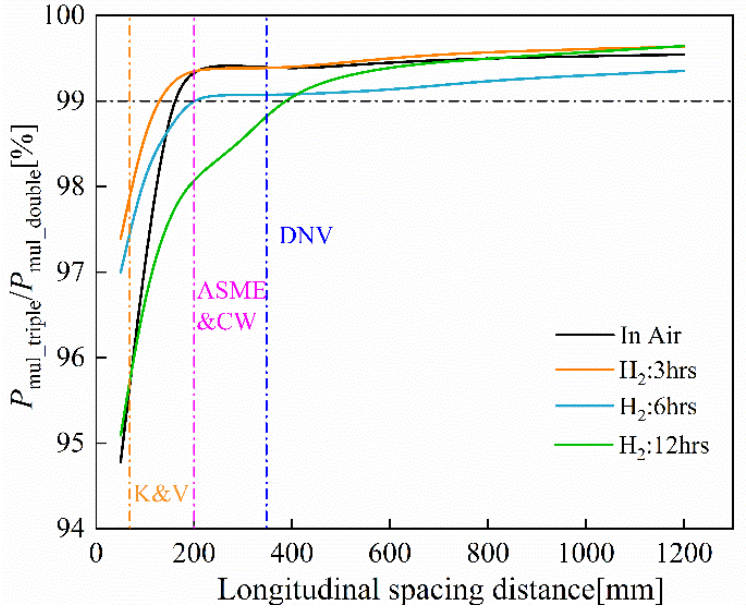

Figure 4-22 $P_{mul\_triple}/P_{mul\_double}$ of the X100 pipeline with a corrosion colony and separated corrosion with different hydrogen charging time under different longitudinal spacing distance.

4.5 Conclusions

Hydrogen damage is one of the major threats to pipelines transporting hydrogen, which could deteriorate the material performance and pipeline's bearing capacity. Hydrogen damage could also make matters worse for high-strength corroded pipelines. In this chapter, several approaches, including FEM, regression analysis, orthogonal test, genetic algorithm and artificial neural network method, are applied to investigate the effect of hydrogen damage on failure behaviors, residual strength, and interacting effect between adjacent corrosions of the high-strength pipeline. Besides, a new burst model and GA-BP ANN are constructed to estimate the residual strength of the corroded pipeline after hydrogen damage. The main conclusions are as follows:

(1) Hydrogen damage weakens the intact and corroded pipeline's maximum bearing capacity. With the rise of hydrogen charging time, the growth rate of PEEQ versus

operation pressure grows while the maximum PEEQ decreases.

(2) With the increase in the degree of hydrogen damage, the residual strength of the corroded pipeline decreases. Meanwhile, hydrogen damage barely affects the change rule of the residual strength versus corrosion geometric features. In addition, the residual strength of the pipeline after hydrogen damage significantly decreases with the growth of the corrosion length and corrosion depth to thickness ratio, while corrosion width has a negligible effect. Furthermore, the growth rate of the burst pressure versus the wall thickness decreases with the hydrogen charging time.

(3) Among six classic burst pressure models, the Shell92 model and CSA model have the best burst pressure estimation performance for the corroded pipeline after hydrogen damage.

(4) Based on the simulation results and regression analysis, a new burst model considering hydrogen damage is developed and validated. In addition, a GA-BP neural network is established and trained for a more accurate estimation of residual strength and relief of the computational burden of FEM.

(5) An orthogonal test is designed and performed to investigate the contributions of key factors to the residual strength. The results indicate that the contribution of hydrogen damage is close to that of corrosion length.

(6) For the high-strength pipeline with multiple internal corrosions, hydrogen damage has an evident effect on the interacting effect and could reduce the limited distance between adjacent corrosions. Moreover, the impact of hydrogen damage on the interacting effect and limited spacing distance between a separated corrosion defect and a corrosion colony is significant.

The results obtained in this chapter are valuable for further integrity management of steel pipelines carrying hydrogen. In future work, the dynamic corrosion growth of the pipeline transporting hydrogen should be considered to model a more accurate degradation process.

Appendix

Appendix A

Relative error of the burst pressure estimated burst models for the corroded pipeline in air.

Number	*t*(mm)	*DTR*	*l*(mm)	ASME modified	Shell92	DNV	CSA	RPA	PCORRC
1	10	0.5	400	13.7	12.8	12.7	6.7	13.7	9.6
2	15	0.5	400	13.9	12.3	15.4	7.9	13.9	12.2
3	20	0.5	400	12.8	12.8	16.2	9.1	12.8	12.4
4	25	0.5	400	11.3	13.6	16.2	10.4	11.3	11.4
5	30	0.5	400	10.8	13.7	16.9	10.7	10.8	11.2
6	35	0.5	400	9.9	14.2	17	11.2	9.9	10.3
7	40	0.5	400	9	14.6	16.9	11.8	9	9.3
8	22.9	0.1	400	8.9	21.2	4.6	19.5	8.9	10.8
9	22.9	0.2	400	6.7	20.7	2	18.6	6.7	8.2
10	22.9	0.3	400	3.1	19.4	1.9	17	3.1	4.1
11	22.9	0.4	400	2.6	17.2	7.6	14.3	2.6	2.1
12	22.9	0.5	400	11	14	15.2	10.6	11	10.9
13	22.9	0.6	400	23.5	9.8	25.2	6	23.5	23.4
14	22.9	0.7	400	36	9.5	31.1	5.5	36	33.9
15	22.9	0.8	400	60.9	9.2	38.1	6	60.9	49.4
16	22.9	0.5	50	4.5	17.2	0.1	15.2	4.5	9.2
17	22.9	0.5	100	3.5	18.7	2.4	15.8	3.5	7.9
18	22.9	0.5	150	2.5	16	9.7	12.3	2.5	0.6
19	22.9	0.5	200	6.4	14.5	14.2	10.5	6.4	5
20	22.9	0.5	300	10.3	13.6	16.8	9.7	10.3	10.6

21	22.9	0.5	400	11.4	13.7	15.7	10.3	11.4	11.3
22	22.9	0.5	600	13.6	12.9	13.7	10.2	13.6	9.6
23	22.9	0.5	800	12.3	14.4	9.6	12	2.2	3.7
24	22.9	0.5	1000	12.8	14.3	8.1	12.1	9.3	0.3
25	22.9	0.5	1200	13.3	14.3	7.1	12	8.8	2.4

Appendix B

Relative error of the burst pressure estimated burst models for the corroded pipeline with 3-hour hydrogen charging.

Number	*t*(mm)	*DTR*	*l*(mm)	ASME modified	Shell92	DNV	CSA	RPA	PCORRC
1	10	0.5	400	35	0.2	29	6.9	35	25.5
2	15	0.5	400	36.4	1.3	33.3	6.4	36.4	29.7
3	20	0.5	400	35.4	0.9	34.5	5.2	35.4	30
4	25	0.5	400	34.7	0.8	35.6	4.7	34.7	30.1
5	30	0.5	400	34.2	0.8	36.6	4.4	34.2	29.9
6	35	0.5	400	33.3	0.5	36.9	3.9	33.3	29.1
7	40	0.5	400	33.5	0.9	38.2	4.2	33.5	29.1
8	22.9	0.1	400	4.8	20.6	3.9	18.8	4.8	10.1
9	22.9	0.2	400	0.5	17.6	1.8	15.4	0.5	4.6
10	22.9	0.3	400	8.3	13.2	9.9	10.5	8.3	3.4
11	22.9	0.4	400	19.5	7	20.8	3.7	19.5	14.7
12	22.9	0.5	400	33.9	0.1	34.1	4	33.9	29.1
13	22.9	0.6	400	52.8	7.6	49.5	12.2	52.8	47.3
14	22.9	0.7	400	80.5	15.9	67.7	20.9	80.5	71.4
15	22.9	0.8	400	118	18.7	80.6	22.9	118	95.3
16	22.9	0.5	50	3.3	13.7	4.4	11.6	3.3	5.3

17	22.9	0.5	100	16.6	5.2	19.4	1.8	16.6	7.4
18	22.9	0.5	150	25.7	0.6	29.8	3.8	25.7	17.6
19	22.9	0.5	200	30.8	1.3	35.3	6	30.8	24.4
20	22.9	0.5	300	34.5	1.7	37.5	6.2	34.5	30.1
21	22.9	0.5	400	33.7	0.1	33.9	3.8	33.7	28.9
22	22.9	0.5	600	30	3.9	25.5	0.9	30	20.9
23	22.9	0.5	800	28.2	5.7	20.7	3.1	11.7	14.2
24	22.9	0.5	1000	27.3	6.7	17.7	4.3	2.4	9.1
25	22.9	0.5	1200	27.4	7	16.2	4.5	2.5	5.9

Appendix C

Relative error of the burst pressure estimated burst models for the corroded pipeline with 6-hour hydrogen charging.

Number	*t*(mm)	*DTR*	*l*(mm)	ASME modified	Shell92	DNV	CSA	RPA	PCORRC
1	10	0.5	400	33.1	2.2	26.3	4.7	33.1	22.9
2	15	0.5	400	36.2	0.5	32.2	5.6	36.2	28.6
3	20	0.5	400	36.8	1.3	35	5.6	36.8	30.6
4	25	0.5	400	35.3	0.6	35.4	4.4	35.3	29.8
5	30	0.5	400	35.4	1	36.9	4.6	35.4	30.2
6	35	0.5	400	35.1	1.2	37.9	4.6	35.1	30
7	40	0.5	400	36	2.1	39.8	5.5	36	30.7
8	22.9	0.1	400	4.1	20.4	3.8	18.7	4.1	10
9	22.9	0.2	400	1.1	17.6	1.8	15.5	1.1	4.7
10	22.9	0.3	400	8.7	13.4	9.6	10.7	8.7	3.1
11	22.9	0.4	400	21.1	6.3	21.8	3	21.1	15.5
12	22.9	0.5	400	33.5	0.8	32.9	3.1	33.5	27.9

13	22.9	0.6	400	55.6	8.9	51.3	13.6	55.6	49
14	22.9	0.7	400	79.5	14.5	65.7	19.5	79.5	69.4
15	22.9	0.8	400	116.5	17.1	78.1	21.3	116.5	92.7
16	22.9	0.5	50	3.9	13.7	4.4	11.6	3.9	5.3
17	22.9	0.5	100	17.6	5	19.6	1.6	17.6	7.6
18	22.9	0.5	150	28.4	0.8	31.7	5.3	28.4	19.3
19	22.9	0.5	200	30	0	33.6	4.7	30	22.8
20	22.9	0.5	300	35.5	1.8	37.6	6.3	35.5	30.2
21	22.9	0.5	400	33.5	0.8	32.9	3.1	33.5	27.9
22	22.9	0.5	600	31.2	3.6	25.8	0.6	31.2	21.2
23	22.9	0.5	800	29.5	5.4	21.1	2.8	12.7	14.6
24	22.9	0.5	1000	27.9	6.9	17.5	4.4	2.9	9
25	22.9	0.5	1200	27.5	7.6	15.5	5.1	2.6	5.3

Appendix D

Relative error of the burst pressure estimated burst models for the corroded pipeline with 12-hour hydrogen charging.

Number	*t*(mm)	*DTR*	*l*(mm)	ASME modified	Shell92	DNV	CSA	RPA	PCORRC
1	10	0.5	400	33.1	60.5	15	48.6	23.1	60.5
2	15	0.5	400	36.2	63.3	17.5	54.6	23.4	63.3
3	20	0.5	400	36.8	71.9	24.2	65.5	29.4	71.9
4	25	0.5	400	35.3	71	24	66.8	28.7	71
5	30	0.5	400	35.4	72.3	25.4	69.9	29.8	72.3
6	35	0.5	400	35.1	76.7	29	75.9	33.4	76.7
7	40	0.5	400	36	79	31.1	79.6	35.5	79
8	22.9	0.1	400	4.1	4.8	15.3	2.5	13.4	4.8

9	22.9	0.2	400	1.1	17.8	6.4	15.7	3.9	17.8
10	22.9	0.3	400	8.7	29.9	1	27.7	4.1	29.9
11	22.9	0.4	400	21.1	47.3	11.1	44.4	15	47.3
12	22.9	0.5	400	33.5	63.8	18.6	59	23.3	63.8
13	22.9	0.6	400	55.6	82.6	24.6	73.1	30	82.6
14	22.9	0.7	400	79.5	106.5	28.5	86	34	106.5
15	22.9	0.8	400	116.5	160.6	37.5	109.1	42.4	160.6
16	22.9	0.5	50	3.9	39.3	12.9	36.5	15.5	39.3
17	22.9	0.5	100	17.6	53.2	20.6	51.8	24.9	53.2
18	22.9	0.5	150	28.4	58.1	21.1	58.2	26.4	58.1
19	22.9	0.5	200	30	69.2	27	69.6	32.9	69.2
20	22.9	0.5	300	35.5	70.6	25	68.9	30.5	70.6
21	22.9	0.5	400	33.5	66.8	20.8	61.9	25.5	66.8
22	22.9	0.5	600	31.2	60.5	15	50.1	18.6	60.5
23	22.9	0.5	800	29.5	59.4	13.6	45.3	16.7	38.8
24	22.9	0.5	1000	27.9	59.3	13.1	42.7	16	28.1
25	22.9	0.5	1200	27.5	59.6	12.9	41.1	15.9	28.5

Chapter 5. Numerical investigation of the mechanical behaviors of the high-strength spanning pipeline with internal corrosion

5.1 Overview

As one of the most powerful methods of transporting energy products, like natural gas, petroleum, and gaseous hydrogen, pipelines have been built and operated worldwide to ensure the global energy supply [227,228]. Many long-distance pipelines are confronted with complex and volatile geological conditions [229]. In regions where the geological condition is unstable, such as mountains, oceans, and rivers, pipeline spanning could occur due to geological hazards (soil erosion, ground subsidence, etc.), extreme weather (flood, hurricane, etc.), and artificial factors (submarine equipment connection, residual stress, etc.) [33,34]. Pipeline spanning is commonly defined as a part or several parts of a pipeline becoming supportless. Spanning parts of a pipeline could result in significant deformation, stress concentration, and vibration [230]. Without proper maintenance strategies, pipeline spanning might eventually lead to unexpected pipeline failures, like fractures and buckling. Some pipeline failures that occurred in the past years because of the spanning phenomenon are listed in Table 5-1 [231]. Corrosion inevitably occurs on steel pipelines due to the surrounding environment and transmission media during operations. As a result, a pipeline's bearing capacity and structural reliability are weakened. According to the previous report [232], about 23% of pipeline failures are caused by corrosion defects, as shown in Figure 5-1. Thus, there is a strong possibility that a spanning pipeline is corroded. In such a scenario, the spanning pipeline could be more likely to be failed and lead to disastrous pipe accidents, such as pipeline leakage and burst. Therefore, conducting a mechanical behavior analysis for spanning pipelines with corrosion is essential.

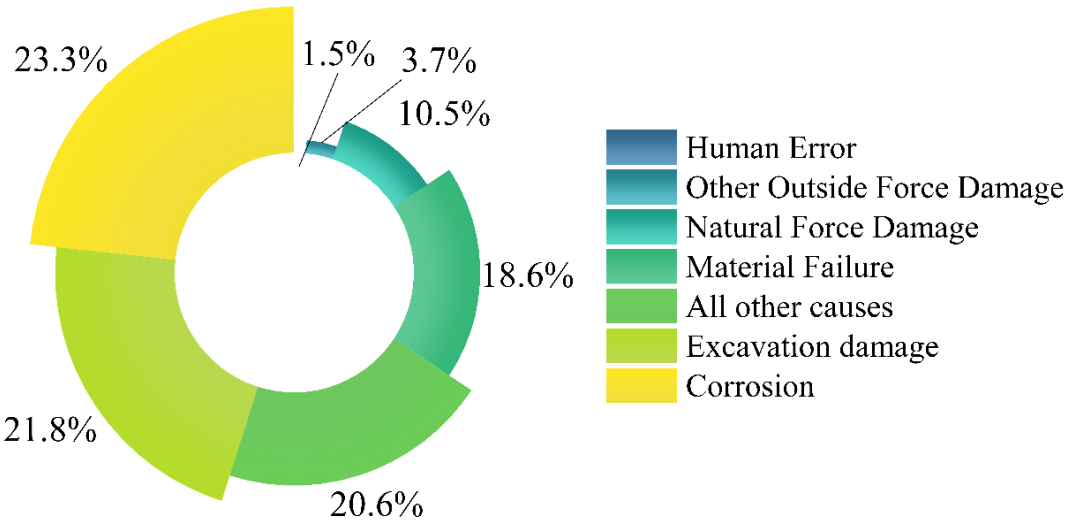

Figure 5-1 Percentages of pipeline damage causes [232].

Table 5-1. Pipeline failures because of spanning.

Year	Place	Cause	Consequence
1996	U.S offshore water pipelines	Hurricane	Non-buried pipelines move
2009	Ledong gas field	Climbing and scouring	Exceeding the allowable span length
2010	Huizhou Natural Gas submarine pipeline	Scouring	Fatigue damage
2012	The East China Sea	Hurricane	Leakage

Over the past years, extensive studies have investigated corroded pipelines' mechanical and burst behaviors. Most of them focus on free pipeline segments subjected to internal pressure only. Based on experimental and numerical methods, several theoretical burst models, such as ASME B31G, PCORRC, CSA Z662-07, etc., have been developed and widely used to estimate the residual strength of corroded pipelines [70]. In the author's previous work [3], the effect of hydrogen damage on mechanical behaviors and the residual strength of the corroded pipeline were systematically investigated by a series of FE models. It is found that the corrosion length and hydrogen charging time have similar contributions to the residual strength. Through the combination of the finite element method (FEM) and

artificial neural network, Gholami et al. [233] realized an accurate and effective burst pressure prediction for corroded high-strength pipelines. Moreover, in recent years, the mechanical behaviors of corroded pipelines under complex loading conditions have been attracting growing attention. Mondal [234] established FE models to investigate the effect of the combined loading of axial forces and bending moments on the residual strength of the pipeline with external corrosion. Based on experimental and numerical approaches, Chegeni et al. [235] discussed how the corrosion geometric features affect the bending capacity of pipelines under combined internal pressure and 4-point bending loading. Taking the X80 pipeline as the research subject, Shuai et al. [236] used FEM to study the effect of external corrosion on the compressive strain capacity of pipelines subjected to the combination of the bending moment and internal pressure. In addition, a new strain-based method was proposed for buckling instability prediction. Previous research has emphasized that the simultaneous presence of corrosion and complex loading conditions significantly impacts steel pipelines' mechanical and failure behaviors.

As extreme weather frequency has increased in the past decades, disasters such as floods, hurricanes, and debris flow have become increasingly common. These disasters could result in pipeline spanning. Thus, more and more studies have focused on spanning pipelines to prevent possible failures. Reduced fatigue life, fracture, and buckling are significant risks for spanning pipelines. Fatigue of a free-spanning pipeline can be caused by a variety of loading conditions, but one of the most common is fluctuating longitudinal stresses which can be caused by factors such as thermal expansion and contraction, pressure changes, and movement of water or wind [237–242]. The fatigue analysis method proposed by DNV-RP-F105 [122] has been widely used in previous research. Shabani et al. [243] carried out a fatigue analysis based on the First-Order Reliability Method, Monte Carlo simulation, and DNV-RP-F105 to investigate the effects of the spanning length and soil type on the fatigue life capacity. He et al. [116] took the factors of the typhoon, current, wave, and pipeline assembly into consideration to predict the allowable spanning length

through FEM and fatigue cumulative damage theory proposed by the DNV code. Badamchi [244] investigated the buckling behavior of a free-span pipeline under axial compression load and external pressure through experimental, numerical, and analytical methods. The results show that axial compression load has an ignorable impact on the external pressure in the linear phase. Xu and Lin [245] applied Vector Form Intrinsic Finite Element method to investigate the upheaval buckling behaviors of unburied submarine pipelines subjected to initial stress. It is found that the initial stress has a significant impact on the axial force of the spanning pipeline. In addition, research on spanning pipelines with defects started to attract many scholars' attention. Based on FEM, Li and Lin [246] established a group of FE models of a spanning pipeline with randomly distributed external corrosions and discussed the impacts of external corrosions and the pipeline's mean outer diameter on the displacement and stress state of the spanning pipeline. A parametric analysis is performed by Wang et al. [36] to study the effects of butt welds' features and spanning length on the stress concentration factor (SCF) of the spanning pipeline. Li et al. [231] employed FEM to determine the critical dimension of the external corrosion on the spanning pipeline subjected to flooding load and self-weight.

Despite significant contributions made to failure and mechanical analysis of corroded and spanning pipelines by previous studies, previous studies barely discussed the influence of the joint action of internal corrosion and spanning phenomenon. For spanning pipelines, internal corrosion is prone to occur due to the bow caused by the deformation. Moreover, to the authors' best knowledge, the discussion of plastic responses of a spanning high-strength pipeline with internal corrosion hasn't been mentioned before. However, plastic deformation is usually more critical than elastic deformation for spanning pipelines suffering large deformation. In addition, the effects of essential parameters on the SCF of corroded spanning pipelines haven't been systematically investigated.

Therefore, a series of numerical models of the spanning X100 pipeline with internal corrosion is established in this chapter to investigate their mechanical behaviors.

Parametric analysis is employed to study the effects of significant factors on the corroded spanning pipeline. The innovation of this chapter is that a more accurate investigation of the mechanical behaviors of spanning pipelines is achieved by considering internal corrosion and the pipe-soil coupling effect. Moreover, plastic responses and SCF of a spanning high-strength pipeline with internal corrosion under the effects of different pipeline features, corrosion, and working conditions are systematically discussed first. The results of this chapter are valuable for further fatigue life estimation, subsequent optimization design, and integrity management.

5.2 Numerical model and material parameters

Figure 5-2 shows a schematic plot of a spanning pipeline. Two major parts should be considered, i.e., the pipeline and the surrounding soil. The free span length is generally defined as the distance between the ends of the span. For spanning pipelines, liquid, impurities, and debris are more likely to accumulate in the middle of the span due to the large deformation and vertical displacement caused by gravity. Thus, internal corrosion is prone to occur in the middle of the span. Compared to buried pipelines, spanning pipelines sometimes must face worse working conditions, like environmental loadings caused by floods, wind, or temperature.

Performing a full-scale experiment on a spanning pipeline with internal corrosion can be extremely costly. Furthermore, the adjustment process of the experiment is arduous and tedious. On the contrary, FEM is more cost-effective. Over the past years, FEM has been widely used and demonstrated exemplary performance in analyzing the mechanical behaviors of both corroded pipelines and spanning pipelines, which involve geometrical, material, and contact nonlinearities [11]. Therefore, FEM is employed in this chapter to investigate the mechanical behaviors of the spanning high-strength pipeline with internal corrosion.

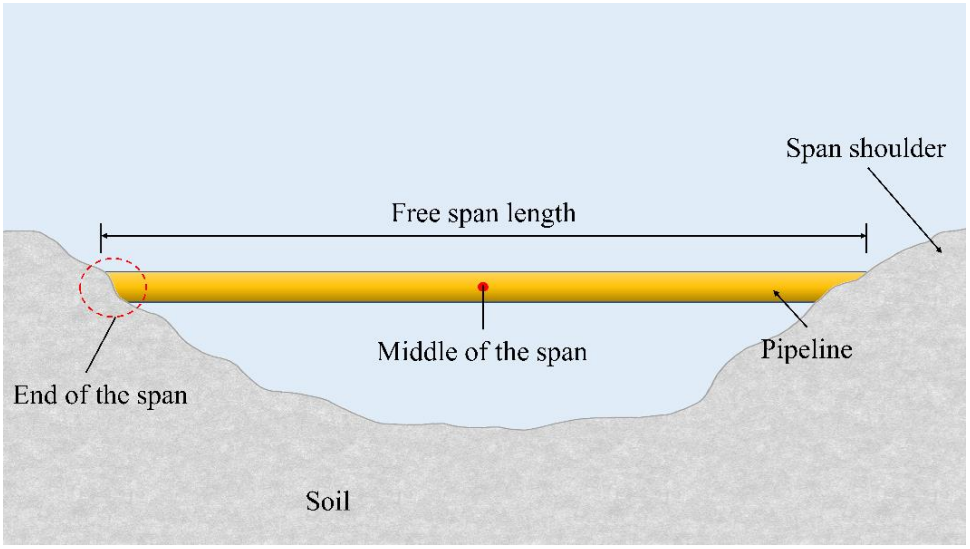

Figure 5-2 Schematic plot of a spanning pipeline.

5.2.1 Numerical model

The 3D numerical simulation model of the spanning high-strength pipeline with internal corrosion is shown in Figure 5-3. The FE model is established in Abaqus 2020 and consists of two parts, i.e., pipeline and soil. Because of the symmetric features of the geometrical structure and applied load, a quarter model is established and implemented to improve computing efficiency and lower cost. According to previous research [11], a quarter model will not impair the simulation accuracy. The outer diameter of pipeline D is 1320mm, and the wall thickness t is 22.9mm. The corrosion defect is on the internal wall of the middle span. The corrosion length l and width w are 400mm and 20°, respectively. The corrosion depth is 11.45mm. The geometric parameters of the soil part are: the height equals 10m, the width equals 10m, and the length equals 20m [247]. The buried depth of the pipeline is 2m. The bottom surface of the soil part is totally fixed and surfaces vertical to the z-axis are fixed in the z-direction. The pipeline is fixed along in the z-direction and supported by the soil part. The symmetric boundary condition is applied to the extra surfaces which appear when the quarter model is established. Eight-node and hexahedron elements are applied to mesh the numerical model. The meshes around the corrosion area are refined to

enhance the simulation accuracy without losing computing efficiency, while meshes of other regions remain relatively coarse. Except for the spanning part, other pipeline parts are buried under the soil. Thus, the pipeline and soil interaction should be precisely described. Based on the contact theory, the contact penalty function describes the soil-pipe interaction. Furthermore, the friction between the pipeline's surface and the surrounding soil is 0.3. The internal pressure is 12MPa.

Due to the complexity of a spanning corroded pipeline's degradation process, which could be influenced by many external factors, it is impractical to build FE models exactly according to the actual situations. Thus, to make the research more feasible, some rational assumptions are made [36]:

(1) The profile of the internal corrosion is simplified as a rectangle shape combined with smooth rounding.

(2) Only gravity load, internal pressure, and overburden pressure are considered. Other external loadings are ignored, like temperature stress, residual stress, flooding load, etc.

(3) The pipeline is horizontally laid in the soil.

(4) The surrounding soil is isotropic and without rocks, pits, or protrusions.

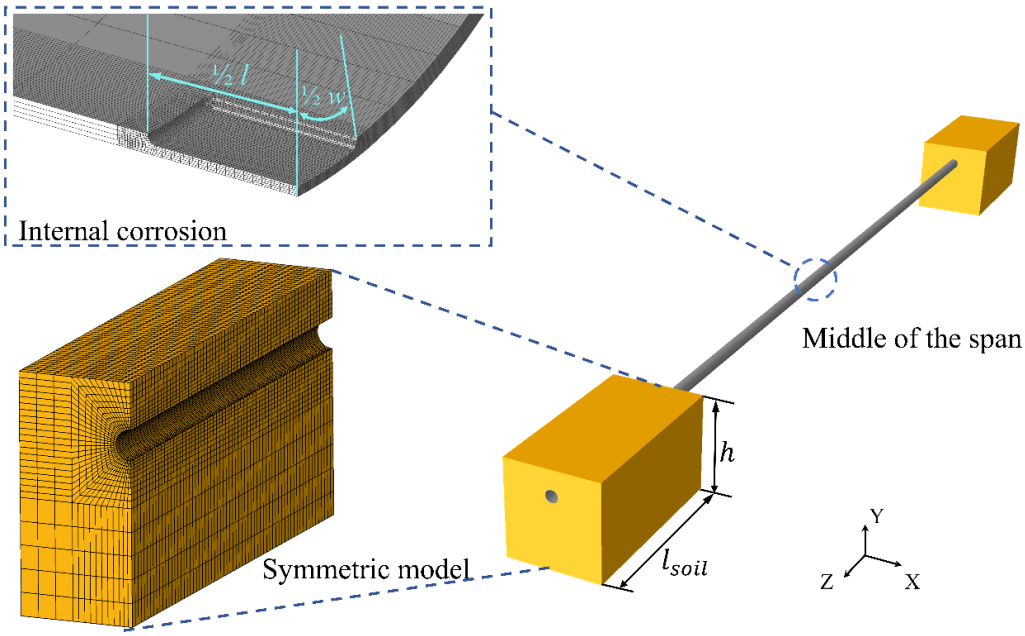

Figure 5-3 3D model of the spanning X100 pipeline with internal corrosion.

5.2.2 Material properties

As high-strength steel, X100 steel is usually used to make long-distance pipelines, which could reduce energy transmission costs. In this chapter, the X100 steel is selected as the material for the spanning pipeline. The mass density of the X100 steel is 7800 kg/m^3, Young's modulus is 210GPa, and Poisson's ratio is 0.3. Plastic characteristics of the X100 steel, such as hardening behaviors, should be considered. The stress-strain curve of the X100 steel, which is obtained by a tensile test, is shown in Figure 5-4. The soil material is selected as clay, and the Mohr-Coulomb constitutive model describes the soil material's mechanical behaviors. The mass density of the soil is 1950kg/m^3, Young's modulus is 50MPa, Poisson's ratio is 0.3, cohesion is 30kPa, and the friction angle is 22.5° [247].

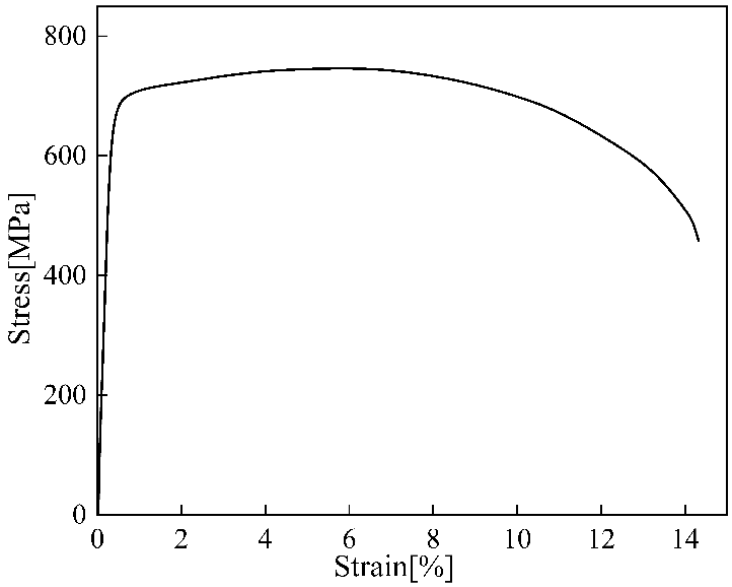

Figure 5-4 Stress-strain curve of the X100 steel.

5.2.3 Numerical model validation

The feasibility and reliability of utilizing FEM to address problems about spanning pipelines and corroded pipelines are usually verified by comparing simulation results and experimental results. The relative error between simulation results and experimental results is defined by Eq. (5-1). Moreover, in the authors' previous work [248], four burst tests of

corroded pipelines from Ref. [23,191] are selected to validate the simulation results. The detailed geometric features, such as corrosion depth (d), length (l), width (w), pipeline diameter (D), and wall thickness (t), of the test specimens, as well as the experimental and FEA results, are listed in Table 5-2. The average relative error of the burst pressure (P_b) obtained through FEM is only around 3.7%. A numerical model of the spanning pipeline considering internal pressure, gravity, and soil-pipeline coupling effect is established based on the experiment conducted by Zhao [249]. The maximum longitudinal stress of the spanning pipeline obtained by numerical simulation is 118.6 MPa, while that obtained by the experimental method is 125MPa. The relative error of the maximum stress is 5.12%. Therefore, the FEM is feasible and reliable for conducting mechanical behavior analysis of the spanning pipeline with internal corrosion.

$$error_r = \left(\frac{|R_{FEM} - R_e|}{R_e}\right) \times 100\% \tag{5-1}$$

where $error_r$ is the relative error, R_{FEM} is the result obtained by FEM, R_e is the result obtained by experiment.

The gravitational loading applied to the spanning pipeline is the weight of the spanning part, and it is defined as Eq. (5-2).

$$G = \rho l_s g \frac{\pi}{4}(2Dt - t^2) \tag{5-2}$$

where ρ is the density of the pipeline steel, l_s is the spanning length, g is the gravitational acceleration.

Table 5-2. Geometric features and result comparison of corroded pipeline specimens.

Specimen	D(mm)	t(mm)	d(mm)	l(mm)	w(mm)	Experimental P_b(MPa)	FEM P_b(MPa)	$error_r$ (%)
IDTS-2	458.8	8.1	5.39	39.6	21.9	22.68	22.06	2.7
IDTS-3	458.8	8.1	5.31	39.6	31.9	20.31	20.82	2.5
IDTS-4	458.8	8.1	5.62	39.6	32	21.14	22.34	5.7
X65-DB	762	17.5	8.8	200	50	21.76	20.87	4.1

5.3 Simulation results and discussions

Internal corrosion could weaken the bearing capacity and structural reliability of a pipeline. Under the influences of gravitational load and internal pressure, spanning pipelines must face large deformation and stress concentration. Once internal corrosion and spanning appear simultaneously, the pipeline is at higher risk. For a spanning pipeline, longitudinal stress is usually the most important one because it has a direct relationship with the overall dynamic responses due to environmental impacts. Since the pipeline is fixed along the z-direction and soil-pipe coupling effect, the spanning pipeline suffers from bending moment resulting in evident longitudinal stress under the impact of the gravity load. By simplification, the boundary conditions of the spanning pipelines can be regarded as two fixed support ends. Since the internal pressure could lead to pipeline expansion along radial direction, it could result in longitudinal stress.

Figure 5-5 shows the Von Mises stress distributions and deformations of the spanning high-strength pipeline with and without an internal corrosion defect in the middle of the span. The spanning part of the pipeline bends downward with gravity. With the increase of the distance from the end of the span, the vertical displacement gradually grows. The maximum vertical displacement occurs in the middle of the span. For the intact spanning pipeline, the maximum Von Mises stress appears on the bottom surface of the span end. However, the maximum Von Mises stress is in the corrosion area for the spanning pipeline with internal corrosion. Under the same working condition, the maximum Von Mises stress of the intact spanning pipeline is 407.68MPa, while that of the corroded spanning pipeline is 707.58MPa, and the increment is about 73.56%. Therefore, the primary concern of this chapter is the mechanical behaviors of the corrosion area instead of the span end area.

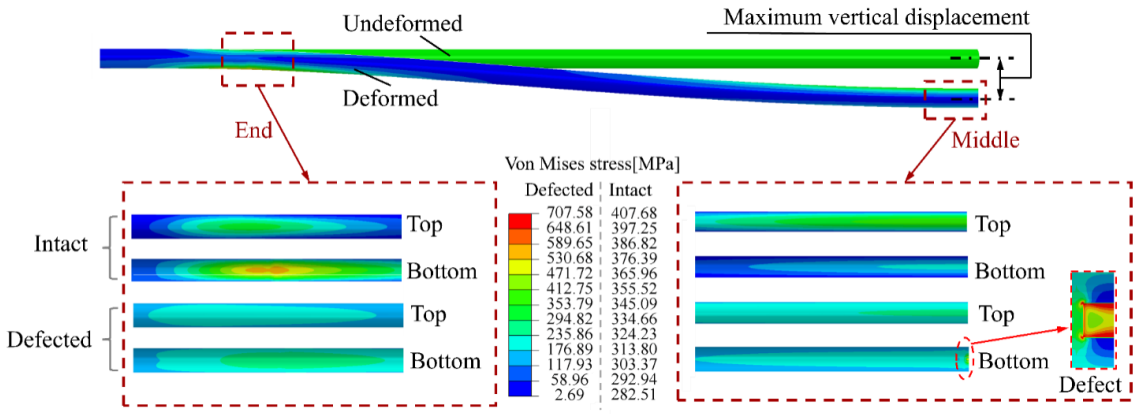

Figure 5-5 Von Mises stress distributions of the spanning pipeline with and without internal corrosion.

5.3.1 Effect of spanning length

Because of gravity, the increase of the spanning length could result in more significant gravitational loading that causes more considerable bending and stretching. Figure 5-6 shows the maximum Von Mises stresses and Von Mises stress distributions of the X100 pipeline with internal corrosion under different spanning lengths. Under such working conditions, no matter how long the spanning length is, the high-stress region always appears in the corrosion area. When the spanning length is no greater than 80m, the maximum Von Mises stress occurs both on the corrosion edges along the axial direction and corners. When the spanning length is larger than 100m, with an increase in the spanning length, high stress starts to appear in the middle of the corrosion, and the corrosion edges are perpendicular to the axial direction. The maximum Von Mises stress of the spanning pipeline grows with the increase in the spanning length when the spanning length is larger than 60m. The increment of the maximum Von Mises stress when the spanning length changes from 60m to 140m is about 0.675%. However, when the spanning length is relatively short, the spanning length has little impact on the maximum Von Mises stress due to the soil end having a more significant supportive effect and the small gravitational

loading. When the spanning length ranges from 20m to 40m, the variation of the maximum Von Mises stress is only about 0.05%.

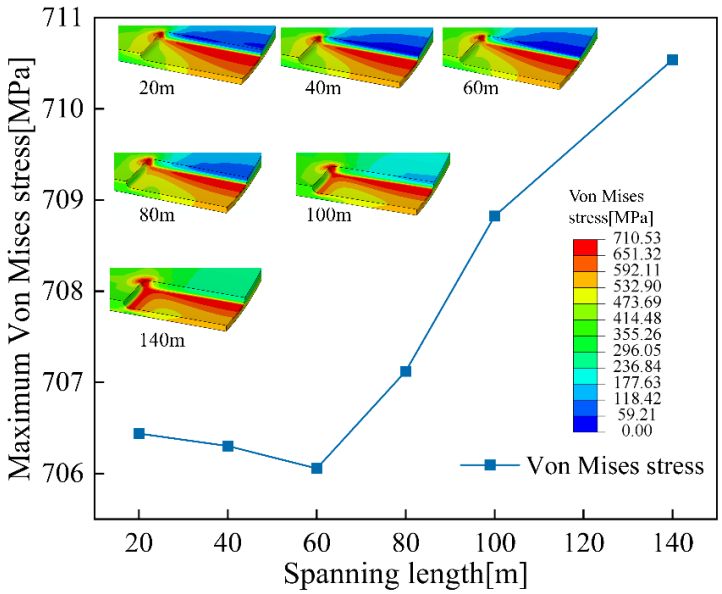

Figure 5-6 Maximum Von Mises stresses and distributions of the corroded spanning pipeline under different spanning lengths.

The maximum longitudinal stresses and distributions of the pipeline are shown in Figure 5-7. No obvious high longitudinal stress area occurs in the corrosion area when the spanning length is smaller than 80m. The maximum longitudinal stress area first appears around the corrosion edge perpendicular to the axial as the spanning length grows. Due to the internal corrosion profile and the internal pressure effect, compressive longitudinal stress occurs in the region near the corrosion. However, compressive stress is much smaller than tensile stress. With the increase of the spanning length, the maximum longitudinal stress shows an upward trend with different growth rates. Compared with the growth rate of the pipeline when the spanning length is from 20m to 60m, that of the pipeline with 60m to 100m is relatively higher. Nonetheless, when the spanning length is larger than 100m, the growth rate of the longitudinal stress decreases. When the spanning length increases from 20m to 140m, the growth in the longitudinal stress is about 122.6%.

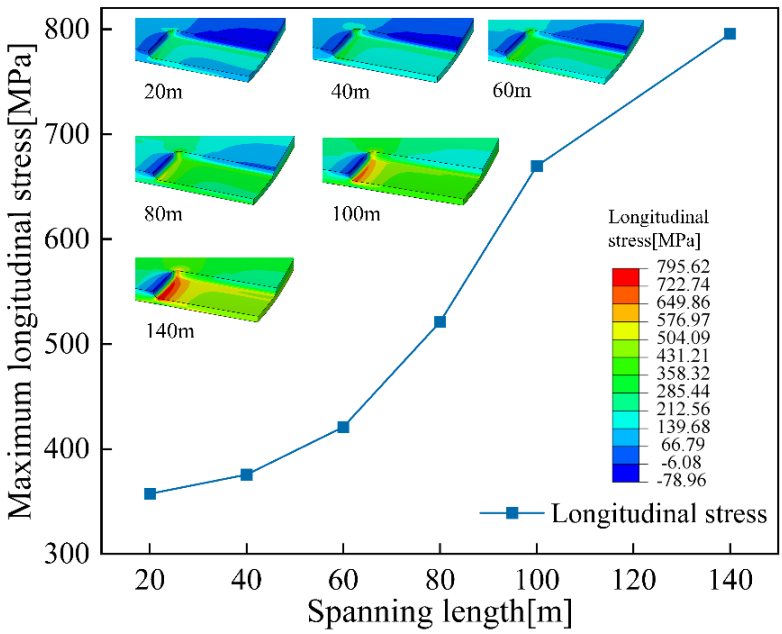

Figure 5-7 Maximum longitudinal stresses and distributions of the corroded spanning pipeline under different spanning lengths.

Figure 5-8 shows the longitudinal strain distributions and values of the corroded spanning pipeline with different spanning lengths. As the spanning length grows, both the longitudinal strain and the region that suffers from tensile strain increase. High longitudinal strain mainly appears in the area around the corrosion edge perpendicular to the axis. Once the spanning length is larger than 100m, an apparent longitudinal strain appears on the corner of the corrosion.

Stress concentration is commonly defined as a point or location in a part where the stress is much greater than that of its surrounding area because of an interruption of the stress flow. Corrosion defects cause irregularities and discontinuities in the pipeline geometry, eventually increasing local stress. SCF is a dimensionless index used to represent the severity of stress concentration. Moreover, combined with the fatigue analysis method proposed by DNV-RP-F105, SCFs of the defects on spanning pipelines can be used to estimate the fatigue life. For spanning pipelines, the SCF of the longitudinal stress is the most significant one [250]. Therefore, the SCF of the longitudinal is studied in detail. The SCF corresponding to longitudinal stress is expressed as:

$$\mathrm{SCF} = \frac{\sigma_{lmax}}{\sigma_{lref}} \tag{5-3}$$

where SCF is the stress concentration factor corresponding to longitudinal stress, σ_{lmax} is the maximum longitudinal stress in corrosion area, σ_{lref} is the reference longitudinal stress of the intact pipeline (same area, same loading conditions, without corrosion).

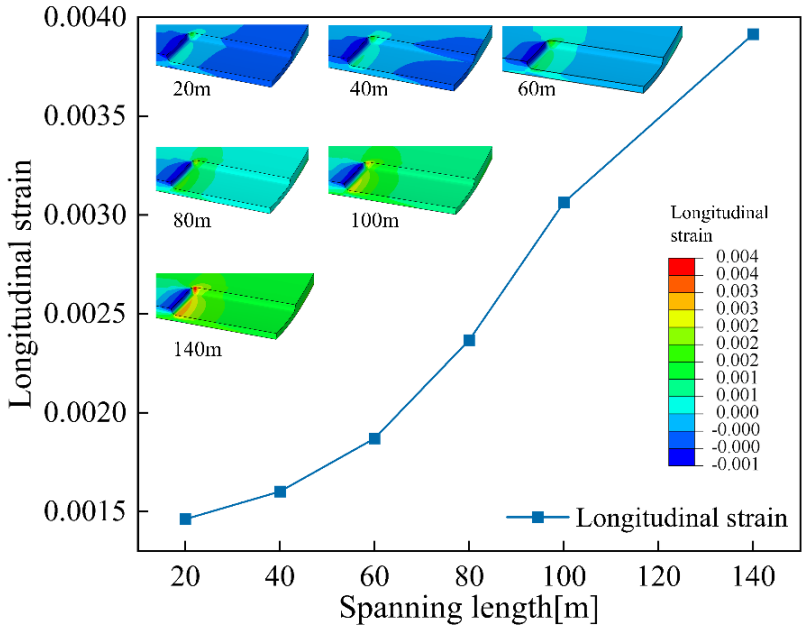

Figure 5-8 Maximum longitudinal strain values and distributions of the corroded spanning pipeline under different spanning lengths.

Figure 5-9 describes the variation trends of SCF and the maximum vertical displacement of the pipeline with different spanning lengths. With the increase of the spanning length, SCF gradually decreases with a tapering growth rate. This phenomenon occurs because the growth in the longitudinal stress of the intact spanning pipeline is more evident than that of the corroded spanning pipeline. When the spanning length changes from 20m to 140m, SCF decreases by 35.2%. The longer the spanning length is, the more obvious the effect of gravitational loading can be. When the spanning length is 20m, the maximum vertical displacement is only 0.019m. With the increase of the spanning length, the maximum vertical displacement of the middle of the span significantly increases. The maximum vertical displacement of the pipeline with a 140m span is about 105 times bigger than that

of the pipeline with a 20m span.

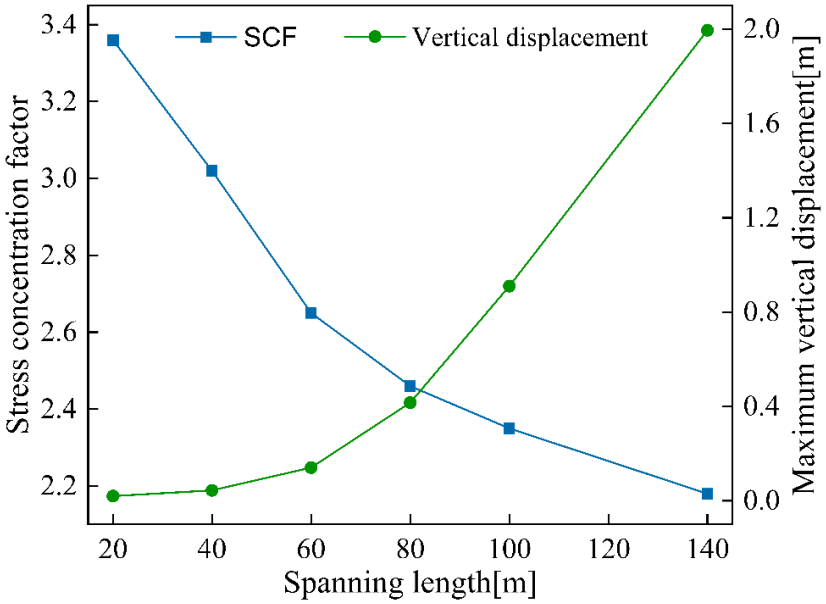

Figure 5-9 SCFs and the maximum vertical displacements of the corroded spanning pipeline under different spanning lengths.

5.3.2 Effect of corrosion location

For intact spanning pipelines, stress concentration mainly appears at the end. However, for a spanning pipeline with internal corrosion, the high-stress area usually occurs around the corrosion area. Although the bottom surface of the middle of the span is most likely to be corroded, other locations could also be corroded. Thus, the location of the internal corrosion could impact the mechanical behaviors of the spanning pipeline. Figure 5-10 shows the maximum Von Mises stresses and the distributions of the pipeline with different corrosion locations. The location of the internal corrosion is denoted by a fraction of the spanning length (l_s). When the corrosion location is 0/10 l_s, representing the internal corrosion at the junction of the soil and span, the high-stress area almost fills the corrosion area. With the increase of axial location, the high stress gradually increases in the middle of the corrosion. When the axial location of the corrosion is larger than 3/10 l_s, the maximum Von Mises stress mainly occurs on the corrosion corners and edges along the

axial direction. The maximum Von Mises stress remains stable as the axial location changes. In addition, except for 5/10 l_s, corrosion location barely influences the maximum Von Mises stress of the middle of the span.

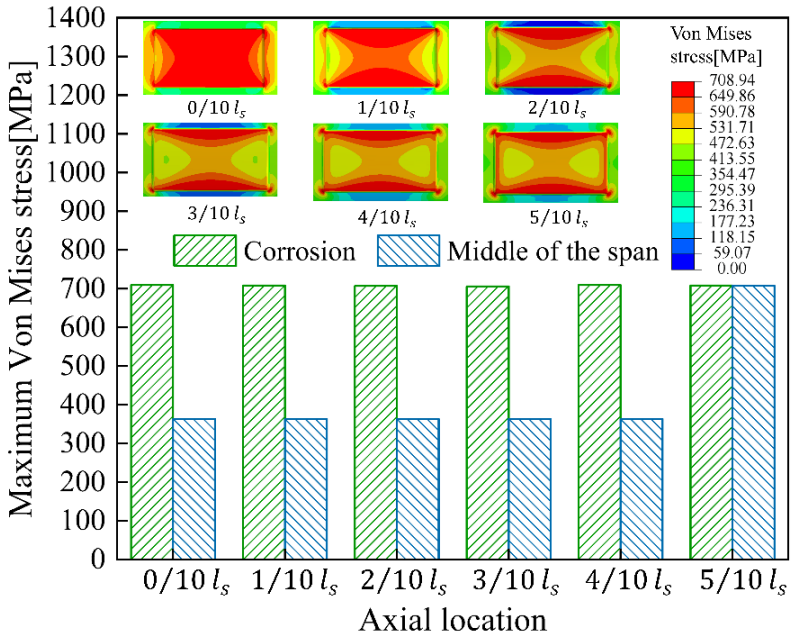

Figure 5-10 Maximum Von Mises stresses and distributions of the pipeline with different corrosion locations.

The maximum longitudinal stresses and distributions of the pipeline with different axial locations are shown in Figure 5-11. When the axial location is 0/10 l_s, the dominant longitudinal stress is compressive stress, whose value is -360.1MPa. With the increase of the axial location, the bending effect caused by the gravitational loading becomes more significant. Therefore, high longitudinal stress starts to appear on the corrosion edges perpendicular to the pipeline axis and gradually increases as the axial location grows. Obviously, the internal corrosion hardly has any impact on the longitudinal stress of areas away from it.

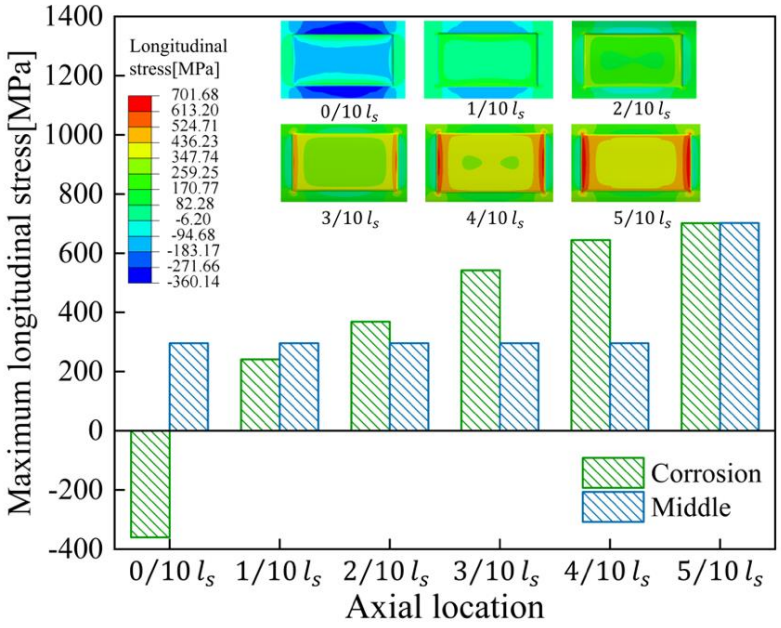

Figure 5-11 Maximum longitudinal stresses and distributions of the pipeline with different corrosion locations.

Figure 5-12 shows the longitudinal strain and distributions of the corroded spanning pipeline with different axial locations. Since the surrounding soil restricts the buried section's deformation, when the axial location is 0/10l_s, the longitudinal strain of the internal corrosion is compressive. For the corrosion on the 1/10l_s, the maximum longitudinal strain is also compressive because of the combination of the support from the soil and the gravitational loading. The maximum longitudinal strain of the pipeline with the internal corrosion on 0/10l_s and 1/10l_s appears in the middle of the corrosion, and the value is -0.00195 and -0.00112, respectively. With the increase in the axial location, high longitudinal stress first appears in the middle of the edges perpendicular to the pipeline axis and then gradually expands to corrosion corners. The value of the longitudinal strain grows as the axial location increases. The longitudinal strain of the corrosion on 2/10l_s is 1.97 times larger than that of the corrosion on 5/10l_s.

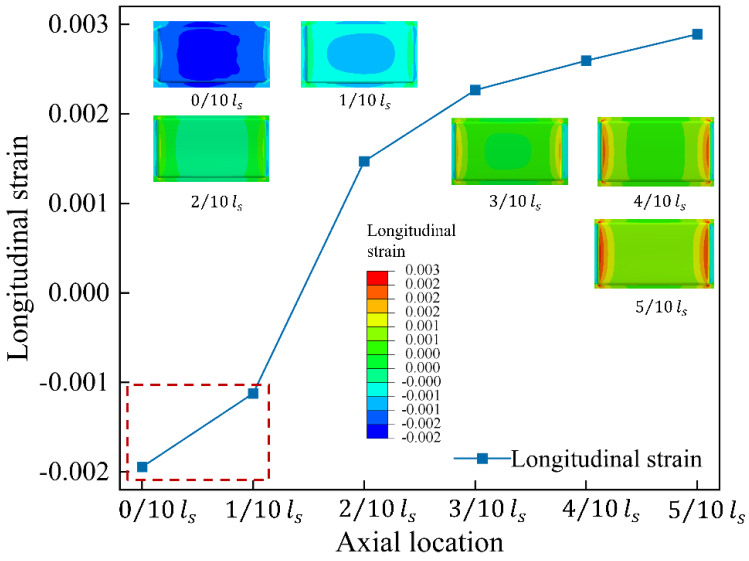

Figure 5-12 Longitudinal strain values and distributions of the pipeline with different corrosion locations.

SCFs and the maximum vertical displacements of the pipeline with different axial locations are presented in Figure 5-13. When the axial location is from 0/10l_s to 4/10l_s, the maximum vertical displacement of the corroded spanning pipeline is barely affected by the axial location. When the internal corrosion is located in the middle of the span, the maximum vertical displacement is about 0.91m, and the increase is 2.62%. The maximum SCF, which is larger than 6, appears when the axial location is 1/10l_s. Due to the supporting effect of the soil end, the longitudinal stress of the intact pipeline is relatively small for the spanning section near the soil. However, once a defect occurs, the longitudinal stress of the same pipeline section will rapidly increase, which results in a dramatic increase in SCF. For the intact spanning pipeline, the site's maximum tensile stress, which is the same as the corrosion site, is relatively small. Except for 0/10l_s, the SCF of the internal corrosion decreases with the increment in the axial location.

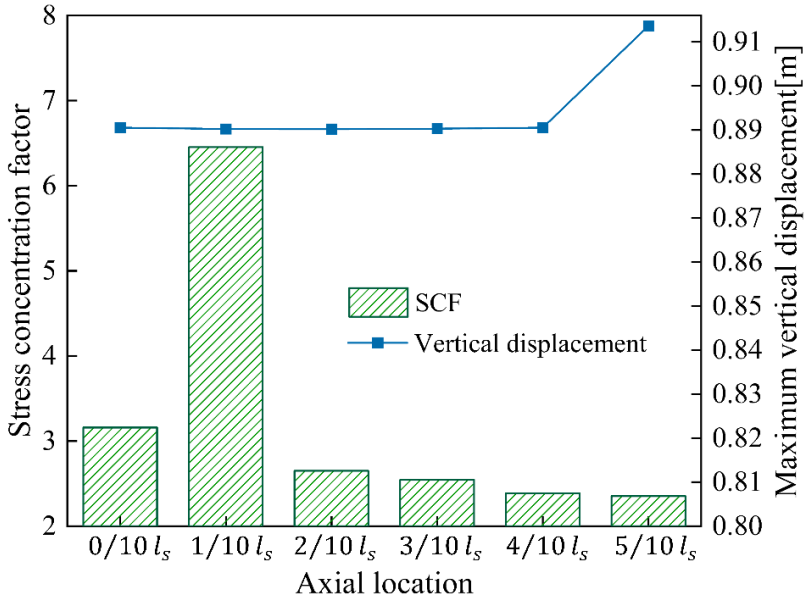

Figure 5-13 SCFs and the maximum vertical displacements of the pipeline with different corrosion locations.

5.3.3 Effect of corrosion depth to wall thickness ratio

Geometric features of the corrosion have a significant impact on the burst behaviors of a corroded pipeline. Thus, the effects of geometric features of the corrosion should be discussed regarding the mechanical behaviors of a corroded pipeline.

The corrosion depth to wall thickness ratio (DTR) is usually defined by Eq. (5-4). Penetration and leakage occur when DTR equals 1. Figure 5-14 shows the maximum Von Mises stresses and distributions of the corroded spanning pipeline with different corrosion DTRs. No apparent stress concentration in the corrosion area is observed when DTR is smaller than 30%. Besides, the maximum Von Mises stress increases significantly, from 407MPa to 692MPa, as DTR grows from 10% to 30%. When DTR is larger than 40%, the high-stress area first appears on the corrosion edges along the axis and corrosion corners. With the growth in corrosion depth, the high-stress area expands to the corrosion edges perpendicular to the axis and then fills the whole corrosion area when DTR reaches 70%. When DTR is 80%, a high-stress area occurs in the area around the corrosion. The

maximum Von Mises stress of the internal corrosion shows an upward trend with DTR growth. The maximum Von Mises stress increases by 95.58% due to wall thinning (DTR 10% to 80%). For corroded pipelines, ultimate tensile stress (*UTS*) is commonly used to determine failure. When DTR is larger than 70%, the pipeline line is out of working condition.

$$DTR = \frac{d}{t} \times 100\% \tag{5-4}$$

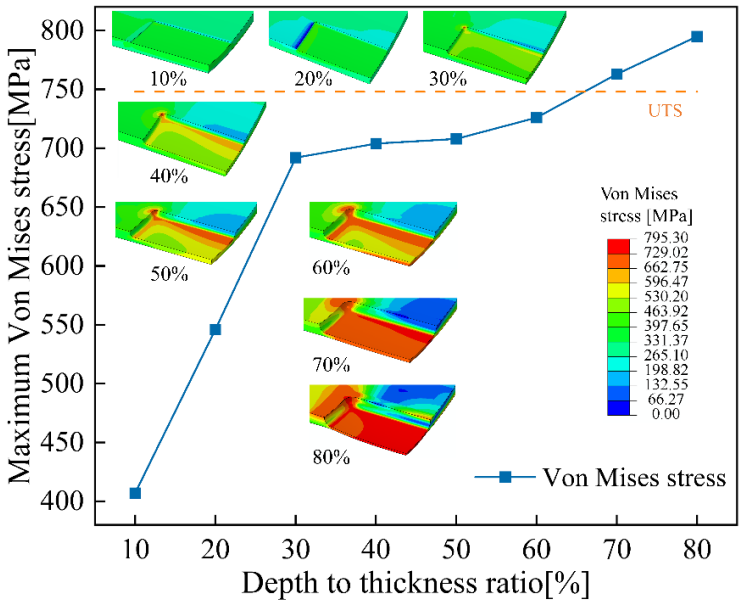

Figure 5-14 Maximum Von Mises stresses and distributions of the pipeline with different DTRs.

The maximum longitudinal stresses and distributions of the internal corrosion on the X100 spanning pipeline under different DTRs are shown in Figure 5-15. When DTR is 10%, there is no apparent longitudinal stress concentration. With the increase in DTR, the high longitudinal stress first appears on the corrosion edges perpendicular to the pipeline axis and then expands to the corrosion center. The longitudinal stress of the corrosion edges perpendicular to the axis is much larger than that of the corrosion center due to the discontinuity around the edges. When DTR is larger than 70%, high longitudinal stress area appears in the area near the corrosion corners. With the corrosion depth growth, the spanning pipeline's longitudinal stress increases. When the DTR is 80%, the longitudinal

stress is the maximum (891.84MPa), which is 2.32 times larger than the pipeline with 10% DTR.

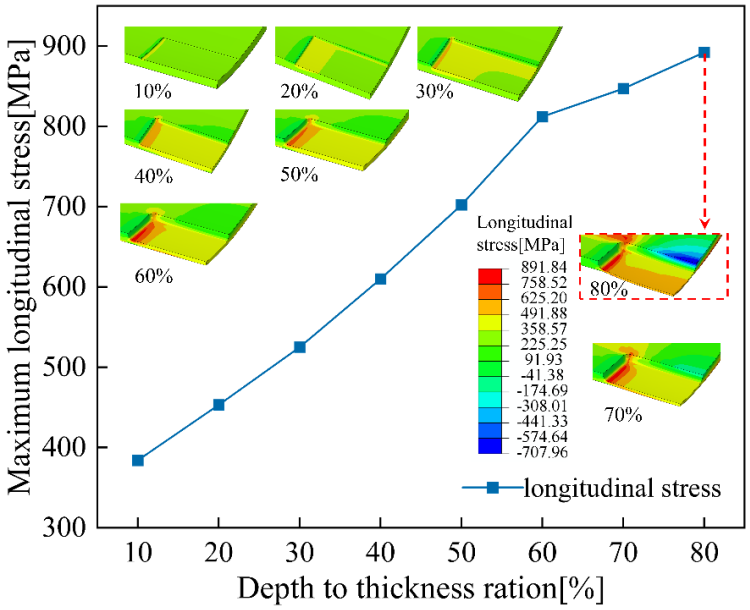

Figure 5-15 Maximum longitudinal stresses and distributions of the pipeline with different DTRs.

Figure 5-16 shows the longitudinal strain values and distributions of the corroded pipeline with different DTRs. With the increase in DTR, the compressive strain of the corrosion area gradually expands in both axial and circumferential directions. When the DTR is 80%, the maximum longitudinal strain appears on the corrosion edges perpendicular to the axis. The variation of the longitudinal strain shows a rising tendency as DTR increases. The longitudinal strain linearly and slowly grows when DTR is smaller than 60%. However, once DTR is larger than 60%, a sharp increment in the longitudinal strain can be observed. When DTR changes from 10% to 80%, the increment in the longitudinal strain is about 2976.422%.

The maximum vertical displacements and SCFs of the spanning pipeline with different corrosion DTR are shown in Figure 5-17. With the growth in DTR, both SCF and the maximum vertical displacement show an upward trend but with varying growth rates. When DTR is smaller than 60%, the growth rate of SCF is larger than that with DTR larger

than 60%. Inversely, the growth rate of the maximum vertical displacement suddenly rises once DTR is larger than 60%. Thus, the corroded spanning pipeline is at a higher risk if *DTR* is larger than 60%.

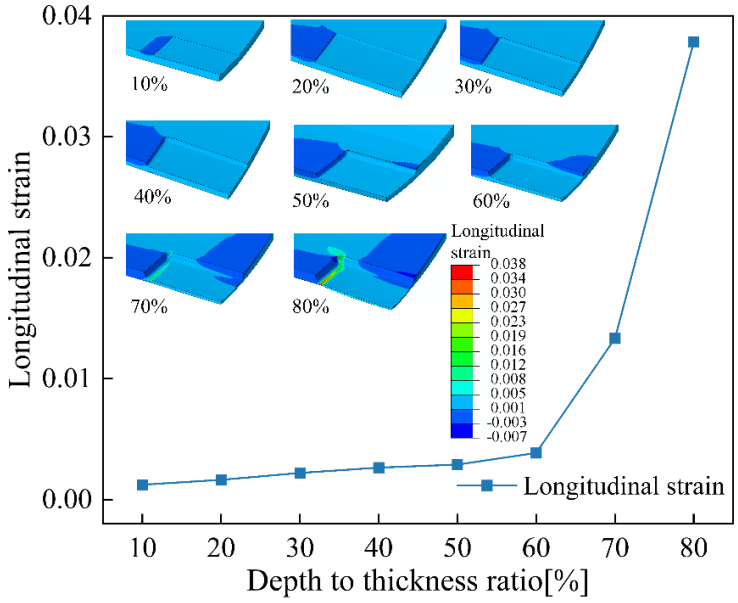

Figure 5-16 Longitudinal strain values and distributions of the pipeline with different DTRs.

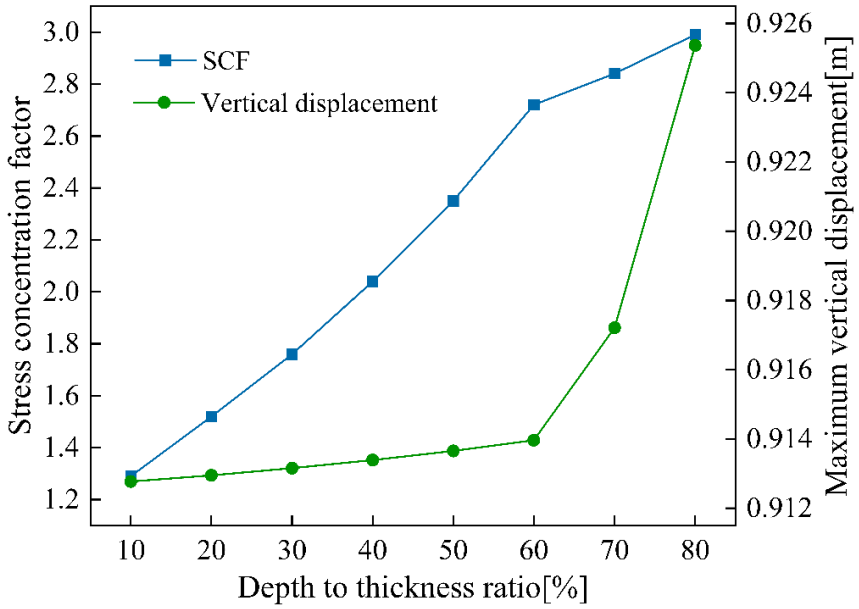

Figure 5-17 SCFs and the maximum vertical displacements of the pipeline with different DTRs.

5.3.4 Effect of corrosion length

Corrosion length is a primary parameter that significantly affects the failure behaviors of corroded pipelines. During the operation process, the corrosion length grows with different working conditions. For spanning pipelines, variable corrosion lengths could result in different mechanical behaviors. Figure 5-18 shows the maximum Von Mises stresses and distributions of the corroded pipeline with varying corrosion lengths. When the corrosion length is smaller than 100mm, the high-stress area mainly appears on the corrosion edges and corrosion corners. Once the corrosion length is longer than 200mm, the high-stress area expands from the corrosion edges along with the axial direction to the center of the corrosion with the growth in the corrosion length. High-stress area expansion could also be observed around the corrosion corners. With the increase in the corrosion length, the maximum Von Mises stress of the corroded spanning pipeline rises. When the corrosion length grows from 50mm to 500mm, the maximum Von Mises stress increases from 698.67MPa to 709.86MPa, and the increment is about 1.6%. When the corrosion length is smaller than 75mm, the maximum Von Mises stress growth rate is higher than others.

The maximum longitudinal stresses and distributions of the pipeline with different corrosion lengths are shown in Figure 5-19. No matter how long the corrosion length is, the high longitudinal stress area appears on the corrosion edges perpendicular to the axis. No evident high-stress area expansion is observed as the corrosion length grows. The corroded spanning pipeline's maximum longitudinal stress increases with the corrosion length growth. Compared with the growth rate of the maximum longitudinal stress when the corrosion length is smaller than 100mm, an evident reduction in the growth rate can be observed once the corrosion length is larger than 100mm.

Figure 5-20 shows the longitudinal strain values and distributions of the pipeline with different corrosion lengths. With the increase in the corrosion length, the high longitudinal strain areas appear on the corrosion edges perpendicular to the axis, and corrosion corners become more severe. However, the area that suffers from high longitudinal strain doesn’t

evidently expand as the corrosion length grows. When the corrosion length is smaller than 75mm, the longitudinal strain remains stable with the variation of the corrosion length. With the growth in the corrosion length from 75mm to 500mm, the longitudinal strain increases by 24.19%.

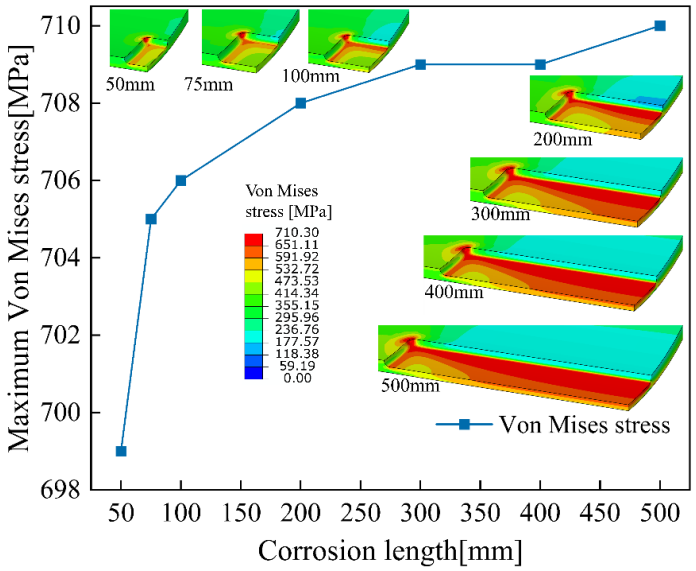

Figure 5-18 Maximum Von Mises stresses and distributions of the pipeline with different corrosion lengths.

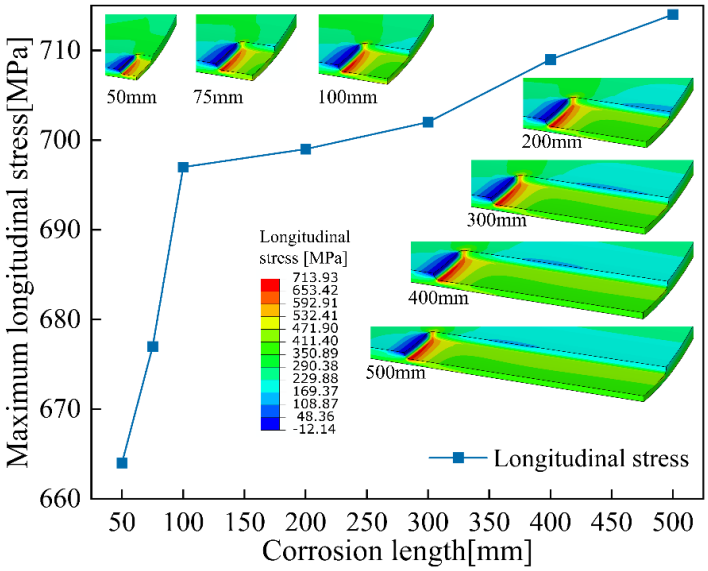

Figure 5-19 Maximum longitudinal stresses and distributions of the pipeline with different corrosion lengths.

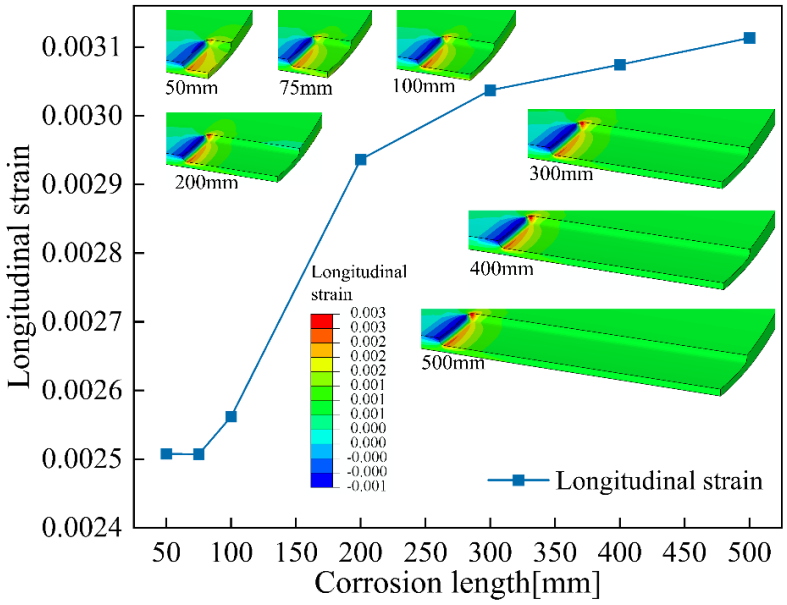

Figure 5-20 Longitudinal strain values and distributions of the pipeline with different corrosion lengths.

Figure 5-21 shows the SCFs and the maximum vertical displacements of the pipeline with different corrosion lengths. Both the SCF and the maximum vertical displacement of the spanning pipeline with internal corrosion show an upward trend as the corrosion length grows. The maximum vertical displacement with a 500mm corrosion length is 0.914m, while that with a 50mm corrosion length is 0.913m. The increment is only 0.15%. When the corrosion length is smaller than 100mm, SCF significantly rises with the growth in the corrosion length. Nevertheless, SCF increases relatively more slowly when the corrosion length is larger than 100mm. The maximum SCF appears when the corrosion length is 500mm, and its value is 2.39, which is 1.08 times larger than when the corrosion length is 50mm.

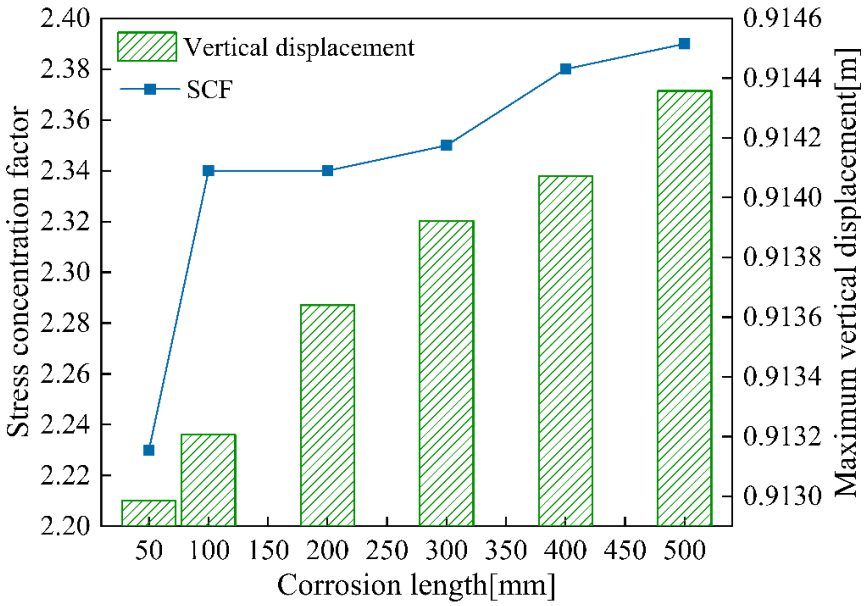

Figure 5-21 SCFs and the maximum vertical displacements of the pipeline with different corrosion lengths.

5.3.5 Effect of corrosion width

For corroded pipelines without spanning, the corrosion width has less impact on the burst behaviors than other geometric features of corrosion, like corrosion length and depth. However, with the effect of spanning, how the corrosion width impacts the mechanical behaviors of the corroded pipeline could be different.

Figure 5-22 shows the maximum Von Mises stresses and distributions of the corroded spanning pipeline with different corrosion widths. When the corrosion width is 5°, the high-stress area appears in the center of the corrosion, and the corrosion edges along the axis. When the corrosion width exceeds 5°, high-stress areas appear on all the corrosion edges and corners. In addition, no obvious high stress appears in the middle of the corrosion. The high-stress area on the corrosion edges along the axis is larger than that on the edges perpendicular to the axis. The corrosion width has a neglectable influence on the maximum Von Mises stress when it is smaller than 20°. However, once the corrosion width exceeds 25°, the maximum Von Mises stress sharply rises. When the corrosion width is 50°, the

maximum value is 812MPa. From 5° to 50°, the maximum Von Mises stress increases by 14.49%.

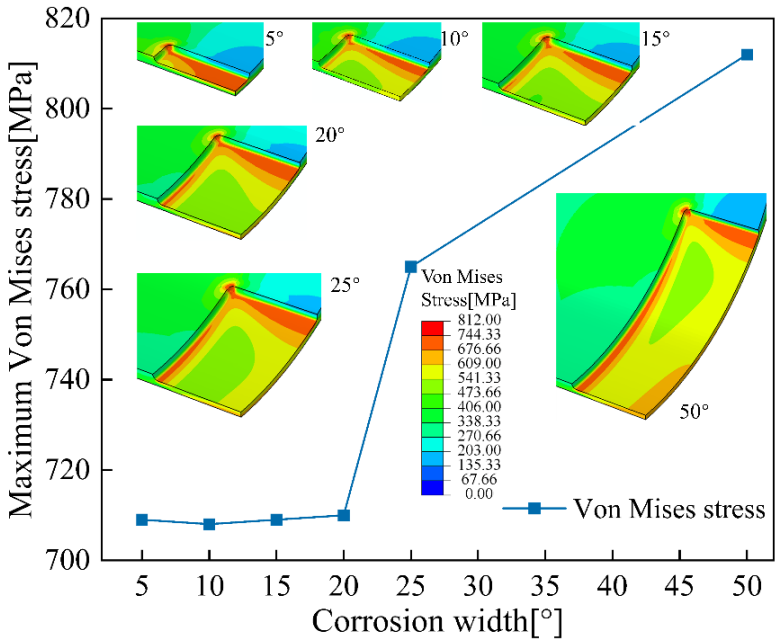

Figure 5-22 Maximum Von Mises stresses and distributions of the pipeline with different corrosion widths.

The maximum longitudinal stresses and distributions of the pipeline with different corrosion widths are shown in Figure 5-23. When the corrosion width is 5°, no prominent high longitudinal stress area shows in the corrosion. With the increase of the corrosion width, the high longitudinal stress area starts to appear on the edges perpendicular to the axis and then becomes more severe. Along with the circumferential direction (from corrosion center to edge), the area of high longitudinal stress reduces because the bottom of the pipeline suffers a more severe gravitational loading. With the growth in the corrosion width, the maximum longitudinal stress increases while the growth rate gradually decreases. When the corrosion width increases from 5° to 50°, the maximum longitudinal stress increases by 36.15%.

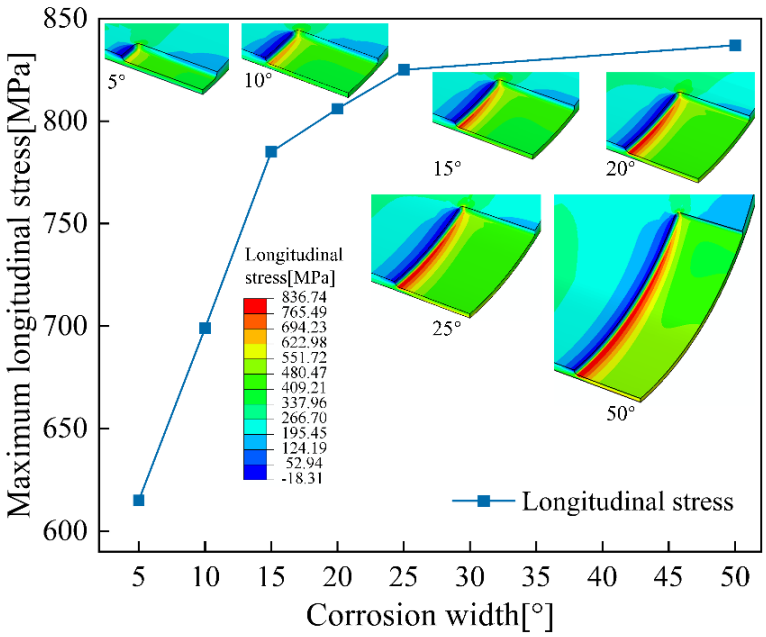

Figure 5-23 Maximum longitudinal stresses and distributions of the pipeline with different corrosion widths.

Figure 5-24 presents the longitudinal strain values and distributions of the pipeline with different widths. No apparent high longitudinal strain occurs for the corroded spanning pipelines with 5° and 10° corrosion widths. However, no matter how wide the corrosion is, compressive strain occurs on the area around the corrosion edges perpendicular to the axis. When the corrosion width is larger than 15°, the area of a high longitudinal strain first appears on the bottom part of the corrosion edges perpendicular to the axis. It then gradually expands along the circumferential direction with the increase in the corrosion width. Meanwhile, the variation of the corrosion width has a neglectable effect on the longitudinal strain distribution of the corrosion center. With the increase in the corrosion width (5° to 50°), the longitudinal strain shows an upward trend and the strain increases by 61.39%. When the corrosion width is smaller than 25°, the increase in the corrosion width results in the longitudinal strain's exponential growth. The growth rate apparently reduces when the corrosion width is larger than 25°.

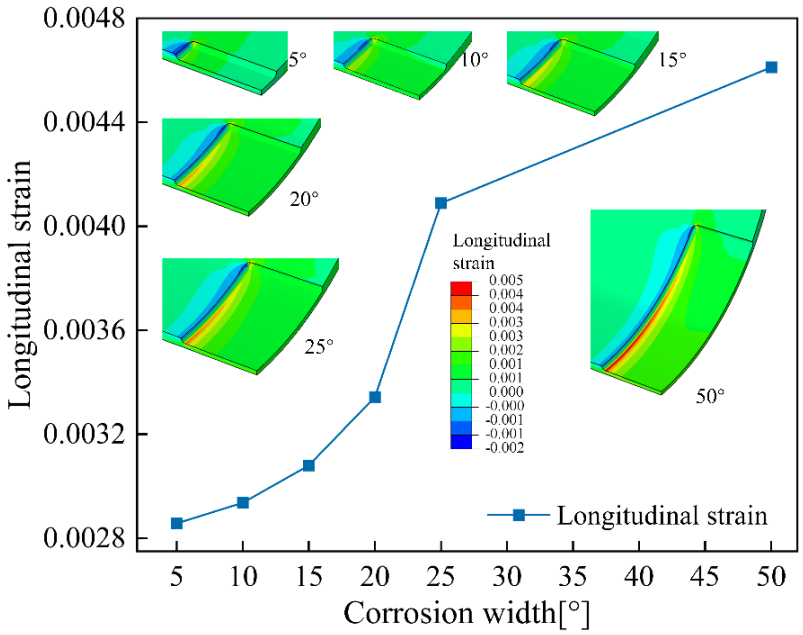

Figure 5-24 Longitudinal strain values and distributions of the pipeline with different corrosion widths.

The SCFs and the maximum vertical displacements of the pipeline under different corrosion widths are plotted in Figure 5-25. Both the SCF and the maximum vertical displacement are on an upward trajectory as the corrosion width grows. However, the SCF increases with a decreasing growth rate. When the corrosion width is 50°, the maximum SCF is 2.81, which increases by 36.1% from 5°. When the corrosion width is smaller than 25°, exponential growth is observed in the maximum vertical displacement. Once the corrosion width exceeds 25°, the growth rate decreases. The increment in the maximum vertical displacement is only 0.38% for the corrosion width ranges from 5° to 50°.

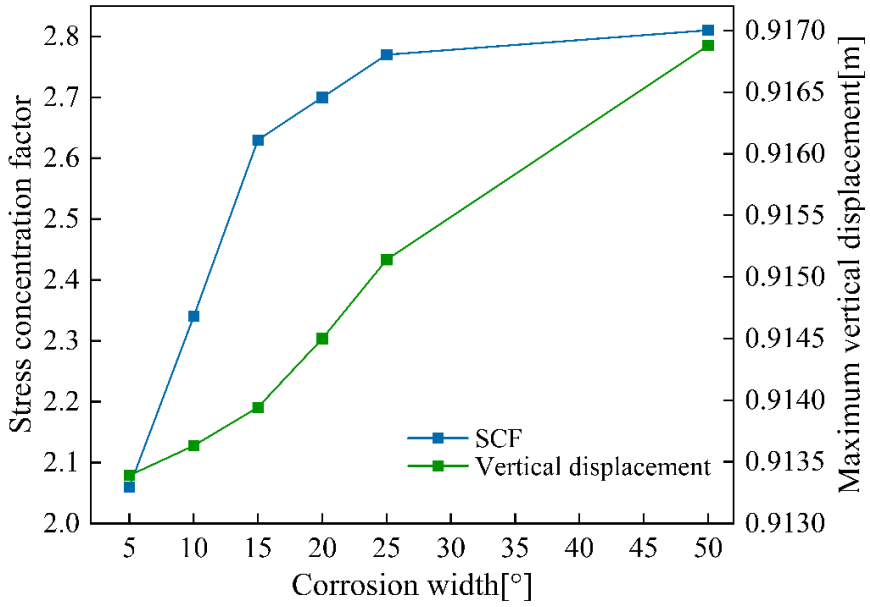

Figure 5-25 SCFs and the maximum vertical displacements of the pipeline under different corrosion widths.

5.3.6 Effect of wall thickness

As one of the most critical factors that affect the structural stiffness of a tubular structure, the wall thickness plays a vital role in the mechanical behavior analysis of the corroded spanning pipeline. To investigate the effect of the wall thickness, DTR is fixed at 50%. Figure 5-26 shows the maximum Von Mises stresses and distributions of the X100 pipeline with different wall thicknesses. High stress occurs in the corrosion area when the wall thickness is 15mm. Moreover, high stress also occurs in the area near the corrosion edges. The increase in the wall thickness will enhance the bearing capacity of the pipeline. Thus, with the rise in the wall thickness, the area of high stress gradually narrows. When the wall thickness exceeds 35mm, the high-stress area mainly appears on the corrosion edges where the geometric discontinuity is significant. With the increase in the wall thickness (15mm to 40mm), the maximum Von Mises stress of the corroded spanning pipeline decreases significantly from 770.91MPa to 613.17MPa. The reduction is by 20.46%.

The maximum longitudinal stresses and distributions of the corroded spanning pipeline are

shown in Figure 5-27. When the wall thickness is smaller than 25mm, the high longitudinal stress area mainly occurs on the corrosion edges perpendicular to the axis. When the wall thickness is 15mm, high longitudinal stress also appears in the area near the corrosion corners. With the increase in the wall thickness, the area of high longitudinal stress gradually decreases, and the high longitudinal stress almost disappears once the wall thickness exceeds 30mm. The maximum longitudinal stress declines (from 839.76MPa to 519.80MPa) with the wall thickness increase (from 15mm to 40mm). The reduction reaches 38.1%.

The values and distributions of the longitudinal strain of the pipeline with different wall thicknesses are presented in Figure 5-28. The high longitudinal strain occurs on the corrosion edges perpendicular to the axis when the wall thickness is 15mm. Once the wall thickness is larger than 20mm, the longitudinal strain distribution of the pipeline under the effects of internal corrosion, internal pressure, and spanning is barely affected by the variation in the wall thickness. With the increase in the wall thickness, the longitudinal strain decreases with different growth rates. When the wall thickness is smaller than 20mm, the reduction in the longitudinal strain with the increase in the wall thickness is sharp. However, the reduction is more moderate when the wall thickness is larger than 20mm.

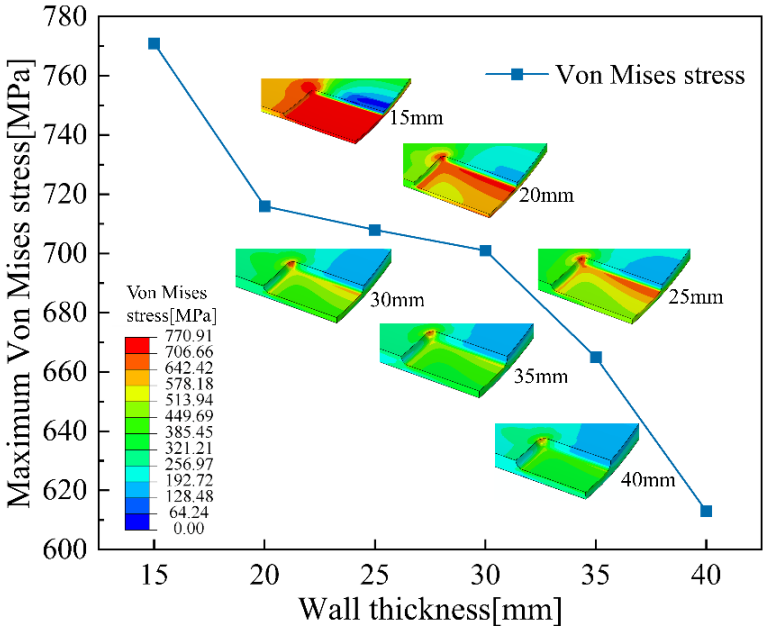

Figure 5-26 Maximum Von Mises stresses and distributions of the spanning with different wall thicknesses.

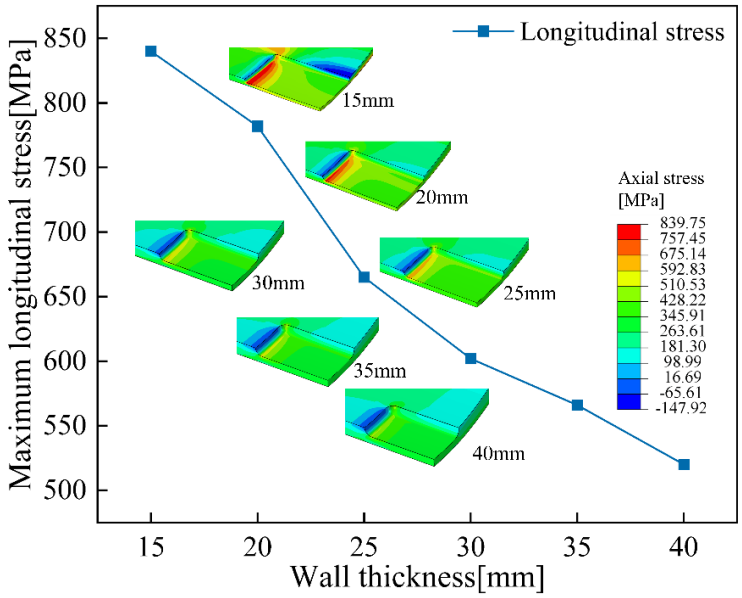

Figure 5-27 Maximum longitudinal stresses and distributions of the pipeline with different wall thicknesses.

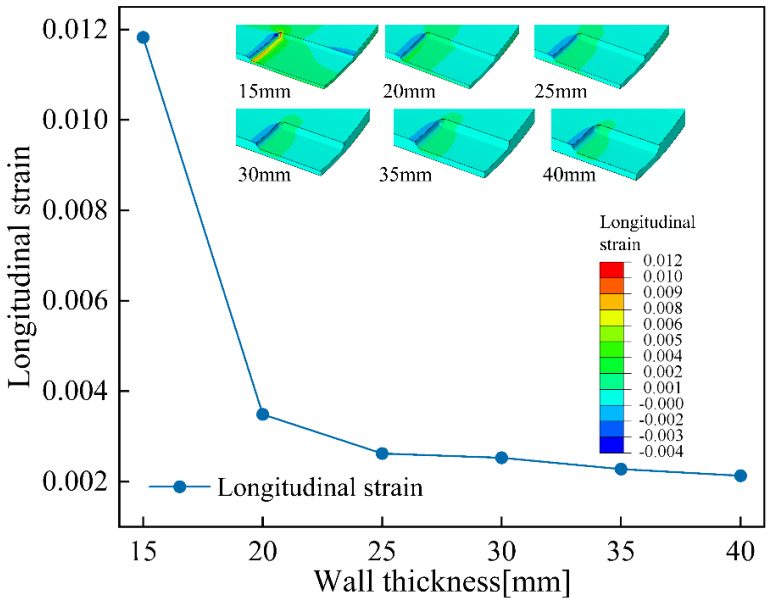

Figure 5-28 Longitudinal strain values and distributions of the pipeline with different wall thicknesses.

Figure 5-29 shows the pipeline's SCFs and the maximum vertical displacements with different wall thicknesses. The minimum SCF appears when the wall thickness is 15mm. The bearing capacity is relatively low for the pipeline with a thinner wall thickness. Thus, the axial stress of the intact pipeline with a 15mm wall thickness is high. When the wall thickness exceeds 20mm, the SCF fluctuates around 2.35. The maximum SCF, which equals 2.39, appears when the wall thickness is 20mm, and the increment from 15mm is 16.04%. Although the longitudinal stresses of both the intact and corroded pipeline decrease with the increase in the wall thickness, they have different growth rates that lead to SCF fluctuations. As the wall thickness increases, the maximum vertical displacement gradually declines with a decreasing growth rate. Although the increase in the wall thickness could enhance the spanning pipeline's deformation-resisting ability, it could also increase the weight of the span part. Therefore, an increase in the wall thickness couldn't continually reduce the vertical displacement of the spanning pipeline. The reduction between the maximum and minimum vertical displacement is about 22.66%.

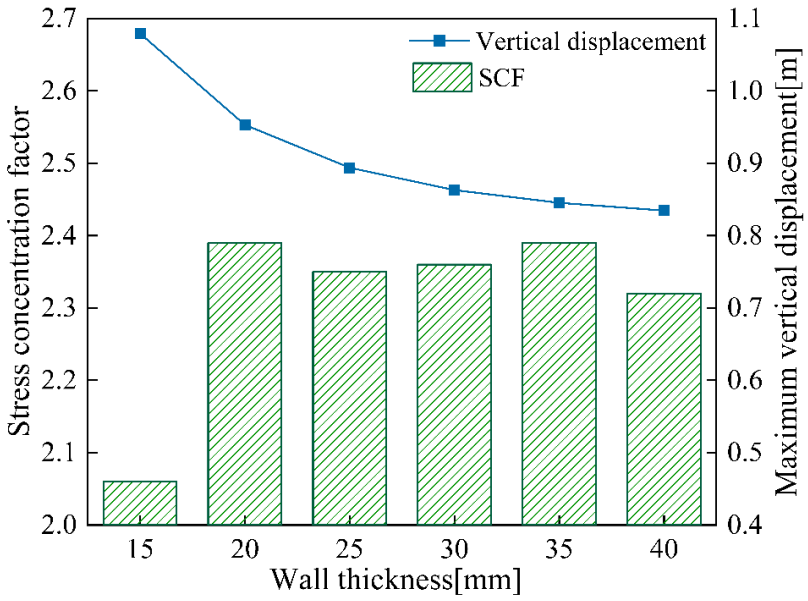

Figure 5-29 SCFs and the maximum vertical displacements of the pipeline with different wall thicknesses.

5.3.7 Effect of internal pressure

In engineering practice, although the allowable internal pressure of a pipeline is usually determined in the design stage, the internal pressure of a pipeline might change or fluctuate due to different transport demands and operations. Thus, the effect of internal pressure should be considered. Figure 5-30 shows the maximum Von Mises stresses and distributions of the corroded spanning pipeline under different internal pressures. When the internal pressure is smaller than 4MPa, no evident high-stress area can be observed in the internal corrosion. Once the internal pressure exceeds 6MPa, and with the growth of the internal pressure, the high-stress area first appears on the corrosion corners, then expands to the corrosion edges, and finally covers the whole corrosion defect. Moreover, when the internal pressure reaches 18MPa, the high-stress area axially extends to the area around the corrosion. The maximum Von Mises stress shows an upward trend as the internal pressure grows. Before the internal pressure reaches 8MPa, the maximum Von Mises stress is in the linear growth phase, indicating that the corroded spanning pipeline is still in the elastic

deformation phase. When the internal pressure is 18MPa, the maximum Von Mises stress of the pipeline is 763.05MPa which exceeds the ultimate tensile stress of the X100 steel. The increment between the maximum Von Mises stress of the pipeline without internal pressure and that of the pipeline with 18MPa is about 217.88%.

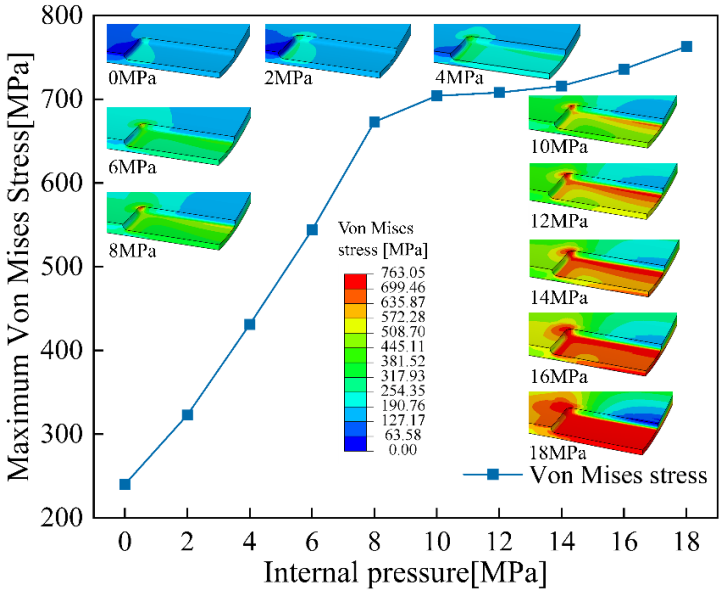

Figure 5-30 Maximum Von Mises stresses and distributions of the pipeline under different internal pressures.

The maximum longitudinal stresses and distributions of the pipeline under different internal pressures are shown in Figure 5-31. When the internal pressure is smaller than 6MPa, no apparent high longitudinal stress occurs in the internal corrosion. After the internal pressure reaches 8MPa, the high longitudinal stress area starts to appear on the corrosion edges perpendicular to the axis and expands along the axial direction as the internal pressure grows. With the increase in the internal pressure, the maximum longitudinal stress linearly grows when the internal pressure is smaller than 14MPa. The growth rate reduces when the internal pressure exceeds 14MPa. The increment of the maximum longitudinal stress for the internal pressure ranging from 0MPa to 18MPa is about 229%.

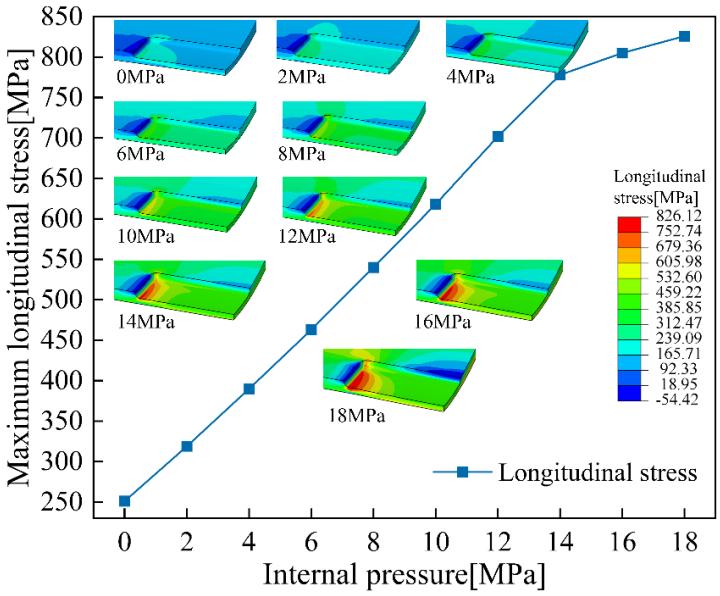

Figure 5-31 Maximum longitudinal stresses and distributions of the pipeline under different internal pressures.

Figure 5-32 presents the longitudinal strain values and distributions of the pipeline under different internal pressures. With increased internal pressure, the tensile strain expands from the corrosion edges perpendicular to the axis to the corrosion center. When the internal pressure is 18MPa, evident high longitudinal strain occurs on the corrosion edges perpendicular to the axis and the corrosion corners. Before the internal pressure reaches 14MPa, the longitudinal strain linearly increases with the growth in the internal pressure. When the internal pressure is larger than 14MPa, the growth rate of the longitudinal strain shows an evident rise. When the internal pressure is 18MPa, the longitudinal strain is the maximum, and its value is 0.0075, which is 6.41 times larger than that of the pipeline without internal pressure.

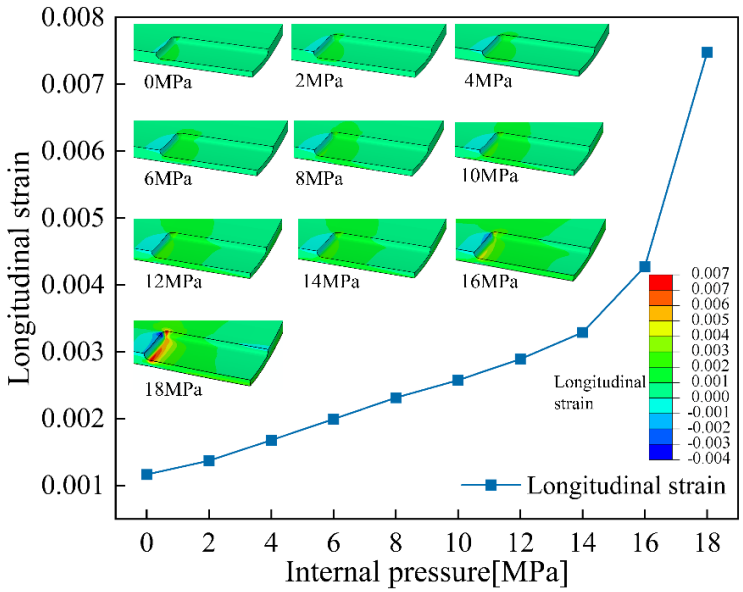

Figure 5-32 Longitudinal strain values and distributions of the pipeline under different internal pressures.

The SCFs and the maximum vertical displacements of the corroded spanning pipeline under different internal pressures are shown in Figure 5-33. The pressure applied on the pipeline's internal surface could result in a corroded pipeline's bulging or even burst behaviors. Thus, the deformation of a corroded pipeline under internal pressure is larger than that of the pipeline without internal pressure. With the increase in the internal pressure, the maximum vertical displacement shows an upward trend. The increment in the maximum vertical displacement is about 76.55%. When the internal pressure is smaller than 12MPa, the SCF grows as the internal pressure increases. However, once the internal pressure exceeds 12MPa, the SCF shows a downward trend. After the internal pressure reaches 12MPa, the growth in the longitudinal stress of the intact pipeline is larger than that of the corroded pipeline. The maximum SCF appears when the internal pressure is 12MPa, which is 1.16 times larger than the minimum SCF when the pipeline is not pressurized.

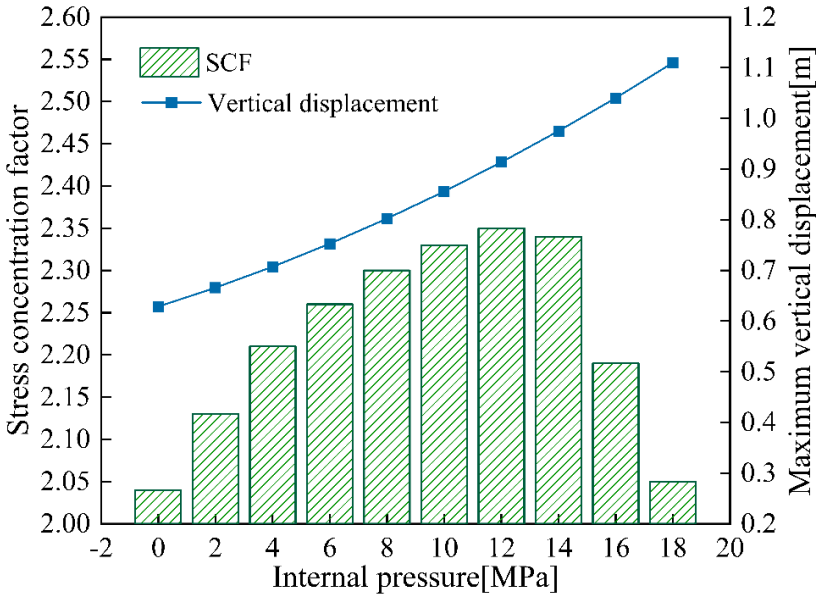

Figure 5-33 SCFs and the maximum vertical displacements of the pipeline under different internal pressures.

5.4 Conclusions

The spanning phenomenon is a major threat to the safety and reliability of long-distance pipelines. The existence of internal corrosion could make matters worse for high-strength spanning pipelines. In this chapter, a series of numerical simulation models are developed to systematically investigate the mechanical behaviors of the high-strength spanning pipeline with internal corrosion. The feasibility and reliability of the numerical model considering the pipe-soil effect and corrosion are validated against experimental results. A parametric analysis is conducted to study the impact of essential factors, such as geometric features of the corrosion, spanning length, internal pressure, etc. The main conclusions are as follows:

(1) Internal corrosion significantly increases the maximum Von Mises stress of the spanning pipeline, indicating a higher risk. For the intact spanning pipeline, the maximum Von Mises stress appears on the bottom surface of the span end. However, the maximum Von Mises stress is in the corrosion of the spanning pipeline with internal corrosion.

(2) The maximum longitudinal stress, longitudinal strain, and the maximum vertical displacement rise with the increase in the spanning length while SCF decreases. When the spanning length is smaller than 60m, it has an ignorable impact on the maximum Von Mises stress. High longitudinal stress and strain area occur on the corrosion edges perpendicular to the axis and the corrosion corners. When the spanning length increases from 20m to 140m, the increment in the maximum longitudinal stress is about 122.6%, while the maximum Von Mises stress is only about 0.675%.

(3) The axial location of the internal corrosion has a neglectable impact on the maximum Von Mises stress. With the increase of the axial location, the maximum longitudinal stress and strain gradually grow while SCF decreases except for $0/10l_s$. The maximum SCF appears when the axial location is $0/10l_s$. When the location is $0/10l_s$ and $1/10l_s$, the dominant longitudinal strain is compressive strain. Axial location barely impacts the maximum vertical displacement except for $1/10l_s$.

(4) Geometric features of the internal corrosion significantly impact the spanning pipeline's mechanical behaviors. Growths in the corrosion length and depth lead to increases in the maximum Von Mises stress, maximum longitudinal stress and strain, SCF, and maximum vertical displacement. The maximum longitudinal stress and strain, SCF, and maximum vertical displacement increase with the growth in the corrosion width. When the corrosion width is smaller than 20°, the maximum Von Mises stress of the pipeline is not sensitive to the variation of the corrosion width. The longitudinal strain increments over the corrosion depth, width, and length variations are 2976.422%, 61.39%, and 24.19%, respectively. Therefore, unlike corroded pipelines without spanning, corroded spanning pipelines could be significantly impacted by the corrosion width.

(5) The thicker the wall thickness is, the stronger the structural stiffness of the spanning pipeline becomes. The high-stress area, high-strain area, maximum Von Mises stress, maximum longitudinal stress, longitudinal strain, and maximum vertical displacement decrease with the wall thickness growth. However, the maximum SCF appears when the

wall thickness is 20mm, and the increment from 15mm is 16.04%.

(6) The corroded spanning pipeline becomes more dangerous as the internal pressure increases. With the rise in the internal pressure, the high-stress area, high-strain area, maximum Von Mises stress, maximum longitudinal stress, longitudinal strain, and maximum vertical displacement all show an upward trend. The increment of the maximum longitudinal stress for the internal pressure ranging from 0MPa to 18MPa is about 229%. However, the maximum SCF appears when the internal pressure is 12MPa.

The results obtained in this chapter are valuable for further fatigue analysis, optimization design, and integrity management of spanning pipelines with internal corrosion. In future work, multiple corrosion defects and other external loadings, such as flood loading, should be considered.

Chapter 6. Study of wear behaviors and prognostics of gears subject to surface wear and pitting

6.1 Overview

In industrial fields, gears are widely used in various applications, such as wind turbines, helicopters, automobiles, and so on. Through meshing with another toothed part, gears are used as fundamental building blocks in mechanical power transmission systems to transmit torque and power [46]. In operation, heavy load and sliding motion on the cut teeth significantly impact gears' health conditions [37]. Throughout the service life, there are four major failure modes for gears, i.e., surface wear, bending fatigue (fatigue cracking), contact fatigue, and scoring. Each failure mode could significantly impact the performance and reliability of gears and ultimately affect the safety of mechanical systems. Previously, relevant research on failures of gears was mainly focused on the effects of the fatigue crack on the health condition. In this chapter, our research emphasizes surface wear as well as the interaction with pitting, which significantly impacts gears' performance.

Through contact and rotation, gears can achieve torque and power transmission. During the meshing process, teeth are forced to contact others, which could result in heavy contact pressure on the mating surfaces. The tangential velocity of different teeth is different, causing sliding motion between the contacted pairs. Surface wear will appear on mating tooth flanks due to sliding contact. As a result, removal or displacement of materials happens to gear teeth. Although lubricant can be used for wear reduction, metal-to-metal contact and wear are unavoidable due to the high contact pressure [251,252]. During the wear propagation, material losses will gradually change the tooth profile and further contact status, increasing vibration and noise and accelerating gear failure [47]. Predicted information about wear conditions is required to avoid unexpected failures and downtime.

Wear depth is usually regarded as an index of wear propagation. With a certain wear severity threshold and wear information, the RUL of a gear can be estimated.

Over the past years, surface wear behaviors of meshing gears have received great interest for gear performance improvement. The experimental method is the most widely used approach to investigating the surface wear behaviors of gears. Amarnath et al. [253] investigated the effects of surface wear on the performance of spur gears through accelerated tests. It is found that wear severity directly influences the decrease in mesh stiffness. Krantz and Kahraman [254] experimentally investigated how the lubricant viscosity and additives impact the wear behaviors of spur gears. It is found that the wear rate of meshing surfaces shows an upward trend with a decrease in the viscosity of the lubricant. Based on Taguchi's method, Sudhagar and Rao [255] designed a series of tests to study the wear behaviors of spur gears performing in dry conditions. A pinion is the smaller gear of a pair of meshing gears. It is found that for a gearbox with one gear and pinion, the pinion shows more severe wear than the gear. Besides, the increase in the local contact temperature could cause a higher wear rate. Thus, the wear rate of meshing gears plays a vital role in wear behaviors. In recent years, the finite element method (FEM) gradually started to be employed to simulate the wear process. Based on FEM and Archard's model, Qin et al. [256] proposed an integrated method to determine the wear coefficient in mixed lubrication. Based on Archard's model, Hegadekatte et al. [257] developed the Global Incremental Wear Model to simulate micro gears wear.

Pitting is a common metal loss defect that occurs on gear teeth due to the long-period contact fatigue caused by the periodical contact between the mating surfaces [258]. Pitting on the tooth surface could impair the bearing capacity, change the tooth profile and result in apparent changes in mesh stiffness and load distribution, which could influence the failure behaviors and remaining useful life (RUL) of defected gears [40]. Besides, the wear propagation process will also be affected due to changes in the contact status. Unlike surface wear, pitting damage belongs to localized tooth faults which might lead to more

severe damage. Without proper handling, pitting would result in serviceability loss in mechanical power transmission systems and even serious accidents. Gear pitting is prone to be affected by several factors, such as lubrication condition, surface roughness, material properties, sliding-rolling ratio, etc. Experimental, analytical, and numerical methods are the three widely used approaches for studying how pitting affects gears. The application of experimental and analytical methods can be found in Ref. [259–261]. Moreover, FEM is usually used as a substitute or supplement to experimental methods. The application of FEM for the investigation of gears with pitting is presented in Ref. [164,165,262].

Although previous research contributed a lot to the effects of surface wear and pitting on the performance of meshing gears, barely any previous research involved the interaction between surface wear and pitting. Thus, it is essential to investigate the impact of the pitting on the surface wear behaviors of spur gears. It is valuable for future prognostics and failure analysis of gears to prevent potential gearbox failures efficiently.

The research results of mechanical and wear behaviors of meshing gears are fundamental for the further prediction of surface wear propagation. With the essential information on wear behaviors and predicted wear depth, the dynamic performance of meshing gears can be assessed to prevent unexpected failures and optimize maintenance strategies. Many researchers and companies have put great efforts into prognostic methods to avoid unexpected failures due to gear surface wear. Physics-based, data-driven and integrated methods are the three major types of prognostic methods applied.

The physics-based methods for gear failures are mainly based on physical models, such as Archard's model and Paris' law [128,263,264]. Shen et a. [265] employed Archard's model to estimate the surface wear evolution of spur gears and then investigated the wear-induced fault mechanism of planetary gears. Based on the "single point observation principle" and Archard's model, Flodin and Andersson [136] developed a modified wear model for surface wear prognostics in helical gears. Considering the impact of elastohydrodynamic lubrication (EHL), Wang et al. [266] extended Archard's model to a lubricated situation

and then estimated the wear degradation process through the extended Archard's model. Although physics-based methods seem convenient to be applied, they have limited application scenarios that are simple and specific. Besides, extra efforts are often needed to modify physical laws. In physics-based methods, model parameters are usually assumed as constant without considering any uncertainty or changes happening in the degradation.

When experimental data or monitoring data is sufficient, data-driven methods can be applied for health estimation and RUL prediction [267–269]. Based on the neural networking method, Zhang et al. [150] proposed an adaptive trend prediction method to predict gears' degradation accurately. Ni et al. [270] developed a new health indicator to reflect the variation in modulation characteristics and then proposed a data-driven prognostic scheme to predict the remaining useful life based on the new health indicator. Zaidi et al. [271] proposed a data-driven prognostic method based on hidden Markov models to predict the future fault severity of gears with sparse historical data. Although data-driven methods usually show good performance in prognosis, they do not work well when data is insufficient due to measurement errors and inspection costs. Moreover, data-driven methods may end up with pointless inferences at times.

Thus, integrated methods are up-and-coming in the prognostics field because they benefit from the combination of the physics of failure models and condition monitoring data. For integrated prognostic methods, the essential parameters used in the physics-based models are usually regarded as random variables which can be modified or updated by the usage of condition monitoring data. Based on the particle filter, Zio and Peloni [272] presented an integrated prognostic method for the estimation of the remaining useful life of nonlinear components. As a Monte Carlo-based tool, the particle filter is effective for dealing with non-Gaussian noise. Tian et al. [154,273] investigated the crack propagation of spur gears, where Bayesian inference was employed to update the key parameters in Paris' law. Polynomial chaos expansion was then used to boost the efficiency of the Bayesian inference process. Besides, Tian et al. [46] also applied a similar integrated prognostic

scheme to predict the surface wear propagation of spur gears.

Although the contribution of previous research is valuable for improving integrated prognostic methods of gear wear prediction, some gaps still need to be filled. Existing prognostic methods for gear wear are mainly based on Archard's model, which requires contact pressure and sliding distance at each contact point. However, the contact pressure and sliding distance are commonly evaluated by analytical methods, such as Hertz contact theory and the theoretical sliding distance model mentioned in Ref [46]. Because of limitations of the evaluation process through analytical methods, inaccuracies will be introduced to the wear depth estimation and further RUL prediction. In addition, the contact pressure and sliding distance are usually assumed to be constant during the surface wear propagation without considering the impact of the change in the tooth profile. The ignorance of the impact of change in the tooth profile could result in inaccurate contact pressure and sliding distance evaluations. Furthermore, the effect of friction between meshing surfaces is also ignored. Furthermore, the wear coefficient could dramatically change in value due to different contact material properties or contact conditions. Simply ignoring the change in wear coefficient will result in inaccuracy in FE surface wear simulation as well as the prognostics.

Therefore, in this chapter, FE models of spur gears with and without pitting are established and validated to investigate the effects of pitting on contact status and surface wear. In addition, a new prognostic method, integrating the physics-based model, FEM, and condition monitoring data, is proposed for gears subjected to surface wear to achieve a better wear propagation simulation and prognosis. Unlike classic Hertz contact theory, FEM could better deal with contact problems involving complex contact surfaces, friction, and possible plastic problems. Besides, FEM could better address the problem caused by the tooth profile change introduced by surface wear when estimating the sliding distance. Thus, FEM is applied to accurately calculate meshing gears' contact pressure and sliding distance. Archard's model is used to evaluate the wear depth and provide information for

tooth profile updating. Through tooth profile updating, much more reliable surface wear propagation can be realized. Condition monitoring data and Bayesian inference are employed to update the parameter in Archard's model so that a more accurate wear propagation prediction can be realized.

The remainder of the chapter is organized as follows. Section 6.2 presents the key theoretical models needed in this chapter. Section 6.3 illustrates FE models of the sun gears and the detailed process of the wear simulation. Besides, the FE model validation is conducted. In Section 6.4, the numerical simulation results are presented and discussed. Section 6.5 presents the framework of the proposed prognostic method. Examples to demonstrate and validate the proposed method are provided in Section 6.6. The last part concludes the chapter and outlines the area of future research.

6.2 Theoretical models

6.2.1 Hertz contact theory

The power transmission between meshing gears is achieved through contact between mating surfaces [274]. Contact stress could cause severe damage to gear teeth, such as pitting and wear. Hertz's contact theory is widely used to estimate the contact stress at the contact point. A pair of spur gears mating at the pitch point and stress state depicted by Hertz contact theory are shown in Figure 6-1. According to previous research, Hertzian contact stress is defined as the localized stresses caused by the contact and deformation between two curved surfaces under the action of compressive loads. Hertz's contact theory assumes that the stress across the width follows the elliptical distribution. This theory provides the expression of the contact stress in terms of the normal contact force, the radii of curvature at the contact point, and Young's modulus. Based on the contact between two cylinders, the contact stress between mating spur gears is developed [275]. The Hertz contact theory used in meshing gears can be expressed by Eqs. (6-1~6-3).

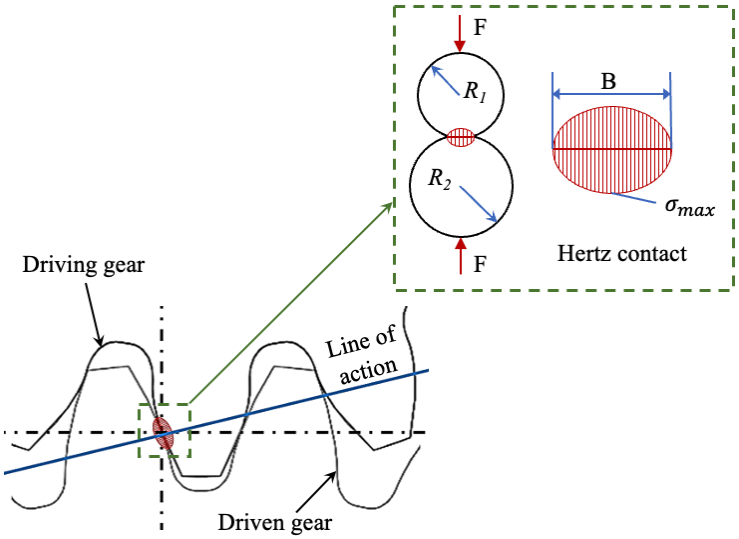

Figure 6-1 Schematic plot of Hertz contact theory applied for mating gears.

$$\sigma_{max} = \sqrt{\frac{F}{\pi l}\left(\frac{\frac{1}{R_1}+\frac{1}{R_2}}{\frac{(1-\gamma_1^2)}{E_1}+\frac{(1-\gamma_2^2)}{E_2}}\right)} \tag{6-1}$$

$$R_1 = r_{p1}\sin\alpha \tag{6-2}$$

$$R_2 = r_{p2}\sin\alpha \tag{6-3}$$

where σ_{max} is the maximum contact stress, E_1 and E_2 are Young's moduli of two gears, γ_1 and γ_2 are Poisson's ratios of two gears, F is the compressive force, l is the face width of the gears, R_1 and R_2 are respective radii of the involute curve at the contact point, and r_{p1} and r_{p2} are the pitch radii of the gears.

6.2.2 Archard's wear model

Archard's wear model is a classic wear model developed based on the theory of asperity contact from a micro point of view [128]. Among the previous research work, Archard's wear model has been widely used to conduct the quantitative analysis on wear progression for machineries, such as gears and bearings. Classic Archard's wear model, expressed as Eq. (6-4), assumes that the wear process of contact surfaces is mainly influenced by the contact stress, sliding distance, and the hardness of materials.

$$h = kps \tag{6-4}$$

where h is the wear depth, k is the dimensional wear coefficient, and p is the contact stress between contact surfaces, s is the sliding distance.

In FEM, Archard's wear model can be discretized into the following form:

$$h_{n+1} = h_n + kp_{n+1}\Delta s_{n+1} \tag{6-5}$$

where h_{n+1} is the wear depth at n+1 wear increment, h_n is the wear depth at n+1 wear increment, p_{n+1} and Δs_{n+1} is the contact stress and the sliding distance at the n+1 wear increment, respectively.

6.2.3 Bayesian inference method

As a classical statistical inference method, Bayesian inference is usually applied to update the probability of a hypothesis once more information can be obtained. For integrated prognostic methods, Bayesian inference is widely used to realize the objective of updating essential parameters with condition monitoring data because of its capacity for sequential learning and uncertainty qualification [276,277]. The general formula of Bayesian inference for determining the posterior distribution is expressed as follows:

$$f_{post}(k|d_w) = \frac{l(d_w|k)f_{prior}(k)}{\int l(d_w|k)f_{prior}(k)\,dk} \tag{6-6}$$

where f_{post} is the prior distribution of k, l is the likelihood, d_w is the wear depth, k is the wear coefficient, f_{prior} represents the prior distribution of k.

The likelihood *l* is used to represent the likelihood of observing the wear depth at inspection points up to *j*, and *l* can be expressed as follows:

$$l\left(d_{w_{1:j}}^{obs}\middle|k^{j-1}\right) = \prod_{i=1}^{j}\frac{1}{\sigma\sqrt{2\pi}}\exp\left(\frac{(d_{w_i}^{obs}-d_{w_i}^{p})^2}{2\sigma^2}\right) \tag{6-7}$$

where $d_{w_{1:j}}^{obs}$ is the observed wear depth at inspection time points 1: *j*, *j* is the number of inspections, k^{j-1} is the wear coefficient at the *j*-1 inspection point, σ represents the standard deviation of the measurement error defined as the difference between the real data and observed data, $d_{w_i}^{obs}$ is the observed wear depth at inspection point *i*, $d_{w_i}^{p}$ is the predicted wear depth at inspection point *i*.

Markov Chain Monte Carlo simulation and sampling methods are widely used to solve Bayesian inference equations. In this chapter, the sampling method is adopted to generate histograms of the wear coefficient from the posterior distribution. Since both the prior distribution and measurement error follow normal distributions in the specific case presented in this chapter, the normal distribution is applied to fit the histograms. Thus, the mean value and standard deviation of the posterior distribution can be obtained.

6.3 Finite element modeling

The finite element method has been widely used as a robust methodology to substitute or supplement experiments. FEM has demonstrated exemplary performance in conducting contact analysis of intact or pitting gears. With the development of numerical simulation, FEM can now be used to realize surface wear simulation. Compared to experimental methods, FEM is more flexible and could consider some complex situations that can't be satisfactorily achieved by experiments. Thus, FEM is employed in this chapter to investigate the effect of pitting on the wear behaviors of the sun gear during the meshing process. Moreover, FEM is also employed as a contact analysis tool to develop the simulation-driven integrated prognostic method.

For wind turbines, helicopters, and other mechanical systems, the planetary gearbox is a significant component used to transmit power and torque. There are usually three different types of gear in a planetary gearbox, i.e., ring gear, planet gears, and sun gear. In this chapter, the sun gear is taken as the research object because it is the driving gear that experiences the most severe wear compared with other gears in the gearbox.

6.3.1 Numerical simulation model

The 3D model of the mating involute spur sun gear and spur planetary gear is established in Abaqus 2020, as shown in Figure 6-2. The physical parameters of the sun gear and planet gear are listed in Table 6-1. The two gears are assembled according to the standard

installation, i.e., the gear center distance is 80mm. The transmission torque is fixed as 25000 lb-in, which is applied on the driven gear (planet gear). For boundary conditions, the gears are fixed except for the rotation along the gear's axis. Friction between mating surfaces is taken into consideration. According to previous research, the coefficient of friction is set as 0.1. A long pit across the whole face width is established on one of the gear teeth. Due to the pure rolling phenomenon at the pitch point, pitting usually appears around the pitch line. Thus, the pit in this model is around the pitch line. The depth and width of the long pit is 0.3mm and 1mm, respectively.

Table 6-1. Physical parameters of the sun gear and planet gear.

Parameters	Sun gear	Planet gear
Number of teeth	19	31
Module (mm)	3.2	3.2
Pressure angle (°)	20°	20°
Face width (mm)	38.1	38.1
Young's modulus (GPa)	206.8	206.8
Poisson's ratio	0.3	0.3

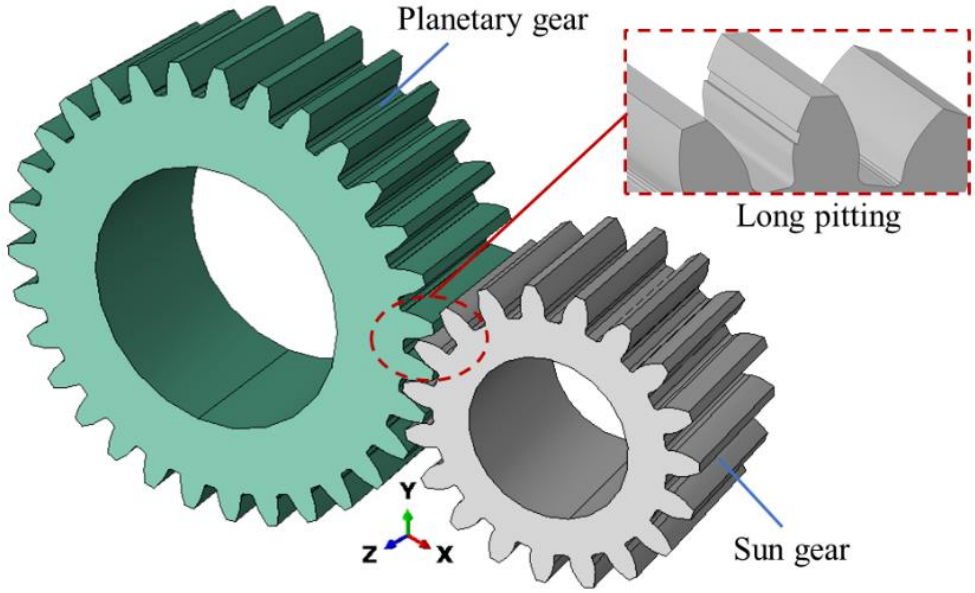

Figure 6-2 Numerical model of meshing spur gears.

Meshes of the sun gear tooth are shown in Figure 6-3. Eight-node and hexahedron elements, widely used in previous studies to deal with problems about meshing gears, are applied to mesh the sun gear and planet gear model. To improve computing efficiency and ensure simulation accuracy, meshes in the region around the contact surface are refined.

To make the research more feasible, some reasonable assumptions are made:

(1) The lubricant condition for meshing gears is neglected.

(2) Only one tooth of the sun gear is taken as an example to simulate the wear process.

(3) Effects of dynamic characteristics are ignored.

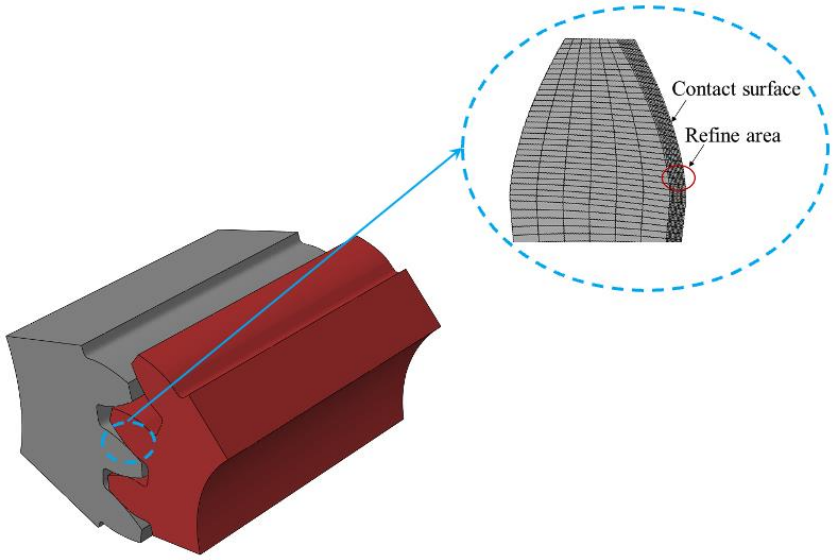

Figure 6-3 Meshes of the gear tooth subjected to wear.

6.3.2 Numerical simulation model validation

UMESHMOTION is a subroutine programmed by Fortran and used to help Abaqus realize wear simulation. Details and example of UMESHMOTION can be found in Abaqus online manual: Chapter 1.1.33 UMESHMOTION. The accuracy of the wear depth estimation in UMESHMOTION is significantly affected by the contact stress obtained from contact analysis conducted by FEM. In previous research, the reliability and feasibility of the FE model of a gear pair are validated by the comparison between the contact stress obtained by FEM and the Hertz contact stress. Although the Hertz contact theory, as expressed in

Eqs. (6-1~6-3), is developed based on some simplifications, it has been widely used to estimate meshing gears' contact stress and proved reliable. The contact stresses of the sun gear at the pitch point calculated through FEM and Hertz contact theory are listed in Table 6-2. The difference in contact stress of FEM from the Hertz equation is only around 0.5%. Although neither FEM contact analysis nor the Hertz contact theory can obtain the actual contact stress value, FEM contact analysis has proven to perform better than the classic Hertz contact theory because FEM could better deal with complex contact surfaces and possible plastic deformation [278]. Thus, the feasibility and reliability of the FE model built in this chapter could be validated.

Table 6-2. Contact stress estimated by FEM and Hertz contact theory.

FEM	Hertz contact theory	Difference
3003.5MPa	2987.6MPa	0.53%

6.3.3 Geometrical feature update

During the wear process, materials are removed from the mating surface, which could change the geometrical features of the gear tooth. When using Abaqus to simulate the wear process, the Fortran subroutine UMESHMOTION is applied to obtain the wear depths and wear directions of the contact nodes on the contact surface. The obtained information will be used to define the node motion, which is applied as re-mesh constraints for contact nodes.

6.3.3.1 ALE adaptive meshing technique

In an analysis, elements could suffer distortion and collapse due to material loss or large deformation, which could significantly influence the simulation accuracy and efficiency. For wear simulation, elements near the contact area should be taken seriously. In some extreme cases, an analysis could be stopped without obtaining final results due to the distorted elements. Thus, these elements should be re-meshed to maintain high quality. The arbitrary Lagrangian-Eulerian (ALE) adaptive meshing technique is a tool in Abaqus used

to ensure the quality of elements by allowing the movement of elements. Throughout the analysis, the movement is independent of the material. Besides, the ALE technique does not change the initial topology of the elements, i.e., no reduction or increase of the number of elements will occur, as shown in Figure 6-4.

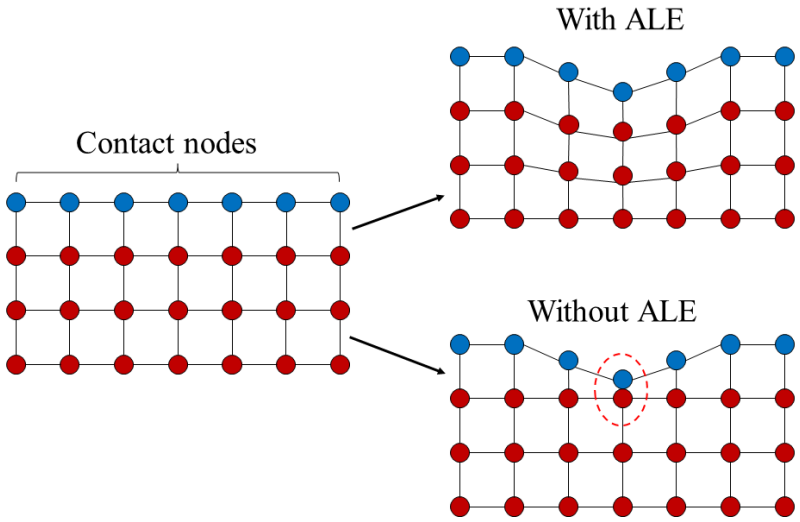

Figure 6-4 Schematic diagram ALE adaptive meshing technique.

6.3.3.2 Wear simulation process in Abaqus

The combination of contact analysis, UMESHMOTION, and ALE meshing technique is applied to realize the simulation of wear propagation on the mating surface of the spur gear. Such wear simulation routine has barely been used for gears. Most applications are dedicated as supplements to wear coefficient tests. The flowchart of the surface wear simulation is shown in Figure 6-5. The first step is to establish an FE model of the gear pair based on primary parameters, such as the geometrical parameter, material property, and boundary condition. Once the FE model is established, contact analysis could be performed to obtain the contact stress ($p_{i,n}$) and relative sliding distance ($\Delta s_{i,n}$) at each contact point in the second step. In the third, the subroutine UMESHMOTION is used to recall the contact stress and sliding distance from the simulation results obtained in the previous step. Based on Archard's model, the wear depth can be calculated, and the wear direction can be determined. In step 4, UMESHMOTION and ALE meshing techniques

are employed to update the geometry of the wear region. If the number of loading cycles is smaller than the maximum number, which is determined by the user, step 2~ step 4 will be repeated. Otherwise, the process of the wear simulation will be stopped. Through this process, the wear process can be simulated and visualized.

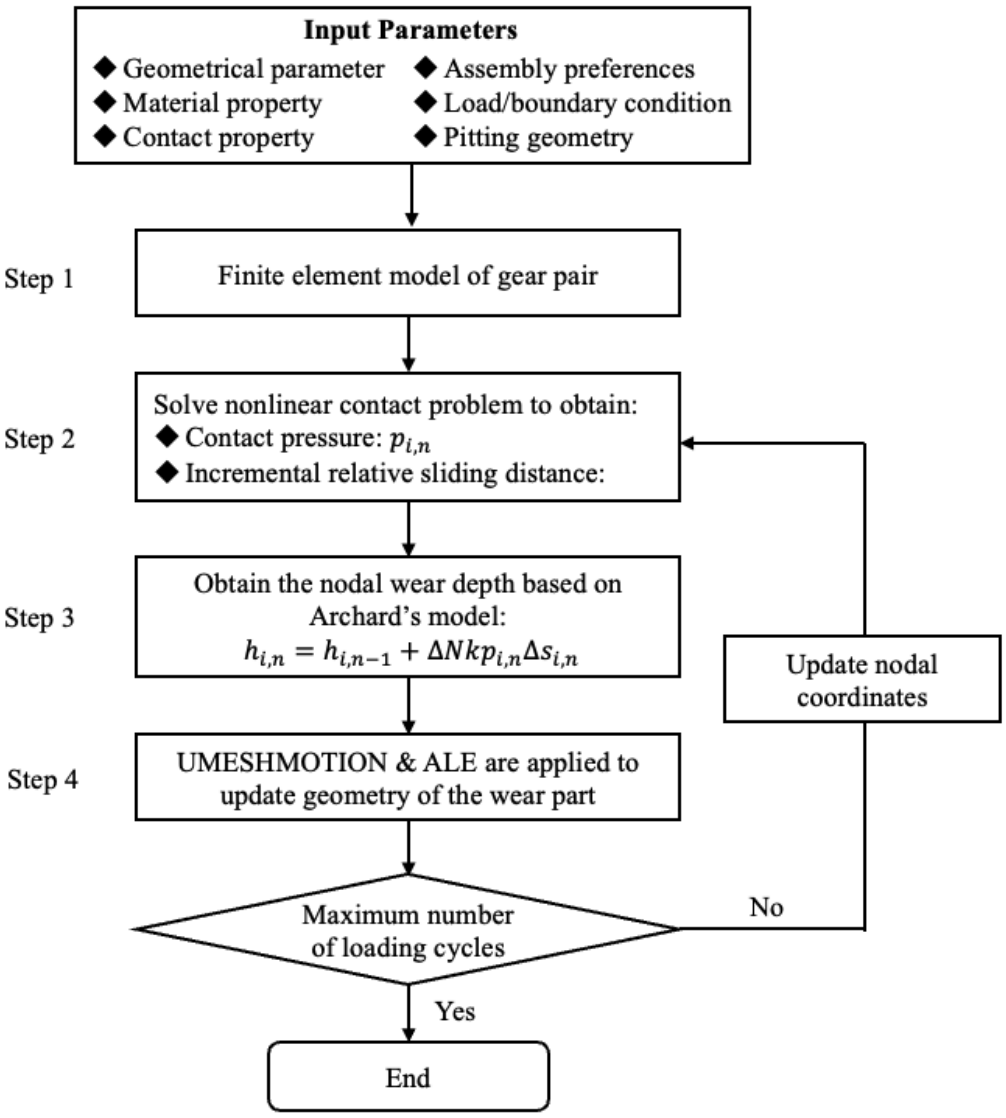

Figure 6-5 Flowchart of wear simulation in Abaqus.

6.4 Numerical simulation results and discussion

6.4.1 Contact stresses of the gear with and without pitting

Pitting is a vital threat to gears' health, which is caused by repeated stress on gear teeth. Pitting could change the contact stress distribution of the contact surface. The comparison between the contact stress distributions of the intact sun gear and that of the sun gear with a long pit is shown in Figure 6-6. Since the reduction in the contact area, the contact stress of the defected gear around the pitch point is higher than that of the intact gear. The maximum contact stress around the pitch line appears at the pit's edges for the sun gear with a long pit.

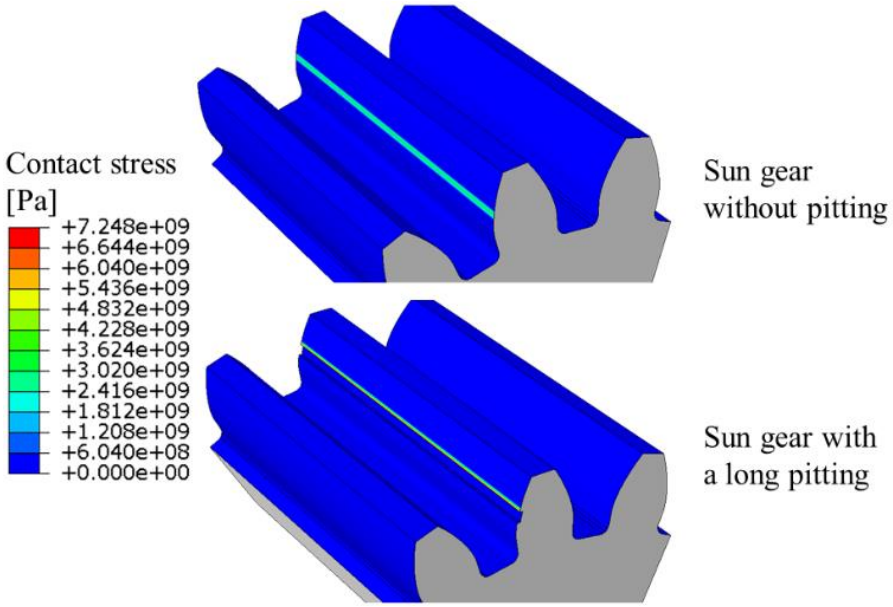

Figure 6-6 Contact stress distributions of the sun gear with and without pitting.

Figure 6-7 shows the comparison of the maximum contact stress along the tooth profile between intact and pitting gears. It is obvious that the maximum contact stresses of the pit edges are dramatically larger than that of the same area on the intact gear's surface. The difference reaches around 3 times. The maximum contact stress of the down edge of the pit, which closes to the gear root, is slightly larger than that of the up edge. With the increase in the meshing cycle from 200 cycles to 4000 cycles, the fluctuation in the maximum contact stress reduces. However, the maximum contact stress of both pit edges almost remains the same. As Archard's model is a function of contact stress, sliding distance, and wear coefficient, the change in contact stress could significantly affect the wear depth

estimation. Thus, pitting could affect the wear propagation process.

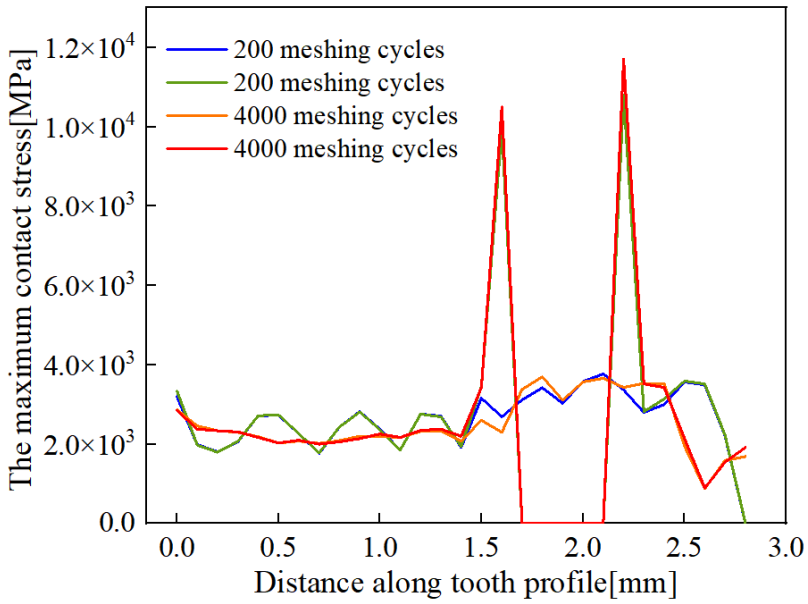

Figure 6-7 Comparison of the contact stresses between intact and pitting gears.

6.4.2 Wear behaviors of the gear with and without pitting

In this section, the wear coefficient is set as 1.27e-15 Pa^{-1}. In this case, each tooth of the sun gear must mesh 3.2 times with the other four planet gears in the gearbox every mesh cycle. After wearing, the tooth profile will be changed. Figure 6-8 plots the comparison between the tooth profiles, which are simulated by FEM, of the gear before and after wearing. It is obvious that surface wear along the tooth profile is uneven. Evident metal loss happens to the areas around the tooth top and root. The change in the tooth profile caused by surface wear is insignificant around the pitch line because the sliding distance in this region is relatively small.

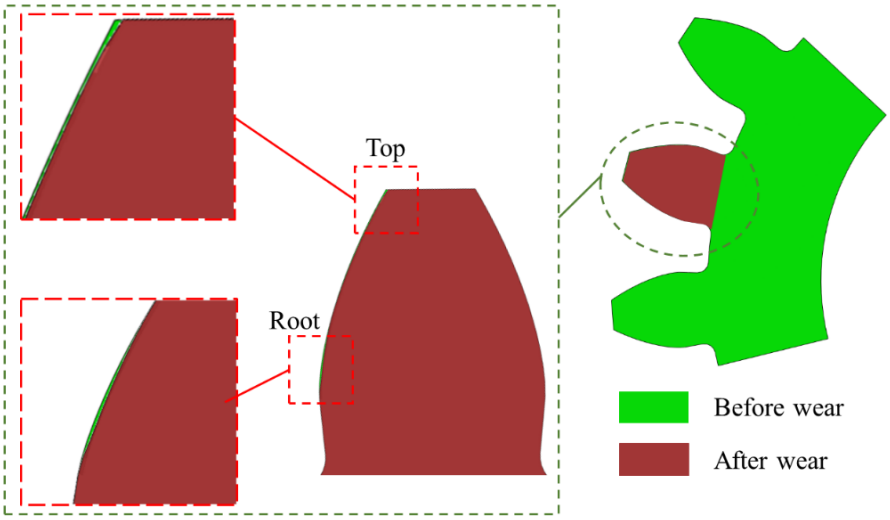

Figure 6-8 Tooth profile change due to surface wear of spur gear.

The change in the tooth profile of the pitting gear caused by surface wear is shown in Figure 6-9. Like the normal spur gear, obvious metal loss occurs around both the gear top and root. However, evident change also can be observed in areas near the pit edges. The pit edge that closes to the gear top is defined as the top edge while the edge closes to the gear root is defined as the bottom edge. The profile changes are more significant around the pit bottom edge than the top edge.

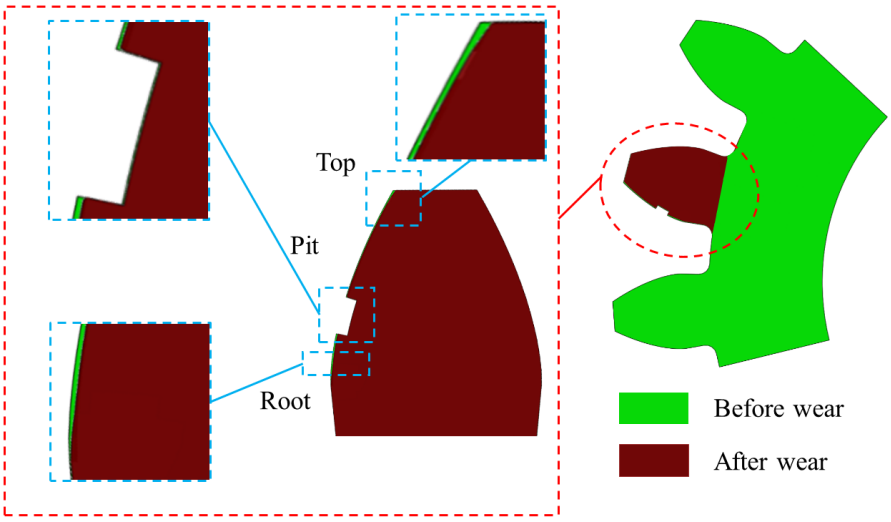

Figure 6-9 Tooth profile change due to surface wear of pitting gear.

The accumulated wear depths of each contact point along the tooth profile of the intact sun gear under different meshing cycles are shown in Figure 6-10. Different curves represent

the accumulated wear depths from 200 cycles to 4000 cycles and the inspection interval is 200 cycles. The maximum accumulated wear depth appears near the root area, while the lowest wear depth is around the pitch line, consistent with previous research based on experimental and analytical methods [279]. Figure 6-11 shows the accumulated wear depths of the sun gear with a long pit from 200 cycles to 4000 cycles. The maximum accumulated wear depth still occurs near the root area. Besides, the value of the maximum accumulated wear depth of the pitting gear is equal to that of the intact gear. Nevertheless, an obvious extra peak of the wear depth appears around the bottom edge of the pit. Although an increment in the accumulated wear depth around the top edge can be observed, it is less evident than that around the bottom edge. No surface wear happens in the pitting area.

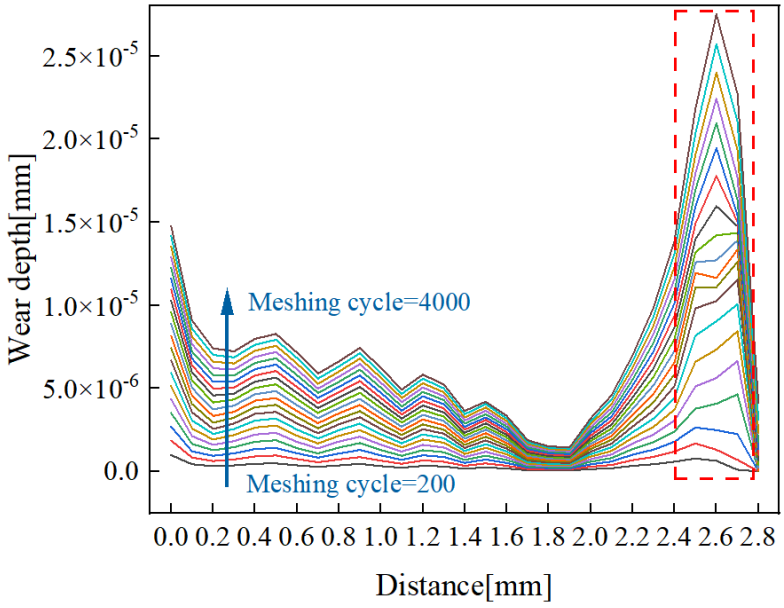

Figure 6-10 Accumulated wear depth of the intact gear under different meshing cycles.

Figure 6-12 shows the accumulated wear depths of pit edge areas of the pitting and intact gears. With the rise in low meshing cycles, the accumulative wear depths of the pitting edge areas show a linear growth trend. Even if the growth of the wear depth in these areas is linear, the contact stress and sliding distance of each point on the tooth surface obtained by FEM are different from cycle to cycle because of the change in the tooth profile.

Therefore, unlike previous studies that treat sliding distance and contact stress as constant, the wear depth obtained here is more accurate. At the same position, i.e., top and bottom edges, the growth rate of the wear depth of the pitting gear is higher than that of the intact gear. When the meshing cycle reaches 4000, the maximum wear depth around the pitting area (top edge) of the pitting gear is almost 4 times larger than that of the intact gear. Therefore, pitting has a significant impact on the wear behaviors of the spur gear, and the area most impacted is around the pit.

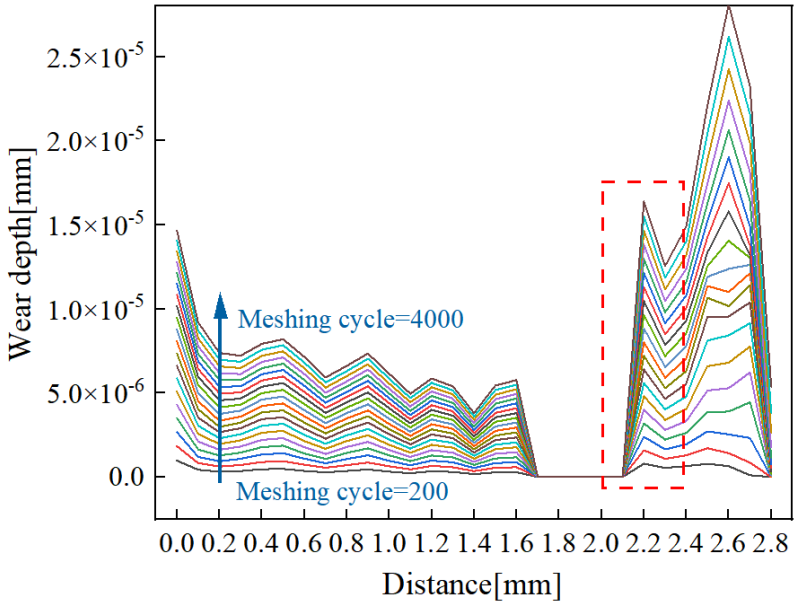

Figure 6-11 Accumulated wear depth of the pitting gear under different mesh cycles.

Since the surface wear of the involute gear is uneven, the wear depth of a contact point is not suitable for estimating the wear severity, average wear depth is selected in this chapter to represent the overall wear situation. Figure 6-13 shows the accumulated average wear depths of the sun gear with and without a long pit. As the meshing cycles increases, the average wear depth grows almost linearly for the gears with and without pitting. It is evident that the pitting gear has more severe surface wear damage because of the larger average wear depth.

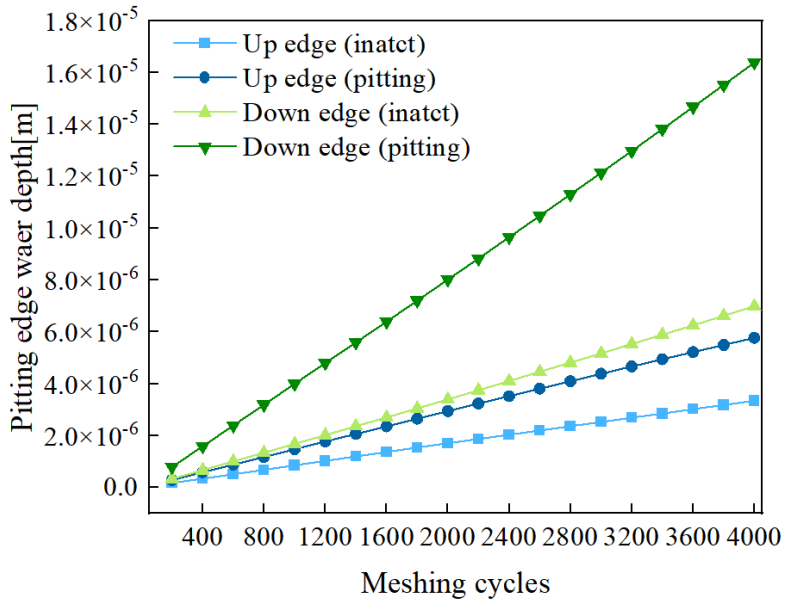

Figure 6-12 Accumulated wear depths of pit edge positions of intact and pitting gears.

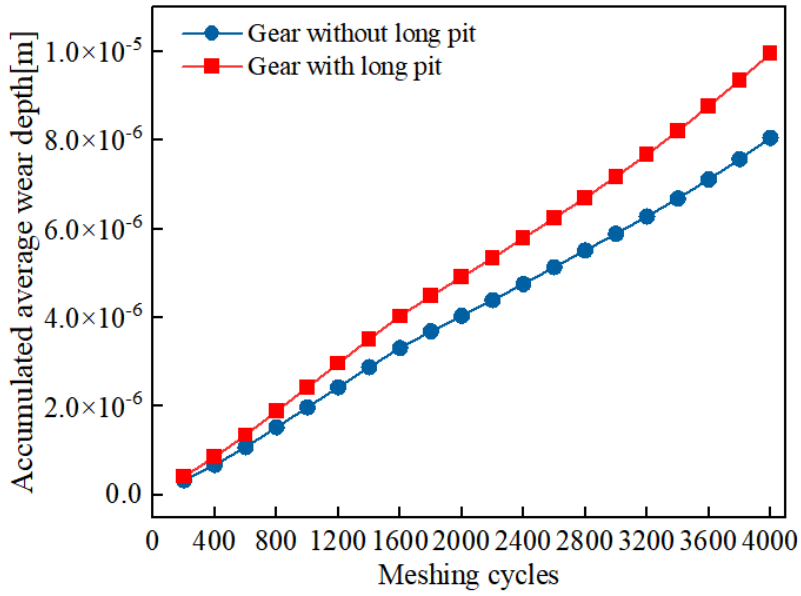

Figure 6-13 Accumulated average wear depths of the gears with and without pit.

6.5 The proposed simulation-driven integrated method for surface wear propagation prediction

The accuracy of physics-based prognostic methods is significantly affected by the model parameters, which require significant effort to be obtained. Contact analysis of gears is

essential for further surface wear evaluation based on the physics-based models because the performance of the contact analysis determines the accuracy of the mating surfaces' contact stress and sliding distance used in the physics-based models. In previous research, contact stress and sliding distance are commonly estimated by analytical methods without considering variations in the geometric features of the tooth profile. The objective of the simulation-driven integrated method is to integrate FEM simulation considering variations in geometric features, physical models, and condition-monitoring data from reliable sources to accurately predict the surface wear propagation and remaining useful life. The framework of the proposed prognostic method in this chapter is shown in Figure 6-14. This framework has four major parts: FEM simulation, physical model, essential parameters update, and data.

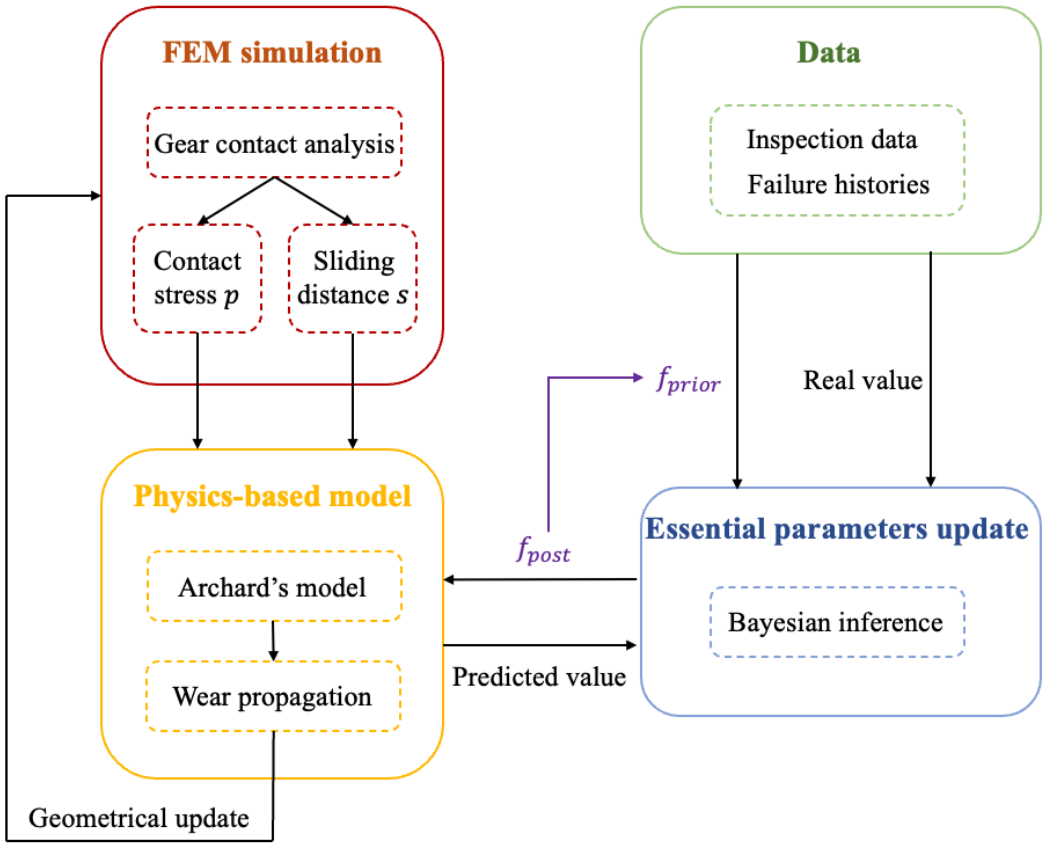

Figure 6-14 Framework of the simulation-driven integrated prognostic method for gear.

6.5.1 FEM simulation

In this part, FEM simulation is employed to perform a contact analysis of meshing gears to obtain contact stress and sliding distance of mating surfaces. The detailed process has been presented in section 6.3.3. Considering the variations in geometric features and friction between mating surfaces, the FEM simulation results of the contact analysis could provide better inputs for further wear depth prediction than analytical models.

6.5.2 Physics-based model

Although several new surface wear models have been developed, Archard's model is still the most recognized and widely used tool for the quantitative evaluation of wear propagation. Eq. (6-5) is applied to describe Archard's model. Combining with subroutine UMESHMOTION and Archard's model, the simulation results can be used to predict the wear depth and then update the tooth profile after wearing. Once the updated wear coefficient is obtained, it will be used in Archard's model.

6.5.3 Data

In this part, two different kinds of data sources are usually required. The first kind is failure histories which could provide prior distribution of the wear coefficient for a population of gears. The second kind is inspection data collected from a particular gear suffering from surface damage and then used in the parameter update process to provide new information. In this chapter, wear depth is employed as an indicator of wear propagation. The data on the wear depth of the gear with the actual coefficient (in tests or FEM) is considered the observed data. Meanwhile, the wear depth evaluated by the physical-based wear model is regarded as the predicted data.

6.5.4 Essential parameters update

The Bayesian inference approach is applied to integrate the physics-based model with the field data in this part. The detailed process of the Bayesian inference approach is presented in section 6.2.3. Since Archard's model is employed in this chapter, the accuracy of the wear coefficient could significantly impact the accuracy of the wear prediction. However, due to different contact material properties or contact conditions, the wear coefficient could change significantly in value. Different gears or different working conditions may result in different wear coefficients. For a population of gears, there could exist uncertainties in the wear coefficient from the population point of view. The uncertainty couldn't be simply ignored. In engineering practice, our focus is on a specific gear instead of a population of gears. Thus, the wear coefficient we care about should be for a particular individual. The uncertainty in wear coefficient and remaining useful life for a specific gear should be less than that for a population. Therefore, a major objective of the proposed method is to achieve uncertainty reduction of the wear coefficient for a better wear prediction.

The initial prior distribution of the wear coefficient is usually obtained from the failure histories of a population of gears or different degradation paths. Thus, the uncertainty of the prior distribution is relatively large. The Bayesian inference will be applied at each inspection point once the predicted and observed data are collected. Posterior distribution could reveal new information after inspections. The posterior distribution of the wear coefficient will be used as the prior distribution for the next update process at the next inspection point. Besides, the mean value of the posterior distribution will be applied to the FEM simulation part and physics-based model part until the next inspection point. If there is no or insufficient information for evaluating the prior distribution, a noninformative prior is acceptable to be used.

6.6 Example based on the numerical simulation data

An example of meshing gears described in Table 6-1 is applied to demonstrate the proposed

integrated prognostic method. Since the experimental conditions are insufficient at this stage, the observed data in this chapter are collected from the FEM simulation results with the real wear coefficient. Although the observed data used in this section are not from experiments, it is enough to clearly demonstrate the proposed method because the FEM simulation can closely mimic the experimental conditions, and the simulation results are reliable.

The actual wear coefficient (k_r) of the specific sun gear is 1.27e-15 Pa^{-1}. The prior distribution of the wear coefficient for a gear population is initially assumed to follow a Gaussian distribution k~N (3e-15, $(1e-15)^2$). Because of the involute tooth profile, the wear depth of each meshing point along the involute line is different. Thus, the average wear depth of all meshing points is selected as the wear propagation indicator for the updating process. By applying the proposed method, the parameter update process is listed in Table 6-3. The updating process for the distribution of the wear coefficient is presented in Figure 6-15. It is obvious that the wear coefficient is progressively updated from its initial distribution to approximate the real value of the specific gear. Moreover, as the number of inspection points increases, the distribution of the wear coefficient gradually narrows, i.e., the uncertainty of the wear coefficient reduces during the updating progress. After six times of updates, the wear coefficient is updated from the initial 3e-15 Pa^{-1} to around 1.2678e-15 Pa^{-1}, and the change rate becomes small. The relative error between the mean value of the wear coefficient distribution and the real wear coefficient dramatically falls from 136.22% to 0.17%.

Table 6-3. The parameter updating process, k_r=1.27e-15 Pa^{-1}.

Inspection #	Meshing cycles	Mean of k	Std of k
0	0	3e-15	1e-15
1	1000	1.2269e-15	4.036e-17
2	2000	1.2572e-15	1.4828e-17
3	3000	1.2590e-15	1.0447e-17
4	4000	1.2643e-15	6.1873e-18
5	5000	1.2667e-15	4.0221e-18
6	6000	1.2678e-15	2.8028e-18

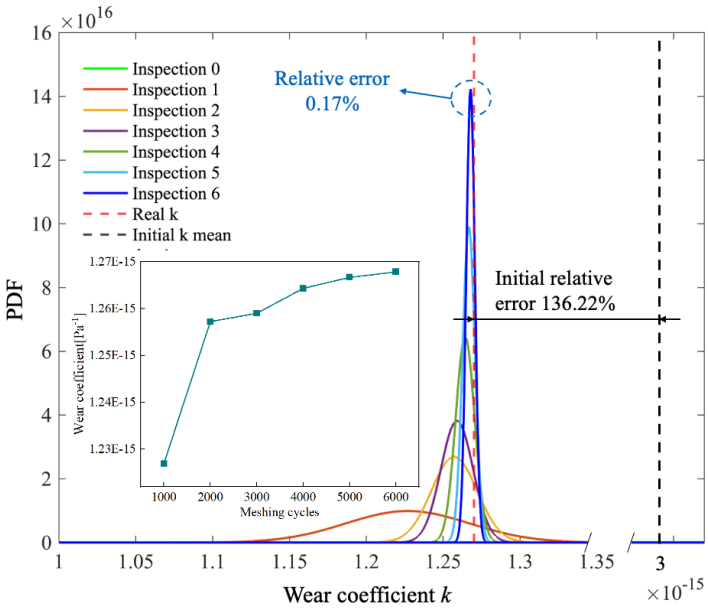

Figure 6-15 Updated process of the distribution of the wear coefficient k_r=1.27e-15 Pa^{-1}.

Two more examples with different real wear coefficients are given to validate the reliability and feasibility of the proposed integrated method. The real wear coefficient is assumed as 1.22e-15 Pa^{-1} and 1.32e-15 Pa^{-1}, respectively. The updating processes of the mean and standard deviation values of k are listed in Table 6-4 and Table 6-5. After several times of updates, the mean values of k distributions all approach their real values. Figure 6-16 and Figure 6-17 show the updating processes of the two wear coefficient distributions. As the updating process continues, the distributions of k gradually narrow and move to the real

values. The relative error of the two examples after the updating process is 0.18% and 0.64%, respectively.

Therefore, the proposed integrated method could be served to reduce uncertainty and approximate the real wear coefficient for a particular gear. Since the proposed method could help to obtain a better model parameter, it can also get a more accurate remaining useful life prediction with a certain wear severity threshold.

Table 6-4. The parameter updating process, k_r=1.22e-15 Pa^{-1}.

Inspection #	Meshing cycles	Mean of k	Std of k
0	0	3e-15	1e-15
1	1000	1.1743e-15	4.0372e-17
2	2000	1.2071e-15	1.3875e-17
3	3000	1.2137e-15	7.4880e-18
4	4000	1.2163e-15	4.7201e-18
5	5000	1.2175e-15	3.2808e-18
6	6000	1.2182e-15	2.3981e-19

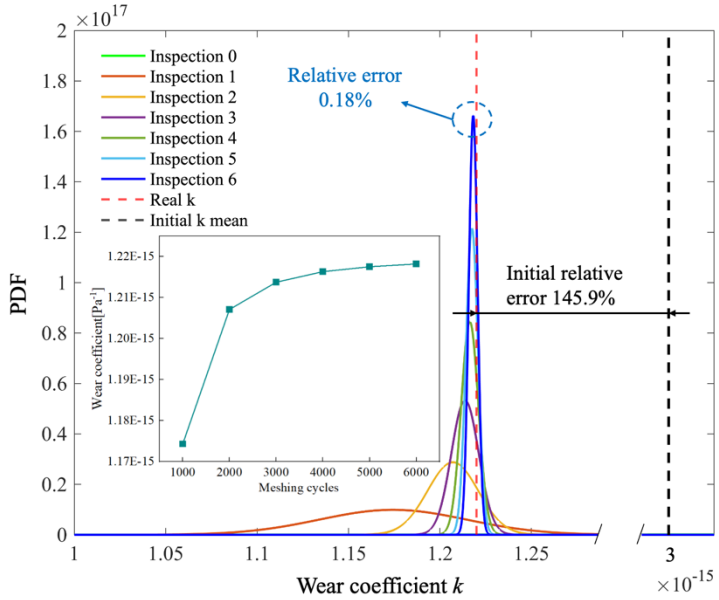

Figure 6-16 Updated process of the distribution of the wear coefficient k_r=1.22e-15 Pa^{-1}.

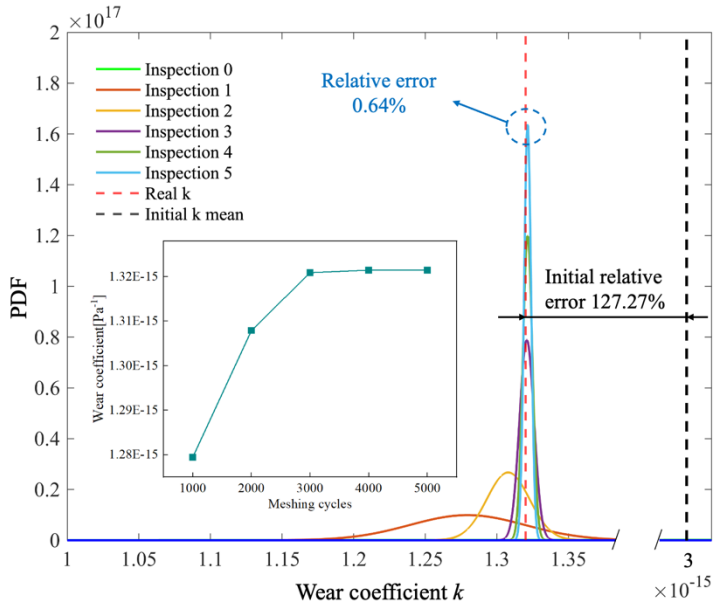

Figure 6-17 Updated process of the distribution of the wear coefficient k_r =1.27e-15 Pa^{-1}.

Table 6-5. The parameter updating process, k_r=1.32e-15 Pa^{-1}.

Inspection #	Meshing cycles	Mean of k	Std of k
0	0	3e-15	1e-15
1	1000	1.2795e-15	4.0341e-17
2	2000	1.3079e-15	1.4943e-17
3	3000	1.3209e-15	5.0503e-18
4	4000	1.3215e-15	3.3183e-18
5	5000	1.3214e-15	2.4243e-18

The comparison between accumulative wear depths of the sun gear estimated by FEM under different wear coefficients, including initial wear coefficient: 3e-15 Pa^{-1}, real wear coefficient: 1.27e-15 Pa^{-1} and the wear coefficients updated by the proposed method, is shown in Figure 6-18. When simulating the surface wear based on the initial wear coefficient from a population of gears, the obtained wear depth increasingly departs from the actual situation as the meshing cycles grow. The discrepancy is defined as:

$$D_e = \frac{|Wd_r - Wd_a|}{Wd_r} \times 100\% \tag{6-8}$$

where D_e it the discrepancy, Wd_r is the wear depth based on the real wear coefficient,

Wd_a is the wear depth based on assumed wear coefficient.

It is evident that with the proposed method, the discrepancy of the accumulated wear depth declines from 142.78% to 0.18% after 6000 meshing cycles. After the first update at 1000 meshing cycles, the accumulative wear depth obtained by the integrated method is almost the same as the reference one. The comparison demonstrates that the proposed integrated prognostic method has the ability to realize accurate wear propagation prediction.

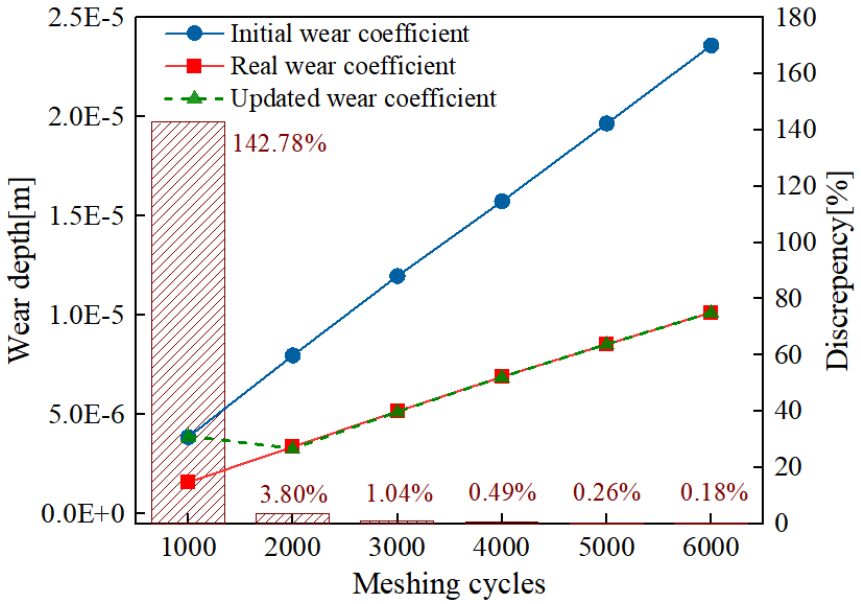

Figure 6-18 Comparison between wear depth prediction performances of different methods.

6.7 Conclusions

In this chapter, the contact analysis and wear propagation simulation of gears with or without pitting are conducted based on the FEM and subroutine UMESHMOTION to investigate the effect of pitting on surface wear behaviors. The results show that the long pit significantly increases the maximum contact stress along the tooth profile. At the same time, it has an ignorable effect on the maximum wear depth that occurs around the gear root. However, wear becomes much more serious in the area close to the pit than that in the intact gear. Pitting makes the overall surface wear propagation more serious. The more

severe wear situation could result in accompanying problems, such as extra loss in mesh stiffness. In the future, we may investigate the joint effect of surface wear and pitting on the mesh stiffness and dynamic characteristics of gears.

Furthermore, a simulation-driven integrated prognostic method is proposed for the surface wear propagation prediction of gears by integrating FEM, physics-based models, and condition monitoring data. Compared to previous integrated prognostic methods, the proposed method considers the impact of variations in the geometric features on the contact stress and sliding distance instead of simply assuming them as constant. Besides, an example is provided to demonstrate and validate the proposed method. It is found that the proposed method could reduce the uncertainty and approximate the actual wear coefficient of a given gear so that the prediction of surface wear propagation could be improved. Moreover, the proposed integrated prognostic method has the ability to realize accurate wear propagation prediction. In the future, we plan to achieve gear wear simulation under a large number of meshing cycles. Moreover, the effects of dynamic characteristics, such as varying rotation speed and collisions, on the wear propagation prediction should also be investigated.

Chapter 7. Conclusions and future work

In recent years, failure analysis and prognostics of equipment and systems used in producing and transporting clean energy have drawn intensive attention from industry and academia. This thesis aims to procure insights into the mechanical and failure characteristics of some equipment subjected to metal loss defects and complex service conditions. Moreover, this research also aims to achieve more accurate failure analysis and develop advanced prognostic methods to prevent potential risks and stabilize energy supplies based on the obtained insights. This research is of tremendous value in ensuring safe operation, lowering maintenance costs, and avoiding unexpected failures of clean energy equipment. In this chapter, the study in this thesis is concluded, and several potential research works in the future are suggested.

7.1 Conclusions

Failure analysis and prognostics are widely adopted for the safe operation and cost-effective maintenance of clean energy equipment. However, there is a huge demand for important advances in the failure analysis of clean energy equipment subjected to metal loss defects and complex service conditions to conduct more reliable investigations of failure behaviors and to develop more accurate theoretical models. In addition, there is an urgent need for more advanced prognostic methods to accurately estimate current status, predict future status, effectively prevent unexpected failures and extend the service life of clean energy equipment and systems. In this thesis, pipelines and gears, which are widely used in the clean energy industry, are selected as research objects. Commonly used approaches and significant research outcomes in this research field have been reviewed. Improving failure analysis and developing more accurate prognostics for corroded pipelines and worn gears subjected to complex service conditions are focused on.

The major contributions of the proposed four research topics in this thesis are summarized

as follows.

(1) An integrated reliability method with a newly developed interaction rule for steel pipelines with multiple corrosion defects

Failure analysis and prognostics of corroded pipelines are vital for improving reliability and preventing failures. Although valuable contributions have been made to improve the safe operation of corroded pipelines, the interacting effect between adjacent corrosion defects is rarely considered, let alone the effects of the corrosion depth and steel grade on the interacting effect and the limit spacing distance. They result in inaccuracies in the residual strength estimation and reliability analysis of pipelines with multiple corrosion defects. This topic first investigates how geometric features of corrosion impact the interacting effect between adjacent corrosion defects. Novel interaction rules are developed to realize a more accurate limit spacing distance estimation by considering the influence of corrosion depth and material properties that significantly affect the burst behaviors of corroded pipelines. To more accurately and efficiently estimate the reliability of a pipeline with multiple corrosion defects and possible interacting effects, an integrated prognostic method is proposed by integrating the new interaction rule, burst pressure model, MCS, sensitivity analysis, feature scaling, and artificial neural network. The proposed method could not only achieve fast and reliable reliability prediction but is also valuable for more complex corroded situations. Moreover, some insights into how the interacting effect, interaction rules, and internal pressure fluctuations on the corroded pipeline's reliability are obtained, which are important for improving pipeline integrity management.

(2) Failure analysis of corroded high-strength pipeline subject to hydrogen damage based on FEM and GA-BP neural network

Although pipelines are the most significant approach to realizing large-scale and long-distance hydrogen transportation, they could be critically impaired by hydrogen damage, such as reductions in ductility and plasticity. Bending gaseous hydrogen into existing natural gas pipeline grids is a promising and cost-effective hydrogen transportation method.

For existing natural gas pipelines, corrosion is somehow inevitable. Blending hydrogen into natural gas grids could result in the coexistence of corrosion defects and hydrogen damage that could make matters worse for pipelines. However, how hydrogen damage impacts the performance and safety of corroded pipelines is barely investigated in previous studies. In this topic, a series of validated FE models are established based on the information from previous experiments to investigate how the hydrogen damage impacts the failure behaviors, residual strength, and the interacting effect between adjacent corrosion defects of the corroded high-strength pipeline. Insights procured in this chapter are valuable for ensuring the safe operation of hydrogen pipelines and promoting hydrogen-natural gas blending transportation technologies. To achieve a more accurate burst pressure estimation of pipelines transporting hydrogen, a novel burst model is developed by considering the effect of hydrogen damage. Thus, the gap that barely any burst model is designed for hydrogen pipelines can be filled. Besides, a GA-BP ANN is structured and trained to realize a better residual strength estimation for corroded pipelines subjected to hydrogen damage as well.

(3) Numerical investigation of the mechanical behaviors of the high-strength spanning pipeline with internal corrosion

For long-distance and submarine pipelines, spanning could occur due to unstable geological conditions and natural disasters. With the increasing climate change, natural disasters have become more frequent, which raises the risk of pipeline spanning and disastrous sequent incidents. As mentioned in Chapter 3 and 4, corrosion damage is very common in pipelines. However, previous research mainly treated pipelines as seamless and intact when conducting failure analysis and further fatigue life estimation. Simply ignoring corrosion defects could lead to an incorrect understanding of failure mechanisms and inaccurate prognostics for spanning pipelines. To help pipelines safely face the challenge that the spanning phenomenon is becoming more frequent, this topic conducts a parametric analysis to systematically study the effects of significant factors, such as spanning length,

corrosion depth, corrosion location, etc., on the mechanical behaviors of spanning pipelines with internal corrosion. Moreover, the influences of these factors on the SCF, which is a significant parameter for the fatigue life estimation of spanning pipelines, are also discussed. The research results are treasured for improving fatigue life estimation and integrity management of spanning pipelines.

(4) Study of wear behaviors and prognostics of gears subject to surface wear and pitting

Pitting and surface wear are two major damages that significantly impact the performance and safety of gears. For gears used in wind turbines, the cyclic and heavy load could result in the coexistence of surface wear and pitting, accelerating a gear's degradation and resulting in unexpected failures. However, previous research barely mentioned the interaction between gear surface wear and pitting. In this topic, how pitting affects the contact status and wear behaviors of meshing gears are investigated by FEM and UMESHMOTION. The obtained insights could provide future studies with a better understanding of gear wear behaviors and RUL prediction under complex conditions. In addition, physics-based prognostic methods use fixed parameters that could result in conservative prediction results and increase the maintenance cost. Prognostic methods proposed in previous studies mainly adopted Hertz contact theory and theoretical sliding distance evaluation models to estimate the contact stress and sliding distance for wear propagation. However, these theoretical models could introduce large inaccuracies. Besides, the changes in the geometric features of gear teeth during the wear process are usually ignored. In this topic, an integrated prognostic method is proposed for gears' surface wear propagation prediction by combining FEM, UMESHMOTION, Archard's model, Bayesian inference, and condition monitoring data. Examples are given to demonstrate and validate that the proposed method could achieve a better prediction. Both the uncertainty in the wear coefficient from a population perspective and the effect of the variations in the tooth profile on wear propagation are incorporated into the proposed method. The proposed

prognostic method is of great significance in reducing parameter uncertainty and improving surface wear propagation simulation.

In conclusion, this thesis's research works significantly contribute to improving safe operation and avoiding unexpected failures of equipment and systems used in the clean energy industry, where several practical engineering issues are well addressed. Several innovative methods are developed for better prediction and estimation of pipelines and gears subjected to metal loss defects and complex service conditions. The obtained insights from this research are valuable for supporting the development of the clean energy industry.

7.2 Future work

Failure analysis and prognostics for pipelines and gears must be continuously evolved, especially for those designed for complex service conditions which are more compliant to the actual cases. With standing on my current research stage, the following research works are recommended for the future.

- In the proposed integrated method, only the internal pressure is considered. However, in engineering practice, pipelines usually must face other loadings, such as temperature stress, traffic loadings, pipe-soil stress, etc. Therefore, future work should consider more complex loading conditions caused by the surrounding environment to achieve a more accurate reliability assessment for pipelines with multiple corrosion defects. Since complex loading conditions will be considered, how circumferentially and diagonally aligned corrosion defects impact the interacting effect should be taken into consideration. Besides, stochastic characteristics of corrosion degradation should be considered to incorporate the uncertainty in corrosion growth.
- Blending hydrogen into natural gas could influence the corrosion mechanism. However, the effects of hydrogen on the degradation process of pipeline corrosion are barely investigated. There is no deep understanding of corrosion degradation under hydrogen damage, such as how corrosion growth is influenced. Therefore, the effects

of hydrogen damage on pipelines' corrosion degradation processes should be studied. Furthermore, a more accurate and reliable prognostic method for corroded pipelines with hydrogen damage could be developed based on corrosion degradation processes considering hydrogen damage.

- The obtained simulation results for the spanning pipeline with internal corrosion, such as SCF, can provide essential information for fatigue life estimation. In future work, the effects of corrosion and its location, number, and geometric features on the fatigue life of spanning pipelines should be investigated.
- Although the integrated prognostic method proposed in this thesis could realize a more accurate simulation and prediction for surface wear propagation of gears, more tests are required to be performed to validate the proposed methods. Besides, future work should also investigate the effects of dynamic characteristics, such as varying rotation speed and collisions, on the wear propagation prediction.

Reference

[1] Zhang H, Tian Z. An Integrated Reliability Method with a Newly Developed Interaction Rule for Steel Pipelines with Multiple Corrosion Defects. J Pipeline Syst Eng Pract 2022;13:04022045. https://doi.org/10.1061/(ASCE)PS.1949-1204.0000683.

[2] Zhang H, Tian Z. Reliability assessment of corroded pipeline considering multiple defects interaction based on an artificial neural network method. 2020 Asia-Pac. Int. Symp. Adv. Reliab. Maint. Model. APARM, 2020, p. 1–6. https://doi.org/10.1109/APARM49247.2020.9209428.

[3] Zhang H, Tian Z. Failure analysis of corroded high-strength pipeline subject to hydrogen damage based on FEM and GA-BP neural network. Int J Hydrog Energy 2022;47:4741–58. https://doi.org/10.1016/j.ijhydene.2021.11.082.

[4] Liu H, Liang D. A review of clean energy innovation and technology transfer in China. Renew Sustain Energy Rev 2013;18:486–98. https://doi.org/10.1016/j.rser.2012.10.041.

[5] Dincer I, Acar C. A review on clean energy solutions for better sustainability. Int J Energy Res 2015;39:585–606. https://doi.org/10.1002/er.3329.

[6] Ge Y, Zhi Q. Literature Review: The Green Economy, Clean Energy Policy and Employment. Energy Procedia 2016;88:257–64. https://doi.org/10.1016/j.egypro.2016.06.159.

[7] Leung GCK. Natural Gas as a Clean Fuel. Handb. Clean Energy Syst., John Wiley & Sons, Ltd; 2015, p. 1–15. https://doi.org/10.1002/9781118991978.hces055.

[8] IEA. Electricity Market Report. Paris: IEA; 2022. https://www.iea.org/reports/electricity-market-report-july-2022

[9] Layouni M, Hamdi MS, Tahar S. Detection and sizing of metal-loss defects in oil and gas pipelines using pattern-adapted wavelets and machine learning. Appl Soft Comput 2017;52:247–61. https://doi.org/10.1016/j.asoc.2016.10.040.

[10] Xie M, Tian Z. A review on pipeline integrity management utilizing in-line

inspection data. Eng Fail Anal 2018;92:222–39.
https://doi.org/10.1016/j.engfailanal.2018.05.010.
[11] Zhang H, Zhang J, Lin R, Li Y. Numerical Investigation of the Damage Mechanism of Offshore Pipeline Impacted by the Lump-Shaped Falling Object. J Press Vessel Technol 2020;143. https://doi.org/10.1115/1.4049146.
[12] Shuai Y, Wang X-H, Cheng YF. Modeling of local buckling of corroded X80 gas pipeline under axial compression loading. J Nat Gas Sci Eng 2020;81:103472. https://doi.org/10.1016/j.jngse.2020.103472.
[13] Oil and Gas Pipelines Length and Capacity and Capital Expenditure (CapEx) Forecast by Region, Countries and Companies including details of New Build and Expansion (Announcements and Cancellations) Projects, 2022-2026. New York: GlobalData; 2022. https://www.reportlinker.com/p06290001/Oil-and-Gas-Pipelines-Length-and-Capacity-and-Capital-Expenditure-CapEx-Forecast-by-Region-Countries-and-Companies-including-details-of-New-Build-and-Expansion-Announcements-and-Cancellations-Projects.html?utm_source=GNW.
[14] Ahmed SK, Kabir G. An Integrated Approach for Failure Analysis of Natural Gas Transmission Pipeline. CivilEng 2021;2:87–119. https://doi.org/10.3390/civileng2010006.
[15] Pipeline Construction Market By Pipe Type, By Application, By End User: Global Opportunity Analysis and Industry Forecast, 2021-2031. Dublin: 2022. https://www.researchandmarkets.com/reports/5640446/pipeline-construction-market-by-pipe-type.
[16] Zhang J, Liang Z, Han CJ. Failure Analysis and Finite Element Simulation of Above Ground Oil–Gas Pipeline Impacted by Rockfall. J Fail Anal Prev 2014;14:530–6. https://doi.org/10.1007/s11668-014-9847-x.
[17] Pearson MW. Characterization of Mechanical Adhesion Failure in Epoxy Nanocomposites by Acoustic Emission Method. PhD Thesis. North Dakota State

University, 2021. https://hdl.handle.net/10365/32664
[18] Liao K, Qin M, He G, Yang N, Zhang S. Study on corrosion mechanism and the risk of the shale gas gathering pipelines. Eng Fail Anal 2021;128:105622. https://doi.org/10.1016/j.engfailanal.2021.105622.
[19] Han J. Galvanic mechanism of localized corrosion for mild steel in carbon dioxide environments. Ph.D. Ohio University, 2009. http://rave.ohiolink.edu/etdc/view?acc_num=ohiou1258393107
[20] Mansoori H, Mirzaee R, Esmaeilzadeh F, Vojood A, Dowrani AS. Pitting corrosion failure analysis of a wet gas pipeline. Eng Fail Anal 2017;82:16–25. https://doi.org/10.1016/j.engfailanal.2017.08.012.
[21] Kang Y, Chen W, Kania R, Boven GV, Worthingham R. Simulation of crack growth during hydrostatic testing of pipeline steel in near-neutral pH environment. Corros Sci 2011;53:968–75. https://doi.org/10.1016/j.corsci.2010.11.029.
[22] Netto TA. On the effect of narrow and long corrosion defects on the collapse pressure of pipelines. Appl Ocean Res 2009;31:75–81. https://doi.org/10.1016/j.apor.2009.07.004.
[23] Fekete G, Varga L. The effect of the width to length ratios of corrosion defects on the burst pressures of transmission pipelines. Eng Fail Anal 2012;21:21–30. https://doi.org/10.1016/j.engfailanal.2011.12.002.
[24] Arumugam T, Karuppanan S, Ovinis M. Finite element analyses of corroded pipeline with single defect subjected to internal pressure and axial compressive stress. Mar Struct 2020;72:102746. https://doi.org/10.1016/j.marstruc.2020.102746.
[25] Arumugam T, Karuppanan S, Ovinis M. Residual strength analysis of pipeline with circumferential groove corrosion subjected to internal pressure. Mater Today Proc 2020;29:88–93. https://doi.org/10.1016/j.matpr.2020.05.699.
[26] Chen Y, Zhang H, Zhang J, Liu X, Li X, Zhou J. Failure assessment of X80 pipeline with interacting corrosion defects. Eng Fail Anal 2015;47:67–76.

https://doi.org/10.1016/j.engfailanal.2014.09.013.
[27] Benjamin AC, Freire JLF, Vieira RD. Part 6: Analysis of pipeline containing interacting corrosion defects. Exp Tech 2007;31:74–82. https://doi.org/10.1111/j.1747-1567.2007.00190.x.
[28] Benjamin AC, Freire JLF, Vieira RD, Cunha DJS. Interaction of corrosion defects in pipelines – Part 1: Fundamentals. Int J Press Vessels Pip 2016;144:56–62. https://doi.org/10.1016/j.ijpvp.2016.05.007.
[29] Mah AXY, Ho WS, Bong CPC, Hassim MH, Liew PY, Asli UA, et al. Review of hydrogen economy in Malaysia and its way forward. Int J Hydrog Energy 2019;44:5661–75. https://doi.org/10.1016/j.ijhydene.2019.01.077.
[30] Dimitriou P, Tsujimura T. A review of hydrogen as a compression ignition engine fuel. Int J Hydrog Energy 2017;42:24470–86. https://doi.org/10.1016/j.ijhydene.2017.07.232.
[31] Duncan A, Lam P-S, Adams T. Tensile Testing of Carbon Steel in High Pressure Hydrogen. PVP2007, Volume 6: Materials and Fabrication: 2007, p. 519–25. https://doi.org/10.1115/PVP2007-26736.
[32] Merzlikin SV, Hassel AW, Steinhoff KP, Wildau M. An Investigation of the Different Methods of Removing Specimens for Hydrogen Analysis from Damaged Cold Finishing Rolls. Prakt Metallogr-Pract Metallogr 2011;48:365–75. https://doi.org/10.3139/147.110120.
[33] Caruso M, Ferris G, Heggen HO, Delanty B. Challenges Related to Pipeline Free Spans in Watercourse Crossings, American Society of Mechanical Engineers Digital Collection; 2021. https://doi.org/10.1115/IPG2021-65070.
[34] Pan H, Li H-N, Li C. Seismic behaviors of free-spanning submarine pipelines subjected to multi-support earthquake motions within offshore sites. Ocean Eng 2021;237:109606. https://doi.org/10.1016/j.oceaneng.2021.109606.
[35] Liu M, Jin X, Wang L, Yang F, Tang J. Numerical investigation of local scour

around a vibrating pipeline under steady currents. Ocean Eng 2021;221:108546. https://doi.org/10.1016/j.oceaneng.2020.108546.
[36] Wang L, Tang Y, Ma T, Zhong J, Li Z, Zhang Y, et al. Stress concentration analysis of butt welds with variable wall thickness of spanning pipelines caused by additional loads. Int J Press Vessels Pip 2020;182:104075. https://doi.org/10.1016/j.ijpvp.2020.104075.
[37] Zhao F, Tian Z, Zeng Y. Overview on Gear Health Prognostics. In: Ekwaro-Osire S, Gonçalves AC, Alemayehu FM, editors. Probabilistic Progn. Health Manag. Energy Syst., Cham: Springer International Publishing; 2017, p. 49–65. https://doi.org/10.1007/978-3-319-55852-3_4.
[38] Bajpai P, Kahraman A, Anderson NE. A Surface Wear Prediction Methodology for Parallel-Axis Gear Pairs. J Tribol 2004;126:597–605. https://doi.org/10.1115/1.1691433.
[39] Liu J, Wang C, Wu W. Research on Meshing Stiffness and Vibration Response of Pitting Fault Gears with Different Degrees. Int J Rotating Mach 2020;2020:e4176430. https://doi.org/10.1155/2020/4176430.
[40] Huangfu Y, Chen K, Ma H, Li X, Han H, Zhao Z. Meshing and dynamic characteristics analysis of spalled gear systems: A theoretical and experimental study. Mech Syst Signal Process 2020;139:106640. https://doi.org/10.1016/j.ymssp.2020.106640.
[41] Elattar HM, Elminir HK, Riad AM. Prognostics: a literature review. Complex Intell Syst 2016;2:125–54. https://doi.org/10.1007/s40747-016-0019-3.
[42] Byington CS, Roemer MJ, Galie T. Prognostic enhancements to diagnostic systems for improved condition-based maintenance [military aircraft]. Proc. IEEE Aerosp. Conf., vol. 6, 2002, p. 6–6. https://doi.org/10.1109/AERO.2002.1036120.
[43] Voisin A, Levrat E, Cocheteux P, Iung B. Generic prognosis model for proactive maintenance decision support: application to pre-industrial e-maintenance test bed. J Intell Manuf 2010;21:177–93. https://doi.org/10.1007/s10845-008-0196-z.

[44] Pipeline Safety Global Market Report 2022 – By Component (Solutions, Services), By End User (Natural Gas, Crude Oil, Refined Products), By Application (Onshore, Offshore) – Market Size, Trends, And Global Forecast 2022-2026. New York: Business Research Company; 2022. https://www.reportlinker.com/p06246508/Pipeline-Safety-Global-Market-Report.html?utm_source=GNW.

[45] Global Wind Turbine Market Report 2022. Brussels: Global Wind Energy Council; 2022. https://www.reportlinker.com/p06377786/Wind-Turbine-Casting-Global-Market-Report-Ukraine-Russia-War-Impact.html?utm_source=GNW.

[46] Zhao F, Tian Z, Liang X, Xie M. An Integrated Prognostics Method for Failure Time Prediction of Gears Subject to the Surface Wear Failure Mode. IEEE Trans Reliab 2018;67:316–27. https://doi.org/10.1109/TR.2017.2781147.

[47] Mao K. Gear tooth contact analysis and its application in the reduction of fatigue wear. Wear 2007;262:1281–8. https://doi.org/10.1016/j.wear.2006.06.019.

[48] Hegadekatte V, Huber N, Kraft O. Modeling and Simulation of Wear in a Pin on Disc Tribometer, American Society of Mechanical Engineers Digital Collection; 2008, p. 567–75. https://doi.org/10.1115/IJTC2006-12063.

[49] Sfantos GK, Aliabadi MH. Wear simulation using an incremental sliding Boundary Element Method. Wear 2006;260:1119–28. https://doi.org/10.1016/j.wear.2005.07.020.

[50] Wang H, Yajima A, Y. Liang R, Castaneda H. A Bayesian model framework for calibrating ultrasonic in-line inspection data and estimating actual external corrosion depth in buried pipeline utilizing a clustering technique. Struct Saf 2015;54:19–31. https://doi.org/10.1016/j.strusafe.2015.01.003.

[51] Verink E, Jr HR. Evaluation of the tendency for dealloying in metal systems. vol. 72. ASTM International; 1972.

[52] Vanaei HR, Eslami A, Egbewande A. A review on pipeline corrosion, in-line inspection (ILI), and corrosion growth rate models. Int J Press Vessels Pip 2017;149:43–54. https://doi.org/10.1016/j.ijpvp.2016.11.007.

[53] Karami M. Review of Corrosion Role in Gas Pipeline and Some Methods for Preventing It. J Press Vessel Technol 2012;134. https://doi.org/10.1115/1.4006124.
[54] Engineers AS of M. Manual for Determining the Remaining Strength of Corroded Pipelines: A Supplement to ASME B31 Code for Pressure Piping: an American National Standard. American Society of Mechanical Engineers; 2012.
[55] Kiefner JF, Vieth PH. PC program speeds new criterion for evaluating corroded pipe. Oil Gas J USA 1990;88:34. https://www.osti.gov/biblio/6828231.
[56] Association CS, others. Oil and Gas Pipeline Systems-CSA Z662-15. CSA Group; 2015.
[57] Corroded pipelines : recommended practice DNVGL-RP-F101. Edition September 2019. Det Norske Veritas AS; 2019.
[58] Leis BN, Stephens DR. An Alternative Approach to Assess the Integrity of Corroded Line Pipe - Part I: Current Status, OnePetro; 1997. https://onepetro.org/ISOPEIOPEC/proceedings-abstract/ISOPE97/All-ISOPE97/ISOPE-I-97-490/24221.
[59] Ritchie D, Last S. Burst criteria of corroded pipelines-defect acceptance criteria. Proc. EPRGPRC 10th Bienn. Jt. Tech. Meet. Line Pipe Res., 1995, p. 1–11.
[60] Bhardwaj U, Teixeira AP, Guedes Soares C. Uncertainty quantification of burst pressure models of corroded pipelines. Int J Press Vessels Pip 2020;188:104208. https://doi.org/10.1016/j.ijpvp.2020.104208.
[61] Mondal BC, Dhar AS. Burst pressure assessment of corroded pipelines using fracture mechanics criterion. Eng Fail Anal 2019;104:139–53. https://doi.org/10.1016/j.engfailanal.2019.05.033.
[62] Ma B, Shuai J, Liu D, Xu K. Assessment on failure pressure of high strength pipeline with corrosion defects. Eng Fail Anal 2013;32:209–19. https://doi.org/10.1016/j.engfailanal.2013.03.015.
[63] Belachew CT, Ismail MC, Karuppanan S. Burst strength analysis of corroded

pipelines by finite element method. J Appl Sci 2011;11:1845–50. https://doi.org/10.3923/jas.2011.1845.1850.

[64] Chandra Mondal B, Sutra Dhar A. Finite-Element Evaluation of Burst Pressure Models for Corroded Pipelines. J Press Vessel Technol 2016;139. https://doi.org/10.1115/1.4034408.

[65] Zhang S, Zhou W. A Burst Capacity Model for Corroded Pipelines Subjected to Combined Internal Pressure and Longitudinal Compression. J Press Vessel Technol 2021;144. https://doi.org/10.1115/1.4051368.

[66] Vijaya Kumar SD, Karuppanan S, Ovinis M. Failure Pressure Prediction of High Toughness Pipeline with a Single Corrosion Defect Subjected to Combined Loadings Using Artificial Neural Network (ANN). Metals 2021;11:373. https://doi.org/10.3390/met11020373.

[67] Lo M, Karuppanan S, Ovinis M. ANN- and FEA-Based Assessment Equation for a Corroded Pipeline with a Single Corrosion Defect. J Mar Sci Eng 2022;10:476. https://doi.org/10.3390/jmse10040476.

[68] Phan HC, Dhar AS. Predicting pipeline burst pressures with machine learning models. Int J Press Vessels Pip 2021;191:104384. https://doi.org/10.1016/j.ijpvp.2021.104384.

[69] Zhang S, Zhou W. Cost-based optimal maintenance decisions for corroding natural gas pipelines based on stochastic degradation models. Eng Struct 2014;74:74–85. https://doi.org/10.1016/j.engstruct.2014.05.018.

[70] Amaya-Gómez R, Sánchez-Silva M, Bastidas-Arteaga E, Schoefs F, Muñoz F. Reliability assessments of corroded pipelines based on internal pressure – A review. Eng Fail Anal 2019;98:190–214. https://doi.org/10.1016/j.engfailanal.2019.01.064.

[71] Shuai Y, Shuai J, Xu K. Probabilistic analysis of corroded pipelines based on a new failure pressure model. Eng Fail Anal 2017;81:216–33. https://doi.org/10.1016/j.engfailanal.2017.06.050.

[72] Abyani M, Bahaari MR. A comparative reliability study of corroded pipelines based on Monte Carlo Simulation and Latin Hypercube Sampling methods. Int J Press Vessels Pip 2020;181:104079. https://doi.org/10.1016/j.ijpvp.2020.104079.
[73] Bhardwaj U, Teixeira AP, Guedes Soares C. Uncertainty in reliability of thick high strength pipelines with corrosion defects subjected to internal pressure. Int J Press Vessels Pip 2020;188:104170. https://doi.org/10.1016/j.ijpvp.2020.104170.
[74] Pourahmadi M, Saybani M. Reliability analysis with corrosion defects in submarine pipeline case study: Oil pipeline in Ab-khark island. Ocean Eng 2022;249:110885. https://doi.org/10.1016/j.oceaneng.2022.110885.
[75] Wen K, He L, Liu J, Gong J. An optimization of artificial neural network modeling methodology for the reliability assessment of corroding natural gas pipelines. J Loss Prev Process Ind 2019;60:1–8. https://doi.org/10.1016/j.jlp.2019.03.010.
[76] El Amine Ben Seghier M, Keshtegar B, Correia JAFO, Lesiuk G, De Jesus AMP. Reliability analysis based on hybrid algorithm of M5 model tree and Monte Carlo simulation for corroded pipelines: Case of study X60 Steel grade pipes. Eng Fail Anal 2019;97:793–803. https://doi.org/10.1016/j.engfailanal.2019.01.061.
[77] Chouchaoui B, Pick R. Interaction of closely spaced corrosion pits in line pipe. Proc. Int. Conf. OFFSHORE Mech. Arct. Eng., American Society of Mechanical Engineers; 1993, p. 203–203.
[78] Chouchaoui BA, Pick RJ. Behaviour of circumferentially aligned corrosion pits. Int J Press Vessels Pip 1994;57:187–200. https://doi.org/10.1016/0308-0161(94)90052-3.
[79] Benjamin AC, Freire JLF, Vieira RD, Cunha DJS. Interaction of corrosion defects in pipelines – Part 2: MTI JIP database of corroded pipe tests. Int J Press Vessels Pip 2016;145:41–59. https://doi.org/10.1016/j.ijpvp.2016.06.006.
[80] Han C, Zhang H, Zhang J. Failure pressure analysis of the pipe with inner corrosion defects by FEM. Int J Electrochem Sci 2016;11:5046–62.
[81] Sun J, Cheng YF. Assessment by finite element modeling of the interaction of

multiple corrosion defects and the effect on failure pressure of corroded pipelines. Eng Struct 2018;165:278–86. https://doi.org/10.1016/j.engstruct.2018.03.040.
[82] Lamontagne M. Interaction Rules - An Integral Factor, CORROSION 2002, OnePetro; 2002. https://onepetro.org/NACECORR/proceedings-abstract/CORR02/All-CORR02/NACE-02080/114581.
[83] Li X, Bai Y, Su C, Li M. Effect of interaction between corrosion defects on failure pressure of thin wall steel pipeline. Int J Press Vessels Pip 2016;138:8–18. https://doi.org/10.1016/j.ijpvp.2016.01.002.
[84] Benjamin AC, de Andrade EQ, Jacob BP, Pereira LC, Machado PRS. Failure Behavior of Colonies of Corrosion Defects Composed of Symmetrically Arranged Defects, American Society of Mechanical Engineers Digital Collection; 2008, p. 417–32. https://doi.org/10.1115/IPC2006-10266.
[85] Xu W-Z, Li CB, Choung J, Lee J-M. Corroded pipeline failure analysis using artificial neural network scheme. Adv Eng Softw 2017;112:255–66. https://doi.org/10.1016/j.advengsoft.2017.05.006.
[86] Guillal A, Ben Seghier MEA, Nourddine A, Correia JAFO, Bt Mustaffa Z, Trung N-T. Probabilistic investigation on the reliability assessment of mid- and high-strength pipelines under corrosion and fracture conditions. Eng Fail Anal 2020;118:104891. https://doi.org/10.1016/j.engfailanal.2020.104891.
[87] Gong C, Zhou W. First-order reliability method-based system reliability analyses of corroding pipelines considering multiple defects and failure modes. Struct Infrastruct Eng 2017;13:1451–61. https://doi.org/10.1080/15732479.2017.1285330.
[88] Eliaz N, Shachar A, Tal B, Eliezer D. Characteristics of hydrogen embrittlement, stress corrosion cracking and tempered martensite embrittlement in high-strength steels. Eng Fail Anal 2002;9:167–84. https://doi.org/10.1016/S1350-6307(01)00009-7.
[89] LaChance J, Tchouvelev A, Ohi J. Risk-informed process and tools for permitting hydrogen fueling stations. Int J Hydrog Energy 2009;34:5855–61.

https://doi.org/10.1016/j.ijhydene.2009.01.057.
[90]Schmetz E, Miller L. Hydrogen production and delivery from coal, 2005 annual DOE hydrogen program review. US Dep Energy Off Sequestration Hydrog Clean Coal Fuels 2005:4. https://www.hydrogen.energy.gov/pdfs/review05/pd_schmetz.pdf.
[91]Moradi R, Groth KM. Hydrogen storage and delivery: Review of the state of the art technologies and risk and reliability analysis. Int J Hydrog Energy 2019;44:12254–69. https://doi.org/10.1016/j.ijhydene.2019.03.041.
[92] White CM, Steeper RR, Lutz AE. The hydrogen-fueled internal combustion engine: a technical review. Int J Hydrog Energy 2006;31:1292–305. https://doi.org/10.1016/j.ijhydene.2005.12.001.
[93] Satyapal S, Farmer R. DOE hydrogen and fuel cells program record 2015. https://www.hydrogen.energy.gov/program_records.html.
[94] Baldwin D. Development of high pressure hydrogen storage tank for storage and gaseous truck delivery. Hexagon Lincoln LLC, Lincoln, NE (United States); 2017.
[95] Lee H, Lee S. Economic Analysis on Hydrogen Pipeline Infrastructure Establishment Scenarios: Case Study of South Korea. Energies 2022;15:6824. https://doi.org/10.3390/en15186824.
[96] Agency IE. Global Hydrogen Review 2021. OECD Publishing; 2021. iea.org/reports/global-hydrogen-review-2021.
[97] Melaina MW, Antonia O, Penev M. Blending Hydrogen into Natural Gas Pipeline Networks: A Review of Key Issues 2013. https://www.nrel.gov/docs/fy13osti/51995.pdf.
[98] Dickinson RR, Battye DL, Linton VM, Ashman PJ, Nathan G (Gus) J. Alternative carriers for remote renewable energy sources using existing CNG infrastructure. Int J Hydrog Energy 2010;35:1321–9. https://doi.org/10.1016/j.ijhydene.2009.11.052.
[99] Florisson O. Preparing for the hydrogen economy by using the existing natural gas system as a catalyst. Nat Proj Rep 2010. http://www.naturalhy.net/docs/project_reports/Final_Publishable_Activity_Report.pdf.

[100] Tzimas E, Castello P, Peteves S. The evolution of size and cost of a hydrogen delivery infrastructure in Europe in the medium and long term. Int J Hydrog Energy 2007;32:1369–80. https://doi.org/10.1016/j.ijhydene.2006.10.017.

[101] Yıldırım A. NATURALHY (The Potential of Existing Natural Gas Network for Hydrogen Delivery) Project Objectives and Some Results, European Association of Geoscientists & Engineers; 2011, p. cp. https://doi.org/10.3997/2214-4609-pdb.377.155.

[102] Elazzizi A, Hadj Meliani M, Khelil A, Pluvinage G, Matvienko YG. The master failure curve of pipe steels and crack paths in connection with hydrogen embrittlement. Int J Hydrog Energy 2015;40:2295–302. https://doi.org/10.1016/j.ijhydene.2014.12.040.

[103] Capelle J, Dmytrakh I, Azari Z, Pluvinage G. Evaluation of electrochemical hydrogen absorption in welded pipe with steel API X52. Int J Hydrog Energy 2013;38:14356–63. https://doi.org/10.1016/j.ijhydene.2013.08.118.

[104] Briottet L, Moro I, Lemoine P. Quantifying the hydrogen embrittlement of pipeline steels for safety considerations. Int J Hydrog Energy 2012;37:17616–23. https://doi.org/10.1016/j.ijhydene.2012.05.143.

[105] Nanninga NE, Levy YS, Drexler ES, Condon RT, Stevenson AE, Slifka AJ. Comparison of hydrogen embrittlement in three pipeline steels in high pressure gaseous hydrogen environments. Corros Sci 2012;59:1–9. https://doi.org/10.1016/j.corsci.2012.01.028.

[106] Briottet L, Batisse R, de Dinechin G, Langlois P, Thiers L. Recommendations on X80 steel for the design of hydrogen gas transmission pipelines. Int J Hydrog Energy 2012;37:9423–30. https://doi.org/10.1016/j.ijhydene.2012.02.009.

[107] Zhang T, Chu WY, Gao KW, Qiao LJ. Study of correlation between hydrogen-induced stress and hydrogen embrittlement. Mater Sci Eng A 2003;347:291–9. https://doi.org/10.1016/S0921-5093(02)00600-7.

[108] Rigas F, Amyotte P. Myths and facts about hydrogen hazards. 13th Int. Symp. Loss Prev. Saf. Promot. Process Ind. Florence Italy May 12-15 2013, 2013.

https://www.aidic.it/cet/13/31/153.pdf.

[109] Wang P, Wang J, Zheng S, Qi Y, Xiong M, Zheng Y. Effect of H2S/CO2 partial pressure ratio on the tensile properties of X80 pipeline steel. Int J Hydrog Energy 2015;40:11925–30. https://doi.org/10.1016/j.ijhydene.2015.04.114.

[110] Ohaeri E, Eduok U, Szpunar J. Hydrogen related degradation in pipeline steel: A review. Int J Hydrog Energy 2018;43:14584–617. https://doi.org/10.1016/j.ijhydene.2018.06.064.

[111] ASME B31.8 :2003: Gas Transmission and Distribution Piping Systems. ASME; 2003.

[112] Xu J, Li G, Horrillo JJ, Yang R, Cao L. Calculation of maximum allowable free span length and safety assessment of the DF1-1 submarine pipeline. J Ocean Univ China 2010;9:1–10. https://doi.org/10.1007/s11802-010-0001-4.

[113] Mandal M, Roy P. Influence of Pipeline Specifications and Support Conditions on Natural Frequency of Free Spanning Subsea Pipelines. In: Matsagar V, editor. Adv. Struct. Eng., New Delhi: Springer India; 2015, p. 663–72. https://doi.org/10.1007/978-81-322-2190-6_53.

[114] Fyrileiv O, Mørk KJ, Ronold KO. Free Span Design according to the DNV-RP-F105 for Free Spanning Pipelines. Proc. Offshore Pipeline Technol. Conf. Amst. Neth., vol. 1, 2002. https://doi.org/10.1115/OMAE2005-67453.

[115] Xu T, Lauridsen B, Bai Y. Wave-induced fatigue of multi-span pipelines. Mar Struct 1999;12:83–106. https://doi.org/10.1016/S0951-8339(99)00009-X.

[116] He Z, Wei Y, Liu S. Analysis of Safe Span Length and Fatigue Life of Submarine Pipelines. China Ocean Eng 2020;34:119–30. https://doi.org/10.1007/s13344-020-0012-x.

[117] Blevins R. Flow-induced vibration van nostrand reinhold company. N Y 1977:363.

[118] Nielsen FG, Sotreide TH, Kvarme SO. VIV Response of Long Free Spanning

Pipelines, American Society of Mechanical Engineers Digital Collection; 2009, p. 121–9. https://doi.org/10.1115/OMAE2002-28075.

[119] Wang J, Steven Wang F, Duan G, Jukes P. VIV analysis of pipelines under complex span conditions. J Mar Sci Appl 2009;8:105–9. https://doi.org/10.1007/s11804-009-8109-x.

[120] Choi HS. Free spanning analysis of offshore pipelines. Ocean Eng 2001;28:1325–38. https://doi.org/10.1016/S0029-8018(00)00071-8.

[121] Anfinsen KA. Review of Free Spanning Pipelines, OnePetro; 1995, ISOPE-I-95-114. https://onepetro.org/ISOPEIOPEC/proceedings-abstract/ISOPE95/All-ISOPE95/ISOPE-I-95-114/22978.

[122] Fyrileiv O, Mørk K, Chezhian M. Experiences Using DNV-RP-F105 in Assessment of Free Spanning Pipelines, American Society of Mechanical Engineers Digital Collection; 2008, p. 571–8. https://doi.org/10.1115/OMAE2005-67453.

[123] Rezazadeh K, Zhu L, Bai Y, Zhang L. Fatigue Analysis of Multi-Spanning Subsea Pipeline, American Society of Mechanical Engineers Digital Collection; 2010, p. 805–12. https://doi.org/10.1115/OMAE2010-20847.

[124] Hagen O, Mørk K, Sigurdsson G, Nielsen FG. Evaluation of Free Spanning Pipeline Design in a Risk Based Perspective, American Society of Mechanical Engineers Digital Collection; 2009, p. 789–99. https://doi.org/10.1115/OMAE2003-37419.

[125] Esplin GD, Stappenbelt B. Reducing conservatism in free spanning pipeline vortex-induced vibration fatigue analysis. Aust J Mech Eng 2011;8:11–20. https://doi.org/10.1080/14484846.2011.11464591.

[126] Hariharan M, Cerkovnik M, Thompson H. The Significance of Low Velocity Near Bottom Currents on the In-Line Vortex-Induced Vibration Response of Rigid Subsea Jumpers. Tech Pap 2H Offshore 2004. https://doi.org/10.4043/26228-MS

[127] Ghanbari Ghazijahani T, Jiao H, Holloway D. Fatigue tests of damaged tubes under flexural loading. Steel Compos Struct 2015;19:223–36.

https://doi.org/10.12989/scs.2015.19.1.223

[128] Archard J. Contact and rubbing of flat surfaces', Journal of Applied Physics. Vol 1953;24:918–88. https://doi.org/10.1063/1.1721448.

[129] Andersson S. Wear Simulation, Advanced Knowledge Application in Practice, Igor Fuerstner (Ed.), ISBN: 978-953-307-141-1, InTech 2010.

[130] Jardine AKS, Lin D, Banjevic D. A review on machinery diagnostics and prognostics implementing condition-based maintenance. Mech Syst Signal Process 2006;20:1483–510. https://doi.org/10.1016/j.ymssp.2005.09.012.

[131] Nielsen A, Mallet-Paret J, Griffin K. Probabilistic Modeling of Crack Threats and the Effects of Mitigation, American Society of Mechanical Engineers Digital Collection; 2014. https://doi.org/10.1115/IPC2014-33511.

[132] Sutton A, Hubert Y, Textor S, Haider S. Allowable Pressure Cycling Limits for Liquid Pipelines, American Society of Mechanical Engineers Digital Collection; 2014. https://doi.org/10.1115/IPC2014-33566.

[133] Li CJ, Lee H. Gear fatigue crack prognosis using embedded model, gear dynamic model and fracture mechanics. Mech Syst Signal Process 2005;19:836–46. https://doi.org/10.1016/j.ymssp.2004.06.007.

[134] Blake JW, Cheng HS. A Surface Pitting Life Model for Spur Gears: Part I—Life Prediction. J Tribol 1991;113:712–8. https://doi.org/10.1115/1.2920683.

[135] Budynas RG, Nisbett JK, others. Shigley's mechanical engineering design. vol. 9. McGraw-hill New York; 2011.

[136] Flodin A, Andersson S. A simplified model for wear prediction in helical gears. Wear 2001;249:285–92. https://doi.org/10.1016/S0043-1648(01)00556-7.

[137] Wang H, Zhou C, Lei Y, Liu Z. An adhesive wear model for helical gears in line-contact mixed elastohydrodynamic lubrication. Wear 2019;426–427:896–909. https://doi.org/10.1016/j.wear.2019.01.104.

[138] Zhu D, Martini A, Wang W, Hu Y, Lisowsky B, Wang QJ. Simulation of Sliding

Wear in Mixed Lubrication. J Tribol 2007;129:544–52. https://doi.org/10.1115/1.2736439.

[139] Wu S, Cheng HS. Sliding Wear Calculation in Spur Gears. J Tribol 1993;115:493–500. https://doi.org/10.1115/1.2921665.

[140] Wu S, Cheng HS. A Sliding Wear Model for Partial-EHL Contacts. J Tribol 1991;113:134–41. https://doi.org/10.1115/1.2920579.

[141] Ding H, Kahraman A. Interactions between nonlinear spur gear dynamics and surface wear. J Sound Vib 2007;307:662–79. https://doi.org/10.1016/j.jsv.2007.06.030.

[142] Kundu P, Darpe AK, Kulkarni MS. An ensemble decision tree methodology for remaining useful life prediction of spur gears under natural pitting progression. Struct Health Monit 2020;19:854–72. https://doi.org/10.1177/1475921719865718.

[143] Aherwar A. An investigation on gearbox fault detection using vibration analysis techniques: A review. Aust J Mech Eng 2012;10:169–83. https://doi.org/10.7158/M11-830.2012.10.2.

[144] Randall RB. A New Method of Modeling Gear Faults. J Mech Des 1982;104:259–67. https://doi.org/10.1115/1.3256334.

[145] Decker HJ. Spiral bevel pinion crack detection in a helicopter gearbox. National aeronautics and space administration cleveland oh glenn research center; 2003.

[146] Decker HJ. Crack detection for aerospace quality spur gears. Defense Technical Information Center; 2002.

[147] Li CJ, Limmer JD. Model-based condition index for tracking gear wear and fatigue damage. Wear 2000;241:26–32. https://doi.org/10.1016/S0043-1648(00)00356-2.

[148] Hu C, Smith WA, Randall RB, Peng Z. Development of a gear vibration indicator and its application in gear wear monitoring. Mech Syst Signal Process 2016;76–77:319–36. https://doi.org/10.1016/j.ymssp.2016.01.018.

[149] Wu S, Gebraeel N, Lawley MA, Yih Y. A Neural Network Integrated Decision Support System for Condition-Based Optimal Predictive Maintenance Policy. IEEE

Trans Syst Man Cybern - Part Syst Hum 2007;37:226–36. https://doi.org/10.1109/TSMCA.2006.886368.

[150] Zhang X, Xiao L, Kang J. Degradation Prediction Model Based on a Neural Network with Dynamic Windows. Sensors 2015;15:6996–7015. https://doi.org/10.3390/s150306996.

[151] Wang WQ, Golnaraghi MF, Ismail F. Prognosis of machine health condition using neuro-fuzzy systems. Mech Syst Signal Process 2004;18:813–31. https://doi.org/10.1016/S0888-3270(03)00079-7.

[152] Deutsch J, He D. Using Deep Learning-Based Approach to Predict Remaining Useful Life of Rotating Components. IEEE Trans Syst Man Cybern Syst 2018;48:11–20. https://doi.org/10.1109/TSMC.2017.2697842.

[153] Zhao F, Tian Z, Zeng Y. Uncertainty Quantification in Gear Remaining Useful Life Prediction Through an Integrated Prognostics Method. IEEE Trans Reliab 2013;62:146–59. https://doi.org/10.1109/TR.2013.2241216.

[154] Zhao F, Tian Z, Bechhoefer E, Zeng Y. An Integrated Prognostics Method Under Time-Varying Operating Conditions. IEEE Trans Reliab 2015;64:673–86. https://doi.org/10.1109/TR.2015.2407671.

[155] Zhao F-Q, Xie M-J, Tian Z-G, Zeng Y. Integrated Equipment Health Prognosis Considering Crack Initiation Time Uncertainty and Random Shock. Chin J Mech Eng 2017;30:1383–95. https://doi.org/10.1007/s10033-017-0200-7.

[156] He D, Bechhoefer E, Dempsey P, Ma J. An Integrated Approach for Gear Health Prognostics, Fort Worth, TX: 2012.

[157] Choi S, Li CJ. Practical gear crack prognosis via gear condition index fusion, gear dynamic simulator, and fast crack growth model. Proc Inst Mech Eng Part J Syst Control Eng 2007;221:465–73. https://doi.org/10.1243/09596518JSCE248.

[158] Ambaye A. The Performance of Gear with Backlash: A Review. J App Mech Eng 2021;10:389.

[159] Errichello R, Muller J. How to analyze gear failures. J Fail Anal Prev 2002;2:8–16. https://doi.org/10.1007/BF02715492.

[160] Liang X, Zuo MJ, Feng Z. Dynamic modeling of gearbox faults: A review. Mech Syst Signal Process 2018;98:852–76. https://doi.org/10.1016/j.ymssp.2017.05.024.

[161] Ding Y, Rieger NF. Spalling formation mechanism for gears. Wear 2003;254:1307–17. https://doi.org/10.1016/S0043-1648(03)00126-1.

[162] Aslantaş K, Taşgetiren S. A study of spur gear pitting formation and life prediction. Wear 2004;257:1167–75. https://doi.org/10.1016/j.wear.2004.08.005.

[163] Chaari F, Fakhfakh T, Haddar M. Dynamic analysis of a planetary gear failure caused by tooth pitting and cracking. J Fail Anal Prev 2006;6:73–8. https://doi.org/10.1361/154770206X99343.

[164] Liang X, Zhang H, Liu L, Zuo MJ. The influence of tooth pitting on the mesh stiffness of a pair of external spur gears. Mech Mach Theory 2016;106:1–15. https://doi.org/10.1016/j.mechmachtheory.2016.08.005.

[165] Lei Y, Liu Z, Wang D, Yang X, Liu H, Lin J. A probability distribution model of tooth pits for evaluating time-varying mesh stiffness of pitting gears. Mech Syst Signal Process 2018;106:355–66. https://doi.org/10.1016/j.ymssp.2018.01.005.

[166] Chen K, Ma H, Che L, Li Z, Wen B. Comparison of meshing characteristics of helical gears with spalling fault using analytical and finite-element methods. Mech Syst Signal Process 2019;121:279–98. https://doi.org/10.1016/j.ymssp.2018.11.023.

[167] Zhang B, Liu H, Zhu C, Li Z. Numerical simulation of competing mechanism between pitting and micro-pitting of a wind turbine gear considering surface roughness. Eng Fail Anal 2019;104:1–12. https://doi.org/10.1016/j.engfailanal.2019.05.016.

[168] Kiefner JF, Vieth PH. A modified criterion for evaluating the remaining strength of corroded pipe. Battelle Columbus Div., OH (USA); 1989.

[169] Chebaro MR, Zhou W. A Limit State Function for Pipelines Containing Long Corrosion Defects, 2010, p. 511–7. https://doi.org/10.1115/IPC2010-31324.

[170] Klever FJ, Stewart G. New developments in burst strength predictions for locally corroded pipelines, American Society of Mechanical Engineers, New York, NY; 1995. https://www.osti.gov/biblio/205464.

[171] Benjamin AC, Andrade EQ de. Modified method for the assessment of the remaining strength of corroded pipelines 2003. https://www.osti.gov/etdeweb/biblio/20919099

[172] Kiefener J, Maxey W, Eiber R, Duffy A. Failure stress levels of flaws in pressurised cylinders. Prog Flaw Growth Fract Toughness Test 1973:461–81. https://www.astm.org/stp49657s.html.

[173] Mondal BC, Dhar AS. Improved Folias Factor and Burst Pressure Models for Corroded Pipelines. J Press Vessel Technol 2017;140. https://doi.org/10.1115/1.4038720.

[174] Kroese DP, Brereton T, Taimre T, Botev ZI. Why the Monte Carlo method is so important today. WIREs Comput Stat 2014;6:386–92. https://doi.org/10.1002/wics.1314.

[175] Pressman RS. Software engineering: a practitioner's approach. Palgrave macmillan; 2005.

[176] Kang L, Dixon S, Wang K, Dai J. Enhancement of signal amplitude of surface wave EMATs based on 3-D simulation analysis and orthogonal test method. NDT E Int 2013;59:11–7. https://doi.org/10.1016/j.ndteint.2013.05.003.

[177] Ji YB, Ru X, Yu M, Wang SW, Lu L, Qiao AN, et al. Extraction and determination of total flavonoids in jujube by alcohol extraction. IOP Conf Ser Earth Environ Sci 2017;100:012054. https://doi.org/10.1088/1755-1315/100/1/012054.

[178] Zhang H, Zhang J, Lin R, Li Y. Numerical Study on Mechanism Responses of Submarine Pipeline Impacted by Bar-Shaped Falling Object. J Pipeline Syst Eng Pract 2020;11:04020051. https://doi.org/10.1061/(ASCE)PS.1949-1204.0000505.

[179] Askari M, Aliofkhazraei M, Afroukhteh S. A comprehensive review on internal corrosion and cracking of oil and gas pipelines. J Nat Gas Sci Eng 2019;71:102971. https://doi.org/10.1016/j.jngse.2019.102971.

[180] Peng S, Zhang Z, Liu E, Liu W, Qiao W. A new hybrid algorithm model for prediction of internal corrosion rate of multiphase pipeline. J Nat Gas Sci Eng 2021;85:103716. https://doi.org/10.1016/j.jngse.2020.103716.

[181] Zakikhani K, Nasiri F, Zayed T, others. A review of failure prediction models for oil and gas pipelines. J Pipeline Syst Eng Pr 2020;11:03119001. https://ascelibrary.org/doi/abs/10.1061/%28ASCE%29PS.1949-1204.0000407.

[182] Palencia OG, Teixeira AP, Guedes Soares C. Safety of Pipelines Subjected to Deterioration Processes Modeled Through Dynamic Bayesian Networks. J Offshore Mech Arct Eng 2018;141. https://doi.org/10.1115/1.4040573.

[183] Abdelmoety AK, Zheng Q, Li Y, Kainat M, Yoosef-Ghodsi N, Adeeb S. Probability of Failure Associated with Design and Safety Factors for Intact and Corroded Pipes under Internal Pressure. J Pipeline Syst Eng Pract 2021;12:04021010. https://doi.org/10.1061/(ASCE)PS.1949-1204.0000544.

[184] Lu H, Xu Z-D, Iseley T, Matthews JC. Novel Data-Driven Framework for Predicting Residual Strength of Corroded Pipelines. J Pipeline Syst Eng Pract 2021;12:04021045. https://doi.org/10.1061/(ASCE)PS.1949-1204.0000587.

[185] Sun J, Cheng YF, Woo J, Kainat M, Hassanien S. Assessment of Interaction Between a Dent and an Adjacent Corrosion Feature on Pipelines and the Effect on Pipeline Failure Pressure by Finite-Element Modeling. J Pipeline Syst Eng Pract 2021;12:04021029. https://doi.org/10.1061/(ASCE)PS.1949-1204.0000570.

[186] Zhang S, Zhou W. Development of a burst capacity model for corroded pipelines considering corrosion defect width and a revised Folias factor equation. J Nat Gas Sci Eng 2021;88:103812. https://doi.org/10.1016/j.jngse.2021.103812.

[187] Bao J, Zhou W. Influence of depth thresholds and interaction rules on the burst capacity evaluation of naturally corroded pipelines. J Pipeline Sci Eng 2021;1:148–65. https://doi.org/10.1016/j.jpse.2021.01.001.

[188] Zhang S, Zhou W. Assessment of the interaction of corrosion defects on steel

pipelines under combined internal pressure and longitudinal compression using finite element analysis. Thin-Walled Struct 2022;171:108771. https://doi.org/10.1016/j.tws.2021.108771.

[189] Jones N, Birch SE, Birch RS, Zhu L, Brown M. An Experimental Study on the Lateral Impact of Fully Clamped Mild Steel Pipes. Proc Inst Mech Eng Part E J Process Mech Eng 1992;206:111–27. https://doi.org/10.1243/PIME_PROC_1992_206_207_02.

[190] Netto TA, Ferraz US, Estefen SF. The effect of corrosion defects on the burst pressure of pipelines. J Constr Steel Res 2005;61:1185–204. https://doi.org/10.1016/j.jcsr.2005.02.010.

[191] Benjamin AC, Cunha DJS. New Method For the Prediction of the Failure Pressure of Interacting Corrosion Defects, OnePetro; 2007. https://onepetro.org/ISOPEIOPEC/proceedings-abstract/ISOPE07/All-ISOPE07/ISOPE-I-07-171/11804.

[192] Zhang S, Zhou W, Zhang S. Development of a Burst Capacity Model for Corroded Pipelines Under Internal Pressure and Axial Compression Using Artificial Neural Network, American Society of Mechanical Engineers Digital Collection; 2021. https://doi.org/10.1115/IPC2020-9631.

[193] Shuai Y, Zhang X, Feng C, Han J, Cheng YF. A novel model for prediction of burst capacity of corroded pipelines subjected to combined loads of bending moment and axial compression. Int J Press Vessels Pip 2022;196:104621. https://doi.org/10.1016/j.ijpvp.2022.104621.

[194] Caleyo F, González JL, Hallen JM. A study on the reliability assessment methodology for pipelines with active corrosion defects. Int J Press Vessels Pip 2002;79:77–86. https://doi.org/10.1016/S0308-0161(01)00124-7.

[195] Bin Suo, Xinhui Guo. Sensitivity Analysis for Epistemic Uncertain System Based on Sobol'Method. J Donghua Univ Ed 2018;35:344–7. http://www.cqvip.com/qk/86692x/20184/676186633.html.

[196] Tee KF, Pesinis K. Reliability prediction for corroding natural gas pipelines. Tunn Undergr Space Technol 2017;65:91–105. https://doi.org/10.1016/j.tust.2017.02.009.

[197] Council H. How hydrogen empowers the energy transition (2017) 2021.

[198] Looney B. Statistical Review of World Energy. 69th ed. London, UK: BP; 2020; 69:66. https://www.bp.com/en/global/corporate/energy-economics/statistical-review-of-world-energy.html.

[199] Mah AXY, Ho WS, Bong CPC, Hassim MH, Liew PY, Asli UA, et al. Review of hydrogen economy in Malaysia and its way forward. Int J Hydrog Energy 2019;44:5661–75. https://doi.org/10.1016/j.ijhydene.2019.01.077.

[200] Uson LC, Aguarta IA, Elu LR, Burkhalter E, Hermosilla A. Green hydrogen from wind and solar: Design, construction and one year operation of the ITHER project. vol. 1, 2008, p. 206–9. https://nvlpubs.nist.gov/nistpubs/jres/115/6/V115.N06.A04.pdf.

[201] Ogden JM. Prospects for Building a Hydrogen Energy Infrastructure. Annu Rev Energy Environ 1999;24:227–79. https://doi.org/10.1146/annurev.energy.24.1.227.

[202] Dadfarnia M, Sofronis P, Brouwer J, Sosa S. Assessment of resistance to fatigue crack growth of natural gas line pipe steels carrying gas mixed with hydrogen. Int J Hydrog Energy 2019;44:10808–22. https://doi.org/10.1016/j.ijhydene.2019.02.216.

[203] Taskin M, Utsumi G, Kato Y. Observation of ultrasonic signal and measurement of H2 concentration from the exterior of a metal pipe. Int J Hydrog Energy 2019;44:23503–12. https://doi.org/10.1016/j.ijhydene.2019.06.159.

[204] Melaina MW, Antonia O, Penev M. Blending Hydrogen into Natural Gas Pipeline Networks: A Review of Key Issues 2013. https://doi.org/10.2172/1068610.

[205] Elazzizi A, Hadj Meliani M, Khelil A, Pluvinage G, Matvienko YG. The master failure curve of pipe steels and crack paths in connection with hydrogen embrittlement. Int J Hydrog Energy 2015;40:2295–302. https://doi.org/10.1016/j.ijhydene.2014.12.040.

[206] Zhou W, Hong HP, Zhang S. Impact of dependent stochastic defect growth on

system reliability of corroding pipelines. Int J Press Vessels Pip 2012;96–97:68–77. https://doi.org/10.1016/j.ijpvp.2012.06.005.

[207] Zhang S, Zhou W, Qin H. Inverse Gaussian process-based corrosion growth model for energy pipelines considering the sizing error in inspection data. Corros Sci 2013;73:309–20. https://doi.org/10.1016/j.corsci.2013.04.020.

[208] Heidary R, Gabriel SA, Modarres M, Groth KM, Vahdati N. A Review of Data-Driven Oil and Gas Pipeline Pitting Corrosion Growth Models Applicable for Prognostic and Health Management. Int J Progn Health Manag 2018;9. https://doi.org/10.36001/ijphm.2018.v9i1.2695.

[209] Zhou W, Xiang W, Hong HP. Sensitivity of system reliability of corroding pipelines to modeling of stochastic growth of corrosion defects. Reliab Eng Syst Saf 2017;167:428–38. https://doi.org/10.1016/j.ress.2017.06.025.

[210] Liu ZG, Mu ZT. Research on Aircraft LY12CZ Aluminum Alloy Corrosion Damage Prediction Based on ARIMA Model. Adv Mater Res 2011;308–310:1016–22. https://doi.org/10.4028/www.scientific.net/AMR.308-310.1016.

[211] Nanninga NE, Levy YS, Drexler ES, Condon RT, Stevenson AE, Slifka AJ. Comparison of hydrogen embrittlement in three pipeline steels in high pressure gaseous hydrogen environments. Corros Sci 2012;59:1–9. https://doi.org/10.1016/j.corsci.2012.01.028.

[212] Briottet L, Batisse R, de Dinechin G, Langlois P, Thiers L. Recommendations on X80 steel for the design of hydrogen gas transmission pipelines. Int J Hydrog Energy 2012;37:9423–30. https://doi.org/10.1016/j.ijhydene.2012.02.009.

[213] Ohaeri E, Eduok U, Szpunar J. Hydrogen related degradation in pipeline steel: A review. Int J Hydrog Energy 2018;43:14584–617. https://doi.org/10.1016/j.ijhydene.2018.06.064.

[214] Chen Z, Chen Y, Wang W, Lu K, Yang H, Zhu W. Failure pressure analysis of hydrogen storage pipeline under low temperature and high pressure. Int J Hydrog Energy

2020;45:23142–50. https://doi.org/10.1016/j.ijhydene.2020.06.129.

[215] Mondal BC, Dhar AS. Interaction of multiple corrosion defects on burst pressure of pipelines. Can J Civ Eng 2017. https://doi.org/10.1139/cjce-2016-0602.

[216] Zhang H, Tian Z. Reliability assessment of corroded pipeline considering multiple defects interaction based on an artificial neural network method. 2020 Asia-Pac. Int. Symp. Adv. Reliab. Maint. Model. APARM, 2020, p. 1–6. https://doi.org/10.1109/APARM49247.2020.9209428.

[217] ASME B31G : Manual for Determining the Remaining Strength of Corroded Pipelines. New York: American Society of Mechanical Engineers, 9780791834480; 2012. https://www.asme.org/codes-standards/find-codes-standards/b31g-manual-determining-remaining-strength-corroded-pipelines.

[218] Tiwari GP, Bose A, Chakravartty JK, Wadekar SL, Totlani MK, Arya RN, et al. A study of internal hydrogen embrittlement of steels. Mater Sci Eng A 2000;286:269–81. https://doi.org/10.1016/S0921-5093(00)00793-0.

[219] Titov AI, Lun-Fu AV, Gayvaronskiy AV, Bubenchikov MA, Bubenchikov AM, Lider AM, et al. Hydrogen Accumulation and Distribution in Pipeline Steel in Intensified Corrosion Conditions. Materials 2019;12:1409. https://doi.org/10.3390/ma12091409.

[220] Barrera O, Bombac D, Chen Y, Daff TD, Galindo-Nava E, Gong P, et al. Correction to: Understanding and mitigating hydrogen embrittlement of steels: a review of experimental, modelling and design progress from atomistic to continuum. J Mater Sci 2018;53:10593–4. https://doi.org/10.1007/s10853-018-2291-7.

[221] Wang H. Study on the hydrogen embrittlement susceptibility of X100 pipeline steel. Tian Jing University, 2017. https://xuewen.cnki.net/CMFD-1019701593.nh.html

[222]Benjamin A C, Cunha D J S. New method for the prediction of the failure pressure of interacting corrosion defects, The Seventeenth International Offshore and Polar Engineering Conference. OnePetro, 2007. https://onepetro.org/ISOPEIOPEC/proceedings-abstract/ISOPE07/All-ISOPE07/ISOPE-

I-07-171/11804.

[223]Chiodo MSG, Ruggieri C. Failure assessments of corroded pipelines with axial defects using stress-based criteria: Numerical studies and verification analyses. Int J Press Vessels Pip 2009;86:164–76. https://doi.org/10.1016/j.ijpvp.2008.11.011.

[224] Xie M, Tian Z. Risk-based pipeline re-assessment optimization considering corrosion defects. Sustain Cities Soc 2018;38:746–57. https://doi.org/10.1016/j.scs.2018.01.021.

[225] Benjamin AC, Freire JLF, Vieira RD, Diniz JLC, de Andrade EQ. Burst Tests on Pipeline Containing Interacting Corrosion Defects, American Society of Mechanical Engineers Digital Collection; 2008, p. 403–17. https://doi.org/10.1115/OMAE2005-67059.

[226] Li C, Yang Z, Yan H, Wang T. The Application and Research of the GA-BP Neural Network Algorithm in the MBR Membrane Fouling. Abstr Appl Anal 2014;2014:e673156. https://doi.org/10.1155/2014/673156.

[227] Li Y, Gong J, Yu W, Huang W, Wen K. Gas Supply Reliability Analysis of a Natural Gas Pipeline System Considering the Effects of Demand Side Management. J Press Vessel Technol 2021;143. https://doi.org/10.1115/1.4049743.

[228] Lu D, Cong G, Li B. A New Risk Assessment Model to Check Safety Threats to Long-Distance Pipelines. J Press Vessel Technol 2022;144. https://doi.org/10.1115/1.4053224.

[229] Li S, Qi Y, Li Z, Li H, Zhang J. A novel treatment method and construction technology of the pipeline gushing water geohazards in karst region. Tunn Undergr Space Technol 2021;113:103939. https://doi.org/10.1016/j.tust.2021.103939.

[230] Liu M, Jin X, Wang L, Yang F, Tang J. Numerical investigation of local scour around a vibrating pipeline under steady currents. Ocean Eng 2021;221:108546. https://doi.org/10.1016/j.oceaneng.2020.108546.

[231] Li S, Duan Q, Zhang H, Wang J. Failure analysis of the floating pipeline with

defect under flooding load. Eng Fail Anal 2017;77:65–75. https://doi.org/10.1016/j.engfailanal.2017.02.011.

[232] Baker Jr M, Fessler R R. Pipeline corrosion final report[J]. Rep. No. DTRS56-02-D-70036, US Department of Transportation Pipeline and Hazardous Materials Safety Administration Office of Pipeline Safety, Washington, DC, 2008. https://www.phmsa.dot.gov/pipeline/gas-distribution-integrity-management/dimp-pipeline-corrosion-final-report-michael-baker-jr-november-2008.

[233] Gholami H, Shahrooi S, Shishesaz M. Predicting the Burst Pressure of High-Strength Carbon Steel Pipe with Gouge Flaws Using Artificial Neural Network. J Pipeline Syst Eng Pract 2020;11:04020034. https://doi.org/10.1061/(ASCE)PS.1949-1204.0000478.

[234] Mondal BC, Dhar AS. Burst pressure of corroded pipelines considering combined axial forces and bending moments. Eng Struct 2019;186:43–51. https://doi.org/10.1016/j.engstruct.2019.02.010.

[235] Chegeni B, Jayasuriya S, Das S. Effect of corrosion on thin-walled pipes under combined internal pressure and bending. Thin-Walled Struct 2019;143:106218. https://doi.org/10.1016/j.tws.2019.106218.

[236] Shuai Y, Wang X-H, Feng C, Zhu Y, Wang C-L, Sun T, et al. A novel strain-based assessment method of compressive buckling of X80 corroded pipelines subjected to bending moment load. Thin-Walled Struct 2021;167:108172. https://doi.org/10.1016/j.tws.2021.108172.

[237] Xiao ZG, Zhao XL. Prediction of natural frequency of free spanning subsea pipelines. Int J Steel Struct 2010;10:81–9. https://doi.org/10.1007/BF03249514.

[238] Taheri A, Shabani M, Daghigh M. Investigation of the Effect of Local Buckling and VIV Fatigue on Failure Probability of Subsea Pipelines in Iranian South Pars Gas Field. Int J Marit Technol 2018;9:23–32. https://doi.org/10.29252/ijmt.9.23.

[239] Van den Abeele F, Boël F, Hill M. Fatigue Analysis of Free Spanning Pipelines

Subjected to Vortex Induced Vibrations, American Society of Mechanical Engineers Digital Collection; 2013. https://doi.org/10.1115/OMAE2013-10625.

[240] Hart JD, Sause R, Ford GW, Row DG. Mitigation of wind-induced vibration of arctic pipeline systems. Proc. Int. Conf. OFFSHORE Mech. Arct. Eng., American Society of Mechanical Engineers; 1992, p. 169–169. http://ssdinc.com/documents/WIV_OMAE92.pdf.

[241] Collins MG, Hart JD. The Impact of High Frequency Wind-Induced Vibration On Arctic Pipeline Systems, OnePetro; 2006. https://onepetro.org/ISOPEIOPEC/proceedings-abstract/ISOPE06/All-ISOPE06/ISOPE-I-06-324/9932.

[242] Cunha DJS, Benjamin AC, Silva RCC, Guerreiro JNC, Drach PRC. Fatigue analysis of corroded pipelines subjected to pressure and temperature loadings. Int J Press Vessels Pip 2014;113:15–24. https://doi.org/10.1016/j.ijpvp.2013.10.013.

[243] Shabani MM, Taheri A, Daghigh M. Reliability assessment of free spanning subsea pipeline. Thin-Walled Struct 2017;120:116–23. https://doi.org/10.1016/j.tws.2017.08.026.

[244] Badamchi K, Showkati H. Experiments on buckling behavior of thin-walled steel pipes subjected to axial compression and external pressure. Thin-Walled Struct 2022;174:109122. https://doi.org/10.1016/j.tws.2022.109122.

[245] Xu L, Lin M. Numerical study on critical axial forces of upheaval buckling for initially stressed submarine pipelines on uneven seabed. Ocean Eng 2017;145:344–58. https://doi.org/10.1016/j.oceaneng.2017.09.013.

[246] Li L, Lin M. Modeling and Analysis of a Free Spanning Pipeline With Randomly Distributed Corrosion, American Society of Mechanical Engineers Digital Collection; 2010, p. 751–8. https://doi.org/10.1115/OMAE2010-20781.

[247] Zhang J, Xie R. Mechanical Behavior Analysis of Suspended Pipelines Caused by Ground Subsidence. J Pipeline Syst Eng Pract 2021;12:04021030.

https://doi.org/10.1061/(ASCE)PS.1949-1204.0000556.

[248] Zhang H, Tian Z. Failure analysis of corroded high-strength pipeline subject to hydrogen damage based on FEM and GA-BP neural network. Int J Hydrog Energy 2022;47:4741–58. https://doi.org/10.1016/j.ijhydene.2021.11.082.

[249] Zhao X. Deformation and stress analysis of buried pipeline crossing mining subsidence area and remote monitoring. Chin MS Thesis Coll Mechatron Eng Southwest Pet Univ 2015. https://kns.cnki.net/kcms/detail/detail.aspx?dbcode=CMFD&dbname=CMFD201502&filename=1015599297.nh&uniplatform=NZKPT&v.

[250] Benjamin A, Cunha D, Campello G, Roveri F, Silva R, Guerreiro J. Fatigue Life Assessment of a Drilling Riser Containing Corrosion Pits. 2008. https://doi.org/10.4043/19251-MS.

[251] De la Cruz M, Chong WWF, Teodorescu M, Theodossiades S, Rahnejat H. Transient mixed thermo-elastohydrodynamic lubrication in multi-speed transmissions. Tribol Int 2012;49:17–29. https://doi.org/10.1016/j.triboint.2011.12.006.

[252] Castro J, Seabra J. Global and local analysis of gear scuffing tests using a mixed film lubrication model. Tribol Int 2008;41:244–55. https://doi.org/10.1016/j.triboint.2007.07.005.

[253] Amarnath M, Chandramohan S, Seetharaman S. Experimental investigations of surface wear assessment of spur gear teeth. J Vib Control 2012;18:1009–24. https://doi.org/10.1177/1077546311399947.

[254] KRANTZ TL, KAHRAMAN A. An Experimental Investigation of the Influence of the Lubricant Viscosity and Additives on Gear Wear. Tribol Trans 2004;47:138–48. https://doi.org/10.1080/05698190490278949.

[255] Sudhagar S, Bhaskara Rao L. Analytical and Experimental Studies on Wear in Spur Gear Running in Dry Condition. J Tribol 2021;144. https://doi.org/10.1115/1.4050903.

[256] Qin W, Zhang Y, Li C. Determination of wear coefficient in mixed lubrication using FEM. Appl Math Model 2018;59:629–39. https://doi.org/10.1016/j.apm.2018.02.024.

[257] Hegadekatte V, Hilgert J, Kraft O, Huber N. Multi time scale simulations for wear prediction in micro-gears. Wear 2010;268:316–24. https://doi.org/10.1016/j.wear.2009.08.017.

[258] Asi O. Fatigue failure of a helical gear in a gearbox. Eng Fail Anal 2006;13:1116–25. https://doi.org/10.1016/j.engfailanal.2005.07.020.

[259] Wei J, Zhang A, Gao P. A study of spur gear pitting under EHL conditions: Theoretical analysis and experiments. Tribol Int 2016;94:146–54. https://doi.org/10.1016/j.triboint.2015.08.037.

[260] Luo Y, Baddour N, Liang M. Dynamical modeling and experimental validation for tooth pitting and spalling in spur gears. Mech Syst Signal Process 2019;119:155–81. https://doi.org/10.1016/j.ymssp.2018.09.027.

[261] Amarnath M, Sujatha C, Swarnamani S. Experimental studies on the effects of reduction in gear tooth stiffness and lubricant film thickness in a spur geared system. Tribol Int 2009;42:340–52. https://doi.org/10.1016/j.triboint.2008.07.008.

[262] Wu J, Yang Y, Cheng J. A novel estimation method of friction coefficient for evaluating gear pitting fault. Eng Fail Anal 2021;129:105715. https://doi.org/10.1016/j.engfailanal.2021.105715.

[263] Mao K, Li W, Hooke CJ, Walton D. Friction and wear behaviour of acetal and nylon gears. Wear 2009;267:639–45. https://doi.org/10.1016/j.wear.2008.10.005.

[264] Paris P, Erdogan F. A Critical Analysis of Crack Propagation Laws. J Basic Eng 1963;85:528–33. https://doi.org/10.1115/1.3656900.

[265] Shen Z, Qiao B, Yang L, Luo W, Yang Z, Chen X. Fault mechanism and dynamic modeling of planetary gear with gear wear. Mech Mach Theory 2021;155:104098. https://doi.org/10.1016/j.mechmachtheory.2020.104098.

[266] Wang H, Tang L, Zhou C, Shi Z. Wear life prediction method of crowned double helical gear drive in point contact mixed elastohydrodynamic lubrication. Wear 2021;484–485:204041. https://doi.org/10.1016/j.wear.2021.204041.

[267] Gebraeel NZ, Lawley MA. A Neural Network Degradation Model for Computing and Updating Residual Life Distributions. IEEE Trans Autom Sci Eng 2008;5:154–63. https://doi.org/10.1109/TASE.2007.910302.

[268] Tian Z, Wong L, Safaei N. A neural network approach for remaining useful life prediction utilizing both failure and suspension histories. Mech Syst Signal Process 2010;24:1542–55. https://doi.org/10.1016/j.ymssp.2009.11.005.

[269] Varela F, Yongjun Tan M, Forsyth M. An overview of major methods for inspecting and monitoring external corrosion of on-shore transportation pipelines. Corros Eng Sci Technol 2015;50:226–35. https://doi.org/10.1179/1743278215Y.0000000013.

[270] Ni Q, Ji J, Feng K. Data-driven prognostic scheme for bearings based on a novel health indicator and gated recurrent unit network. IEEE Trans Ind Inform 2022:1–1. https://doi.org/10.1109/TII.2022.3169465.

[271] Zaidi SSH, Aviyente S, Salman M, Shin K-K, Strangas EG. Prognosis of Gear Failures in DC Starter Motors Using Hidden Markov Models. IEEE Trans Ind Electron 2011;58:1695–706. https://doi.org/10.1109/TIE.2010.2052540.

[272] Zio E, Peloni G. Particle filtering prognostic estimation of the remaining useful life of nonlinear components. Reliab Eng Syst Saf 2011;96:403–9. https://doi.org/10.1016/j.ress.2010.08.009.

[273] Zhao F, Tian Z, Zeng Y. A stochastic collocation approach for efficient integrated gear health prognosis. Mech Syst Signal Process 2013;39:372–87. https://doi.org/10.1016/j.ymssp.2013.03.004.

[274] Rao PS, Sriraj N, Farookh M. Contact stress analysis of spur gear for different materials using ANSYS and Hertz equation. Int J Mod Stud Mech Eng 2015;1:45–52. https://www.arcjournals.org/international-journal-of-modern-studies-in-mechanical-

engineering/volume-1-issue-1/5

[275] Gupta B, Choubey A, Varde GV. Contact stress analysis of spur gear. Int J Eng Res Technol 2012;1:1–7. https://www.ijert.org/research/contact-stress-analysis-of-spur-gear-IJERTV1IS4052.pdf

[276] Coppe A, Haftka RT, Kim NH, Yuan F-G. Uncertainty reduction of damage growth properties using structural health monitoring. J Aircr 2010;47:2030–8. https://doi.org/10.2514/1.C000279

[277] An D, Choi J-H, Kim NH. Identification of correlated damage parameters under noise and bias using Bayesian inference. Struct Health Monit 2012;11:293–303. https://doi.org/10.1177/1475921711424520.

[278] Abodol Rasoul S, Ali Maozemi G, Reza Akbari A. Finite Element Analysis of Elastic-Plastic Contact Mechanic Considering the Effect of Contact Geometry and Material Properties. J Surf Eng Mater Adv Technol 2011;2011. https://doi.org/10.4236/jsemat.2011.13019.

[279] Sari MR, Haiahem A, Flamand L. Effect of Lubricant Contamination on Gear Wear. Tribol Lett 2007;27:119–26. https://doi.org/10.1007/s11249-007-9215-z.